



Peifer Bezerra, Daniel (2018) *The pattern and style of landscape evolution in post-orogenic settings*. PhD thesis.

<https://theses.gla.ac.uk/30680/>

Copyright and moral rights for this work are retained by the author

A copy can be downloaded for personal non-commercial research or study, without prior permission or charge

This work cannot be reproduced or quoted extensively from without first obtaining permission in writing from the author

The content must not be changed in any way or sold commercially in any format or medium without the formal permission of the author

When referring to this work, full bibliographic details including the author, title, awarding institution and date of the thesis must be given

Enlighten: Theses

<https://theses.gla.ac.uk/>  
[research-enlighten@glasgow.ac.uk](mailto:research-enlighten@glasgow.ac.uk)

# THE PATTERN AND STYLE OF LANDSCAPE EVOLUTION IN POST-OROGENIC SETTINGS

**Daniel Peifer Bezerra**

BSc, MSc, Federal University of Minas Gerais

Submitted in the fulfilment of the requirements  
for the Degree of Doctor of Philosophy (Ph.D.)

School of Geographical and Earth Sciences  
College of Science and Engineering



April 2018

## **Declaration of Originality**

I declare that, except where explicit reference is made to the contribution of others, that this dissertation is the result of my own work and has not been submitted for any other degree at the University of Glasgow or any other institution.

A handwritten signature in black ink, reading "Daniel Peifer Bezerra", is written over a solid horizontal line. The signature is written in a cursive style with a large initial 'D'.

Daniel Peifer Bezerra



## Abstract

The long-lasting persistence of mountainous topography in tectonically stable, intraplate settings remains enigmatic. Conceptual and numerical models have indicated that the cessation of tectonic activity, and thus the absence of counteracting forces to the destructive surface processes, leads to a long-term decline of relief. However, there are several examples of post-orogenic mountain belts (e.g., the Appalachians, the Cape Mountains, the Ural Mountains) that are marked by a current ‘residual’ topography, with locally steep hillslopes and channel gradients that, according to the models, should have long since been flattened. The question of how these mountains have survived without any significant active tectonics remains unanswered. The key conundrum is that rates of denudation worldwide are known to vary primarily with topographic relief, yet post-orogenic landscapes characterised by high relief are often found to have low denudation rates.

This thesis presents data that quantify the relationships between topography, denudation rates, and lithology in a classic post-orogenic setting, to investigate how post-orogenic landscapes develop through time. This fundamental objective was met by (i) performing quantitative analysis of channel and hillslope topography, and (ii) measuring the rates at which the land surface has developed. The case study area is Brazil’s Quadrilátero Ferrífero (QF), an unglaciated, high relief, ancient landscape that is thought to have been tectonically stable for the last 500 Myr; the area is remote (~400 km) from the distant base level and consists of both resistant and weak lithologies.

A suite of modern geomorphic techniques was used to extract quantitative topographic information of the QF over different scales, ranging from local channel and hillslope morphology to catchment-averaged parameters, including basins of different orders. The topographic analyses demonstrated that the topography of the QF is complex, featuring a wide range of topographic forms, with an overall subdued steepness and relief but marked by rare, extremely steep channels and gradients. Topographic forms are adjusted to rock type, whereby high relief is associated with resistant rocks, contrasting with the lower relief associated with low-resistance rocks. Whereas stream profiles of rivers flowing in the southwestern part of the QF are concave-up, many channels are convex-up in

form, notably over the eastern part of the QF. Knickpoints are common features in the drainage network, associated primarily with resistant rocks but also lying close to pre-Paleozoic faults. In summary, the post-orogenic topography of the QF is not featureless, and relief is primarily controlled by the exposed bedrock resistance.

Estimates of catchment-averaged denudation rates were derived from measurements of the concentration of in situ cosmogenic  $^{10}\text{Be}$  in fluvial sediments. The sampling strategy was based on the results of the quantitative topographic analysis, including drainage basins displaying different topographic characteristics, ranging from subdued to pronounced topography, and different exposed bedrock resistance, from resistant quartzites to weak (under tropical conditions) gneisses and granitic rocks.  $^{10}\text{Be}$ -derived catchment-averaged denudation rates for the QF are overall low ( $\leq 30$  m/Myr). Still, denudation rates are not the same everywhere; denudation rates vary by a factor of  $\sim 5$ , from the east ( $< 4$  m/Myr) to the southwest (up to 30 m/Myr). Catchment-averaged denudation rates display a negative correlation with every catchment-averaged topographic parameter, including channel and hillslope steepness. On the other hand, rock resistance and basin topography are positively related to the QF; the more resistant the exposed rock is to denudation, the higher and more rugged is the basin relief.

These results indicate that the spatial distribution of rocks with different resistance is the first-order control on the pattern of denudation in the QF. The extremely low denudation rates of the quartzite basins, irrespective of their steep topography, and the higher denudation rates of basins underlain by less resistant rocks and less rugged topography, demonstrate that the spatial variability in bedrock resistance is effectively overriding channel and hillslope steepness in determining denudation rates, even inverting the normal, positive relationship between denudation and relief. Also, the spatial variability in denudation rates, with low denudation rates in the uplands and higher in the lowlands, implies that relief is increasing with time instead of decreasing. The empirical dataset suggests that the QF has an ancient origin and has survived for many millions of years controlled primarily by the resistance of the underlying bedrock plus the effect of denudational isostatic rebound.

# Table of Contents

Declaration of Originality .....	2
Abstract .....	4
Table of Contents .....	6
List of Tables.....	10
List of Figures.....	12
Acknowledgements .....	17
Acronyms .....	20
Abbreviations and Symbols .....	22
<b>CHAPTER 1: Introduction.....</b>	<b>30</b>
1.1 Background to the research.....	30
1.2 Project objectives .....	32
1.3 Research design, innovative character and thesis outline .....	34
<b>CHAPTER 2: The Study Area - The Quadrilátero Ferrífero (Brazil).....</b>	<b>38</b>
2.1 Why the QF? .....	38
2.2 Regional background .....	41
2.3 Geological context of the qf.....	45
2.4 Geomorphic research in the QF .....	57
<b>CHAPTER 3: Quantifying Topography in the QF: Theoretical Background and Methods .....</b>	<b>62</b>
3.1 Introduction .....	62
3.2 Theoretical background .....	63
3.2.1 Evolution of erosive landscapes .....	63
3.2.2 Timescale of relief reduction in post-orogenic landscapes.....	67
3.3 Methods and data.....	75
3.3.1 Overview .....	75
3.3.2 Topographic parameters.....	76
3.3.3 Local topography analysis .....	79

3.3.4 Catchment-averaged topographic analysis .....	79
3.3.5 Cluster analysis .....	83
3.3.6 Stream-profile analysis .....	87
<b>CHAPTER 4: Quantifying Topography in the QF: Results and Discussion .....</b>	<b>96</b>
4.1 Results .....	96
4.1.1 Local topography analysis .....	96
4.1.2 Local topography versus lithology.....	106
4.1.3 Catchment-averaged topographic metrics.....	108
4.1.4 Cluster analysis .....	115
4.1.5 Stream-profile analysis .....	119
4.1.6 Summary of the results .....	131
4.2 Discussion .....	132
4.2.1 Topography of the qf as a classic post-orogenic setting .....	133
4.2.2 River channels in the qf .....	136
4.2.3 Catchment-averaged topography .....	139
4.2.4 Topography and landscape evolution in the qf .....	139
4.3 Conclusion .....	141
<b>CHAPTER 5: Quantifying Denudation Rates in the QF .....</b>	<b>144</b>
5.1 Introduction .....	144
5.2 Theoretical background .....	145
5.2.1 Estimating denudation rates .....	145
5.2.2 Principles of the analysis of cosmogenic isotopes.....	147
5.2.3 Denudation rates from in situ cosmogenic isotopes.....	151
5.3 Methods and data.....	157
5.3.1 Overview .....	157
5.3.2 Sampling strategy.....	158
5.3.3 Catchment-averaged geomorphic parameters .....	167
5.3.4 Sampling.....	168

5.3.5 Sample processing .....	168
5.3.6 Estimating denudation rates from $^{10}\text{Be}$ concentrations.....	171
5.3.7 Bivariate regressions between denudation rates and geomorphic parameters.....	175
5.3.8 Preliminary estimation of bedrock erodibility factor for the QF.....	175
5.4 Results.....	176
5.4.1 Pattern of denudation of the qf.....	176
5.4.2 Bivariate regressions between catchment-averaged parameters.....	190
5.4.3 Denudation rates versus geomorphic metrics .....	198
5.4.4 Lithology and its influence on topography and denudation rates.....	203
5.4.5 Preliminary estimates of the relative values of $K$ in the QF.....	206
5.4.6 Summary of the results .....	209
5.5 Discussion .....	210
5.6 Conclusion .....	218
<b>CHAPTER 6: Key contributions, Interpretation, and Future Research .....</b>	<b>222</b>
6.1 Key contributions .....	222
6.2 Interpretation .....	224
6.2.1 Theoretical context .....	224
6.2.2 Final remarks: towards a new hypothesis on how post-orogenic landscapes evolve.....	227
6.3 Future research opportunities.....	230
<b>References .....</b>	<b>232</b>
<b>Appendix A .....</b>	<b>264</b>
<b>Appendix B .....</b>	<b>272</b>



## List of Tables

Table 1. The fundamental features that make the QF an optimal test site for post-orogenic landscapes. ....	40
Table 2. Different topographic models for a varying number of cluster solutions. ....	85
Table 3. Mean $R^2$ values between every pairwise combination of catchment-averaged parameters for the dataset comprising basins with area > 5 km <sup>2</sup> .....	110
Table 4. Mean $R^2$ values between every pairwise combination of catchment-averaged parameters for the dataset comprising second-order basins. ....	111
Table 5. Results of the post-hoc test for the lithological and topographic models for two, three, and four-cluster solutions. ....	118
Table 6. Information on commonly used cosmogenic nuclides .....	152
Table 7. Assumptions for the use of in situ cosmogenic nuclides for catchments. ....	156
Table 8. Average density values per lithology. ....	173
Table 9. Catchment-averaged density values for the analysed basins using the values on Table 8 as input.....	174
Table 10. <sup>10</sup> Be analytical results and derived denudation rate data .....	179
Table 11. Correlation matrix between the catchment-averaged parameters. $R^2$ values denote the goodness-of-fit of linear regressions. ....	197
Table 12. Goodness-of-fit of linear and power models for bivariate plots between denudation rates and catchment-averaged parameters.....	203
Table 13. Bedrock erodibility factor ( $K$ ) values reported in this contribution and by Stock and Montgomery (1999).....	207



## List of Figures

Figure 1. The geographical context of the QF - Brazil.....	39
Figure 2. Different landforms in the QF.....	44
Figure 3. Simplified geology of the QF - Brazil.....	46
Figure 4. A representative stratigraphic column of the rocks underlying the QF.. .....	47
Figure 5. Main structural features of the QF .....	50
Figure 6. Three simplified geological cross-sections of the QF.....	51
Figure 7. Metamorphic zones of the QF .....	52
Figure 8. The spatial distribution of the historic earthquakes in the QF .....	53
Figure 9. Simplified lithological map of the QF.....	55
Figure 10. The spatial distribution of Cenozoic units in the QF, excluding iron duricrusts.....	56
Figure 11. Schematic representation of post-orogenic relief reduction through time following Ahnert (1970).. .....	70
Figure 12. Simplified scheme of a ‘declining’ transient landscape following Baldwin et al. (2003).. .....	71
Figure 13. Bivariate regressions between (1) catchment-averaged mean slope angle and (2) normalised steepness index .....	77
Figure 14. Schematic representation of the stream-order classification by Strahler (1957).. .....	80
Figure 15. The distribution of the analysed second-order and third-order basins. .....	81
Figure 16. The distribution of the analysed fourth-order, fifth-order, sixth-order, and seventh-order basins. ....	82
Figure 17. An example of how different topographic clusters are associated with varying topographic characteristics.....	86
Figure 18. Schematic example of how the algorithm for the automatic extraction of knickpoints by Neely et al. (2017) works.. .....	89
Figure 19. The ‘unfiltered’ output of knickpoints for the QF .....	91
Figure 20. The ‘filtering’ of knickpoints with a magnitude higher than 50 m. ....	92
Figure 21. The spatial distribution of elevation for the QF; and the histogram of its distribution.....	98

Figure 22. The spatial distribution of slope for the QF; and the histogram of its distribution .....	99
Figure 23. The spatial distribution of normalised steepness index for the QF; and the histogram of its distribution.....	100
Figure 24. The spatial distribution of the parameter local relief for the QF; and the histogram of its distribution.....	102
Figure 25. The spatial distribution and superposition of the 4 <sup>th</sup> quartile of the local topographic parameters elevation, local relief, and slope .....	103
Figure 26. The spatial distribution of the kernel density of faults for the QF; and the histogram of its distribution.....	104
Figure 27. The spatial distribution of the mean annual precipitation for the QF; and the histogram of its distribution .....	105
Figure 28. The distribution of local geomorphic parameters per lithology.....	107
Figure 29. The distribution of catchment-averaged mean slope angle; and normalised steepness index for datasets comprising second-, third-, fourth, fifth-order basins.....	108
Figure 30. Scatter plot of catchment-averaged mean slope angle and normalised steepness index for datasets consisting of: second-order basins; third-order basins. ....	113
Figure 31. Scatter plot of catchment-averaged mean slope angle and normalised steepness index for datasets consisting of: fourth-order basins; all basins with an area > than 5 km <sup>2</sup> . ....	114
Figure 32. Lithological and topographic clusters for a two-cluster solution ....	115
Figure 33. Lithological and topographic clusters for a three-cluster solution ..	116
Figure 34. Lithological and topographic clusters for a four-cluster solution ...	117
Figure 35. Longitudinal profiles of channels flowing in different geomorphic contexts in the QF .....	120
Figure 36. Composite stream-profiles and associated log slope versus log area plots for rivers flowing in different geomorphic contexts in the QF .....	122
Figure 37. The spatial distribution of the filtered knickpoints with a magnitude > 50 m.....	123
Figure 38. The distribution of the elevations of knickpoints for the QF. ....	124
Figure 39. The distribution of knickpoints by elevation bins .....	125

Figure 40. The spatial distribution and superposition of the knickpoints of the QF, and areas in the 4 <sup>th</sup> quartile of the distribution: elevation, local relief, and slope .....	126
Figure 41. Frequency counts of knickpoints per lithological groups.....	127
Figure 42. The superposition of knickpoints, the lithological boundaries from strong to weak rocks, and the lithology map for the QF .....	128
Figure 43. The distribution of knickpoint parameters versus northing coordinates. ....	129
Figure 44. The distribution of knickpoint parameters versus easting coordinates. ....	130
Figure 45. A representative sketch of the temporal evolution of a relative base level fall event within a particular basin .....	138
Figure 46. The workflow of the methodological steps of the research. ....	158
Figure 47. Scatter plot of catchment-averaged local relief and mean slope angle for the analysed basins .....	159
Figure 48. The spatial distribution of the basins sampled by Salgado and colleagues .....	160
Figure 49. The topographic characteristics of the 25 basins analysed in this study and the eight sampled by Salgado et al. ....	161
Figure 50. The main lithology of the 25 basins analysed in this study and the eight sampled by Salgado et al .....	162
Figure 51. Examples of longitudinal profiles of rivers flowing away from the eastern part of the Caraça Range.. ....	164
Figure 52. The spatial distribution of the nested basins in the eastern part of the Caraça Range. ....	165
Figure 53. The spatial distribution of lithology in the nested basins in the eastern part of the Caraça Range.. ....	166
Figure 54. Sampling sites in the QF. ....	170
Figure 55. Scatter plot of basin denudation quantified using either a standard density for each sample of 2.6 g/cm <sup>3</sup> or a catchment-averaged density.....	173
Figure 56. The spatial distribution of <sup>10</sup> Be-derived catchment-averaged denudation rates for the QF. ....	178
Figure 57. Scheme representing the denudation rates for the nested basins in the eastern part of the Caraça Range. ....	181

Figure 58. Denudation rates for the nested basins in the eastern part of the Caraça Range .....	182
Figure 59. Denudation rates for the basins in the western part of the Caraça Range. ....	184
Figure 60. Typical longitudinal profile of the trunk river of a mixed lithology basin .....	185
Figure 61. Denudation rates for the basins in the eastern part of the Upper Das Velhas River basin .....	186
Figure 62. Examples of concave-up profiles of rivers associated with the central-south portion of the QF .....	188
Figure 63. Denudation rates for the basins in the central and south parts of the Upper Das Velhas River basin .....	189
Figure 64. Scatter plot of catchment-averaged local relief and normalised steepness index for the analysed basins .....	190
Figure 65. The spatial distribution of catchment-averaged ‘normalised steepness index’ for the analysed basins. ....	192
Figure 66. The spatial distribution of catchment-averaged ‘mean slope angle’ for the analysed basins. ....	193
Figure 67. Scatter plot of catchment-averaged mean elevation and mean annual precipitation for the analysed basins. ....	194
Figure 68. Scatter plot of catchment-averaged local relief and the areal contribution of hard rocks for the analysed basins. ....	195
Figure 69. Scatter plot of catchment-averaged mean slope angle and the normalised steepness index .....	195
Figure 70. Scatter plot of catchment-averaged denudation rates and the local relief for the analysed basins .....	198
Figure 71. Scatter plot of catchment-averaged denudation rates and normalised steepness index for the analysed basins .....	199
Figure 72. Scatter plot of catchment-averaged denudation rates and mean slope angle for the analysed basins .....	199
Figure 73. Scatter plot of catchment-averaged denudation rates and basin area for the analysed basins. ....	201
Figure 74. Scatter plot of catchment-averaged denudation rates and the mean EVI for the analysed basins .....	201

Figure 75. Mosaic of scatter plots between catchment-averaged denudation rates and the geomorphic parameters: areal contribution of strong rocks; mean knickpoint relief; maximum elevation; maximum slope angle; mean annual precipitation; and kernel density of faults .....	202
Figure 76. The distribution of catchment-averaged normalised steepness index per lithological group. ....	204
Figure 77. The distribution of catchment-averaged maximum slope angle and kernel density of faults per lithological group. ....	205
Figure 78. The distribution of catchment-averaged denudation rates per lithological group. ....	206
Figure 79. Scatter plot of the preliminary estimates of K per basin, and its associated denudation rates. Assuming $m = 0.4$ , and $n = 2/3$ .....	208
Figure 80. Scatter plot of the preliminary estimates of K per basin, and its associated denudation rates. Assuming $m = 0.4$ , and $n = 1$ . ....	208
Figure 81. Scatter plot of the preliminary estimates of K per basin, and its associated denudation rates. Assuming $m = 0.4$ , and $n = 2$ . ....	209
Figure 82. Schematic representation of the Twidale-type landscape.....	214
Figure 83. Schematic representation of how denudation rates and mean elevation are related in tectonically active settings, and in ‘dead’ orogens .....	217

## Acknowledgements

I dedicate this thesis to my wife Amanda, my mother Kátia, my father José and my sister Mariana. Amanda is the most loving person in the world, always pushing me forward, thinking positively, enduring my anxiety, dreaming together, and helping me with everything, including the mineral separation for the cosmogenic nuclide analysis. My mother Kátia is my inspiration for her generosity, work ethic, perseverance, creativity, and resilience. Everything that I am, and that I want to be is because of her. My father and my sister are always supporting me and being positive, even when I am not so confident. This project is the result of a long journey, and I am pleased to dedicate this thesis to my family.

I would like to thank my supervisors, Dr Cristina Persano, Prof. Paul Bishop, and Dr Martin Hurst, for their understanding, patience and guidance over the last years. My supervisors were fundamental influences in my formation as a geomorphologist, and each of them has taught me many lessons. I arrived in Glasgow with lots of ideas and dreams, and they helped me to shape my ideas in a cohesive geomorphological framework. I am deeply grateful for their supervision, and I am proud of being under their supervision.

I would also like to thank Dr Derek Fabel, Dr Angel Rodés and Mr Allan Davidson for their support in the cosmogenic nuclide analysis performed in this project. They have 'walked' with me through the entire process of deriving catchment-averaged denudation rates from alluvial sediment, and I am very thankful for that. Also, my sincere thanks to my colleague and friend Dr Bráulio Magalhães Fonseca that realised the entire fieldwork with me. Braulio's help and field expertise were critical for the completion of this project. I would like to thank Dr Cristina Augustin, my MSc supervisor, for always being so supportive to me, to engage in every geomorphological discussion that I proposed, and for helping me to be here now, an ocean away from home.

This thesis is in honour of my aunt Margarida, who passed away during this journey. Margarida had the sweetest smile that I can remember. She lives in my heart, and I wanted to share all the good moments with her. I miss you Margarida, and I hope you are happy right now.

Funding was provided by the Coordination for the Improvement of Higher Education Personnel (CAPES) under a Science without Borders fellowship (n° BEX 12000/13-2). Additional financial support was provided by a Natural Environment Research Council (NERC) Grant for cosmogenic analysis (Application CIAF/9177/0417); the GES school conference fund; the International Association of Geomorphologists (IAG/AIG) Grant for Young Geomorphologists; the German Aerospace Center (DLR) Grant for TanDEM-X data (Project DEM\_GEOL1345).



# Acronyms

**AFTA** - Apatite Fission-Track Analysis

**AMS** - Accelerator Mass Spectrometry;

**ANOVA** - ANalysis Of VAriance

**CAIRN** - Catchment-Averaged denudation Rates from cosmogenic Nuclides

**CRONUS** - Cosmic-Ray prOduced NUclide Systematics (on-line erosion rate calculator)

**DEM** - Digital Elevation Model

**DNPM** - Departamento Nacional de Produção Mineral ('Brazilian National Department of Mineral Production')

**EVI** - Enhanced Vegetation Index

**GDP\_** - Glasgow Daniel Peifer (samples prefix)

**ICP-OES** - Inductively-Coupled Plasma Optical Emission Spectroscopy

**PSA** - Part Sample Aliquot

**QF** - Quadrilátero Ferrífero ('Iron Quadrangle')

**RVI** - Rio das Velhas I magmatic event

**RVII** - Rio das Velhas II magmatic event

**SAD69** - South American Datum 1969

**SB** - Santa Bárbara magmatic event

**SFC** - São Francisco Craton

**SUERC** - Scottish Universities Environmental Research Centre

**TANDEM-X** - TerraSAR-X add-on for Digital Elevation Measurement

**USA** - the United States of America

**UTM** - Universal Transverse Mercator conformal projection



## Abbreviations and Symbols

- A** - upstream drainage area;
- $A_0$**  - reference drainage area used in the chi/integral approach of stream-profile analysis;
- $a$**  - the angular coefficient in the regression between bedrock incision rate ( $E$ ) and elevation ( $H$ );
- Al** - Aluminium (chemical element);
- $\alpha$ -particles** - two protons and two neutrons bound together;
- Be** - beryllium (chemical element);
- $b$**  - the y-intercept in the regression between bedrock incision rate ( $E$ ) and elevation ( $H$ );
- C** - the celerity of upstream migration of a knickpoint;
- C°** - Celsius, a unit of measurement of temperature;
- $C_{inh}$**  - cosmogenic nuclides resulting from previous exposures to cosmic radiation or non-cosmogenic production;
- $C_{sed}$**  - average cosmogenic nuclide concentration in sediment;
- $C_{total}$**  - total cosmogenic nuclide concentration of the surface materials at any depth below the surface;
- $C_1$**  - coefficient for the atmospheric condition used in the calculation of the Enhanced Vegetation Index (EVI);
- $C_2$**  - coefficient for the atmospheric condition used in the calculation of the Enhanced Vegetation Index (EVI);
- cm** - centimetre, a unit of length;
- cm<sup>2</sup>** - square centimetre, a unit of area;
- cm<sup>3</sup>** - cubic centimetre, a unit of volume;
- $d$**  - atmospheric depth (g/cm<sup>2</sup>);
- $e$**  - Euler's number (~2,7182);
- $E$**  - bedrock channel incision rate;
- E** - East (cardinal direction);
- $\varepsilon$**  - long-term constant erosion rate through time;
- Fe** - iron (chemical element);
- g** - gram, a unit of mass;
- g/cm<sup>2</sup>** - grams per square centimetres;
- $h$**  - local elevation of bedrock bed;

$h_t$  - the final topography in the framework of post-orogenic topographic decay.  $h_t$  is a fraction of the current elevation  $H$ ;

$H$  - elevation;

$H_0$  - the initial average topographic parameter (e.g., mean elevation or local relief) in the framework of post-orogenic topographic decay;

$i$  - the various types of nuclear reactions that may produce cosmogenic nuclides (e.g., spallation, neutron capture, muon reactions);

ID - identification

K - potassium (chemical element);

$K$  - constant representing bedrock erodibility;

$K_b$  - constant representing bedrock erodibility for the sediment-flux driven erosion model;

kg - kilogram, a unit of mass;

kg/m<sup>3</sup> - kilograms per cubic metres;

km - kilometre, a unit of length;

km<sup>2</sup> - square kilometre, a unit of area;

$k_s$  - the channel steepness index;

$k_{sn}$  - the channel steepness index normalised to the reference concavity index ( $\theta_{ref}$ );

$L$  - channel length;

$L_c$  - coefficient for the atmospheric condition used in the calculation of the Enhanced Vegetation Index (EVI);

log<sub>10</sub> - logarithm to base 10. Also known as the common logarithm;

$m$  - empirical constant for the area exponent in the stream-power model;

m - metres, the base unit of length in some metric systems;

m<sup>0.2</sup>/yr - the unit for the bedrock erodibility factor  $K$  when the area exponent  $m$  is fixed to 0.4;

m<sup>0.9</sup> - the unit for the normalised steepness index ( $k_{sn}$ ) when the reference concavity index ( $\theta_{ref}$ ) is fixed to 0.45;

m<sup>2</sup> - square metre, a unit of area;

m<sup>3</sup> - cubic metre, a unit of volume;

Ma - millions of years ago (date)

m/Myr - metres per million years;

mm - millimetres, a unit of length;

mm/yr - millimeters per year;

**Myr** - millions of years;  
 **$n$**  - empirical constant for the slope exponent in the stream-power model;  
 **$n$**  - sample population;  
**N** - north (cardinal direction);  
**Nb** - niobium (chemical element);  
**Nd** - neodymium (chemical element);  
**NE** - northeast (cardinal direction);  
**NW** - northwest (cardinal direction);  
 **$N_0$**  - the number of nucleons (comprising a bulk of neutrons) at the surface ( $z = 0$ );  
 **$N_0(atm)$**  - as the maximum number of nucleons at the top of the atmosphere;  
 **$\theta$**  - intrinsic concavity index;  
 **$\theta_{ref}$**  - fixed reference intrinsic concavity index;  
 **$P$**  - the production rate of cosmogenic nuclides at the surface ( $z = 0$ );  
**Pb** - lead;  
 **$P_{cat}$**  - catchment-averaged production rate of cosmogenic nuclides;  
 **$p$ -value** - the probability value that determine statistical significance in a hypothesis test;  
 **$\rho$**  - the density of rock;  
 **$\rho_c$**  - the density of the crust ( $2700 \text{ kg/m}^3$ );  
 **$\rho_m$**  - the density of the mantle ( $3200 \text{ kg/m}^3$ );  
 **$Q$**  - sediment flux;  
 **$R_c$**  - the cutoff rigidity;  
 **$R^2$**  - the coefficient of determination. The  $R^2$  yield information about the goodness of fit of a regression model;  
 **$S$**  - local channel slope. Also represented as  $|\partial h / \partial x|$ ;  
**S** - south (cardinal direction);  
**SE** - southeast (cardinal direction);  
**SW** - southwest (cardinal direction);  
**Sm** - samarium (chemical element);  
**syn** - synchronous;  
 **$t$**  - time elapsed;  
 **$T_{exp}$**  - exposure age for the surface material analysed;  
**Th** - thorium;  
**Ti** - titanium;  
 **$T_{1/2}$**  - radionuclide half-life;

- $\tau_d$  - the erosional time constant for reducing a land surface to  $1/e$  ( $\sim 0.357879441$ ) of the initial topographic parameter  $H_0$ ;
- $U$  - rock uplift rate;
- U** - uranium;
- U-Pb** - uranium-lead dating
- $\chi$  - the longitudinal coordinate chi used in the chi/integral approach of stream-profile analysis, with dimensions of length;
- $x_b$  - the position of the base level used in the chi/integral approach of stream-profile analysis;
- $x_c$  - the channel head gradient in Baldwin's et al. (2003) approach to post-orogenic topographic decay;
- W** - West (cardinal direction);
- WNW** - West-northwest (cardinal direction);
- yr** - years, a unit of time;
- $z_d$  - depth below surface. At surface,  $z_d = 0$ ;
- $z_0$  - a surface depth for which cosmic rays start to produce cosmogenic nuclides in surface materials;
- $z(x_b)$  - elevation at the base level in the chi/integral approach of stream-profile analysis;
- $z(x_c)$  - the channel head elevation in the Baldwin et al. (2003) approach to post-orogenic topographic decay;
- $z_i(x_c)$  - the 'initial' elevation of the channel head gradient ( $x_c$ ) in the Baldwin et al. (2003) approach to post-orogenic topographic decay;
- $z_f(x_c)$  - the 'final' elevation of the channel head gradient ( $x_c$ ) in the Baldwin et al. (2003) approach to post-orogenic topographic decay;
- $\sigma$  - the standard deviation, a measure of dispersion of a dataset;
- $\Delta\phi$  - azimuth angle for topographic shielding;
- $\Delta\theta$  - zenith angle for topographic shielding;
- $\Lambda$  - attenuation length ( $\text{g}/\text{cm}^2$ );
- $\Lambda_s$  - attenuation length for the at the Earth's surface ( $z = 0$ );
- $\lambda$  - the 'decay constant';
- $^\circ$  - degrees, a measurement of a plane angle whose full rotation is 360 degrees
- $^3\text{He}$  - helium-3 (non-radioactive isotope of helium);
- $^{10}\text{Be}$  - beryllium-10 (a radioactive isotope of beryllium);
- $^{14}\text{C}$  - carbon-14 (a radioactive isotope of carbon);

- $^{21}\text{Ne}$  - neon-21 (non-radioactive isotope of neon);
- $^{26}\text{Al}$  - aluminium-26 (a radioactive isotope of aluminium);
- $^{36}\text{Cl}$  - chlorine-36 (a radioactive isotope of chlorine);
- $^{38}\text{Ar}$  - argon-38 (a stable isotope of Argon);
- $^{39}\text{Ar}$  - argon-39 (a radioactive isotope of Argon);
- $^{40}\text{Ar}/^{39}\text{Ar}$  - argon-argon dating;
- $^{53}\text{Mn}$  - manganese-53 (a radioactive isotope of manganese);
- (U-Th)/He** - (uranium-thorium)/helium thermochronology.

**CHAPTER 1:  
INTRODUCTION**



# CHAPTER 1: INTRODUCTION

## 1.1 BACKGROUND TO THE RESEARCH

The long-term evolution of post-orogenic landscapes is often neglected (Baldwin et al., 2003; Bishop, 2007), despite the fact that they represent the bulk of Earth's surface (Bishop, 2007), and that they were the landscapes used to formulate the conceptual models at the base of most geomorphological thoughts (e.g., Davis, 1899; Penck, 1924; King, 1953). Post-orogenic landscapes are fundamentally tectonically stable settings that last experienced tectonic (orogenic) activity hundreds of Myr ago. In the absence of forces that counteract the destructive surface processes, conceptual and numerical models indicate that relief should decline with time (Pelletier, 2008), because “clearly, if there were no coneracting forces we should expect that the land surface, given sufficient time, would be continuously reduced. Eventually, little or no relief would remain” (Leopold et al., 1964, p. 3). However, there are many post-orogenic landscapes that are currently associated with mountainous topography; examples are the Cape Mountains in Africa (e.g., Scharf et al., 2013); the Appalachian Mountains in the USA (e.g., Gallen et al., 2013); southeastern Australia (e.g., Quigley et al., 2007; Bishop and Goldrick, 2010); Sri Lanka (e.g., von Blanckenburg, 2004); and southeastern Brazil (e.g., Cogné et al., 2012). The contradiction between conceptual and numerical estimates of relief decay timescales and the current topography of post-orogenic landscapes forms the “paradox of persistent mountain belts” (Pelletier, 2008, p. 101); the question of how these mountains have survived for hundreds of Myr remains enigmatic.

This thesis represents a modern re-thinking of how post-orogenic landscapes develop through time. I quantitatively investigate the relationship between topography, the exposed lithology, and denudation rates in post-orogenic mountains. The aim of this project has been reached by collecting empirical observations of landforms and processes, and using cosmogenic isotope inventories to determine the rates at which the land surface has developed in the Quadrilátero Ferrífero (QF, southeastern Brazil), a classic post-orogenic setting.

The timescale of relief reduction on post-orogenic landscapes has been a central question since the early stages of geomorphology (Bishop, 2007). The Huttonian realisation that landscapes evolve through time as the result of the (slow) action of surface processes underpins all research in geomorphology (Chorley et al., 1964). In accordance, every classic geomorphological theory is an attempt to explain how landforms and landscapes evolve and come to be as they are. Post-orogenic landscapes were central in the framework of the classic theories of landscape evolution, mainly for two reasons: 1) they constitute the majority of the present Earth's surface; and 2) they represent the 'completion' or the 'end point' of the evolutionary path of a landscape through time. In these terms, the topography of post-orogenic landscapes, which was created actively by the geological "forces of deformation and uplift" (Davis, 1899, p. 483) is thought, over time and with the absence of the forces that built it in first place, to be erased by the action of the destructive surface processes, into an almost featureless plain (Summerfield, 1991). This conceptual framework dominated geomorphic research up to the transition to process-form geomorphology. The traditional *modus operandi* in geomorphology, concerned primarily with explaining the history of landscapes and the stages through which landscapes pass as they develop through time, changed to a 'modern approach', which focuses on quantitatively determining the rate and pattern of surface processes, and how they interact, spatially and temporally, to form the landforms we can observe at the Earth's surface at present (Summerfield, 1991; Bishop, 2007). The latter approach invested so deeply into the philosophical perspective that the topography is a 'now thing', that the history of landscapes, including the notion that 'inheritance' may strongly affect landscape development (e.g., Hack, 1975, p. 101), was neglected, to the extent that landforms and landscapes started to be treated somehow as 'time-independent' (Summerfield, 1991; Bishop, 2007). The result of this transition is that post-orogenic landscapes lost their centrality within the geomorphic research, leading to a relative lack of studies on these settings (Baldwin et al., 2003; Bishop, 2007).

The change of fashion in geomorphology from historical to process-form research was associated with the rise of the viewpoint that landforms are recent developments (Bishop, 2007), and thus the landscape is seen as mainly the result of the surface processes presently active (e.g., Thornbury, 1969; cf. Bishop, 2007).

Dissident voices argued that landscapes may be older than thought or have an ancient origin (e.g., Crickmay, 1975; Twidale, 1976; Young, 1983; Twidale, 1999), and that the surface processes presently acting on the landscape may not be sufficient to account for the complexity and antiquity of many parts of the Earth's surface (Bishop, 2007). The view that some landscapes could be very old was counteracted by measurements, in these very settings, of denudation rates that indicate that these landscapes are, even if slowly, still changing and therefore, in their shape, relatively new (e.g., Belton et al., 2004). At the moment, views on post-orogenic landscape evolution can be summarized in two end-member hypotheses. The first theorises that the topography of post-orogenic settings has an ancient origin and has survived ever since it was created (e.g., Twidale, 1976; Twidale, 1999). The second hypothesis postulates that present relief in post-orogenic settings is a product of a recent topographic rejuvenation episode or episodes (e.g., Gallen et al., 2013). An alternative framework states that post-orogenic settings are currently in a dynamic equilibrium state, eroding everywhere at a constant rate (e.g., Hack, 1975). However, this dynamic equilibrium theory does not seem to be applicable to post-orogenic landscapes as rock uplift is necessary in order to maintain equilibrium, a problematic assumption for these settings that are essentially tectonically stable (cf. Kooi and Beaumont, 1996). To date, the post-orogenic history of many landscapes remains enigmatic (Bishop, 2007) and more work is necessary to constrain and understand their evolution.

## **1.2 PROJECT OBJECTIVES**

This thesis investigates the pattern and style of landscape evolution in a post-orogenic setting. The three models presented in the section above and traditionally used to explain the relief of post-orogenic settings are empirically testable, as they imply different outcomes for how lithology, topography, and denudation rates are related. The first hypothesis theorises that the relief of post-orogenic settings has an ancient origin and has survived ever since, on account of being 'out of reach' of denudation (e.g., Bishop, 1985; Twidale, 1991). In this case, the spatial distribution of lithologies with different strength and the unequal characteristics of the erosional activity lead to a geomorphic differentiation whereby denudation is concentrated in channels flowing through low resistance rocks contrasting with the uplands that, underlain by strong rocks, are associated

with low denudation rates (cf. Twidale, 1999). The spatial variability in denudation rates (low in the uplands and higher in the lowlands) implies that relief is increasing with time.

By contrast, the second hypothesis postulates that relief in post-orogenic settings is a product of a recent topographic rejuvenation episode (or episodes) (e.g., Gallen et al., 2013). In this case, the areas responding to the rejuvenation are associated with higher denudation rates than the areas that did not (or have not yet) experienced it. Whereas this rejuvenation event may be due to ongoing tectonic activity (e.g., Hack, 1982), it is also possible that it is related to denudational isostatic compensation (cf. Bishop and Goldrick, 2010). A third hypothesis is that post-orogenic relief is in a state of dynamic equilibrium whereby relief and the processes sculpting it are part of an open system in which all topographic elements are adjusted to each other, downwasting at the same rate (Hack, 1960, 1975). In this latter case, denudation rates in a landscape evolving for Myr will be spatially invariant irrespective to differences in lithology or relief, in a landscape that is evolving for Myr.

This thesis investigates how post-orogenic landscapes develop through time addressing the primary objective: quantify the relationships between topography, denudation rates, and lithology in a classic post-orogenic setting.

This fundamental objective will be met by (i) performing quantitative analysis of channel and hillslope topography, and (ii) measuring denudation rates. Intrinsically linked with the central question are the associated issues of:

- What is the role of the spatial distribution of lithologies with different resistance to weathering and denudation on the landscape evolution of post-orogenic settings?
- Does relief decline, remain constant or increase during the development over time of post-orogenic landscapes?

The rest of this thesis explores these intriguing questions.

## 1.3 RESEARCH DESIGN, INNOVATIVE CHARACTER AND THESIS OUTLINE

Researchers have used a variety of methods and datasets to explain the evolution of post-orogenic landscapes, and yet no consensus has been reached to explain their evolution through time, either in general terms nor specifically for a particular case study (e.g., Hack, 1960; Matmon et al., 2003a; contrasting with Hack, 1982; Pazzaglia and Gardner, 1994; Gallen et al., 2013). There is not even consensus about the evolution of the Appalachian Mountains, probably the most studied post-orogenic setting in the world (Pazzaglia and Brandon, 1996; Baldwin et al., 2003; Gallen et al., 2013), despite the fact that many modern techniques, such as thermochronology (e.g., McKeon et al., 2014), cosmogenic nuclide analysis (e.g., Matmon et al., 2003a; Portenga et al., 2013), or stream-profile analysis (e.g., Gallen et al., 2013; Prince and Spotilla, 2013) have been applied to constrain their evolution through time.

This project addresses the problem of how post-orogenic landscapes evolve in an innovative way. Using the Cuadrilátero Ferrífero as a classic example of post-orogenic settings, the project centres on (a) the extraction of quantitative topographic parameters (steepness of channel and hillslope gradients) over different spatial scales, from local topography to the different order catchments; and (b) the quantitative determination of the relationship between these parameters and the spatial distribution of strong and weak lithologies. This work defines different 'geomorphic contexts' in the landscape, including areas of pronounced and subdued topography and their associated exposed bedrock lithology. The project then uses the results of (a) and (b) to define a sampling strategy for quantifying denudation rates that are 'effectively representative' of the different geomorphic contexts of the landscape, a novel approach that permits objective identification of the relationships between topography, lithology and denudation rates, without any pre-conceptions. This project compares these catchment-averaged denudation rates with the topographic parameters and exposed lithology, to identify and quantify the relationship between denudation, relief, and exposed lithologies. The determination of 'effectively representative' denudation rates is fundamental for providing the possibility of 'up-scaling' the geomorphic results of a specific dataset from basins (or basin areas) to the

landscape as a whole. The conventional *modus operandi* often consists in collecting a dataset to derive denudation rates and explaining their spatial variation using topography; with the conventional approach, different datasets may be correlated to topography in different ways, resulting in contrasting interpretations of landscape evolution. Reversing the process, and thus performing the quantitative analysis of the topography of the entire landscape before defining where and how to estimate the rates at which the land surface has developed, is an un-biased approach to address the development of landscapes. In this sense, this project has the potential to contribute widely to the field of geomorphological research, by defining a new sampling strategy for cosmogenic isotope inventories.

This thesis consists of five other chapters that set up the methods and the results used to empirically investigate the style and pattern of landscape evolution of a classic post-orogenic setting. Chapter 2 sets the geomorphic background of the case study area. Chapter 3 sets the theoretical background on the current knowledge of how post-orogenic landscapes evolve through time, and the modern approach for investigating landscape evolution using topography, and outlines how the topography of the study area was quantified. Chapter 4 contains the quantitative analysis of the topography of the QF, describing how its current morphology is empirically observed, by using a range of modern geomorphic techniques. In Chapter 5, I quantify the spatial pattern of denudation by measuring in situ  $^{10}\text{Be}$  concentrations on alluvial sediments, and I describe how the topography, denudation and exposed lithology are related in this setting. In Chapter 6, the large empirical dataset of this thesis is synthesised and discussed. The key contributions of this project are listed and an interpretation of how post-orogenic settings develop through time, based on the empirical data, is presented. Finally, future research opportunities are pointed out.

**CHAPTER 2:**  
**THE STUDY AREA -**  
**THE QUADRILÁTERO FERRÍFERO (BRAZIL)**



# CHAPTER 2: THE STUDY AREA – THE QUADRILÁTERO FERRÍFERO (BRAZIL)

## 2.1 WHY THE QF?

The persistence of relief in many post-orogenic landscapes has led to a long-standing debate in geomorphology that is still unanswered (cf. Bishop, 2007). The fundamental point of controversy is that the long-term preservation of post-orogenic relief implies extremely low denudation rates over a long period of time (hundreds of Myr), which is at odds with the current morphology of post-orogenic terrains, often marked by mountainous relief and steepness (e.g., Gallen et al., 2013; Scharf et al., 2013) that, in turn, are expected to drive high denudation rates (e.g., Ahnert, 1970; Portenga and Bierman, 2011; Kirby and Whipple, 2012). The Quadrilátero Ferrífero (QF) in southeastern Brazil is an ideal case study to investigate this conundrum. It is a classic intraplate, high-relief setting, where tectonic activity is considered to have ceased by about 500 Ma (Dorr, 1969; Alkmim and Marshak, 1989; Chemale et al., 1994). The area, which is about 7000 km<sup>2</sup>, has been widely studied by geologists, given its economic importance as one of the major metallogenic provinces in the world (Lobato et al., 2001); its lithological variations and geological history are, therefore, well known. Relief is highly variable in the area, from the flat landforms of the gneiss and granite exposures to the steep slopes of the Caraça Mountains (Figure 1). In these terms, the QF is the perfect setting to investigate the relationships between topography, denudation rates and relief in post-orogenic landscapes (Table 1).

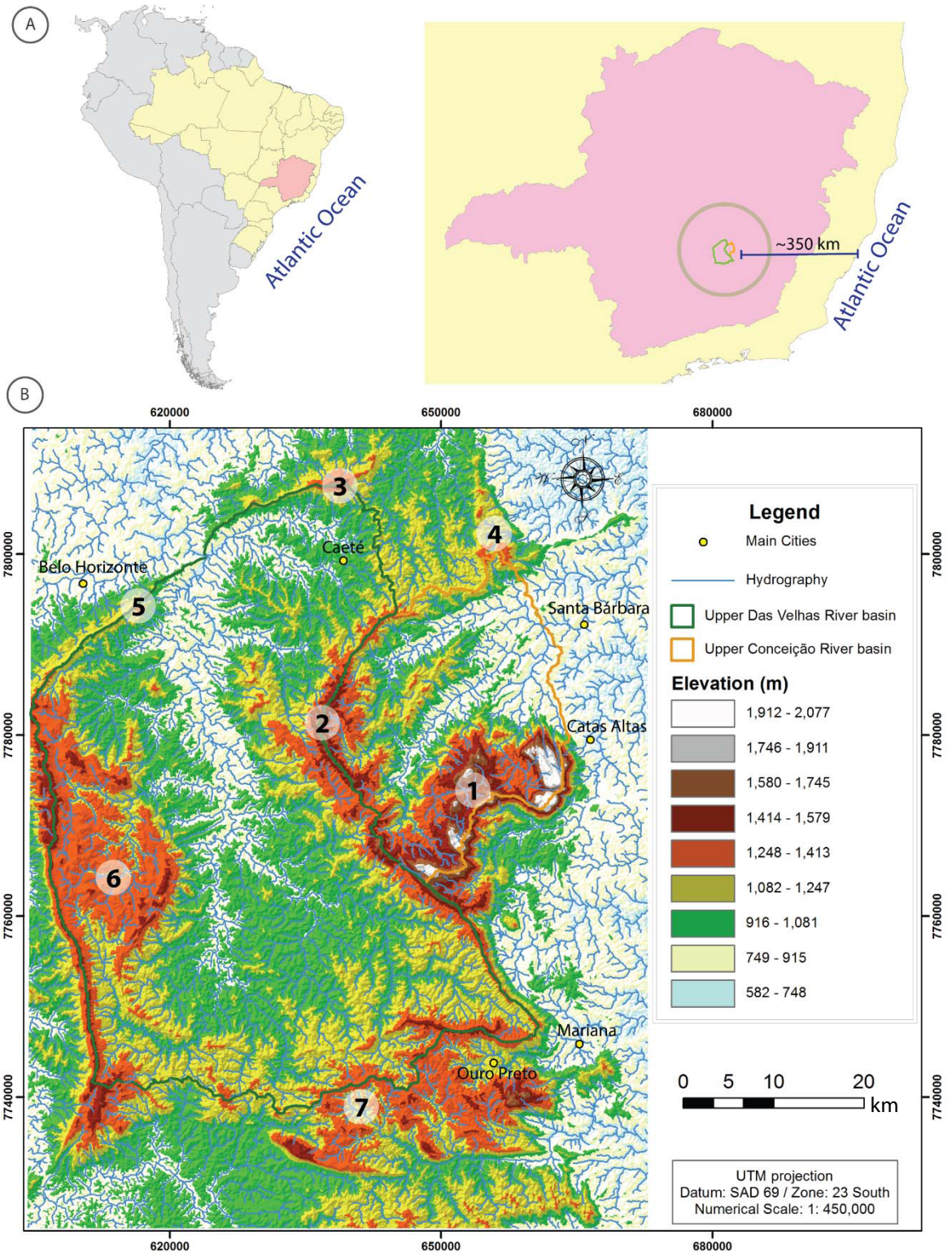


**Figure 1.** The geographical context of the QF. (A) The QF is an upland region in southeastern Brazil (in yellow), in the Minas Gerais state (in red). The two main drainage basins of the QF are the Upper Das Velhas River (in green) and the Upper Conceição River (in orange) basins. The trunk rivers of the two main basins of the QF are represented by lines with the same colours as the basins to which they refer to. (B) The QF represents a regional drainage divide, with a mean elevation of ~1015 m. The highest elevations are associated with the Caraça Range, reaching ~2080 m. The numbers denote critical physiographic features of the QF: (1) the Caraça Range; (2) the Gandarela Range; (3) the Piedade Range; (4) the Cambotas Range; (5) the Curral Range; (6) the Moeda plateaux; (7) the Ouro Branco Range.

**Table 1.** The fundamental features that make the QF an optimal test site for post-orogenic landscapes.

<b>QF's main features</b>	
<b>1</b>	high relief
	divided into two structural regions:
<b>2</b>	eastern QF, affected by many, pre-Palaeozoic thrust faults; western QF, with no main thrust faults <sup>1,4,5</sup>
<b>3</b>	combination of strong and weak lithologies <sup>1,2</sup>
<b>4</b>	continuous exposure since at least the last orogeny (~500 Ma) <sup>1,6</sup>
<b>5</b>	absence of Quaternary glaciation <sup>3</sup>
<b>6</b>	unaffected by Cenozoic eustatic variations <sup>1</sup>
<b>7</b>	allegedly long-term tectonic stability <sup>1,2,3,4,5</sup> , although
<b>8</b>	Cenozoic deformation reported in small graben-like basins <sup>15,16,17,18</sup>
<b>9</b>	historic record of small magnitude earthquakes (M ~3) in the eastern QF <sup>11,12</sup>
<b>10</b>	wide distribution of quartz-rich lithologies <sup>1</sup>
<b>11</b>	abundance of mixed bedrock-alluvial channels <sup>1</sup>
<b>12</b>	detrital <sup>10</sup> Be data suggest that rock resistance sets pattern of denudation in the QF <sup>2,13</sup>
<b>13</b>	controversial geomorphic history <sup>1,15,16</sup>

References: 1. Dorr, 1969; 2. Salgado et al., 2008; 3. Behling, 1998; 4. Chemale et al., 1994; 5. Alkmim and Teixeira, 2017; 6. King, 1956; 7. Farina et al., 2016; 8. Rosière et al., 2001; 9. Varajão, 1991; 10. Barbosa, 1980; 11. Assumpção et al., 2014; 12. Agurto-Detzel et al., 2015; 13. Salgado et al., 2007a; 14. Monteiro, 2018; 15. Cabral and Koglin, 2014; 16. Sant'Anna et al., 1997; 17. Lipski, 2002; 18. Santos et al., 2004.

The QF is one of the highest elevation areas in southeastern Brazil, with a peak elevation of ~2100 m. The main topographic feature is an inland drainage divide that separates rivers flowing inland towards the North and Northwest, from rivers flowing directly to the Atlantic Ocean, ~350 km away in a straight line from the QF (Figure 1A). Strong and weak lithologies are exposed in a complex geologic setting that reflects a polyphase deformational history, having last experienced tectonic activity ~500 Myr ago (Dorr, 1969; Alkmim and Marshak, 1998; Chemale et al., 1994). The QF displays an abundance of mixed bedrock-alluvial channels, deeply incised in some areas, notably where strong rocks are present, and less in others, in a typical erosive landscape where alluvium does not accumulate (Dorr, 1969). The QF did not experience Quaternary glaciation (Behling, 1998) and, given its distance from the ocean, is likely to be unaffected by Cenozoic eustatic

variations (Dorr, 1969; cf. Twidale, 1999). There is evidence suggesting that the QF has been a sub-aerial geomorphic feature for an extended period of time, including  $^{40}\text{Ar}/^{39}\text{Ar}$  and (U-Th)/He geochronology (e.g., King, 1956; Carmo and Vasconcelos, 2004; Spier et al., 2006; Rodríguez Tribaldos et al., 2017; Monteiro et al., 2014; Monteiro et al., 2018). On the other hand, a complex history involving burial followed by removal of ~1-2 km of sedimentary cover between 50-10 Myr, has been hypothesised (e.g., Japsen et al., 2012). Therefore, the geomorphic history of the QF is controversial, similarly to other post-orogenic settings (Pelletier, 2008; Gallen et al., 2013)

All these characteristics indicate that the QF is a classic high-relief post-orogenic landscape ideally suited for the quantitative investigation of the relationships between topography, denudation and exposed lithology in post-orogenic settings. Additional justification for the QF as the test site is the availability of high-resolution data for geology (e.g., Lobato et al., 2005) and elevation (TanDEM-X, 12 m resolution). Also, the QF is one of the most important mining districts in the world, hosting world-class gold and hematite-rich iron ore deposits (Lobato et al., 2001; Vial et al., 2007), whose landscape evolution is of international interest due to its economic importance (e.g., Dorr, 1969; Lobato et al., 2001; Farina et al., 2016).

## 2.2 REGIONAL BACKGROUND

The name Quadrilátero Ferrífero means ‘Iron Quadrangle’ referring both to its vast iron ore reserves and to its roughly rectangular shape, which defines an internal low relief area surrounded by high-relief ridges underlain by quartzites and banded iron formations (Dorr, 1969; Lobato et al., 2001). The abundance of ore deposits, particularly gold, iron and manganese, is the main feature of the QF; their exploitation played a fundamental role in the growth of the Portuguese Empire, as well as the Brazilian economy in the eighteenth and early-nineteenth centuries (Dorr, 1969). The economy of the QF was so prosperous that in 1720 half of the Brazilian population was concentrated in Minas Gerais state (Farina et al., 2016). This economic importance led to focused research, and the QF is currently the most systematically investigated geological domain of Brazil (Lobato et al., 2001). Researchers from across the world have been trying to solve the puzzling geology

of the QF for over one and a half centuries (e.g., von Eschwege, 1833; Gorceix, 1876; Derby, 1906, 1911; Harder and Chamberlin, 1915; Moraes and Guimarães, 1930; Guimarães, 1931; Brajnikov, 1947; King, 1956; Dorr, 1969; Barbosa, 1980). The systematic synthesis of the geology of the QF was developed through a combined effort of the U.S. Geological Survey and the Brazilian National Department of Mineral Production (DNPM) between 1946-1962 and later published by the head of the team, John Van N. Dorr II (Dorr, 1969).

Physiographically, the QF is one of the highest elevation regions in Brazil. It displays a range of topographic elements, including high and craggy peaks, deep river canyons and entrenched meanders, open and gently-sloping valleys, high plateaux, hogback mountain chains, and, allegedly, erosion surface remnants (e.g., King, 1956; Dorr, 1969). The highest elevations occur in the southeastern part of the QF, in the Caraça Ridge, which attains ~2080 m (Figure 2); the lowest elevations, below 600 m, comprise downstream areas of the two principal drainage systems, the Upper Das Velhas River and the Upper Conceição River basins (Fig. 1B).

The north-flowing Upper Das Velhas River is a tributary of the São Francisco River, the longest river entirely in Brazilian territory, draining > 630,000 km<sup>2</sup> between the states of Minas Gerais and Bahia before turning east and flowing towards the Atlantic Ocean. The northeast-flowing Upper Conceição River is a tributary of the Doce River, that flows through the eastern part of the QF and then directly towards the Atlantic Ocean. The Upper Das Velhas River descends through an elevation drop of ~770 m, whereas the Upper Conceição River accounts for an elevation drop of ~1450 m. The QF's main streams are deeply incised (Dorr, 1969). These rivers are often described as profoundly entrenched into harder rocks and less in soft rocks, yet all rivers cut across the resistant ridge-forming rocks at some point (Dorr, 1969). Medium-sized streams sometimes follow the geological structures (i.e., they are often parallel to the thrust faults) and sometimes they cut across; the latter is particularly evident in the tributary streams flowing perpendicularly to the main rivers, and in the eastern part of the QF (Dorr, 1969). Stream piracy has been hypothesised as still active, with a few cases of radical changes in drainage direction being reported (e.g., King, 1956; Dorr, 1964; Dorr, 1969).

Saprolite and products of lateritic weathering are often reported as standard features in the QF; they have been widely interpreted as the result of sub-aerial conditions of the QF in a tropical climate over an extended period of time (Dorr, 1969). Despite this long exposure history and the assumed association between deep weathering and geomorphic 'inertial' conditions (e.g., Vasconcelos, 1999), alluvium has not accumulated greatly in the QF (Dorr, 1969). The few places where alluvial deposits are present are related to abrupt flattening of the channel beds in a piedmont context, restricted to rivers flowing away from the Caraça Range in the eastern QF (Dorr, 1969). Additionally, narrow zones of discontinuous alluvium are found, in a few locations of the QF, in small tributary streams (Dorr, 1969). These observations led Dorr (1969) to explain the QF as a landscape of net erosion, where the gradients of major and minor channels are steep enough to remove all the detrital material brought to them. Also, weathering in the QF breaks most of the rocks down to fine-sized particles that are quickly eliminated in the rainy season (Dorr, 1969).

The QF's regional climate is marked by a wet period from October to March and a dry season between April and September. The annual average rainfall is between 1,250 and 1,500 mm in the main valley bottoms, reaching ~1,700 mm on the interfluvies (SEA, 1980; Abatzoglou et al., 2018). The annual average temperature ranges between 19 and 22 C° (SEA, 1980).



**Figure 2.** Different landforms in the QF. (A) Gently-sloping valleys under gneiss and granitic rocks in the central part of the Upper Das Velhas basin. (B1) The mountainous landforms over the Caraça Range (underlain by quartzites). (B2) Typical channel form in rivers flowing over the Caraça Range, a waterfall with ~50 m of relief (quartzite).

## 2.3 GEOLOGICAL CONTEXT OF THE QF

The QF lies on the southeastern edge of the São Francisco Craton (SFC, Figure 3). The SFC consists of an Archean-Palaeoproterozoic block that has not experienced major tectonic and magmatic events since ~1900 Ma (Almeida et al., 1981; Alkmim and Martins-Neto, 2012; Aguilar et al., 2017). The SFC is surrounded on all sides by Neoproterozoic to Early Ordovician Brasiliano (650-480 Ma) orogenic belts that developed during the Brasiliano/Pan-African collage of West Gondwana (Endo and Fonseca, 1992; Alkmim and Teixeira, 2017; Heilbron et al., 2017).

The QF is, in effect, an 'island' of metavolcanic and metasedimentary successions in a 'sea' of Archean basement assemblages (Dorr, 1969). Stratigraphically, the exposed section of the QF is composed of four main units: (i) Archean granite-gneiss terrains; (ii) Archean volcano-sedimentary sequences (Rio das Velhas Supergroup); (iii) Proterozoic sedimentary coverage and volcano-sedimentary sequences (Minas Supergroup, Itacolomi Group, Espinhaço Supergroup); and (iv) Recent sedimentary cover (Figures 3-4).

The Archean basement of the QF comprises medium- to high-grade metamorphic tonalite-trondhjemite-granodiorite rocks, migmatites and K-rich granitic plutons (Teixeira et al., 2017) that occur as large-scale domes, built by several magmatic pulses (Lana et al., 2013; Farina et al., 2016). The Archean basement is overlain by the Neoproterozoic Rio Das Velhas Supergroup, a typical greenstone belt sequence characterised by the combination of mafic- to ultramafic rocks, volcanoclastic, and immature clastic rocks (Alkmim and Teixeira, 2017). Overlying the Rio das Velhas Supergroup are the metasedimentary successions of the Minas Supergroup and Itacolomi Group. The Minas Supergroup comprises a series of continental to marine siliciclastic and carbonate rocks, representing a sedimentary sequence from a passive-margin to syn-orogenic deposits, lying unconformably onto the Archean greenstone belt (Alkmim and Teixeira, 2017). The Itacolomi Group, overlying the Minas Supergroup, includes an intermontane molasse unit comprising alluvial sediments (Alkmim and Martins-Neto, 2012). Cenozoic sediments filling small graben-like basins are frequent in the QF (Lobato et al., 2005). The stratigraphic column with available age constraints is presented in Figure 4.

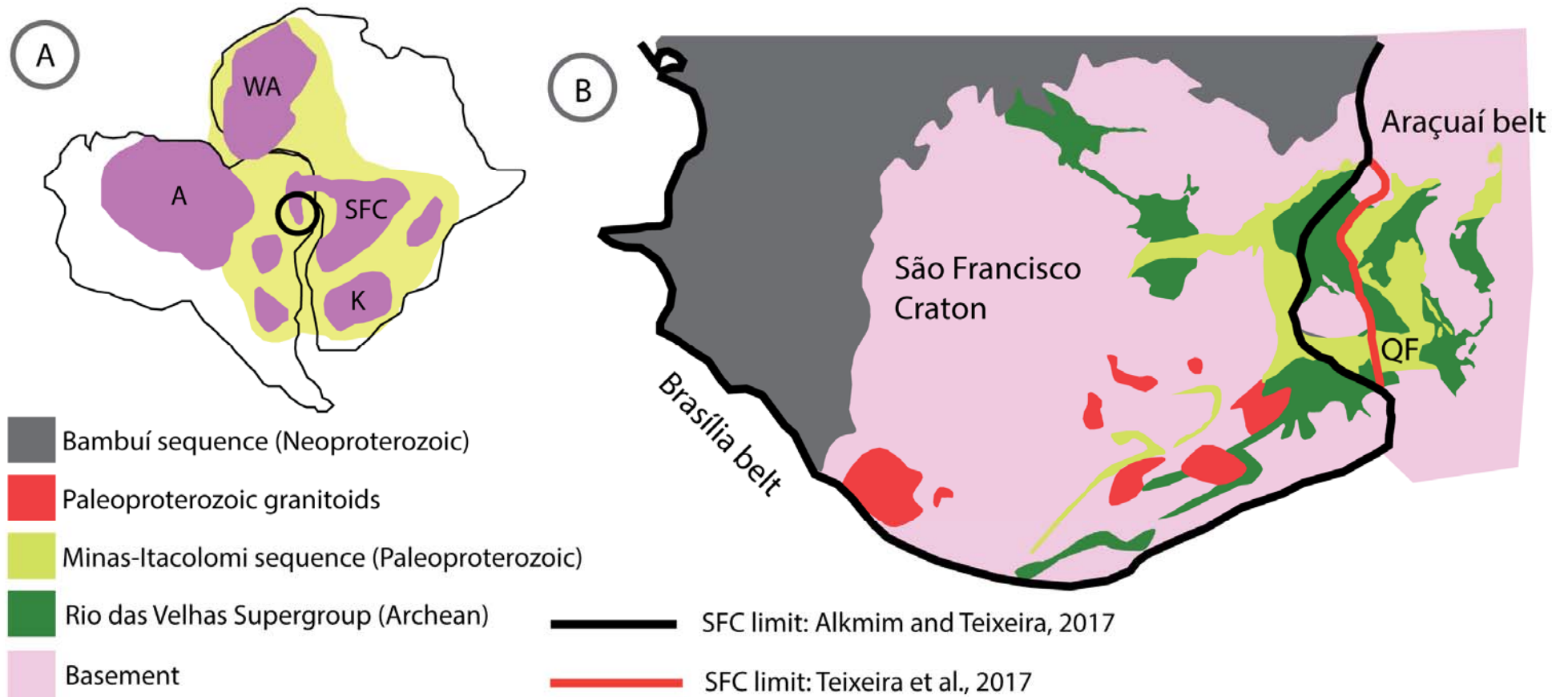


**Figure 3.** Simplified geology of the QF. (A) The tectonic context of the assembly of West Gondwana by the end of the Proterozoic: cratons (in purple) surrounded by Neoproterozoic mobile belts (in yellow); in this reconstruction, the São Francisco craton includes the Congo Craton, now in Africa. Cratons: A - Amazonian; WA - West Africa; SFC - São Francisco-Congo; K - Kalahari. Modified from Alkmim and Martins-Neto (2012). (B) Simplified geological map of the southern São Francisco craton; the western portion of the QF lies within the SFC whereas its eastern part belongs to the Neoproterozoic Araçuaí mobile belt province. Modified from Alkmim and Martins-Neto (2012).

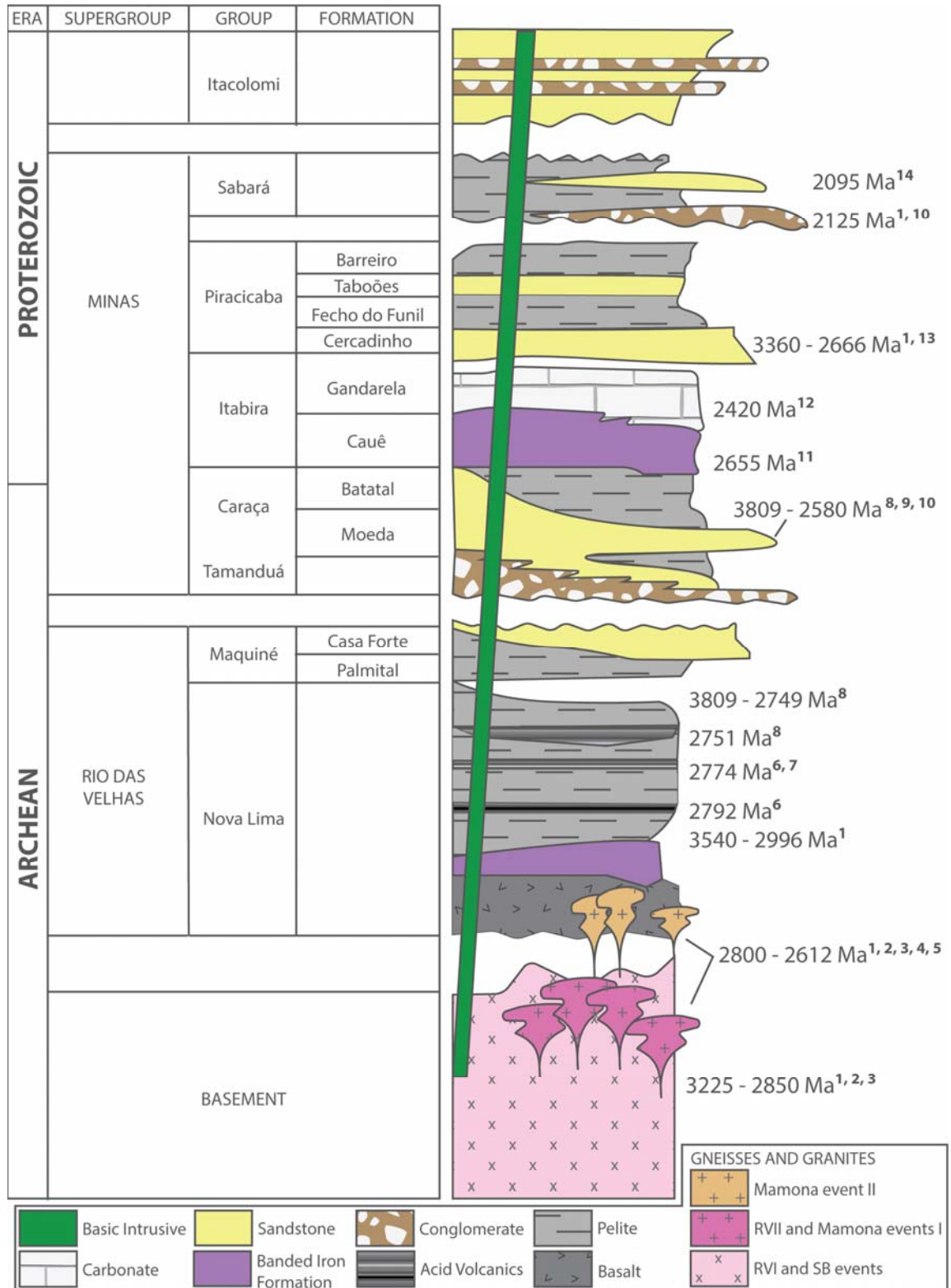


**Figure 4.** A representative stratigraphic column of the rocks underlying the QF. Modified from Farina et al. (2016). Empty spaces are unconformities and represent depositional hiatus or erosion. Abbreviations: RVI and RVII are Rio Das Velhas I and II events, SB is the Santa Barbara ‘magmatic event’; this event, in reality, is composed of several magmatic pulses. Age references: 1. Machado et al., 1996; 2. Lana et al., 2013; 3. Farina et al., 2015; 4. Romano et al., 2013; 5. Noce et al., 1998; 6. Noce et al., 2005; 7. Machado et al., 1992; 8. Hartmann et al., 2006; 9. Koglin et al., 2014; 10. Dopico et al., 2017; 11. Cabral et al., 2012; 12. Babinski et al., 1995; 13. Mendes et al., 2014; 14. Brueckener et al., 2000.

The QF displays a complex structural setting (Alkmim and Teixeira, 2017), which, combined with a lack of geochronological constraints (Farina et al., 2016), has led to a series of controversies regarding its deformational history (Farina et al., 2016; Alkmim and Teixeira, 2017). Irrespective of these details, the consensus is that the QF records a polyphase deformation history, epitomized by three sets of structures that define the geological architecture of the QF (Figures 5-6):

(i) a set of NE-SW-trending, NW-verging regional scale folds that do not show any geometrical relationship with the basement domes (Alkmim and Teixeira, 2017). Examples of structural features within this group are the Gandarela syncline, the Conceição anticline, and the Curral Range homocline (Figure 5);

(ii) a dome-and-keel geological architecture, comprising basement domes and surrounding supracrustal synclines, characteristic of several Archean and some Paleoproterozoic provinces (Marshak et al., 1997; Alkmim and Teixeira, 2017). The basement domes display a clear geometrical relationship with the supracrustal keels. For example, there is a geometrical relationship between the Bação and Bonfim domes and the Moeda and Dom Bosco synclines (Farina et al., 2016; Alkmim and Teixeira, 2017). Additional examples are provided by the Santa Rita and Ouro Fino synclines as well as the Mariana anticline (Figure 5);

(iii) a thrust system, comprising a series of arcuate and WNW-ESE-directed faults that cut the entire Precambrian section of the eastern half of the QF, overprinting pre-existing features (Chemale et al., 1994; Alkmim and Marshak, 1998; Farina et al., 2016).

This structural framework is considered to be the result of three different kinematic phases that have been identified using cross-cutting relationships and kinematic criteria (e.g., Chemale et al., 1994; Alkmim and Marshak, 1998), with limited absolute age constraints (Farina et al., 2016; Alkmim and Teixeira, 2017). The oldest phase (i) is related to a Rhyacian collision; its onset at ~2130 Ma (Machado et al., 1996) is constrained by the depositional age of the Sabará Group involved in the northwest-verging folding (Farina et al., 2016). The second kinematic phase is related to the formation of the dome-and-keel geological architecture. The contacts between the domes and the supracrustal units are tectonic, and kinematic indicators in supracrustal rocks support the hypothesis

that the two came into contact during an extensional event (Hippertt et al., 1992; Farina et al., 2016). Cross-cutting relationships indicate that the doming event post-dated the northwest-verging event (Alkmim and Marshak, 1998; Farina et al., 2016). Syn-kinematic garnets formed in a shear zone at the contact between a dome and the supracrustal units yield a Sm-Nd age of  $2095 \pm 65$  Ma (Marshak et al., 1997). This age is consistent with the U-Pb monazite ages obtained from the basement (e.g., Machado et al., 1992; Aguilar et al., 2015) and it suggests that this kinematic phase is related to the extensional collapse of the Rhyacian orogen (Farina et al., 2016; Alkmim and Teixeira, 2017).

Finally, the youngest phase is related to a compressional Neoproterozoic- to Early Ordovician Brasiliano (650-480 Ma) event that resulted from the development of a west-vergent fold-and-thrust belt (Chemale et al., 1994; Alkmim and Marshak, 1998). The QF represents its intermediate to distal section, without magmatic activity (Chemale et al., 1994; Alkmim and Marshak, 1998). The resulting structures form a continuum with the Brasiliano age structures of the SFC and of the Espinhaço Meridional, north of the QF (Chemale et al., 1994). This compressional event was superimposed on the earlier arrangement of structural highs (domes) and lows (synclines) displaying a wide array of orientations (Chemale et al., 1994). These structural highs acted as obstacles during the collisional tectonics, resulting in an amplification, translation and rotation of the regional synclines (Chemale et al., 1994). The intensity of deformation decreased westward, and thus WNW-ESE thrust faults related to this tectonic phase cut the entire Precambrian section only on the eastern portion of the QF (Chemale et al., 1994; Alkmim and Teixeira, 2017).

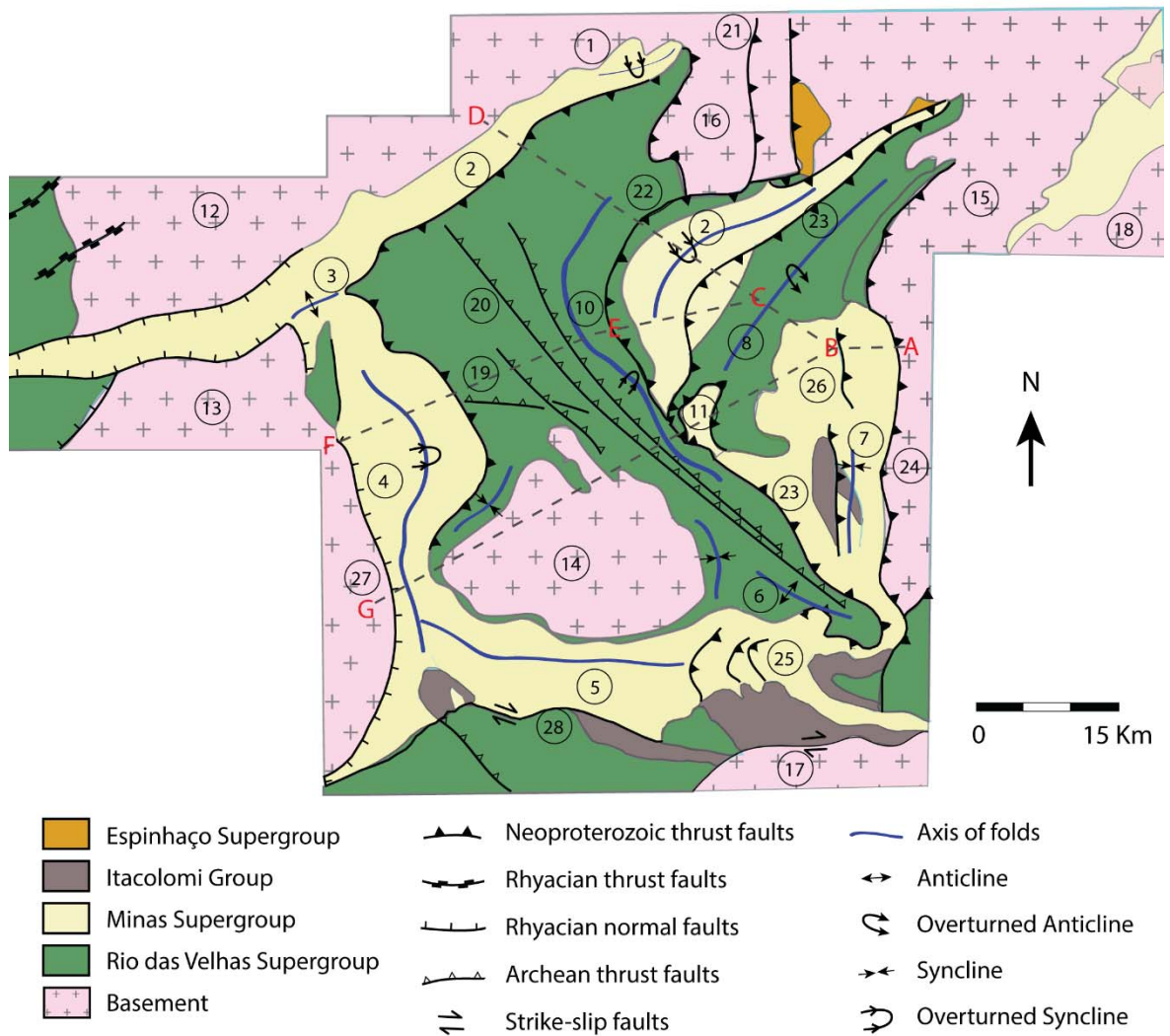


**Figure 5.** Main structural features of the QF. Red letters represent the vertices of the geologic cross-sections (grey dashed lines) displayed in Figure 6. Folds: 1. Piedade syncline; 2. Curral Range homocline; 3. Curral Range anticline; 4. Moeda syncline; 5. Dom Bosco syncline; 6. Marina anticline; 7. Santa Rita syncline; 8. Conceição anticline; 9. Gandarela syncline; 10. Vargem do Lima syncline; 11. Ouro Fino syncline; Granite-gneiss complexes: 12. Belo Horizonte; 13. Bonfim; 14. Bação; 15. Santa Bárbara; 16. Caeté; 17. Santo Antônio do Pirapetinga; 18. Matiqueira. Faults: 19. Bem-Te-Vi; 20. São Vicente; 21. Garimpo Creek thrust system; 22. Cambotas; 23. Fundão; 24. Água Quente; 25. Dom Bosco thrust system; 26. Caraça Range thrust system; 27. Extensional system Moeda-Bonfim; 28. Strike-slip Engenho. Modified from Lobato et al. (2005) and Baltazar and Zucchetti (2007).

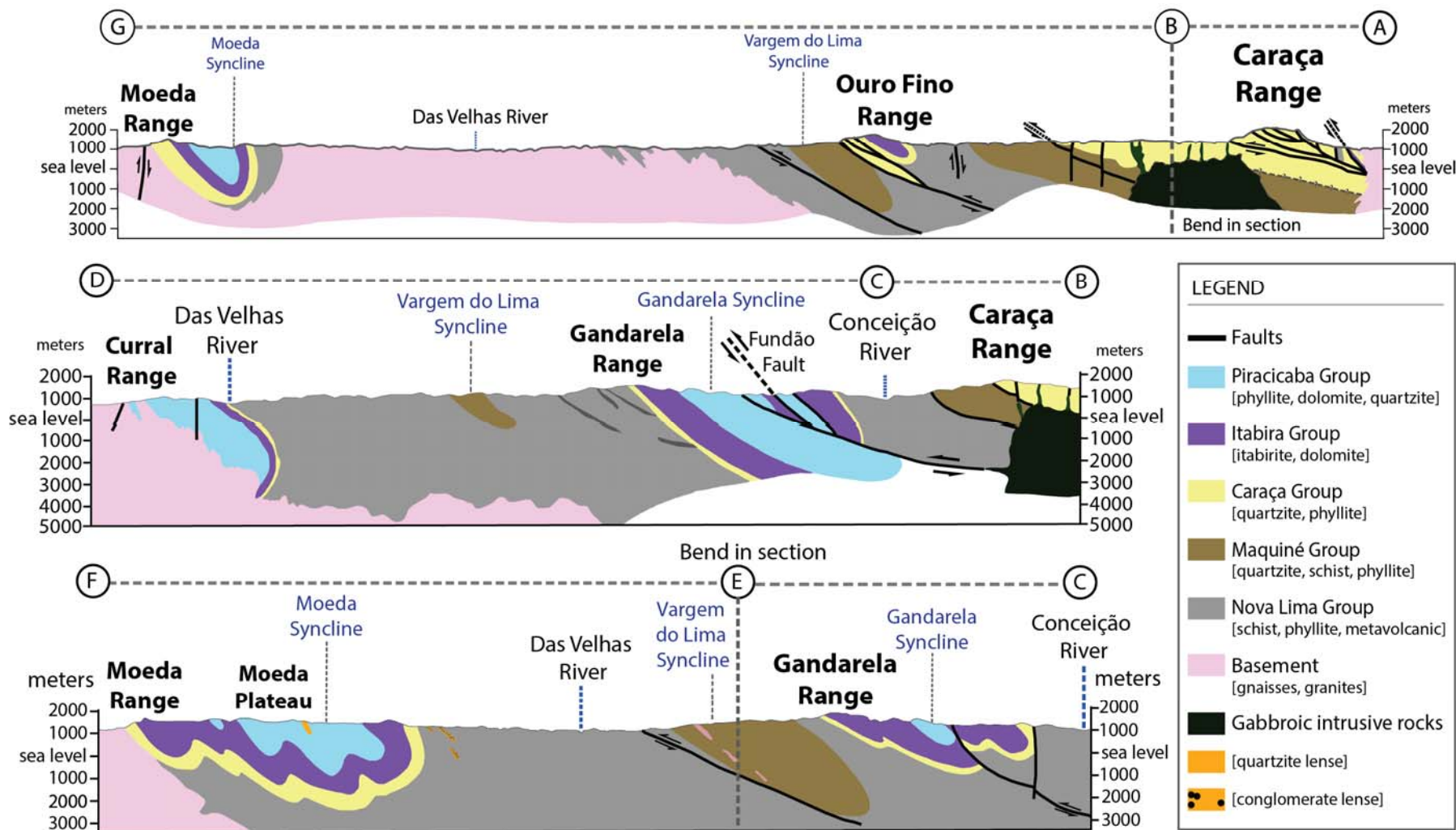
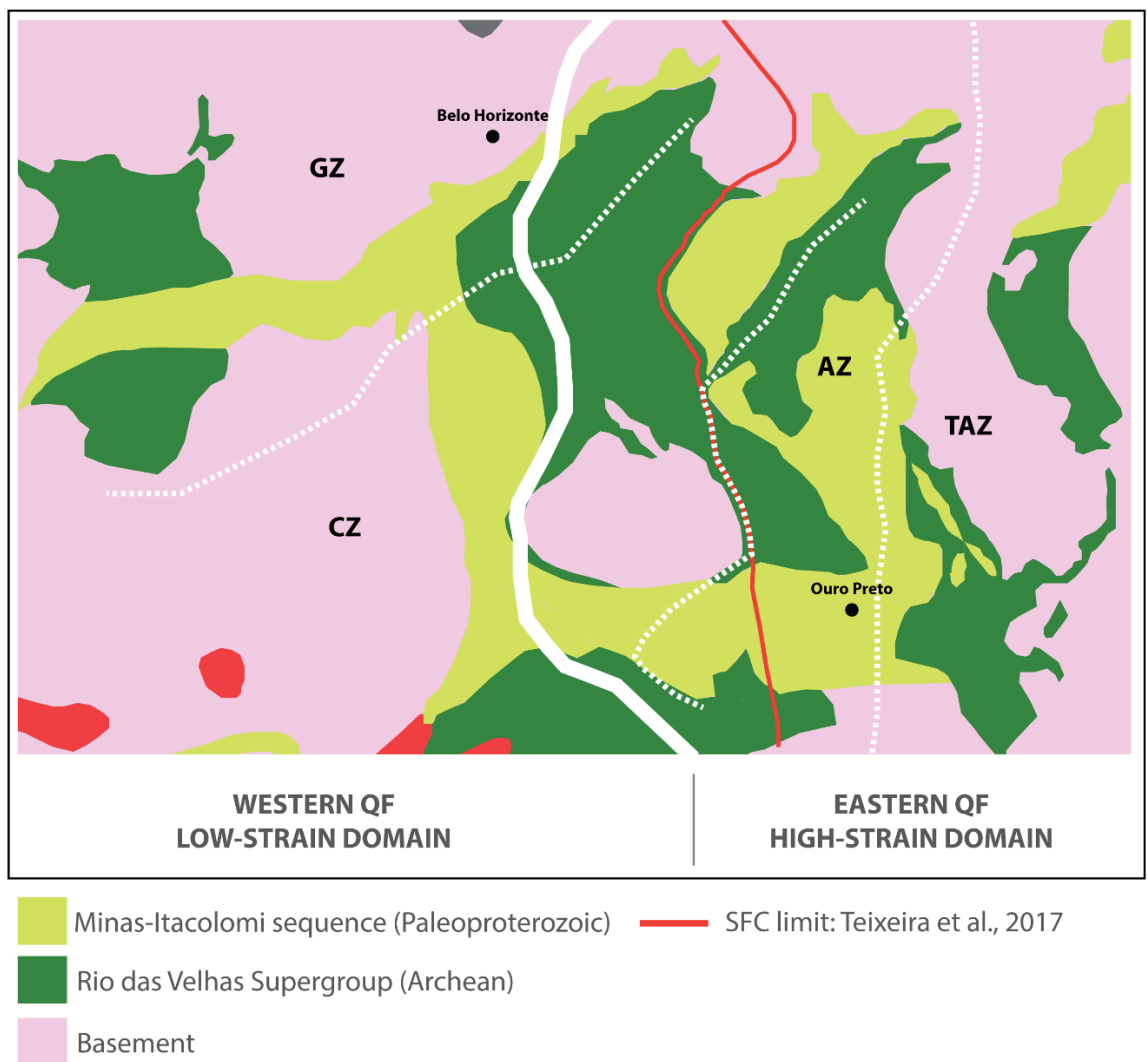


Figure 6. Three simplified geological cross-sections of the QF. The location of each profile is shown in Figure 5. Modified from Dorr (1969).

In summary, the QF's deformational history resulted in its segmentation into two main structural regions: the western domain, displaying mainly records of the older extensional deformation, and the eastern, affected by a younger Brasiliano compressional event of spatially variable magnitude (Chemale et al., 1994). Hence, the QF exhibits a spatial structural anisotropy in that its eastern section displays many thrust faults cutting the entire Precambrian section, contrasting with the less-faulted western QF (Chemale et al., 1994). The metamorphic zonation of the QF follows this trend in the sense that that its eastern and western parts are high- and low-strain domains, respectively (Rosière et al., 2001; Figure 7).



**Figure 7.** Metamorphic zones of the QF, modified from Rosière et al. (2001). Dashed lines separate the metamorphic zones: GZ - grunerite zone, CZ - cummingtonite zone, AZ - zctinolite zone, TAZ - tremolite-anthophyllite zone. The thick white line roughly separates the western QF with low-strain and basically no faults, from the eastern, high-strain domain.

Likewise, the distribution of historical earthquakes in the QF indicate that eastern part of the QF have experienced small magnitude earthquakes ( $M \sim 3$ ) whereas the southwestern part of the QF have not (Figure 8). The recorded earthquakes are of low magnitude ( $M \sim 3$ ) and, therefore, of limited significance; yet the Brazilian catalogue is relatively recent and may not be a true representation of the long-term behaviour of intraplate seismicity, in particular it may not record low frequency, higher magnitude events (Assumpção et al., 2014).

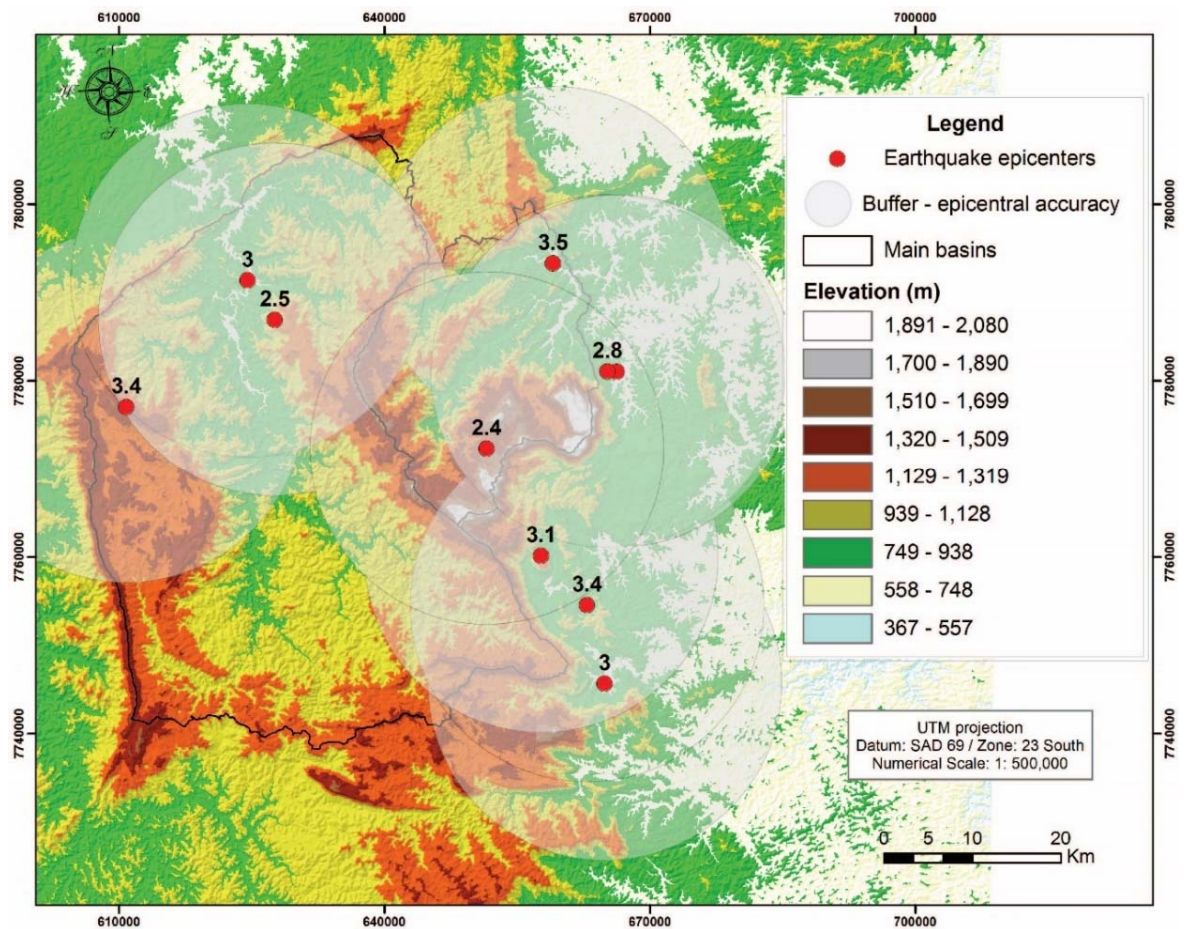


**Figure 8.** The spatial distribution of the historic earthquakes in the QF. Red circles represent earthquake epicentres whereas the large grey circles show the epicentral accuracy (20 km). The numbers next to red circles display the magnitude of these earthquakes. Smaller earthquakes (magnitude  $< 3$ ) started to be recorded only since  $\sim 1980$ . Two earthquakes occurred in 2015 ( $M$  2.8 and 2.4), four between 2011 and 2014, one in 1989 ( $M$  3.4), and two older (date not known) earthquakes ( $M$  3.5/3). Seismic data: Assumpção et al. (2014); Agurto-Detzel et al. (2015).

The lithologies exposed in the QF are many, with complex relationships between each other and of different resistance to weathering (Figure 9). Basement rocks (granites and granitic gneisses) are distributed around the supracrustal units, except for the Bação complex that is exposed in the central portion of the Upper Rio das Velhas basin. Quartzites are concentrated in the eastern QF, notably along the Caraça Range, and they follow a WNW direction in the eastern part of the Upper Das Velhas River basin; they are also exposed in the Cambotas Range and in the southern part of the QF (Figure 9). Schists are primarily associated with the central part of the two main catchments of the QF, as well as the southwestern part of QF (Figure 9). Phyllites are the primary rock type over the central part of the Moeda plateaux; they are also exposed in the southwest part of the Upper Das Velhas River basin. Metavolcanic rocks are limited to north, northeast, and southeast of the QF (Figure 9). Dolomitic units are primarily distributed immediately downstream of areas under banded iron formation and iron duricrusts, notably over the Gandarela syncline and the Moeda plateau. The areal distribution of the other lithologies is limited compared to those described above, including Cenozoic units that fill small basins (Figure 10).

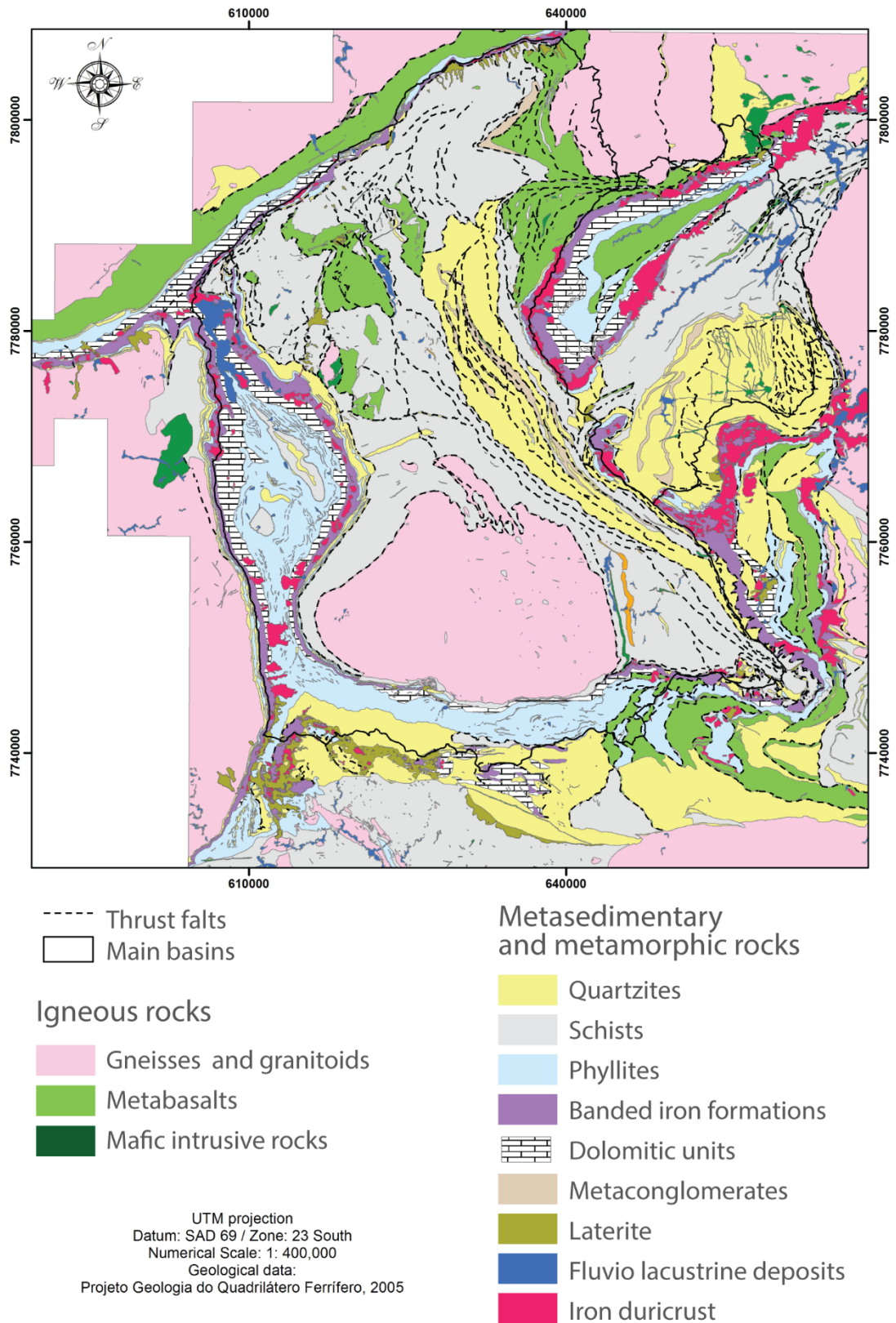
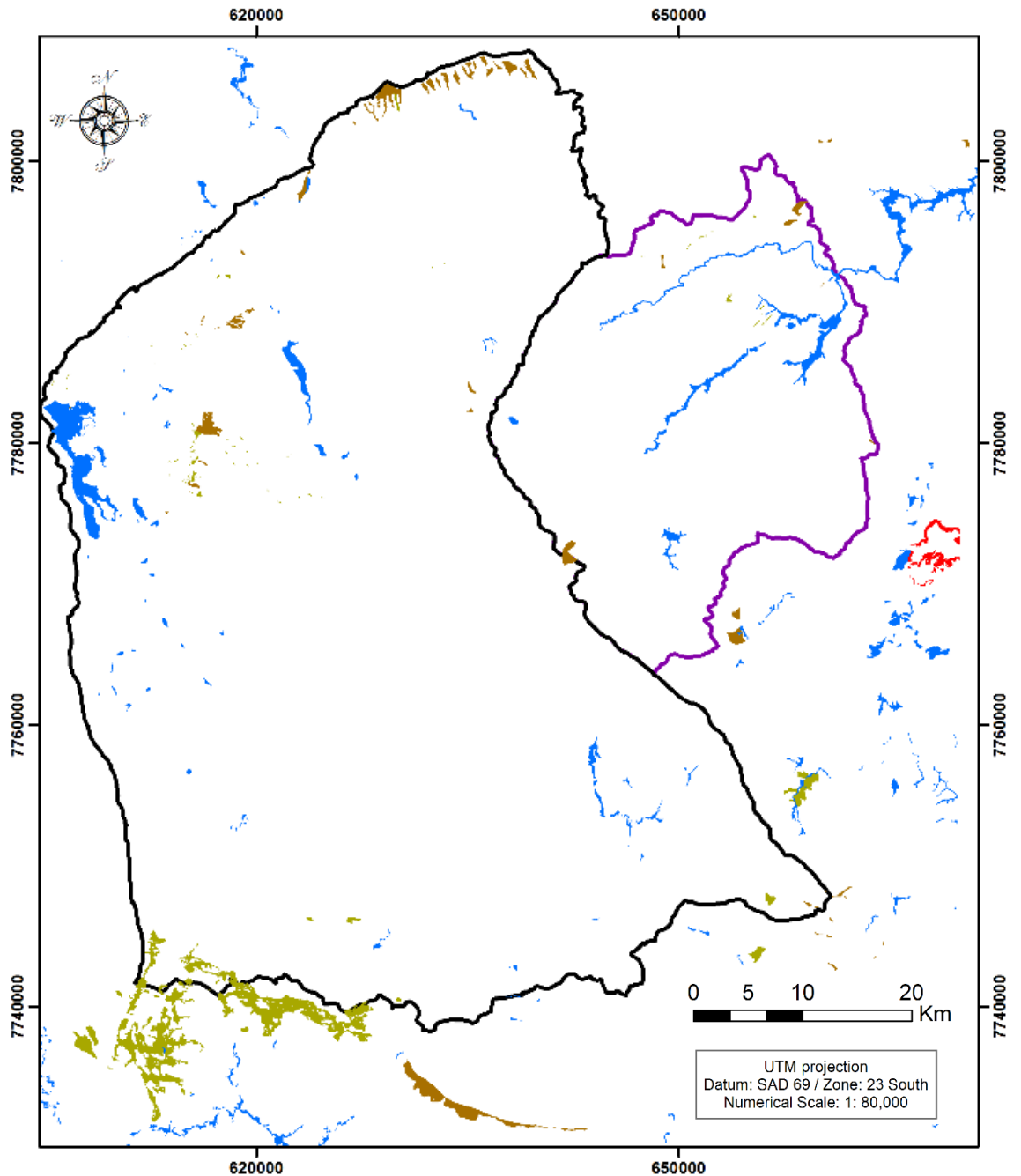


**Figure 9.** Simplified lithological map of the QF. Geological data derived from a geological mapping at 1:25,000. Dashed black lines represent thrust faults. The distribution of rocks per stratigraphic groups was presented in Figures 4-5. Geological data: Lobato et al., 2005.



### Legend

-  Upper Das Velhas River basin
-  Upper Conceição River basin

### Cenozoic deposits

-  Fluvial deposits
-  Colluvium deposits
-  Fonseca formation
-  Laterite

**Figure 10.** The spatial distribution of Cenozoic units in the QF, excluding iron duricrusts. Lobato et al. (2005, p. 53) described the Cenozoic deposits of the QF as ‘tectonically controlled’. Geological data: Lobato et al., 2005. The Fonseca formation refers to clayey and sandy lacustrine deposits (Eocene in age).

## 2.4 GEOMORPHIC RESEARCH IN THE QF

The geomorphic evolution of the QF is controversial. The most accepted hypothesis is that differential denudation of lithologies with different resistance to weathering and erosion has led to a geomorphic differentiation where the uplands, underlain by strong rocks (quartzites and banded iron formations), are high because they have been eroded less and more slowly than their surroundings (e.g., Harder and Chamberlin, 1915; James, 1933; Ruellan, 1950; Varajão, 1991; Salgado et al., 2008). The relief structure of the QF has, however, also been explained as the result of a complicated history of geographic cycles interrupted by epeirogenic uplift e.g., King, 1956; Barbosa and Rodrigues, 1965; Dorr, 1969; Barbosa, 1980; Varajão, 1991).

Existing detrital  $^{10}\text{Be}$  data suggest that erosion is primarily controlled by the different strength of the exposed lithologies (Salgado et al., 2007a, 2007b, 2008). Hence, areas characterised by resistant rocks display low denudation rates (~0.3 to 2 m/My); basins underlain by 'low-resistance' schists and phyllites are associated with 'average' denudation rates (~8 to 12 m/My); and basins underlain by the 'least-resistance' gneisses and granitic rocks have the highest denudation rates (~13 m/My). The existing  $^{10}\text{Be}$  data for the QF is further discussed in Chapter 5.

Field evidence implies that the QF has been a sub-aerial geomorphic feature over an extended period of time (King, 1956; Dorr, 1969). Geochronological  $^{40}\text{Ar}/^{39}\text{Ar}$  ages from weathering profiles located in the Moeda plateau in the western QF (Figure 1) indicate that these areas have been sub-aerial for around ~70 Myr (e.g., Carmo and Vasconcelos, 2004; Spier et al., 2006). The preservation of these weathered profiles has been taken to indicate that at least some areas have remained virtually uneroded for extended periods of time (Vasconcelos, 1999, Spier et al., 2006). The fact that these profiles are only present on the gently-sloping Moeda plateau and are absent from the adjacent, incised valleys to the east of the plateau suggests that the dissected parts of the landscape might be younger than the profiles (Carmo and Vasconcelos, 2004; Spier et al., 2006). Goethite (U-Th)/He ages are overall consistent with this interpretation, suggesting that ridges underlain by banded iron formations and iron duricrusts of the QF are

some of the oldest continually exposed landforms of the Earth, as they are at least ~60 Myr old (Monteiro et al., 2014; Monteiro et al., 2018). The distribution of ages with elevation also indicates that higher elevation surfaces are older than surfaces at lower elevations (Monteiro et al., 2014; Monteiro et al., 2018). Contrasting with this interpretation of continuous sub-aerial exposure for the QF is the work of Japsen et al. (2012), who analysed the organic content of one sample from the Fonseca Formation and produced apatite fission track data (the Fonseca Formation is represented in red in Figure 10). The AFTA data were interpreted to indicate a thermal history involving three cooling events, at 150 Ma, 145-70 Ma, and the youngest in the interval 50-10 Ma. According to Japsen et al.'s (2012) interpretation, the ancient profiles reported by Carmo and Vasconcelos (2004), Spier et al. (2006), Monteiro (2014) and Monteiro (2018) are not the result of a long exposure history associated with resistant lithologies and very slow erosion. Instead, the weathering profiles remained immune to denudation for Myr because they were buried by a kilometer-scale sedimentary cover, that was later completely removed by denudation between 50-10 Ma. Given that this evolutionary scenario is based only on one sample, it needs further investigation.

Evidence of Cenozoic deformation, notably in the eastern part of the QF, includes the formation of small graben-like Cenozoic sedimentary basins (e.g., Saadi, 1991; Saadi et al., 1992; Sant'anna et al., 1997; Santos et al., 2004; Cabral and Koglin, 2014), the post-depositional deformation of these Cenozoic sedimentary deposits (e.g., Saadi, 1991; Maizatto and Castro, 1993; Maizatto, 1997; Sant'anna et al., 1997; Lipski, 2002), and the hydrothermal overprinting of the Cenozoic sediments (Cabral and Koglin, 2014).

**CHAPTER 3:**  
**QUANTIFYING TOPOGRAPHY IN THE QF:**  
**THEORETICAL BACKGROUND AND METHODS**



# CHAPTER 3: QUANTIFYING TOPOGRAPHY IN THE QF: THEORETICAL BACKGROUND AND METHODS

## 3.1 INTRODUCTION

Post-orogenic landscapes have been defined as the ‘elephant in the room’ (Pelletier, 2008), as their evolution and, in particular, the persistence of post-orogenic topography, cannot be explained by the conventional geomorphic models of landscape evolution (Twidale, 1999; Bishop, 2007; Pelletier, 2008). The development through time of post-orogenic topography remains enigmatic, partly because of the relative lack of studies in these settings (Baldwin et al., 2003; Bishop, 2007), but also because of the inherent complexities of post-orogenic terrains (cf. Bishop, 2007; Twidale, 2016). An emblematic example of this problem is given by Baldwin et al. (2003) who limited their analytical study of post-orogenic topographic decay to the southern Appalachians (USA), the Lachlan fold belt (southeastern Australia) and the Ural Mountains (Russia) because “of the many Paleozoic orogenic belts still marked by mountainous topography, only a few have been sufficiently well studied to provide a motivational framework for our analysis” (Baldwin et al., 2003, p. 2).

The quantitative analysis of the topography of ancient, still-elevated mountain belts is critical for the interpretation of their post-orogenic erosive history (Bishop, 2007). To date, there are only a few studies quantifying post-orogenic relief using modern techniques (Baldwin et al., 2013), and even for areas like the southern Appalachians (USA), for which an extended body of geomorphic work is published, there is not a consensus regarding its erosional history or topographic characteristics (e.g., Hack, 1960; Hack, 1982; Pazzaglia and Brandon, 1996; Matmon et al., 2003a; Gallen et al., 2013; Miller et al., 2013; Prince and Spotila, 2013). This chapter is a prelude to the quantitative analysis of the topography of the QF. In section 3.2.1, the modern framework of how landscape evolution of erosive landscapes can be quantified using topography is discussed. The theoretical background of post-orogenic relief development through time is discussed in section 3.2.2. In section 3.3, the methodological steps of this

contribution are described. The results of the quantitative analysis of the topography of the QF are presented and discussed in Chapter 4.

## **3.2 THEORETICAL BACKGROUND**

### **3.2.1 EVOLUTION OF EROSION LANDSCAPES**

Bedrock rivers are the first-order control of relief development in unglaciated erosive landscapes (Whipple and Tucker, 1999, 2002; Kirby and Whipple, 2012). This modern view of landscape evolution on erosive landscapes was first theorised by Gilbert (1877), who proposed the rate of bedrock channel incision to be a function of discharge and local bed slope. The definition of ‘bedrock rivers’ indicates rivers that actively incise into bedrock over long timescales, and when these streams erode vertically, they set the local base level, to which all upstream channels and hillslopes must adjust (Whipple and Tucker, 1999, 2002). By setting the local base level for all upstream channel reaches and hillslopes, the rate of bedrock channel incision regulates the supply of sediment delivered to the channel from hillslopes (Whipple, 1999, 2002; Kirby and Whipple, 2012).

This framework (often implicitly) assumes that landscapes tend (or are trying) to achieve a steady-state condition where there is a long-term balance, or equilibrium, between landscape-scale geomorphic inputs (*i.e.*, rock uplift rate) and outputs (*i.e.*, erosion rates) resulting in a consistent topographic form through time (Schumm and Lichy, 1965; Kirby and Whipple, 2001; Forte et al., 2016). The equilibrium condition is a normative notion that relies on the uniformity of the boundary conditions (*i.e.*, the landscape’s tectonic, climatic and lithological contexts) of a steady-state landscape (Kirby and Whipple, 2001; Kirby and Whipple, 2012). Temporal and spatial changes in the boundary conditions may determine a change in relative base level, causing adjustments in channel form and an overall channel network response in the direction of the steady-state condition (Howard, 1994; Whipple and Tucker, 1999; Kirby and Whipple, 2001; Whipple and Tucker, 2002; Kirby and Whipple, 2012). The duration, pattern and style of landscape response to such transient forcing is a function of the characteristics of the forcing, the scale of the landscape, and feedbacks with hillslope processes (Howard, 1994; Heimsath et al., 1997; Kooi and Beaumont,

1996; Whipple and Tucker, 1999, 2002; Binnie et al., 2007; Whittaker et al., 2007; Ouimet et al., 2009; Kirby and Whipple, 2012).

The rate of bedrock channel incision may be used as a quantitative link between tectonic forcing (or another external forcing), landscape-scale topography, and net channel dynamics (cf. Kirby and Whipple, 2012; Lague, 2014). For that, the stream-power model, first expressed mathematically by Howard and Kerby (1983) but related to theory by Bagnold (1966), is the most commonly used mathematical model for modelling bedrock channel evolution (Pelletier, 2008; Kirby and Whipple, 2012; Lague, 2014). The stream-power model can be derived from a combination of the shear-stress river incision model (or the ‘unit stream power incision model’) and empirical relationships between discharge, catchment hydrology and channel hydraulics (Howard, 1994; Whipple and Tucker, 1999, 2002; Lague, 2014). Hence, bedrock channel incision rate ( $E$ ) is a power function of drainage area and local channel slope (Equation 1):

$$E = KA^mS^n \quad (1)$$

where  $K$  is a constant representing bedrock erodibility and climate,  $A$  is upstream drainage area (a proxy for discharge),  $m$  and  $n$  are empirical constants and  $S$  is channel bed slope. The rate of change in channel bed elevation is equal to the difference between rock uplift rate ( $U$ ) and erosion (Equation 2):

$$\frac{\partial h}{\partial t} = U - E = U - KA^mS^n \quad (2)$$

in which  $h$  is the local elevation of the channel bed, and  $t$  is time. Under the assumption of a steady-state condition,  $U$  is everywhere equal to  $E$ , and thus Equation (2) can be rewritten for  $\partial h/\partial t = 0$  (Equation 3):

$$U = KA^mS^n \quad (3)$$

Equation (3) expresses that for a steady-state bedrock river (i.e., spatially uniform and constant rock uplift, climate, lithology, and incision rates), channel slope is

inversely proportional to a power function of drainage area. Equation (3) can be rearranged as (Equation 4):

$$S = \left(\frac{U}{K}\right)^{\frac{1}{n}} A^{-\frac{m}{n}} \quad (4)$$

The scaling of channel slope with drainage area at steady-state, shown in Equation (4), is the basis of most of the modern quantitative analysis of landscape evolution in erosive landscapes (cf. Kirby and Whipple, 2012). It is often empirically observed that channel profiles display the same inverse relationship between slope and area expressed in Equation (4), even if they are not explicitly in steady-state (e.g., Hack, 1957; cf. Whipple and Tucker, 2002). Equation (4) can be rewritten as (Equation 5):

$$S = k_s A^{-\frac{m}{n}} = k_s A^{-\theta} \quad (5)$$

in which  $k_s$  is the channel steepness index, and  $\theta$  is the concavity index (Flint, 1974). Equation (5) can be used to derive estimates of  $k_s$  and  $\theta$  from regressions of log-transformed  $S$  and  $A$  data (Equation 6):

$$\log_{10} S = \log_{10} k_s + \log_{10} A^{-\theta} = \log_{10} k_s - \theta \log_{10} A \quad (6)$$

When  $\log_{10} S$  is plotted versus  $\log_{10} A$  for a steady-state bedrock river, a straight line should be obtained, with a slope equal to  $-\theta$  (or  $-m/n$ ) and intercept of  $\log_{10} k_s$ . Many studies suggest that  $\theta$  is relatively insensitive to variations in rock uplift rate, lithology or climate, and a range of  $\theta$  values of  $\sim 0.3$ - $0.6$  is often reported (e.g., Hack, 1957; Willgoose et al., 1991; Duvall et al., 2004; Whipple, 2004; Ramsey et al., 2006; Kirby and Whipple, 2012). On the other hand, the steepness index ( $k_s$ ) varies with spatial and temporal changes in rock uplift rate, bedrock erodibility or climate change, with the result that river profiles in a  $\log_{10} S$  versus  $\log_{10} A$  space may look segmented (Kirby and Whipple, 2012). In this case, each segment will display similar scaling as in Equation (5), but with marked differences between segments in  $k_s$  (or in  $\theta$ , if the perturbation is not spatially uniform; e.g., Kirby and

Whipple, 2001; Wobus et al., 2006). One important aspect of Equation (5) that needs to be noted is that the steepness index ( $k_s$ ) and the intrinsic concavity index ( $\theta$ ) covary since  $n$  is a component of both, meaning that a spatial variation in  $\theta$  intrinsically produces a variation in  $k_s$  that does not correspond to a real change in this parameter (Kirby and Whipple, 2012). The standard procedure to account for autocorrelation between these parameters is to define a fixed reference concavity index ( $\theta_{ref}$ ) and to quantify a normalised steepness index ( $k_{sn}$ ) based on  $\theta_{ref}$  (Wobus et al., 2006; Kirby and Whipple, 2012). Typically, a value of 0.45 is used for  $\theta_{ref}$ , which is arbitrary but allows comparison of  $k_{sn}$  values between different landscapes (e.g., Kwang and Parker, 2017). When autocorrelation is taken into account, Equation (5) quantifies the normalised steepness index as (Equation 7):

$$S = k_{sn}A^{-\theta_{ref}} \quad (7)$$

Empirical and numerical geomorphic work support a positive, often non-linear, functional relationship between  $k_{sn}$  and erosion rates (cf. Wobus, 2006; Kirby and Whipple, 2012; Lague, 2014). There are a few caveats to this approach; for example, feedbacks between the supply of sediment delivered from hillslopes and bedrock channel incision that may prolong the response time of the system (e.g., Ouimet et al., 2009; Egholm et al., 2013), are discussed by Kirby and Whipple (2012). However, the landscape-scale distribution of  $k_{sn}$  gradients, coupled with fluvial network geometry and catchment hydrology analysis, has been widely used to provide insights into the geomorphic history of erosive landscapes (cf. Wobus, 2006; Kirby and Whipple, 2012).

In summary, the stream-power model (and its variants, such as the chi or integral method; cf. Perron and Royden, 2013) is a fundamental reference for the investigation of the landscape evolution of erosive landscapes using topography (cf. Wobus et al., 2006; Kirby and Whipple, 2012). Recent examples of the use of the stream-power model approach in post-orogenic settings are given by Bishop and Goldrick (2010), Gallen et al. (2013), Miller et al. (2013), and Prince and Spotila, (2013), and this contribution follows their lead. In the following section,

the theoretical background of landscape evolution in post-orogenic settings is discussed with a focus on the timescale of post-orogenic relief decay and its topographic characteristics.

### **3.2.2 TIMESCALE OF RELIEF REDUCTION IN POST-OROGENIC LANDSCAPES**

Conceptually, in landscapes where active tectonic uplift has ceased for many Myr (or its presence is unknown and therefore of very small magnitude), the absence of counteracting forces to the destructive geomorphic processes determine a long-term decline of relief (Kooi and Beaumont, 1996; Bishop, 2007; Pelletier, 2008). Whereas denudational isostatic compensation may act prolonging the timescale of relief decay (Ahnert, 1970; Bishop and Brown, 1993), relief will still be reduced over long timescales (of hundreds of Myr) due to the net activity of surface processes (Ahnert, 1970; Kooi and Beaumont, 1996; Badwin et al., 2003; Bishop, 2007; Pelletier, 2008). Early geomorphic schemes (e.g., the Davisian ‘geographical cycle’; Davis, 1889) discussed conceptually (i.e., without quantitative data) that relief wanes over time in the absence of uplift. However, the timescale of post-orogenic decay was only investigated quantitatively once our conceptual understanding of the forces that act on the landscape improved, in particular within the framework of plate tectonics, and data on rates of surface processes became available (Bishop, 2007). There are several analytical approaches for estimating the timescale of post-orogenic relief reduction. The application of different methods yielded similar estimates of ~10-25 Myr for lowering the post-orogenic relief into a featureless lowland (Gilluly, 1955; Schumm, 1963; Judson and Ritter, 1964; Ahnert, 1970; Pinet and Souriau, 1988). Adding an isostatic compensation requires a 5/6-fold adjustment in decay timescales (~50-70 Myr), lengthening the life of these landscapes considerably, but still, up to one order of magnitude smaller than the time interval since orogenesis was active (Pelletier, 2008). The disagreement between estimates of relief reduction and the still-mountainous topography in post-orogenic settings determined the “paradox of persistent mountain belts” (Pelletier, 2008, p. 101). This paradox led ultimately to two different explanations for post-orogenic relief: either (1) post-orogenic topographic rejuvenation events are necessary to explain the survival of relief (e.g., Hack, 1982; Pazzaglia and Brandon, 1996); or (2) other processes that act

to inhibit erosion must be accounted for estimates, increasing thus the decay timescale (e.g., Baldwin et al., 2003).

The most straight-forward approach for estimating post-orogenic relief reduction is the simple division of a landscape-scale mean topographic parameter (e.g., mean elevation) by its average denudation rates. These estimates have yielded topographic decay timescales of ~10-25 Myr for all post-orogenic landscapes (e.g., Gilluly, 1955; Schumm, 1963; Judson and Ritter, 1964) that were critical for the establishment of an (almost) consensual viewpoint that landscapes are of recent age, probably all no older than Neogene (e.g., Thornbury, 1969). These early studies assumed denudation rates that were probably faster than the values representative of post-orogenic landscapes (Young, 1983; Bishop, 2007) and did not take account the dependence of denudation on relief (e.g., Schumm, 1956; Ahnert, 1970; Pinet and Souriau, 1988; Summerfield and Hulton, 1994; Whipple and Tucker, 1999, 2002). As a result of these shortcomings, alternative methods for estimating the timescale of relief decay in post-orogenic settings were proposed.

Perhaps the most influential alternative for estimating the timescale of relief decay in post-orogenic settings is the approach that holds denudation as a direct function of relief (e.g., Ahnert, 1970; Pinet and Souriau, 1988). As topography decays over time, so do the denudation rates. If denudation rates are a function of topography, then post-orogenic relief decays exponentially following the differential equation (Equation 8):

$$\frac{\partial h}{\partial t} = -\frac{1}{\tau_d} H \quad (8)$$

Where  $H$  is the mean elevation of the landscape, and  $\tau_d$  is the erosional time constant (Pinet and Souriau, 1988, p. 564), which is the time taken for the relief to be reduced to  $1/e$  (~0.357879441), or around 37% of  $H$ . The solution of Equation (8) is given by Equation (9):

$$H = H_0 e^{-\frac{t}{\tau_d}} \quad (9)$$

where  $t$  is time, and  $H_0$  is the initial value of the mean topographic parameter (e.g., mean elevation) immediately following the cessation of uplift. The erosional time constant  $\tau_d$  is the reciprocal of the angular coefficient ( $a$ ) in the regression between the denudation rates ( $E$ ) and  $H$  (Equation 10-11):

$$E = aH + b \quad (10)$$

$$\tau_d = \frac{1}{a} \quad (11)$$

in which  $a$  is often positive, and  $b$  (the intercept in the regression between  $E$  and  $H$ ) is negative (e.g., Ahnert, 1970; Pinet and Souriau, 1988). An alternative mathematical explanation of post-orogenic topographic decay is provided by Equation 12 (Ahnert, 1970):

$$t = \frac{\log_{10} h_t - \log_{10} h}{\log_{10}(1 - a)} \quad (12)$$

where  $t$  is the time required to reduce the initial mean topographic parameter  $H$  to a lesser relief  $H_t$ . If  $H_t$  is equal to  $(0.357879441 \times H)$ , then the parameter  $t$  will be  $\sim \tau_d$ . Using this approach, Ahnert (1970) estimated that relief reduction to base level (whereby  $H_t = 0.01 \times H$ ) would take 22 Myr in the absence of uplift. The erosion constant  $\tau_d$  was quantified by Ahnert (1970) using the slope of the regression between mean denudation rates (derived from sediment load data) and mean relief over a window size of 20 km<sup>2</sup>. Using a similar approach, Pinet and Souriau (1988) estimated that relief reduction in ‘dead’ orogens had a  $\sim 25$  Myr timescale. Erosion-driven isostatic compensation, due to the contrast between the density of the crust ( $\rho_c = 2700$  kg/m<sup>3</sup>) and the density of the mantle ( $\rho_m = 3300$  kg/m<sup>3</sup>), increases  $\tau_d$  by a factor of approximately 6 (i.e.,  $\rho_c / (\rho_m - \rho_c) \sim 6$ ) (Ahnert, 1970; Baldwin et al., 2003; Pelletier 2008). The estimates of relief reduction reported by Ahnert (1970), including the effect of isostatic compensation, are represented schematically in Figure 11.

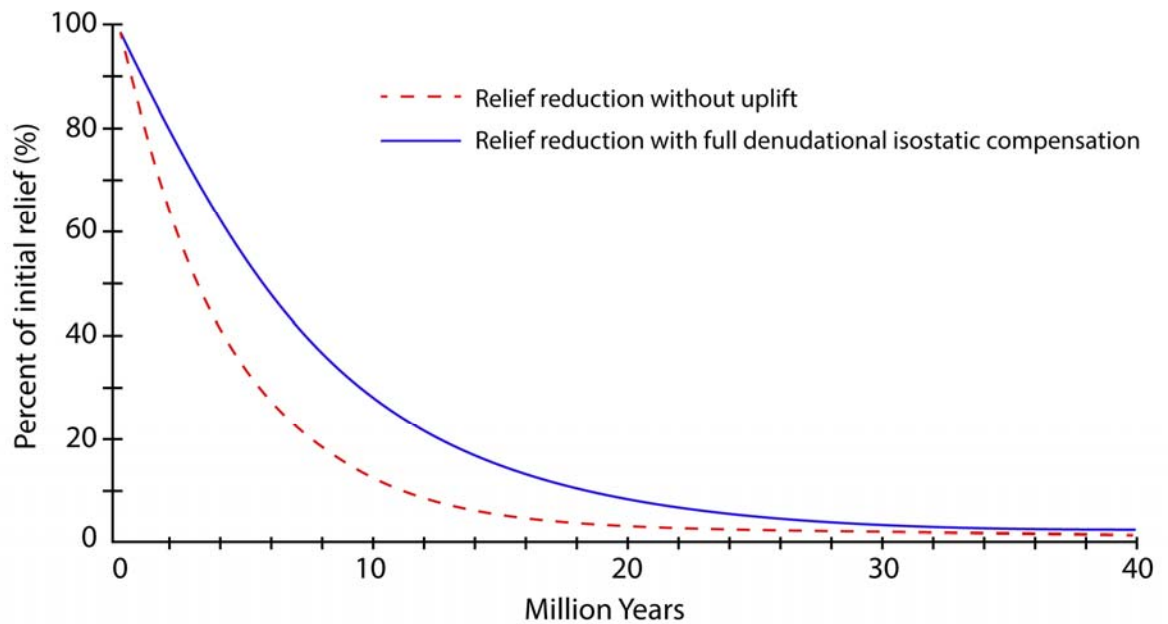


**Figure 11.** Schematic representation of post-orogenic relief reduction through time following Ahnert (1970). The dashed line indicates relief decay without isostatic uplift, whereas the blue line shows the decay in the context of full denudational isostatic compensation.

Another method for estimating post-orogenic topographic decay was given by Baldwin et al. (2003). This approach is a modification of the bedrock channel response to a decrease in uplift rate suggested by Whipple (2001), considering, in this case, a sudden cessation of rock uplift determining a ‘declining’ transient landscape. Baldwin’s et al. (2003) analytical solution relies on the applicability of stream power incision model (discussed in section 3.2.1). Their approach can be envisaged by a transient profile with an abrupt change in local channel slope, a knickpoint, separating an upstream segment that is not yet adjusted to the relief decline, and a downstream reach that has already declined (Figure 12). The erosional decay of this landscape can be set, for example, for when the channel head elevation ( $Z(x_c)$ ) is equal to 1% of the initial topography immediately before the cessation of the uplift  $H_0$  (i.e.,  $Z(x_c) = 0.01 x H_0$ ). In this case, the topographic decay timescale is given by Equation 13 (Whipple and Tucker, 1999):

$$t = \frac{Z_f(x_c) - Z_i(x_c)}{\partial Z(x_c)/\partial t} \quad (13)$$

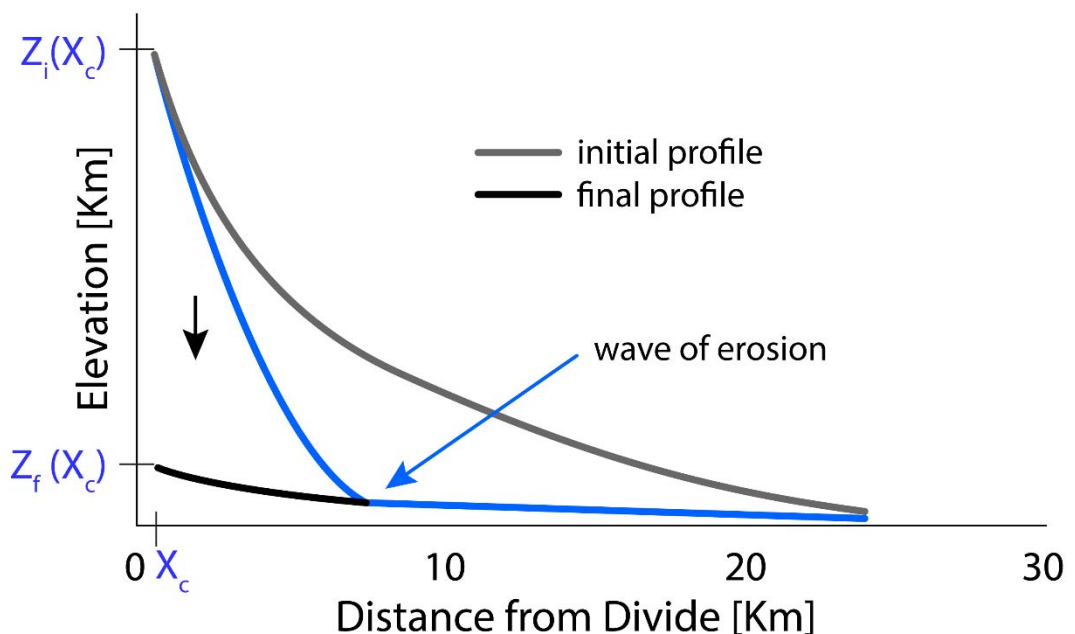


**Figure 12.** Simplified scheme of a ‘declining’ transient landscape following Baldwin et al. (2003). There is an upstream-migrating break in slope separating an upstream segment that has not declined from a downstream segment that has already responded to the cessation of uplift.  $Z_i(x_c)$  is ultimately reduced to  $Z_f(x_c)$ . Modified from Baldwin et al., 2003.

where  $Z$  is elevation,  $x$  represents downstream distance,  $x_c$  denotes the downstream distance at the channel head,  $Z_f(x_c)$  corresponds to the ‘final’ elevation of the channel head, and  $Z_i(x_c)$  represents the ‘initial’ elevation of the channel head immediately following the cessation of uplift. According to this model, the post-orogenic transient response is directly related to the upstream migration of a knickpoint (Figure 12), whose celerity ( $C$ ) is given by Equation 14 (Whipple and Tucker, 2002):

$$C = KA^m S^{n-1} \quad (14)$$

Baldwin et al. (2003) used a ‘reasonable’ set of initial parameters (the initial elevation of the channel head  $Z_i(x_c)$ ; channel length  $L$ ; rock uplift  $U$ ; bedrock erodibility factor  $K$ ; and the slope exponent  $n$ ) for estimating topographic decay times using this approach. The calculation relied on holding  $(U/K)^{-n}$  (the channel steepness; Equation 4) constant, and thus every  $n$  value (namely, 3/2, 1, 2) had a corresponding  $K$  that varied to produce the same magnitude of initial topography (Baldwin et al., 2003). Overall, this approach yielded very short decay timescales for a detachment-limited system with  $n \leq 1$  (~2-5 Myr) (Baldwin et al., 2003). The inclusion of complete denudational isostatic compensation increased the decay time by a factor of 6, thus yielding a topographic decay of ~10-30 Myr for  $n \leq 1$ . For models with  $n > 1$ , however, the timescale of topographic decay increased to hundreds of Myr (Baldwin et al., 2003). This contrast in decay timescales for different values of  $n$  is the result of how  $n$  affects the fluvial response to perturbations (Whipple, 2001). In the case of the sudden cessation of rock uplift (Baldwin et al., 2003), for  $n \leq 1$  the channel steepness at the channel head remains fixed until it is reached by the upstream-migrating knickpoint. By contrast, for  $n > 1$  the steeper parts of the knickpoint migrate upstream faster than its less steep parts and the knickpoint loses its definition, resulting in a decrease in the rate of lowering of the channel head elevation and a more gradual overall reduction of slope than for the  $n \leq 1$  case. This context implies much longer response times for

landscapes associated with  $n > 1$  than for  $n \leq 1$  (Baldwin et al., 2003). Incorporating a transition to a transport-limited condition, whereby long-term sediment flux ( $Q_s$ ) equals or exceeds long-term transport capacity ( $Q_c$ ) with alluvial sediments inhibiting channel bed incision, further increases the decay timescale by a factor of 2-3, corresponding thus to a topographic decay of ~36-90 Myr if isostatic compensation is accounted (Baldwin et al., 2003). Baldwin et al. (2003) demonstrated that persistence of topography for hundreds of Myr in post-orogenic settings can be explained within the stream-power framework, but it requires  $n > 1$ , combined with other processes that act to inhibit erosion, such as denudational isostatic compensation or a transition to a transport-limited condition.

An alternative approach for estimating post-orogenic topographic decay is given by the consideration of an abrasion-saltation sediment flux-driven erosion model, whereby the primary erosional agent is sediment (Sklar and Dietrich, 2001, 2004; Pelletier, 2008). Hence, Equation (2) can be rewritten with bedrock channel incision as a function of sediment flux, instead of drainage area (Equation 15; Pelletier, 2008, p. 8):

$$\frac{\partial h}{\partial t} = U - K_b(Q_s)^m S^n \quad (15)$$

with  $Q_s$  as the sediment flux and  $K_b$  as a new coefficient of erodibility. Pelletier (2008) and Egholm et al. (2013) discussed the implications of a sediment-flux-driven erosion model for the topographic decay of post-orogenic settings, by comparing it with the stream-power model (e.g., Baldwin et al., 2003). Both models are similar for steady-state landscapes, in which denudation is spatially uniform and in equilibrium with  $U$ , with the sediment flux  $Q_s$  proportional to drainage area  $A$  (Pelletier, 2008; Egholm et al., 2013). However, these models predict different geomorphic evolution histories in the context of post-orogenic decay (Pelletier, 2008; Egholm et al., 2013). The cessation of  $U$  determines the decline of relief (that is only balanced by denudational isostatic compensation), which implies that denudation rates will decrease through time. In the context of the sediment flux-driven model, the reduction of hillslope gradients leads to a lower frequency of landslides which, in turn, results in a smaller amount of sediment supplied by hillslopes to channels (Pelletier, 2008; Egholm et al., 2013).

The decline of sediment supply results, in turn, in an overall reduction in channel incision rates due to the absence of abrading tools (Sklar and Dietrich, 2001, 2004; Pelletier, 2008). The drop in channel incision rates further diminishes the frequency of landslides (reinforcing these feedbacks), which ultimately acts to increase the timescale of relief reduction (Pelletier, 2008; Egholm et al., 2013). By contrast, the stream-power model predicts a faster decrease in denudation rates through time because channel incision rates will be fast as long as relief is steep (Pelletier, 2008). In accordance, the mean elevation in the stream-power model decays exponentially with  $\tau_d \sim 30$  Myr (Pelletier, 2008, p. 105), contrasting with a much slower decay for the sediment-flux-driven model, where peak elevations may be as high as 2000 m up to 200 Myr after the cessation of tectonic activity (Egholm et al., 2013). However, the morphology of the ‘residual’ post-orogenic topography is similar for both models, in that it is associated with the overall absence of relief, “with main valleys that become permanently alluviated when the available stream power decreases below the threshold required for sediment transport” (Egholm et al., 2013, p. 477).

The fundamental problem with every estimate of post-orogenic relief reduction is that the persistence of post-orogenic relief implies very low denudation rates for a prolonged period of time (plus denudational isostatic compensation) whereas steep relief leads to high denudation rates. Low denudation rates can only be explained if the ‘residual’ relief of the post-orogenic landscape has topographic characteristics similar to those of steady-state landscapes observed in actively uplifted landscapes (e.g., Hack, 1960; cf. Baldwin et al. 2003), such as smooth, concave-up channel longitudinal profiles with no knickpoints (Lague, 2014). In other words, post-orogenic landscapes should “be considered an old orogen that is approaching planation... this orogen may be on the tail of the response curve and evolving very slowly” (Kooi and Beaumont, 1996, p. 3371). In accordance, the traditional framework for the typical characteristics of post-orogenic channels is that where not ‘perturbed’ by contrast in lithology, channels often exhibit smooth, concave-upward profiles that are very similar to steady state channel forms expected and observed in actively uplifted ranges (Baldwin et al., 2003). There are, however, many post-orogenic settings where the channel profiles have pronounced knickpoints that separate a gentle upstream reach from an ‘adjusted’ downstream segment (e.g., Bishop and Goldrick, 2010; Gallen et al., 2013; Prince

Quantifying Topography in the QF: Theoretical Background and Methods and Spotilla, 2013). Hence, the topographic signature of post-orogenic settings remains poorly constrained. In the following sections, I describe the methodological procedures used to quantify the topography of the QF.

### **3.3 METHODS AND DATA**

#### **3.3.1 OVERVIEW**

I used a range of modern techniques of topographic analysis to extract quantitative topographic information for a classic post-orogenic landscape. The objective of this approach was to quantify the relationship between topography and the geological framework of the study area, which encompasses strong and weak lithologies (see Chapter 2). I also investigated the relationship between different topographic parameters (e.g., steepness, elevation, and relief) over different spatial scales, from the local channel and hillslope morphology to catchment-averaged parameters, scaling from second- to seventh-order basins (Strahler, 1957). In short, my dataset has been collected using four different analyses:

- (1) Local topography analysis
- (2) Catchment-averaged topographic analysis
- (3) Cluster analysis
- (4) Stream-profile analysis

Each of these analyses quantifies the topography of the QF through a different geomorphic ‘lens’. In (1), the spatial distribution of local channel and hillslope morphometry was investigated as a way to assess how different topographic parameters are distributed over the QF, and if the distributions of different parameters are consistent between each other. The local topographic parameters quantified in (1) were used as input to calculate catchment-averaged parameters for all drainage basins of the QF using Strahler’s stream-order classification (Strahler, 1957). In (2), the relationship between different catchment-averaged topographic parameters was quantified. The catchment-averaged parameters that were consistently associated with high goodness-of-fit (i.e.,  $R^2$  values) in bivariate regressions to every other parameter (as a result of 2) were used as input to define topographic clusters in (3). In (3), clusters based on the areal contribution of

different lithologies were statistically compared to clusters based on the topography, to test how well lithological clusters can explain the topographic variability in the QF. Finally, in (4), channel steepness data were analysed, focusing on the distribution and characteristics of knickpoints, to identify their nature and suggest their origin. The comparison of the quantified topographic characteristics with the resistance of exposed bedrock is at the heart of this chapter, as post-orogenic relief is so often assumed to relate to exposed bedrock resistance (e.g., Hack, 1960).

### **3.3.2 TOPOGRAPHIC PARAMETERS**

Geomorphic parameters were extracted for the QF over an area of ~6200 km<sup>2</sup> using a 12 m TanDEM-X (TerraSAR-X add-on for Digital Elevation Measurement) digital elevation model (DEM). The selected topographic parameters are those that previous studies have demonstrated to play an essential role in revealing the pattern and style of landscape evolution of erosive settings, and for which data with adequate resolution was available.

Elevation data was directly extracted from the TanDEM-X DEM, whereas the other parameters were derived from the DEM. Slope measurements were taken for each pixel in the DEM using the ArcGIS v. 10.3 extension 'Spatial Analyst'. This tool fits a plane to the elevation data of a 3x3 matrix around each pixel and calculates slope using the average maximum technique (Burrough and McDonell, 1998). Local relief was quantified as the elevation range within a neighbourhood defined by a circular window with a diameter varying from 0.5 to 10 km (e.g., Montgomery and Brandon 2002; DiBiase et al., 2010). The choice of the local relief window was based on a sensitive analysis following DiBiase et al. (2010); the 2-km diameter window is the one that displays the highest goodness-of-fit in bivariate regressions with the normalised steepness index for every basin order and, therefore, it is the one that has been used throughout (Figure 13).

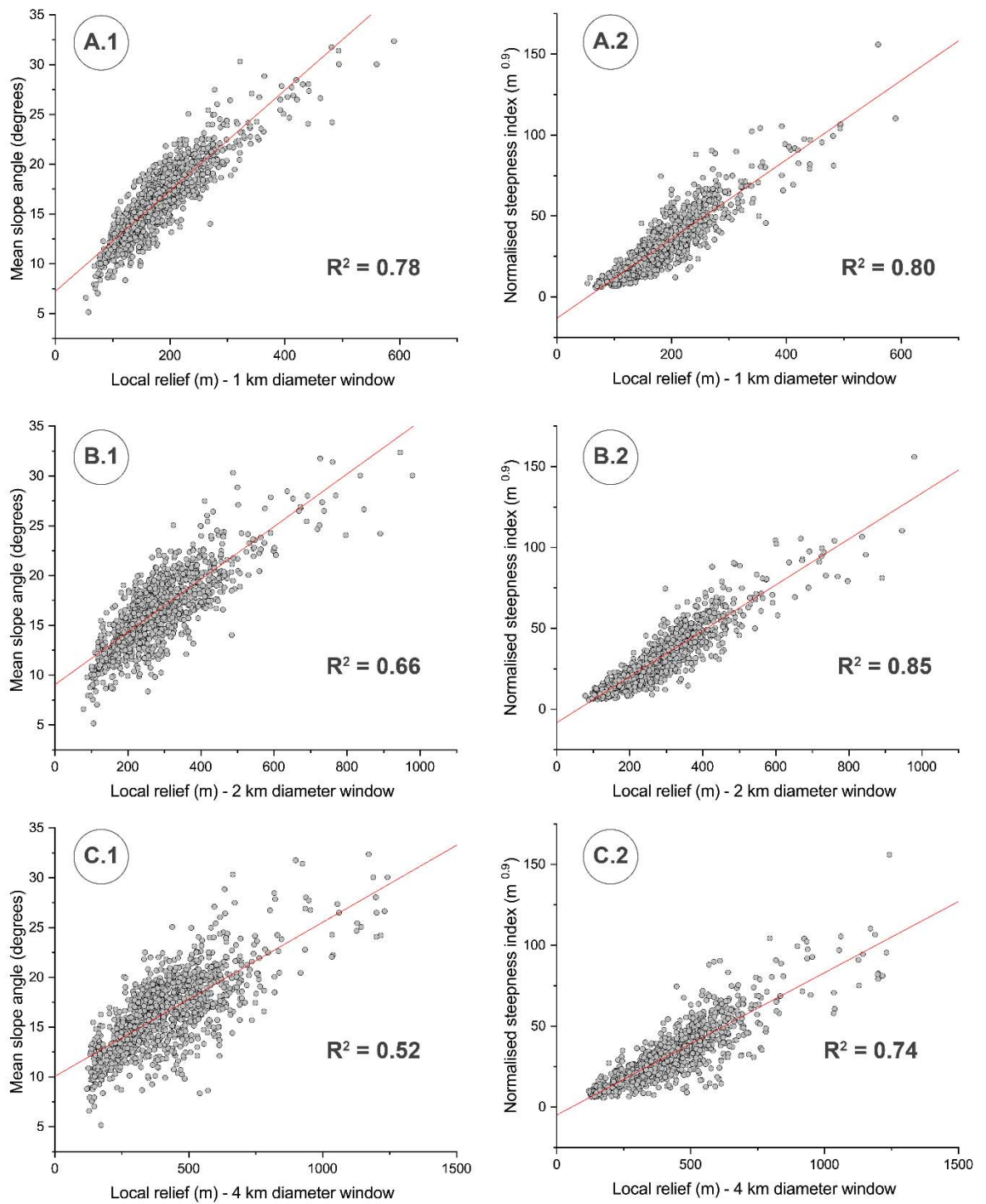


**Figure 13.** Bivariate regressions between (1) catchment-averaged mean slope angle and (2) normalised steepness index. The diameter of the circular window used for the calculation of local relief is: (A) 1 km, (B) 2 km, (C) 4 km. Increasing the window diameter decreases the  $R^2$  of local relief against mean slope angle. By contrast, the 2-km diameter window (B2) exhibits the highest  $R^2$  with the normalised steepness index.

The normalised steepness index ( $k_{sn}$ ) was calculated using Gallen and Wegmann's (2017) ChiProfiler v. 1 software, a MATLAB code that conducts river profile analysis using the chi or integral method (Perron and Royden, 2013). I discuss the chi/integral method further in section 3.3.6. The normalised steepness index was quantified as the derivative of the chi and elevation instead of the more traditional method of using  $\log_{10}S$  versus  $\log_{10}A$  (cf. Wobus et al., 2006) because the integral method does not require estimating slope from the DEM since taking derivatives of elevation results in noisy estimates of channel slope (cf. Perron and Royden, 2013). Precipitation data relied on the TerraClimate database (Abatzoglou et al., 2018), a high-resolution monthly climate dataset that includes global precipitation data from 1958 to 2015. The TerraClimate dataset combines high-resolution climatological normals from the WorldClim dataset (Fick and Hijmans, 2017) with coarser resolution data from other sources, resulting in a monthly dataset including various climatic variables such as precipitation and temperature. The TerraClimate dataset was validated using station data as well as streamflow gauges (Abatzoglou et al., 2018). The density of faults was quantified using ArcGIS's v. 10.3 Kernel Density method, which calculates the density of features in a neighbourhood around those features; for line features, this kernel density function adapts the quadratic kernel function for the density of points (cf. Silverman, 1986, p.76, equation 4.5). Faults were extracted from the 'Projeto Geologia do Quadrilátero Ferrífero' dataset (Lobato et al., 2005) mapped at a scale of 1: 25,000.

The determination of drainage basin perimeter was performed using the TopoToolbox v.2 function 'drainagebasins' (Schwanghart and Scherler, 2014). This function determines drainage basins based on a flow direction matrix. I first generated a stream-order grid for the QF, using TopoToolbox's function 'streamorder' (Schwanghart and Scherler, 2014), and then used this stream-order grid as input to determine basins, based on Strahler's stream-order classification (Strahler, 1957). The output is every drainage basin classified according to the order of its main stream. Basin-wide area and relief were then quantified for each catchment. The area was readily extracted for each basin using the ArcGIS's v. 10.3 'Calculate Geometry' function; basin relief was quantified as the difference between the maximum-minimum elevation within a basin. All topographic work

was done using UTM projected coordinates (with map distance and elevation in m).

### **3.3.3 LOCAL TOPOGRAPHY ANALYSIS**

The spatial configuration and distribution of local geomorphic parameters in the QF, as well as their relationships with the underlying lithology and the distribution of faults, were assessed in the local topography analysis. The spatial arrangement of high and low values of each local topographic metric was the focus of this section, and thus the intersection of extreme values for each pair of metrics was investigated. For that, each local topographic parameter described in section 3.3.2 was quantified from the TanDEM-X DEM, producing a geomorphic surface with a parameter value for every pixel across its extent. Each pixel from the distribution of each topographic parameter was converted into a point feature. Subsequently, these points were used as input to a univariate statistical analysis that quantified the central tendency (mean and median), the dispersion (range, quartiles of the dataset, variance and standard deviation as measures of spread) and the shape of the distribution (skewness and kurtosis) for all topographic parameters, using OriginPro v.2018. The geometric intersection between the distribution of bedrock lithology (Figure 9) and the distribution of each topographic variable was determined using ArcGIS v. 10.3 'Analysis' extension. The dataset of topographic variables for each rock type (e.g., quartzites; schists) was used as input for another univariate statistical analysis that defined the characteristics of the distribution of every topographic parameter by lithology.

### **3.3.4 CATCHMENT-AVERAGED TOPOGRAPHIC ANALYSIS**

In this section, catchment-averaged topographic metrics were quantified for all the basins of the QF, extracted following Strahler's stream order (Strahler, 1957), which is a method of river classification based on the hierarchy of tributaries. First-order streams are those that do not have tributaries; second-order streams are streams formed by the confluence of two first-order streams, and so on (Figure 14). For all the geomorphic parameters calculated in the topographic analysis, the catchment-averaged value of the parameter is the average of all local values within a catchment. For parameters exclusively determined as basin-wide (i.e.,

basin area and basin relief), the catchment-wide values were extracted from the TanDEM-X DEM. The areal contribution of different lithologies for every basin was quantified using ArcGIS's v. 10.3 'Tabulate Area' function.

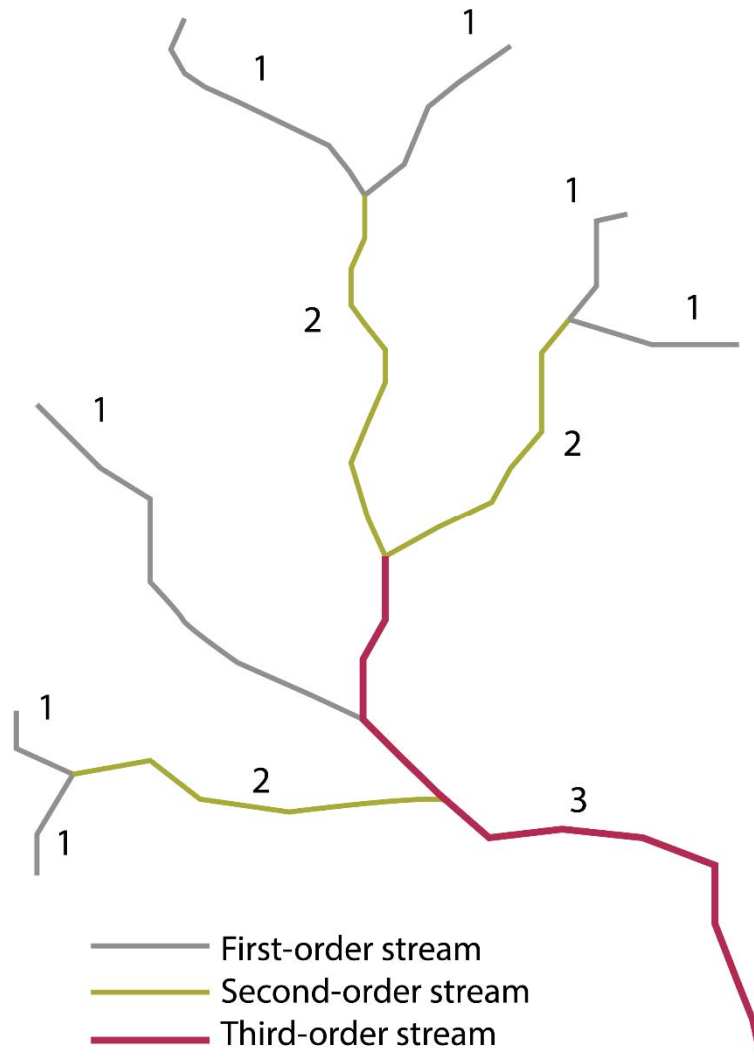


**Figure 14.** Schematic representation of the stream-order classification by Strahler (1957). Numbers represent channel reach stream-order number. In this classification, first-order streams are channel reaches that do not have tributaries; second-order streams are streams formed by the confluence of two first-order streams, and so on.

All the basins of the QF with an order greater than one were investigated; bivariate regression analyses between every combination of catchment-averaged topographic parameters were performed, using OriginPro v.2018, with two main objectives: (1) to determine which topographic variables were going to be used as input for the determination of topographic clusters in the cluster analysis (section 3.3.5), (2) to quantify how different basin geomorphic parameters are related to

each other in a post-orogenic setting. The latter finds justification in the lack of quantitative data published on this issue; for instance, the few datasets available are related to a low number of basins in tectonically passive settings, using global datasets that were collected to investigate the relationship between topography and denudation rates (e.g., Pinet and Souriau, 1988; Milliman and Syvitski, 1992; Summerfield and Hulton, 1994). Also, the results of the bivariate regression analyses (for all the basins of the QF) were later compared to the results of the same analyses in the sub-catchments where denudation rates were quantified (in Chapter 5), to test their consistency (i.e., are the basins analysed in Chapter 5 representative for the different geomorphic contexts of the QF?). The relationship between different parameters within basins of variable size was quantified to investigate any upscaling issue. The different basin datasets included: (i) basins of a given stream-order (i.e., second- to sixth-order); (ii) all basins over first-order; (iii) all basins over second-order; and (iv) all basins with an area greater than 5 km<sup>2</sup>. A dataset consisting of basins with drainage area large than 5 km<sup>2</sup> (iv) was chosen because this value is often used as a threshold separating basins influenced by debris-flow (with drainage areas < 5 km<sup>2</sup>) from basins dominated by fluvial processes (e.g., Montgomery and Foufoula-Georgiou, 1993; Wobus et al., 2006). The distribution of basins of a given stream order, from second- to seventh-order, is shown in Figures 15-16.

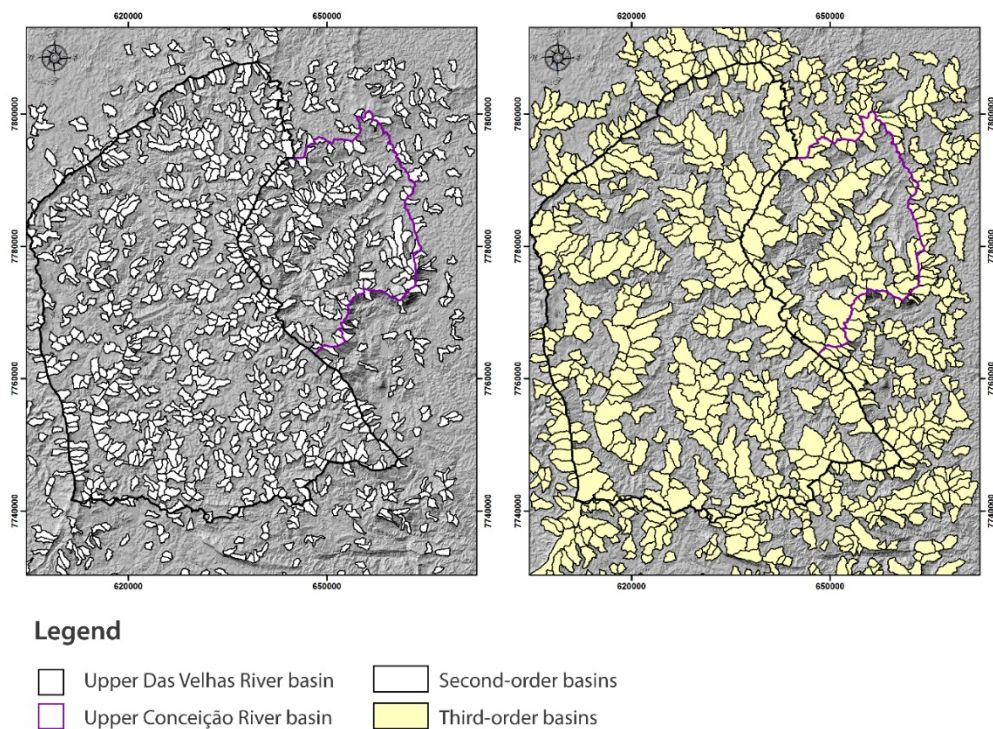
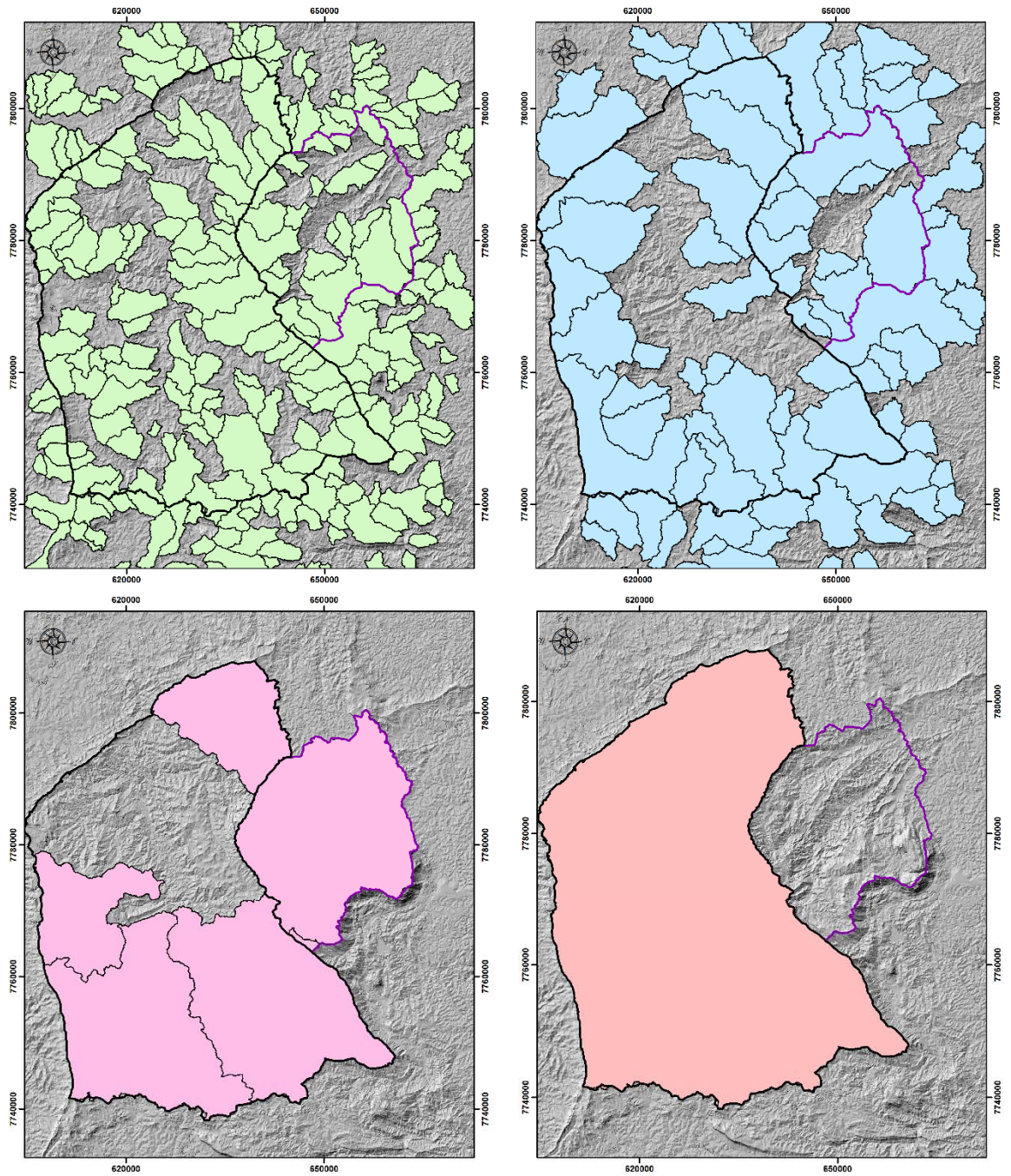


**Figure 15.** The distribution of the analysed second-order (in white) and third-order (in yellow) basins.



**Legend**

- |  |   |   |
|--|---|---|
|  Upper Das Velhas River basin |  Fourth-order basins |  Sixth-order   |
|  Upper Conceição River basin  |  Fifth-order basins  |  Seventh-order |

**Figure 16.** The distribution of the analysed fourth-order (in green), fifth-order (in blue), sixth-order (in pink), and seventh-order (in red) basins.

The TanDEM-X DEM does not edit the elevation data of water bodies (e.g., lakes) because “water bodies are generally very incoherent areas in the underlying DEM scenes and thus derived height estimates are very noisy, and might not contain any meaningful height value at all” (Wessel, 2016, p. 21). Every basin with more than 30% of its area covered by water bodies was excluded from the dataset; in practice, this meant that a few second-order basins were deleted from the dataset.

### **3.3.5 CLUSTER ANALYSIS**

Cluster analysis is a statistical technique for partitioning data into groups that are statistically meaningful, by making quantitative comparisons among a range of variables (Jain, 2010). If plotted in Cartesian space, the objects within a cluster will be close together, whereas objects of different clusters will be farther from each other. Cluster analysis is widely used to reveal the underlying structure of data, with a focus on pattern recognition, detection of anomalies, data summarisation, and so on (Jain, 2010).

In this contribution, cluster analysis is a quantitative test of how well a partitioning of the topography based on the exposed bedrock lithology explains the post-orogenic relief of the QF, compared to a partitioning of the landscape using topographic variables. The cluster analysis consists of two parts: (i) the determination of cluster solutions, and (ii) the statistical test that any differences between the groups are real and not due to chance (or error). The correct determination of the number of clusters in a dataset is often ambiguous (Jain, 2010), and thus different cluster solutions were tested with the number of defined clusters ranging from 2 to 4, rather than trying to determine the best number of cluster solutions. Among the different basin datasets for which bivariate regressions between topographic parameters were quantified in section 3.3.4, the dataset including all the basins with an area greater than 5 km<sup>2</sup> was used in the cluster analysis because it has overall highest R<sup>2</sup> values for the relationships between every pairwise combination of parameters.

For the topographic solutions, the k-means algorithm was used to compute topographic clusters; the k-means is the most often used cluster algorithm (cf. Jain, 2010). Different combinations of topographic parameters were tested for determining topographic solutions for two-, three-, and four-cluster models. The topographic model chosen for each number of cluster solutions was the model associated with the highest ‘Silhouette score’ (Rousseeuw, 1987) and the least number of iterations required for the convergence of clusters centres. The ‘Silhouette score’ provides a measure of how consistent is the cluster solution for a dataset, and thus the higher the ‘Silhouette score’, the better every object lies in its cluster. Different topographic models for varying numbers of cluster solutions are shown in Table 2, and the chosen topographic models are highlighted in blue. Topographic parameters covary: that is, a high elevation basin is also associated with steep channels, higher relief, higher mean and max elevation, and so on. An example of how different topographic clusters are associated with varying topographic characteristics is shown in Figure 17 for a topographic solution with three clusters.

For the lithological solutions, the areal percentage of strong rocks (quartzites, banded iron formation and iron duricrusts) per basin was quantified, (e.g., Hader and Chamberlin, 1915; Dorr, 1969; Salgado et al. 2008; Monteiro et al., 2018), in a similar approach to other studies that infer rock strength from rock type without directly measuring it (e.g., Lague et al., 2000; Korup, 2008; Jansen et al., 2010; Hurst et al., 2013). Hence, lithological cluster solutions separated basins with a lower proportion of strong rocks from basins with a higher proportion of strong rocks. For example, for a lithological model with two clusters, basins with less than 50% of strong rocks were classified as ‘low-resistance’ basins. By contrast, basins associated with 50% or more of strong rocks were defined as ‘high-resistance’ basins.

Table 2. Different topographic models for a varying number of cluster solutions.

Number of clusters	Topographic parameters	Silhouette score	Iterations until convergence
2	$k_{SN}$ , local relief	0.7	14
2	$k_{SN}$ , local relief, basin relief	0.6	18
2	$k_{SN}$ , local relief, slope	0.7	12
2	$k_{SN}$ , local relief, slope, basin relief	0.6	14
2	$k_{SN}$ , local relief, slope, basin relief, max. elevation	0.6	17
2	$k_{SN}$ , local relief, basin relief, knickpoint relief, max. elevation	0.5	15
2	$k_{SN}$ , local relief, slope, basin relief, max. elevation, knickpoint relief	0.5	16
3	$k_{SN}$ , local relief	0.6	11
3	$k_{SN}$ , local relief, basin relief	0.5	11
3	$k_{SN}$ , local relief, slope	0.5	11
3	$k_{SN}$ , local relief, slope, basin relief	0.6	10
3	$k_{SN}$ , local relief, slope, basin relief, max. elevation	0.5	9
3	$k_{SN}$ , local relief, basin relief, knickpoint relief, max. elevation	0.4	25
3	$k_{SN}$ , local relief, slope, basin relief, max. elevation, knickpoint relief	0.4	11
4	$k_{SN}$ , local relief	0.6	16
4	$k_{SN}$ , local relief, basin relief	0.5	26
4	$k_{SN}$ , local relief, slope	0.4	17
4	$k_{SN}$ , local relief, slope, basin relief	0.4	24
4	$k_{SN}$ , local relief, slope, basin relief, max. elevation	0.4	23
4	$k_{SN}$ , local relief, basin relief, knickpoint relief, max. elevation	0.4	23
4	$k_{SN}$ , local relief, slope, basin relief, max. elevation, knickpoint relief	0.4	24

The topographic cluster solution chosen is highlighted in blue. Knickpoint relief is defined in section 3.3.6.

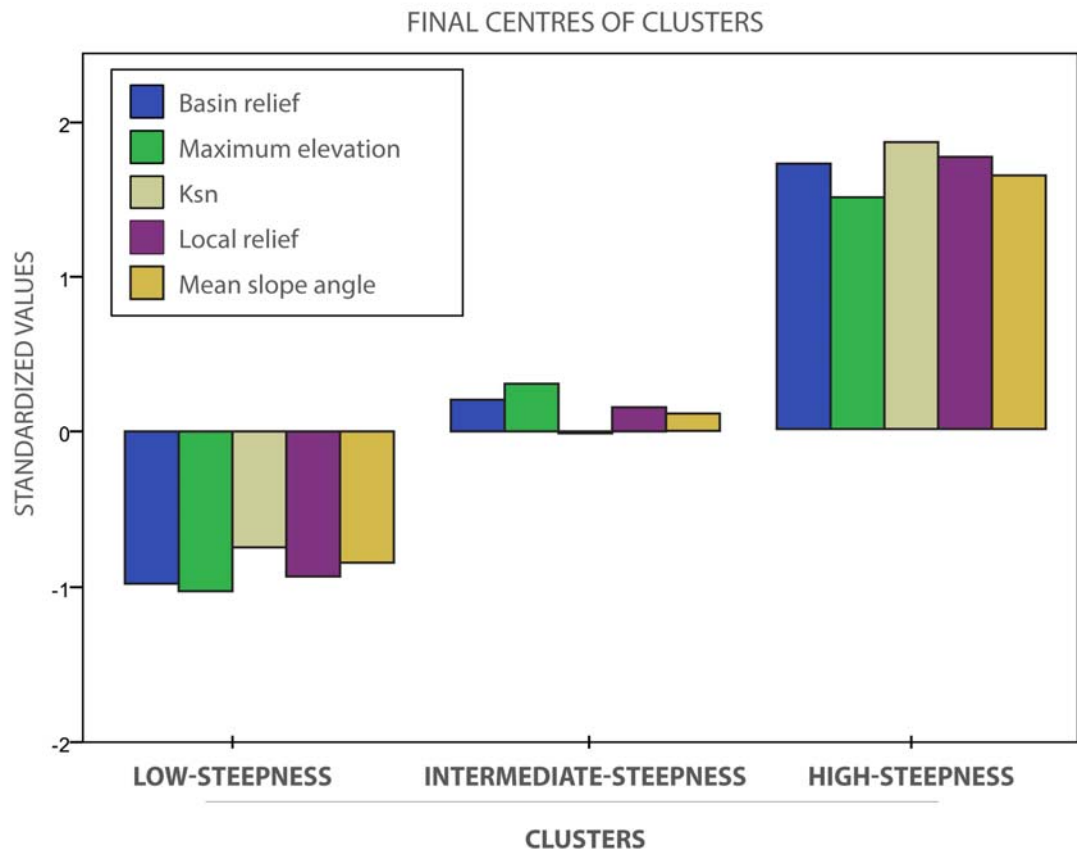


**Figure 17.** An example of how different topographic clusters are associated with varying topographic characteristics. Topographic parameters are high for 'high-steepness' basins. By contrast, topographic parameters are low for 'low-steepness' basins.

The statistical test of the null hypothesis was performed for every cluster solution (lithological and topographic), again using 2 to 4 clusters. For the two-cluster solutions, an independent samples t-test (Marsal, 1979; Larsen and Marx, 2017) was performed with an alpha-level of 0.05 for every catchment-averaged parameter quantified, including the metrics not used in the determination of the clusters. For the three- and four-cluster solutions, a one-way ANOVA (Analysis of Variance) test (Marsal, 1979; Larsen and Marx, 2017) was performed, using an alpha-level of 0.05. A log transformation was performed to normalise the data distribution for each parameter, and a Levene's test was employed for determining if each parameter had equality of variances (Marsal, 1979; Larsen and Marx, 2017). If the data failed the assumption of normality, a Kruskal-Wallis H test was applied, which does not require normality; if the equality of variance assumption failed, a Welch test was performed, which is applicable when the assumption of homogeneity of variances has been violated. All the testing was

done using the software SPSS v. 24 (Green and Salkind, 2016). For testing the null hypothesis, catchments that overlapped spatially (e.g., smaller order basins that are part of a larger order basin) were not used, to ensure the independence of the tested samples.

For the cases where the ANOVA was significant and the null hypothesis was rejected, a post-hoc test using the Tukey HSD method (Meier et al., 2014; Green and Salkind, 2016; Larsen and Marx, 2017) was performed to determine among which groups (and which parameters) the null hypothesis was rejected, since the ANOVA does not provide this answer. Post-hoc tests perform multiple pairwise comparisons between every combination of groups, for every log-normalised catchment-averaged parameter. Hence, this test yields a matrix that identifies homogeneous subsets of means that are not different from each other and for which the null hypothesis is thus not rejected, as well as significantly different group means (rejection of the null hypothesis). Post-hoc tests were executed at an alpha-level of 0.05. In the case where the assumption of equality of variance failed, a Games-Howel post-hoc test was performed in SPSS v. 24 (Meier et al., 2014; Green and Salkind, 2016; Larsen and Marx, 2017).

### **3.3.6 STREAM-PROFILE ANALYSIS**

The stream-profile analysis refers to the investigation of channel steepness data for the QF. The main focus of this section was the determination of the form and characteristics of channel profiles in the QF, as well as the quantitative assessment of the presence, distribution, geomorphic characteristics (e.g., relief) and lithology of the knickpoints in the drainage network. Stream profiles and slope-area data were generated using the functions ‘flowpathapp’ and ‘slopearea’ of the software TopoToolbox v. 2, a MATLAB tool for quantitative topographic analysis (Schwanghart and Scherler, 2014).

The determination of knickpoints used the Neely et al. (2017) algorithm that applies the chi (or integral) approach for the automatic identification of knickpoints (or ‘knickzones’). The Neely et al. (2017) code integrates Equation (2) with respect to the upstream distance from some base level at  $x_b$ , obtaining (Equation 16):

$$z(x) = z(x_b) + \left( \frac{U}{KA_0^m} \right)^{\frac{1}{n}} \chi \quad (16)$$

The longitudinal coordinate chi ( $\chi$ ) is defined by Equation (17):

$$\chi = \int_{x_b}^x \left( \frac{A}{A(x)} \right)^{\frac{m}{n}} dx \quad (17)$$

where  $z$  is elevation,  $x$  is the distance upstream from the base level at  $x_b$ , and  $A_0$  is a reference drainage area that is inserted to make Equation (16) dimensionless (Perron and Royden, 2013; Mudd et al., 2014). All other parameters are the same as the stream-power model (Equations 1-4), from which it is derived. The primary advantage of this method is that slope, a derivative of elevation, is not needed for the calculation, which diminishes noise related to topographic data (cf. Perron and Royden, 2013). A steady-state elevation versus  $\chi$  profile (i.e.,  $dU/dx = dU/dt = dK/dx = dK/dt = 0$ ) features a distinctive linear shape, whereas variations in the slope of elevation versus  $\chi$  might be related to spatial and temporal changes in rock uplift rate, bedrock erodibility or climate change (Mudd et al., 2014; Demoulin et al., 2016). In addition, for  $A_0 = 1$ , the slope of a longitudinal profile in an elevation versus  $\chi$  space is the channel steepness index ( $k_s$ ), or the normalised steepness index ( $k_{sn}$ ) for a fixed  $\theta$ .

The Neely et al. (2017) algorithm builds on this framework, transforming channel profiles into elevation versus  $\chi$  profiles and subsequently quantifying along-channel variations of the observed elevation versus  $\chi$  profiles to the ‘reference’ linear profile, readily determining under- and oversteepened channel reaches. Local maxima in detrended channel steepness values are associated with knickpoints lips, whereas local minima indicate knickpoint bases (Neely et al., 2017; Figure 18).

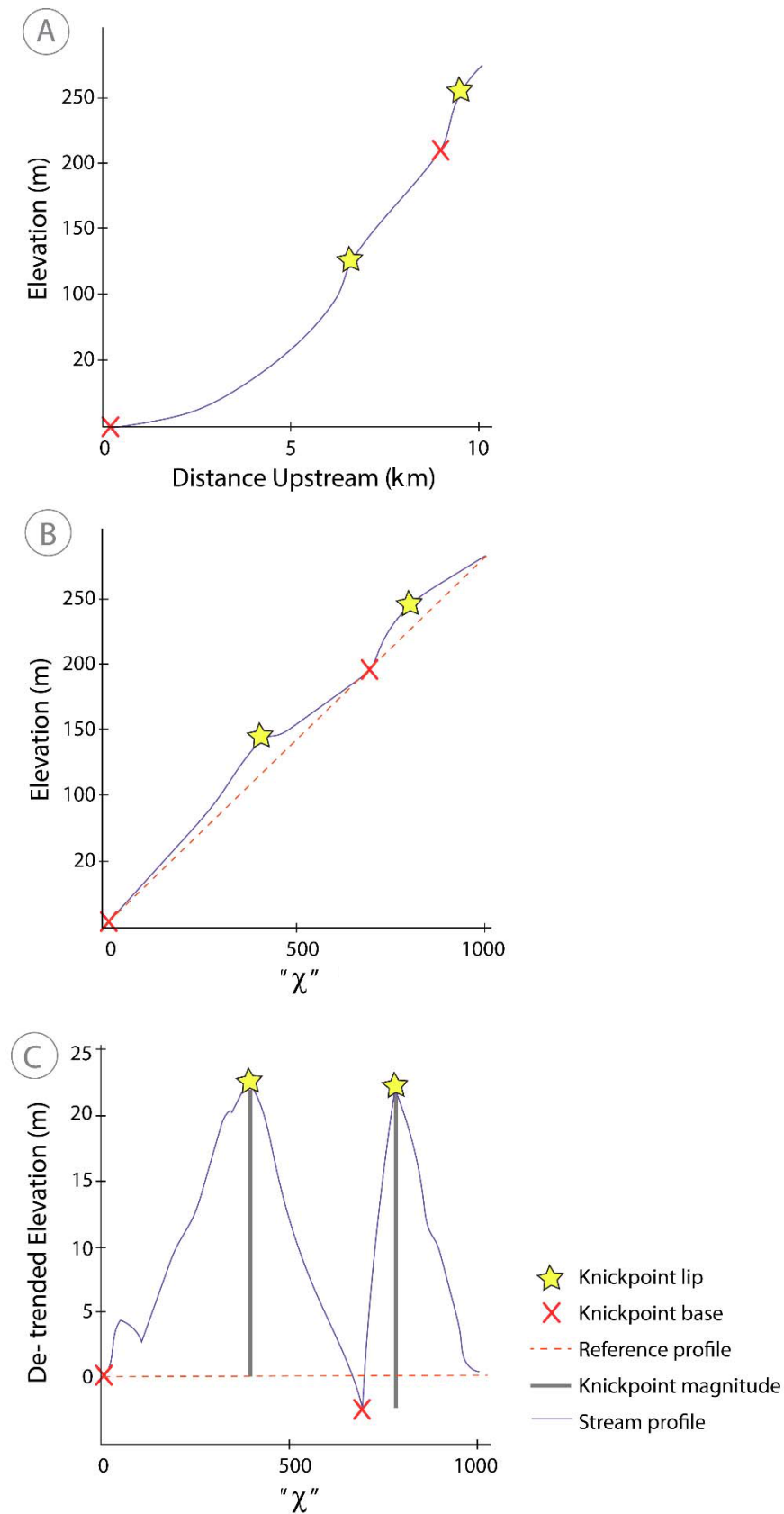
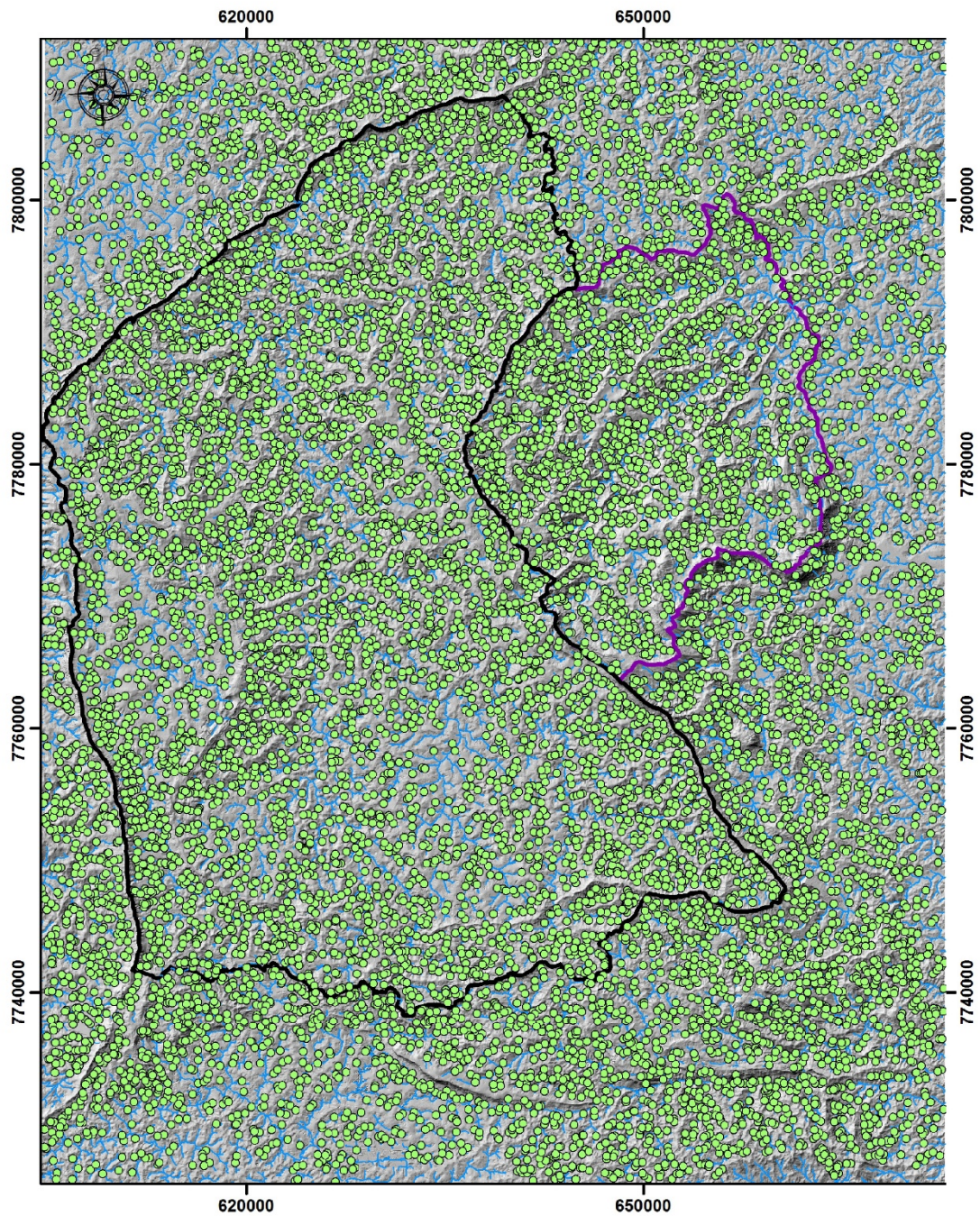


**Figure 18.** Schematic example of how the algorithm for the automatic extraction of knickpoints by Neely et al. (2017) works. (A) Stream profile on which knickpoint lips (yellow stars) and bases (red crosses) are represented. (B) Transformation of the stream-profile into  $\chi$  space; the red dashed line is the reference straight-line (cf. Perron and Royden, 2013). (C) De-trended elevation  $\chi$  plot representing the residual between the profile and the reference line in  $\chi$  space.

The choice of  $\theta$  sets the concavity of the ‘reference’ profile in the elevation versus  $\chi$  plots. I have set a fixed  $\theta$  value of 0.45 for all the analysed rivers. The value was chosen because (i) it is the same  $\theta$  value that I used to quantify local normalised steepness index in section 3.3.3; and (ii) most studies that analysed stream-profiles have also set  $\theta$  to 0.45, which allows comparison between the knickpoints reported in this contribution and knickpoints reported in different landscapes (cf. Kirby and Whipple, 2012). This choice of  $\theta$  implies that the knickpoints in the QF will ultimately represent areas with high local normalised steepness index, which is a straight-forward conceptual interpretation of knickpoints (e.g., Wobus et al., 2006).

The Neely et al. (2017) code uses a range of smoothing and filtering parameter functions that (i) combine knickpoint located closer than a threshold distance in the same river (the parameter ‘lumping window’); and (ii) filter knickpoints with low relief or magnitude (the parameter ‘minimum knickpoint magnitude’). The lumping window constrain the resulting number of knickpoints as well as its position in the drainage network; the higher the lumping window, fewer knickpoints are determined as well as these are located more upstream in the drainage network. In accordance, a higher value of minimum knickpoint magnitude determines a lower number of resulting knickpoints. I used the input parameters suggested by the parameter calibration reported by Neely et al. (2017) for a DEM with 10 m resolution: that is, no smoothing window, lumping window of 100 m; segment length of 120 meters (10 times the raster resolution); minimum pre-lump knickpoint magnitude of 0.5 m; minimum post-lump knickpoint magnitude of 1 m. The output of Neely’s et al. (2017) algorithm is a dataset of statistics for ‘convexities’, including the elevation (m) of the knickpoint; relief (maximum minus minimum elevation, m); magnitude (amount of local oversteepening in an elevation/ $\chi$  plot in relation to the reach ‘reference’ profile; Figure 19); slope ( $dh/dx$ ); contributing drainage area ( $m^2$ ); and easting and northing coordinates. I used the knickpoint magnitude and knickpoint relief parameters to filter small convexities from ‘true’ knickpoints. The ‘unfiltered’ dataset of knickpoints of the QF is shown in Figure 19. For filtering small knickpoints, I plotted knickpoint magnitude versus the number of knickpoints (Figure 20). When magnitudes reach ~50 m, the number of knickpoints only slightly decreases as the magnitude increase. Thus, I used this threshold to establish a

dataset of 'true' knickpoints (with magnitude > 50 m) that are internally consistent across magnitudes.



### Legend

-  Knickpoints
-  Upper Das Velhas River basin
-  Upper Conceição River basin



UTM projection  
Datum: SAD 69 / Zone: 23 South  
Numerical Scale: 1: 440,000

Figure 19. The 'unfiltered' output of knickpoints for the QF (n = 11,534).

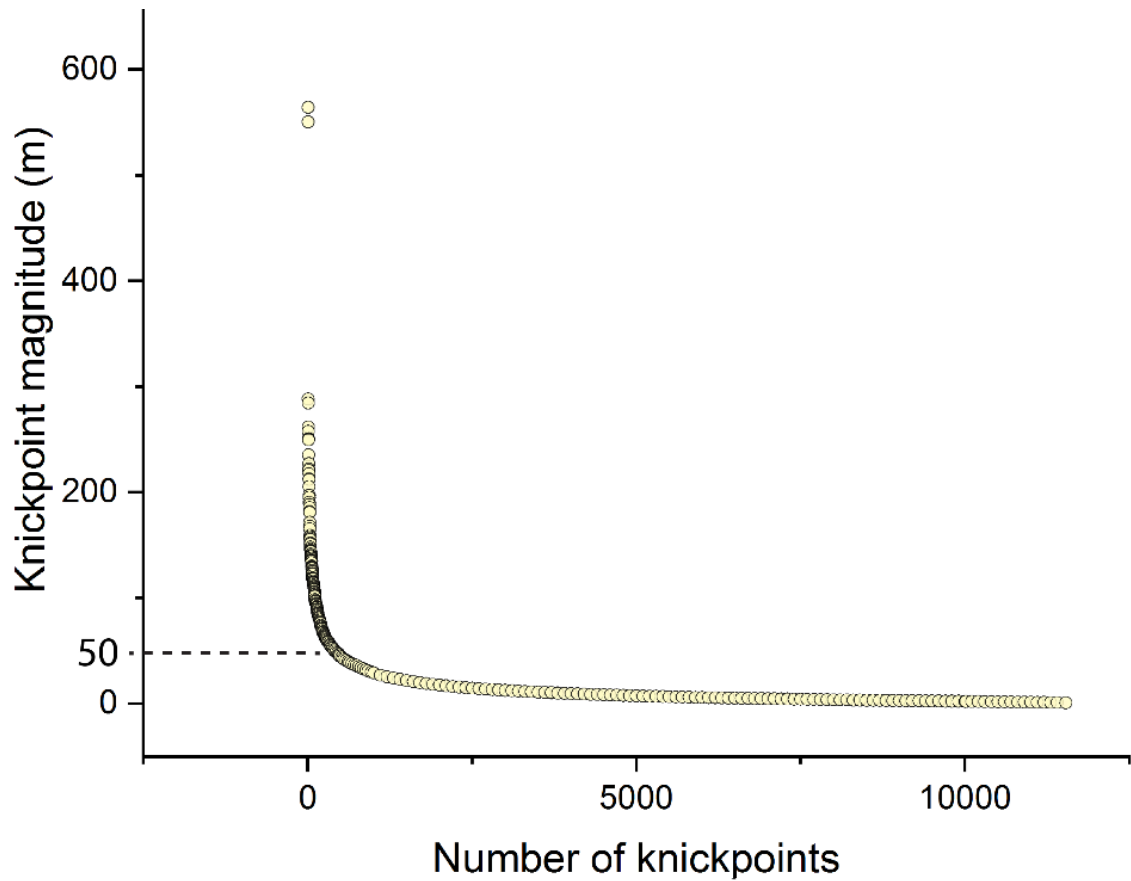


**Figure 20.** The ‘filtering’ of knickpoints with a magnitude higher than 50 m ( $n = 373$ ). Knickpoints with magnitude  $> 50$  m were kept whereas the low magnitude knickpoints (magnitude  $< 50$ ) were excluded.

The analysis of knickpoint distribution was based on the spatial distribution of the knickpoints and its characteristics (knickpoint relief (m), magnitude (m), and the elevation (m) of the knickpoint). The bedrock lithology of each knickpoint and the frequency distribution of knickpoints with elevation were quantified using the ArcGIS v. 10.3 extension ‘Analysis’.

**CHAPTER 4:**  
**QUANTIFYING TOPOGRAPHY IN THE QF:**  
**RESULTS AND DISCUSSION**



## **CHAPTER 4: QUANTIFYING TOPOGRAPHY IN THE QF: RESULTS AND DISCUSSION**

In this chapter, I present data that quantify the topography of the Quadrilátero Ferrífero, using a range of modern topographic techniques that explore the topography over different spatial scales (e.g., local and catchment-averaged topography). The dataset presented in this chapter is relevant in three different ways: (1) it is the result of a systematic quantification of the topography of a post-orogenic setting that can be used to parameterise numerical models of landscape evolution in post-orogenic settings; (2) it has guided the determination of basins to be sampled for the quantification of denudation rates (discussed in Chapter 5); and (3) it adds a quantitative dimension to our existing understanding of how post-orogenic landscapes evolve.

### **4.1 RESULTS**

#### **4.1.1 LOCAL TOPOGRAPHY ANALYSIS**

The local topography of the QF is very diverse, with contrasting features, such as high and craggy peaks, locally deep river canyons and entrenched meanders, as well as gently-sloping valleys and high, low relief plateaux (cf. Dorr, 1969). Every topographic parameter displays a large range of values, and the histograms show a non-normal, right-skewed distribution (with a long upper tail) and with the peak offset toward the lower bins (Figures 21-27). This pattern is the effect of rare, extremely high local topographic values that are observed in the QF; the non-normal distributions make identifying a ‘typical value’ of the local topography of the QF very problematic.

The elevation data of the QF (Figure 21) adequately reflects the above description, exhibiting a sizeable maximum relief of ~1500 m, a mean elevation of 1017 m (median of 996 m), and a peak elevation of ~2080 m. The highest elevation points are concentrated primarily in the Caraça Range; at the regional drainage divide that separates the Upper Das Velhas and the Upper Conceição River basins; and also in the southeastern portion of the QF. The downstream areas of the two main river basins are associated with the lowest elevation in the region,

associated with a low relief of ~150 m (from 730-580 m of elevation). The slope dataset (Figure 22) reveals a similar pattern, with high spatial variability (range of  $\sim 81^\circ$ ), a right-skewed histogram indicating that a sizeable portion of the study area displays low slope angle values, and a low frequency of very high slope values that are distributed over a very long right tail. The mean slope value is around  $16^\circ$ , and the maximum slope is around  $81.5^\circ$ . Although showing similar patterns, the spatial variability of elevation and slope do not always follow each other and there are areas at low elevation with high slopes, and vice-versa.

The distribution of local  $k_{sn}$  values for the QF is unusually variable, ranging from  $5 \text{ m}^{0.9}$  to a maximum of  $\sim 1220 \text{ m}^{0.9}$  (Figure 23). High  $k_{sn}$  values are concentrated in the southeastern portion of the QF, for rivers either flowing away from the Caraça Range or from the other drainage divides in the southeastern QF. The bulk of stream reaches exhibit relatively lower  $k_{sn}$  values of  $\sim 50 \text{ m}^{0.9}$ . The dispersion within the  $k_{sn}$  distribution is so large that its standard deviation ( $\sim 39 \text{ m}^{0.9}$ ) is higher than its mean ( $\sim 30 \text{ m}^{0.9}$ ). The presence of locally extremely high  $k_{sn}$  values is consistent with the well-known presence of many waterfalls within the QF (e.g., Salgado, 2015; waterfalls are often associated with elevation drops of tens of meters). The visual comparison of the local  $k_{sn}$  map (Figure 23) with the elevation and slope datasets (Figures 21-22) indicates that low elevation areas are generally associated with low  $k_{sn}$  values. The spatial distributions of  $k_{sn}$  and local slopes are similar, and thus local high  $k_{sn}$  areas are often associated with the high local slope.

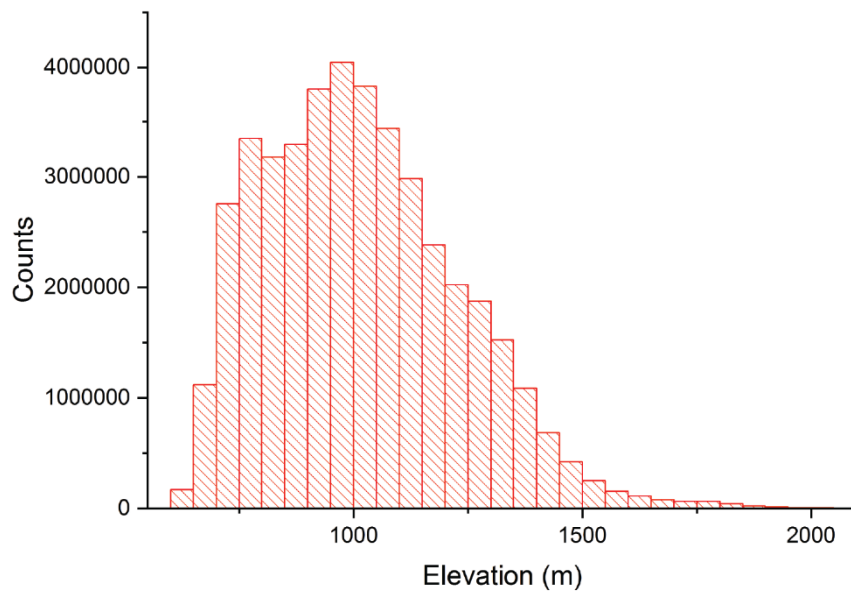
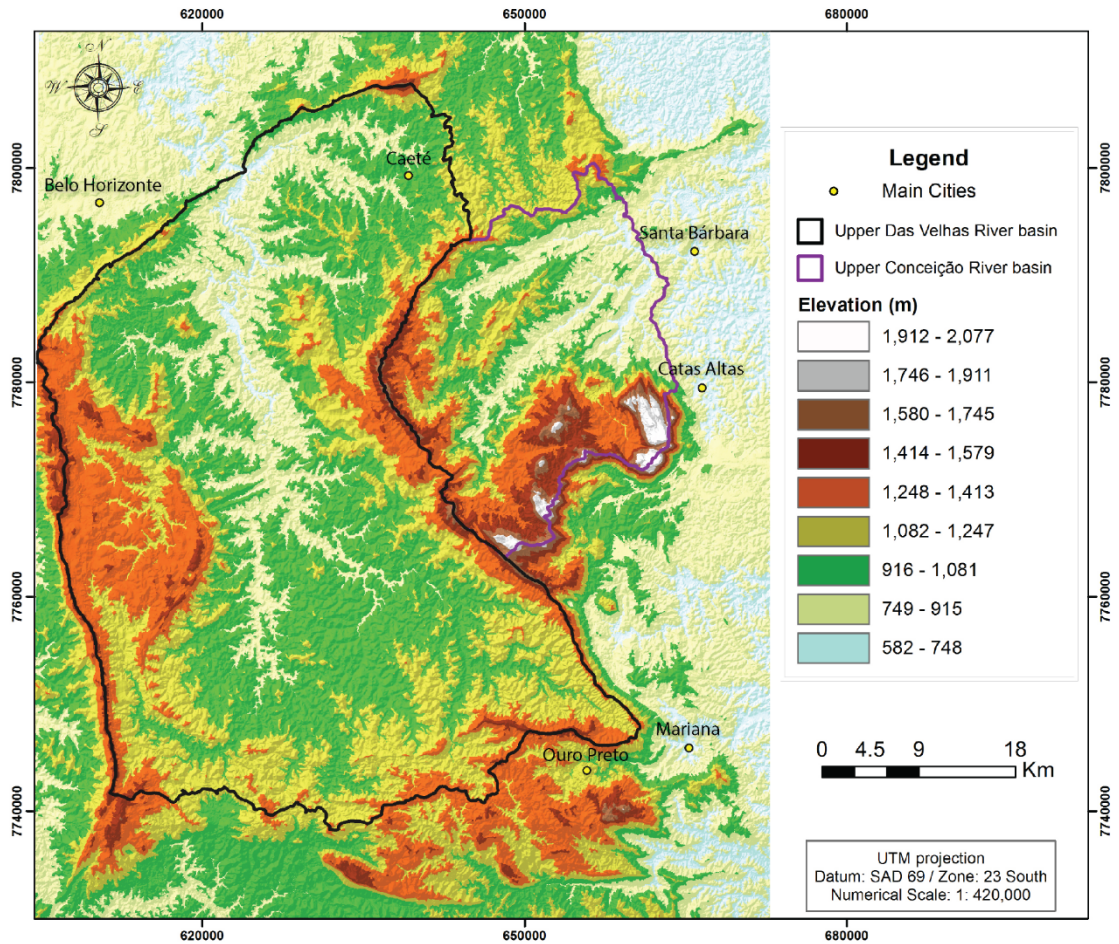
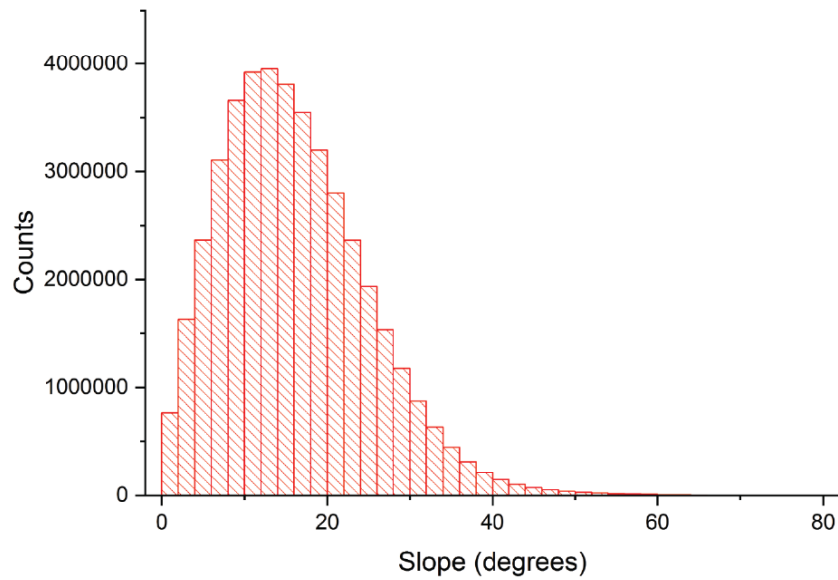
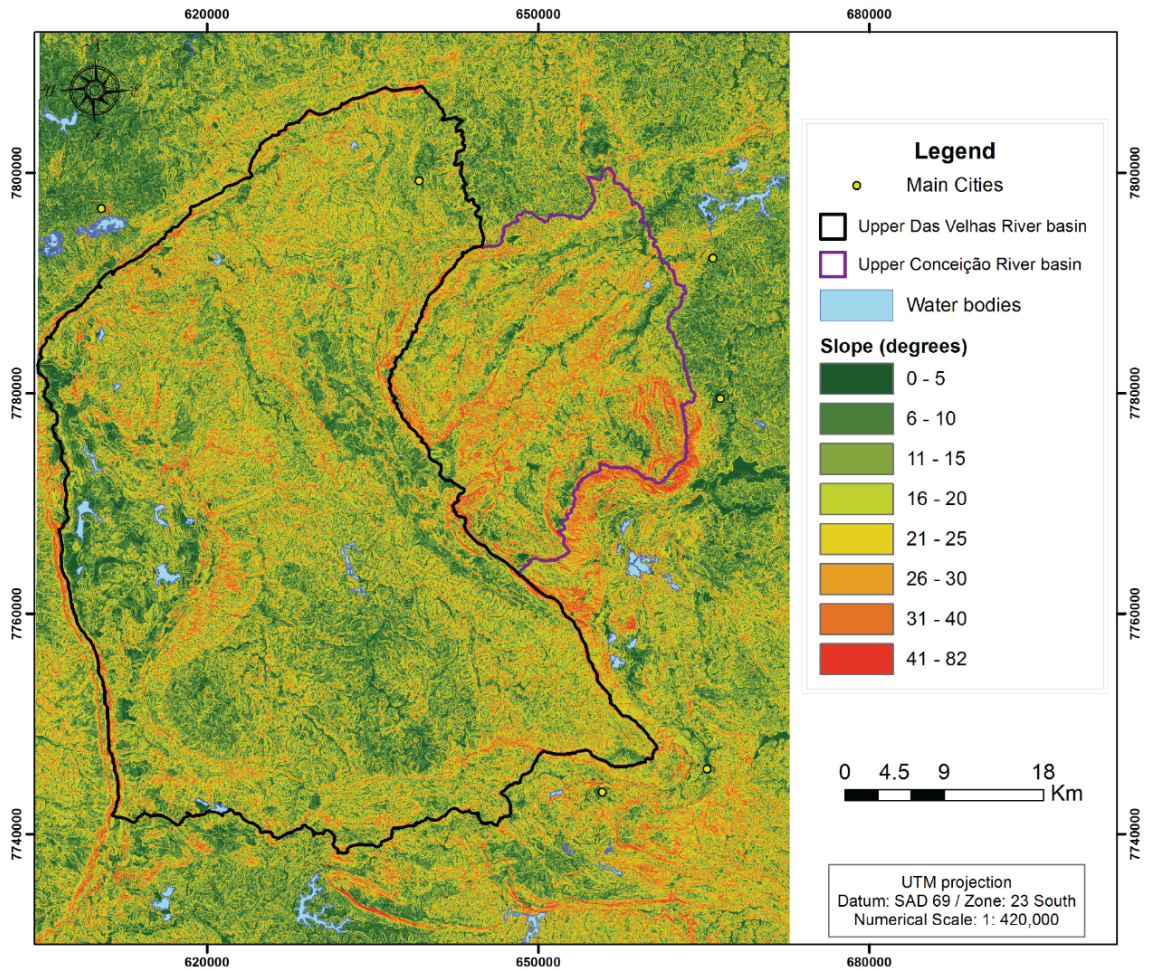
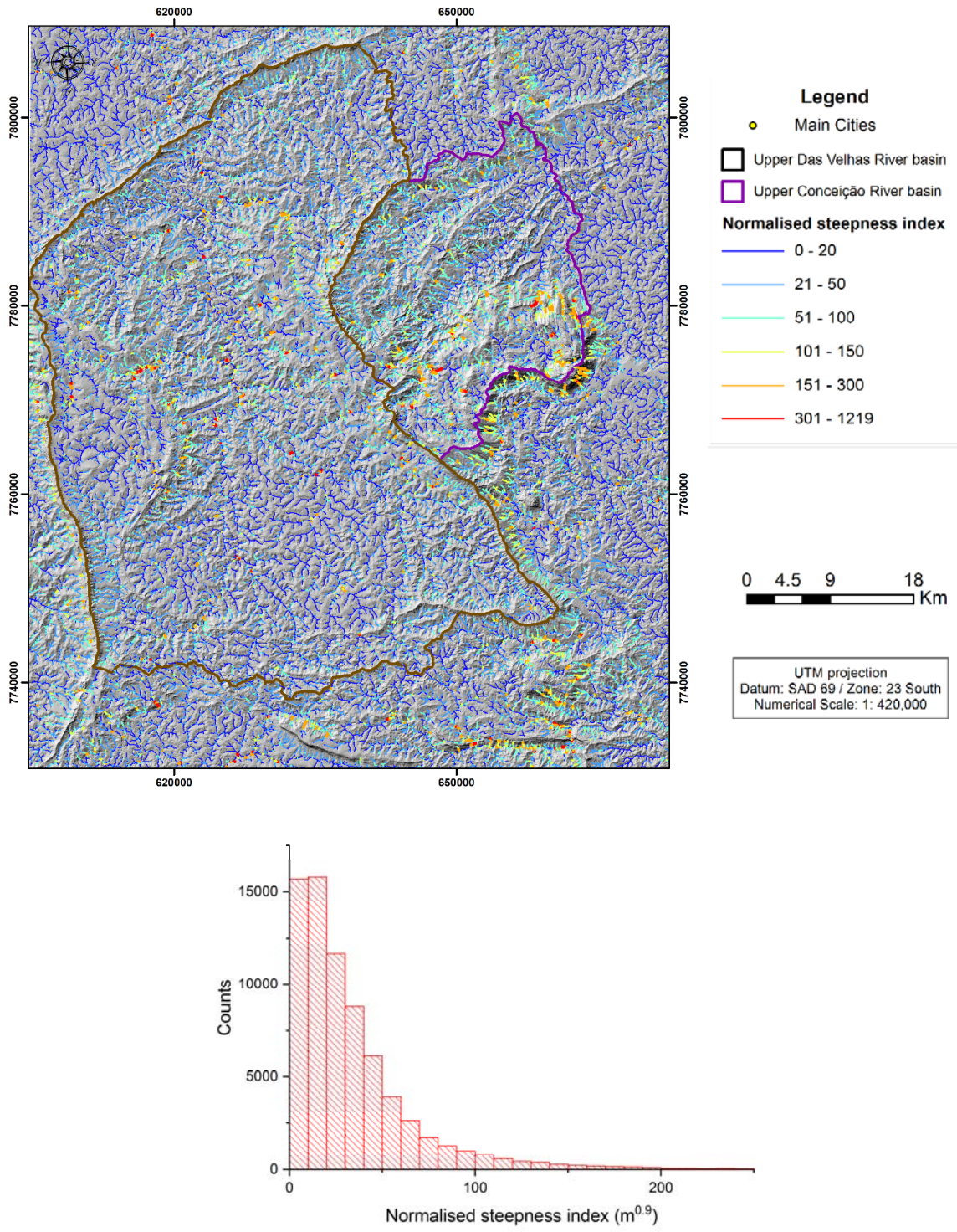


Figure 21. The spatial distribution of elevation for the QF (top); and the histogram of its distribution (bottom).



**Figure 22.** The spatial distribution of slope for the QF (top); and the histogram of its distribution (bottom). Areas in blue represent water bodies that were excluded from the analysis; see section 3.3.4.



**Figure 23.** The spatial distribution of normalised steepness index for the QF (top); and the histogram of its distribution (bottom).

The local relief dataset (Figure 24) displays a pattern that is very similar to the other parameters: a highly right-skewed histogram with a long upper tail, an extensive range of values (~1200 m), a mean (~260 m) larger than the median (~234 m), and a bulk distribution of relatively low values contrasting with a small population of extremely high local relief. The spatial distribution of the upper quartile of the elevation, local relief, and slope datasets suggests a link between these parameters (Figure 25). The highest elevations areas are concentrated around the main drainage divides (encircling these in a buffer-like pattern), around the western QF, at the Caraça Range, and in the southern part of the QF (Figure 25). High local relief, in turn, is distributed primarily within the boundaries of the high elevation areas, as to encircle them. High local relief is also concentrated in the 'internal' portion of the high-elevated terrain within the eastern QF, especially along the Caraça Range (Figure 25). The high-slope distribution shows a more significant scatter than the other parameters, and yet every high local relief domain is also a high slope region. In addition, there are high-elevation areas that are neither high in slope nor in local relief, notably in the western QF.

The kernel density of faults (Figure 26) and the local mean annual precipitation data (Figure 27) show the same distribution as the topographic parameters; they are right-skewed, comprising a large population of low values and a long right tail containing low-frequency higher values. The Kernel density of faults dataset indicates a spatial structural anisotropy in the QF (discussed in section 2.3), whereby the drainage divide between the two main drainage basins as well as the eastern part of the QF are associated with a high density of faults, contrasting with the lack of faults in the southwestern part of the QF. The mean annual precipitation data shows a contrast in mean annual precipitation between drainage divides (reaching ~1,700 mm/yr), and valley bottoms whose mean annual precipitation varies between 1,250-1,500 mm/yr. However, there is no contrast in precipitation between the uplands in the eastern part of the QF (~1700 mm/y) to the uplands in the west part of the QF (~1650 mm/y).

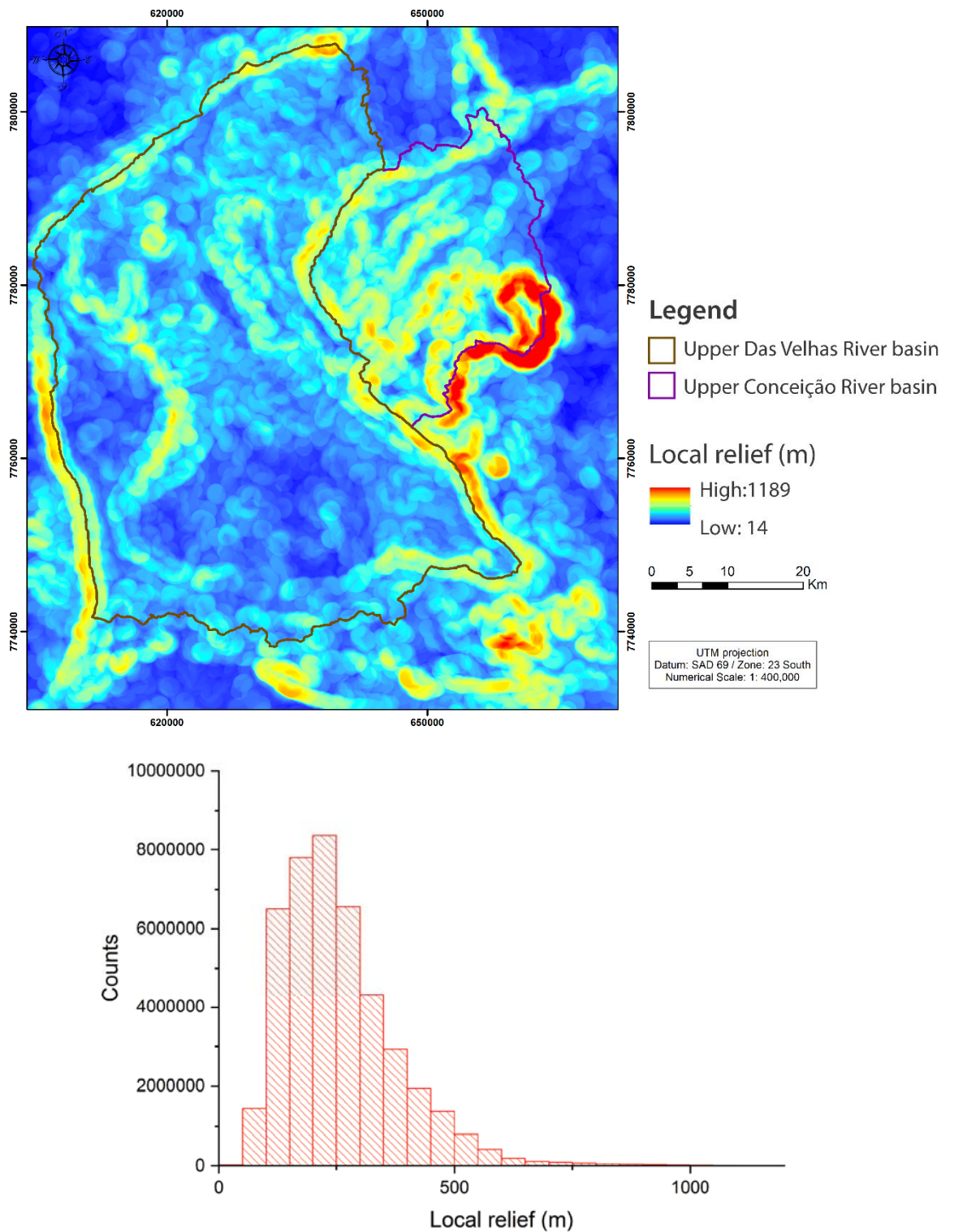
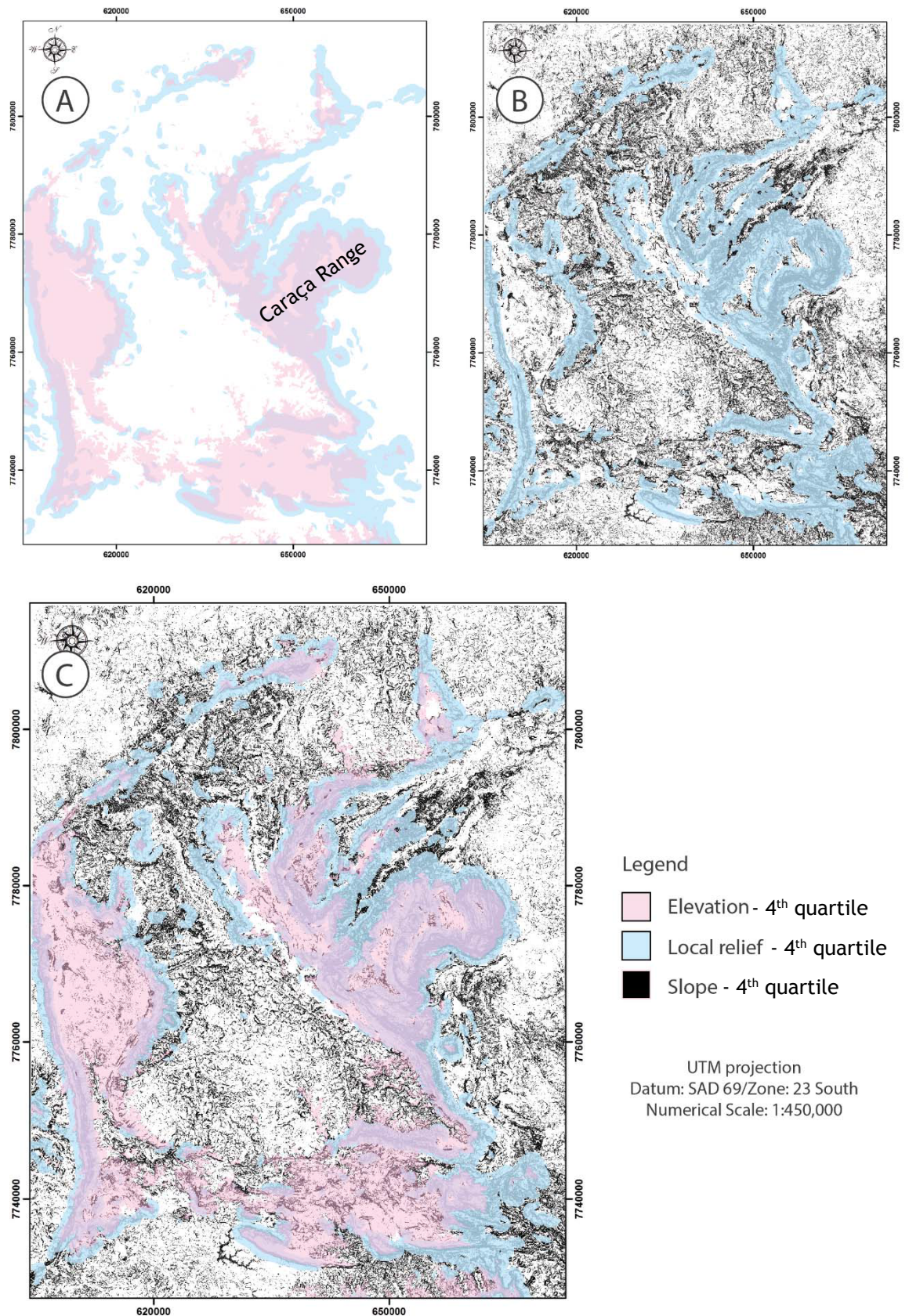
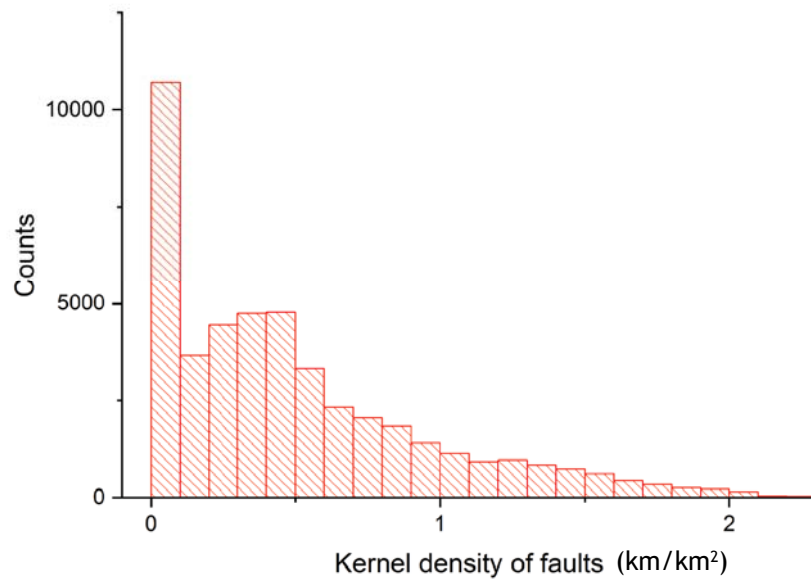
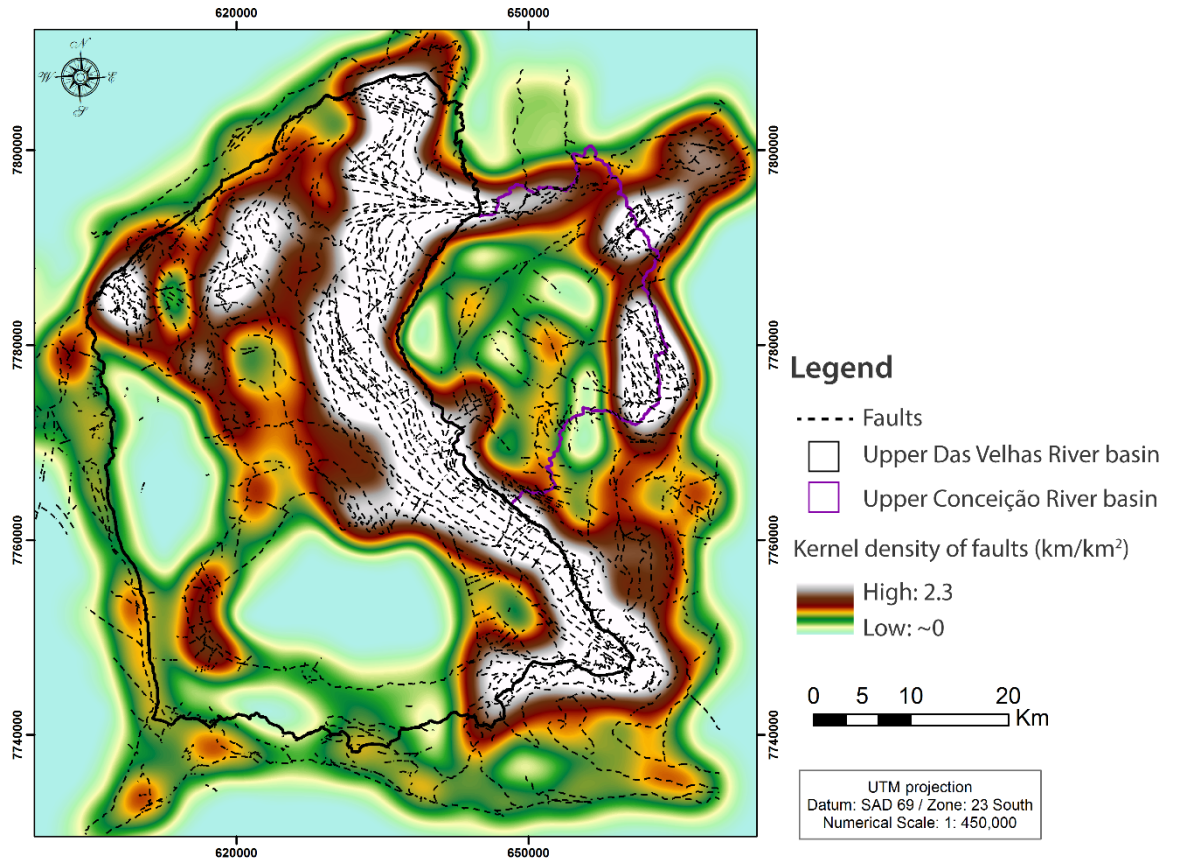


Figure 24. The spatial distribution of local relief for the QF (top); and the histogram of its distribution (bottom). Local relief refers to elevation range in a circular window with 2 km diameter.



**Figure 25.** The spatial distribution and superposition of the 4<sup>th</sup> quartile of the local topographic parameters elevation, local relief, and slope: (A) superposition of the 4<sup>th</sup> quartile of the parameters elevation (pink) and local relief (blue); (B) superposition of the 4<sup>th</sup> quartile of the parameters local relief (blue) and slope (black); and (C) superposition of the 4<sup>th</sup> quartile of the parameters elevation, local relief, and slope.



**Figure 26.** The spatial distribution of the kernel density of faults for the QF (top); and the histogram of its distribution (bottom). Faults, from which the parameter was quantified, are represented as black dashed lines.

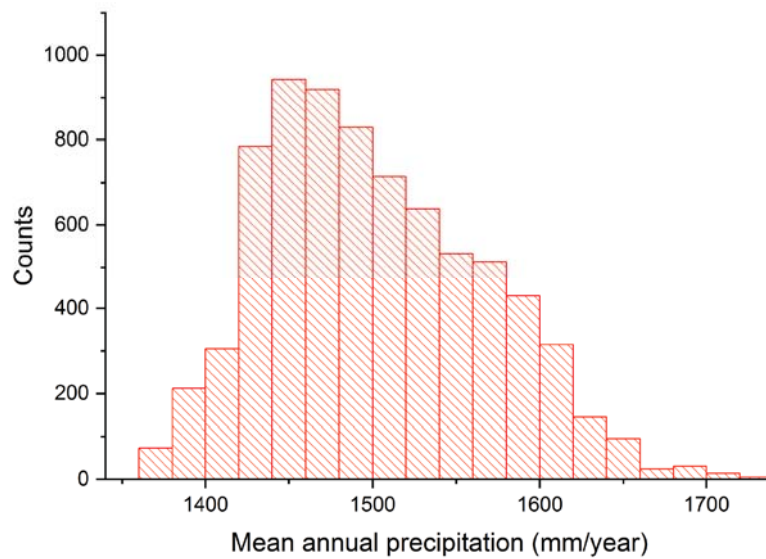
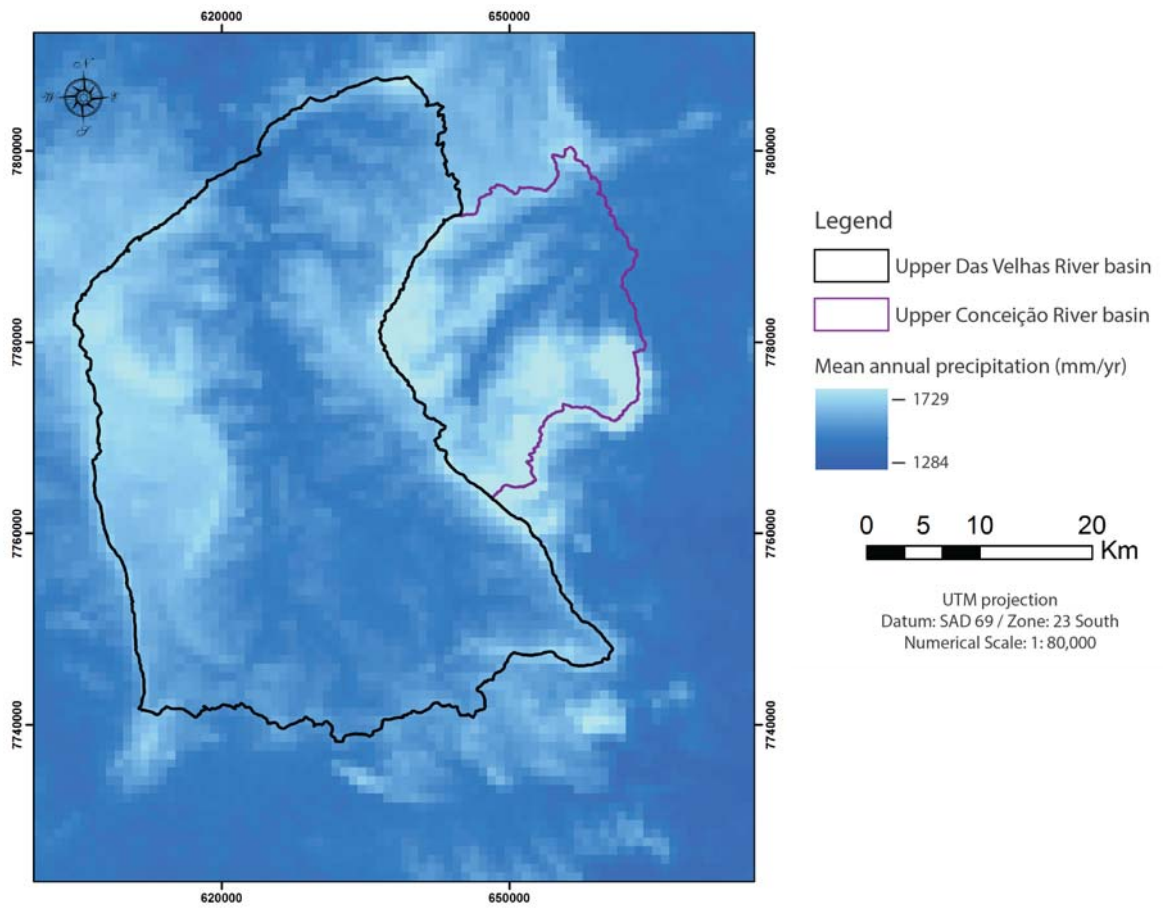


**Figure 27.** The spatial distribution of the mean annual precipitation for the QF (top); and the histogram of its distribution (bottom). There is no contrast in precipitation between the uplands in the eastern part of the QF (~1700 mm/yr) to the uplands in the west part of the QF (~1650 mm/y). Precipitation data derived from Abatzoglou et al. (2018).

### 4.1.2 LOCAL TOPOGRAPHY VERSUS LITHOLOGY

The distributions of local geomorphic parameters with lithology demonstrate that areas where quartzites and banded iron formations are exposed consistently exhibit higher topographic metrics than the areas with other lithologies (Figure 28). By contrast, areas of gentle topography are characteristic of gneisses and granites. The other lithologies (schists, iron duricrusts, phyllites, metabasalts and dolomitic units) lie between these two end-members, with intermediate values of elevation, relief, local slope, and  $k_{sn}$ . Iron duricrusts display the highest topographic characteristics of this middle group of lithologies. In detail, areas under banded iron formations and quartzites display marked variable topographic metrics with their upper and lower whiskers (i.e., the interquartile range) showing considerable variation (Figure 28). By contrast, gneiss and granite areas are characterised by less dispersion in their topographic metrics, with their central values being typically low. The intermediate group has a variance that is not as high as the quartzite and banded iron formations terrains, but not as low as the areas under gneisses and granites. Every lithology, independently of the group to which it belongs, has ‘abnormally’ high values when compared with the rest of the dataset, but quartzites are the rocks where these abnormal values are most common.

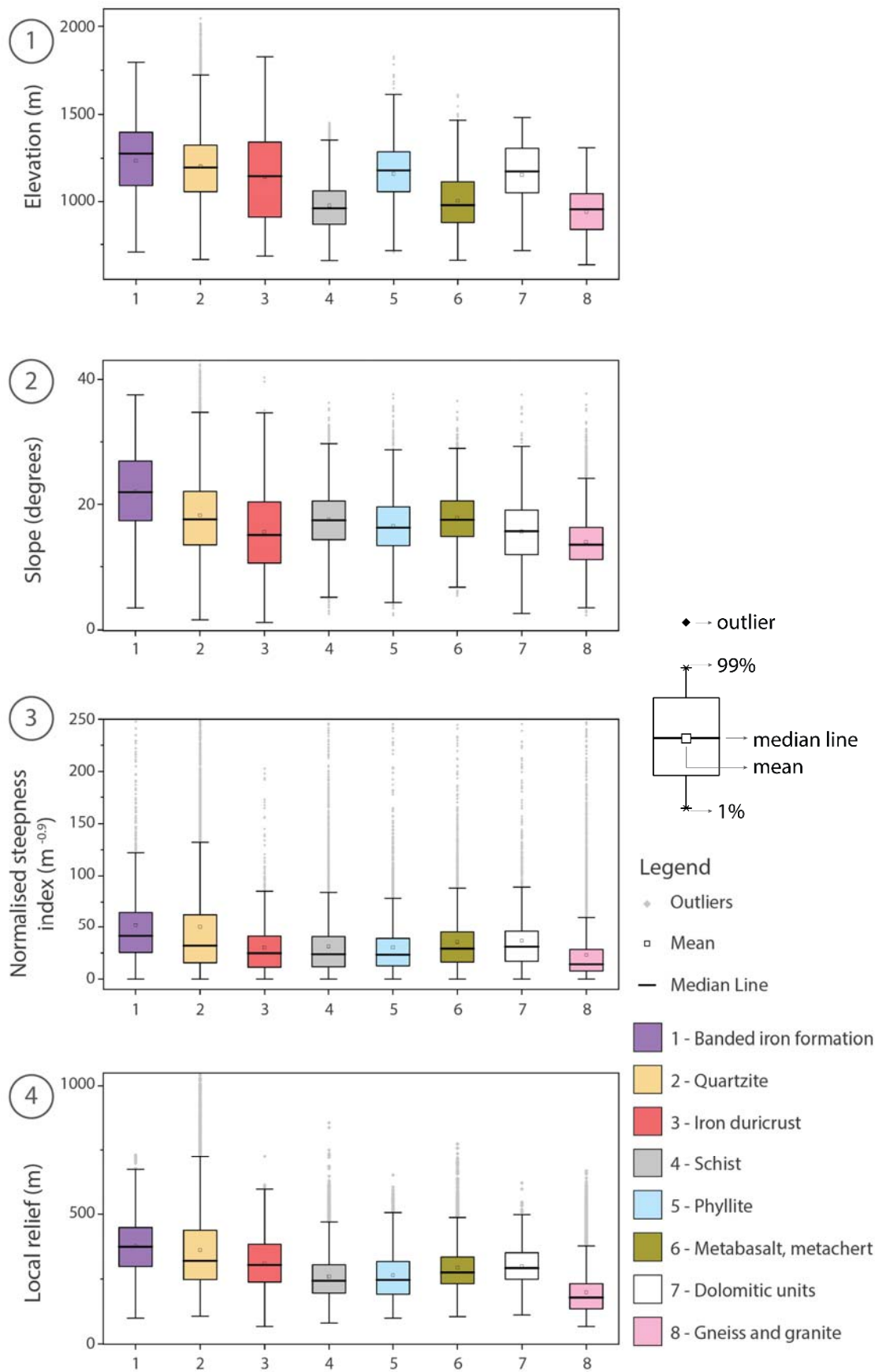


**Figure 28.** The distribution of local geomorphic parameters per lithology. From the top to the bottom of the figure, the parameters represented are: (1) elevation; (2) slope; (3) normalised steepness index; and (4) local relief. Lithologies are represented by the same colour scheme in each plot, detailed in the right bottom of the figure.

### 4.1.3 CATCHMENT-AVERAGED TOPOGRAPHIC METRICS

The central tendencies of the distribution of catchment-averaged topography in the QF are similar for every basin order (Figure 29). The mean and median values are nearly identical for every basin-order dataset, and so are the interquartile ranges. However, the range of their upper and lower 25% extreme values is wider for smaller order basins, specifically for the second- and third-orders. Also, outliers are more frequent for smaller order basins. However, there is spatial overlap between basins of different orders because higher order incorporate smaller order basins.

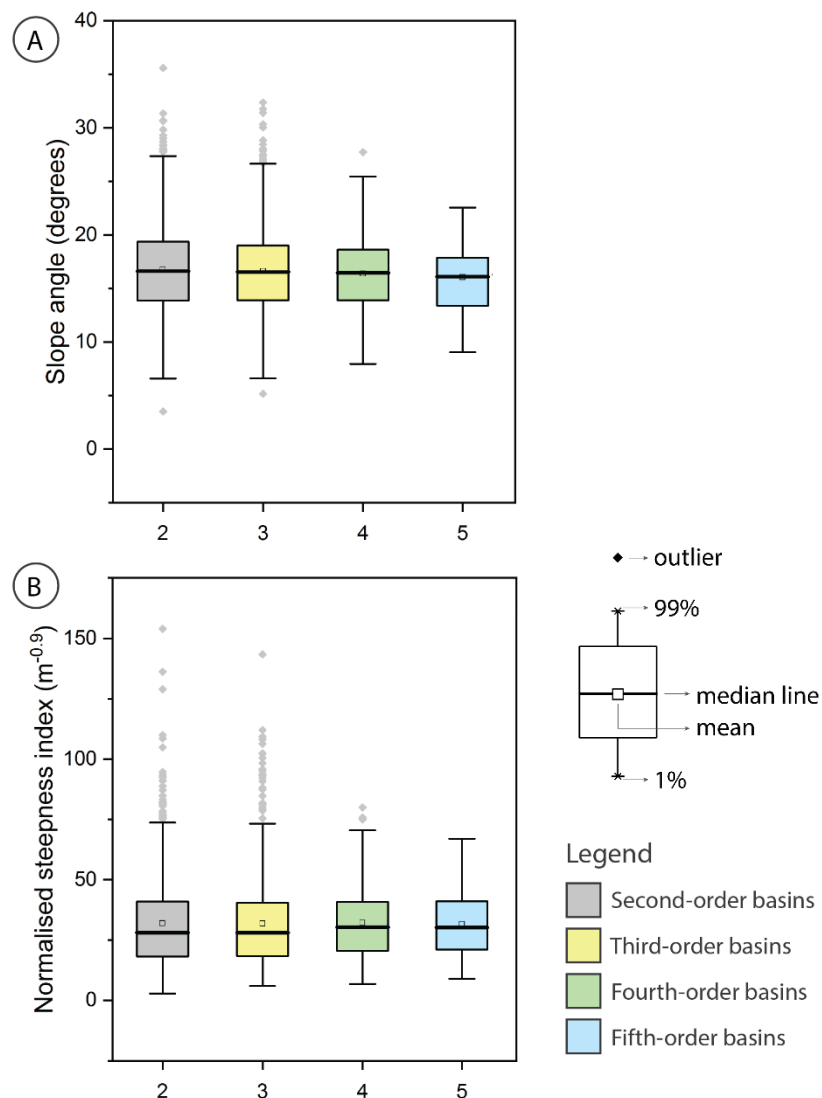


**Figure 29.** The distribution of catchment-averaged (A) mean slope angle; and (B) normalised steepness index for datasets comprising second-, third-, fourth-, fifth-order basins. The colour scheme of each box plot is detailed in the bottom right of the figure.

The goodness-of-fit between all pairwise combinations of catchment-averaged parameters was quantified for datasets consisting of: (i) basins of a given stream-order (i.e., second- to sixth-order); (ii) all basins over first-order; (iii) all basins over second-order; (iv) all basins with an area greater than 5 km<sup>2</sup>. Bivariate-regression results all display similar patterns and trends, irrespective of the stream order or the number of samples per dataset. However, the goodness-of-fit of linear regressions increases slightly for larger stream orders, which may be an artifact of the decrease in sample numbers (see below for further investigation of this point). The quantified goodness-of-fit for every dataset is reported in the Appendix A. Apart from these small differences, the bivariate regressions of each of the pairs of topographic parameters produce, overall, a similar  $R^2$  for all the catchment sizes and orders.

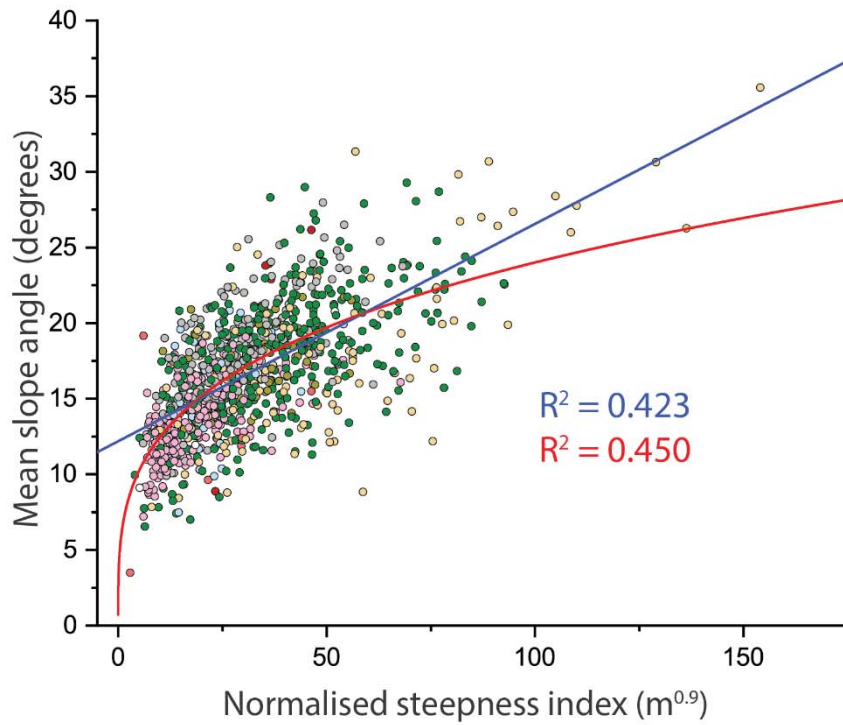
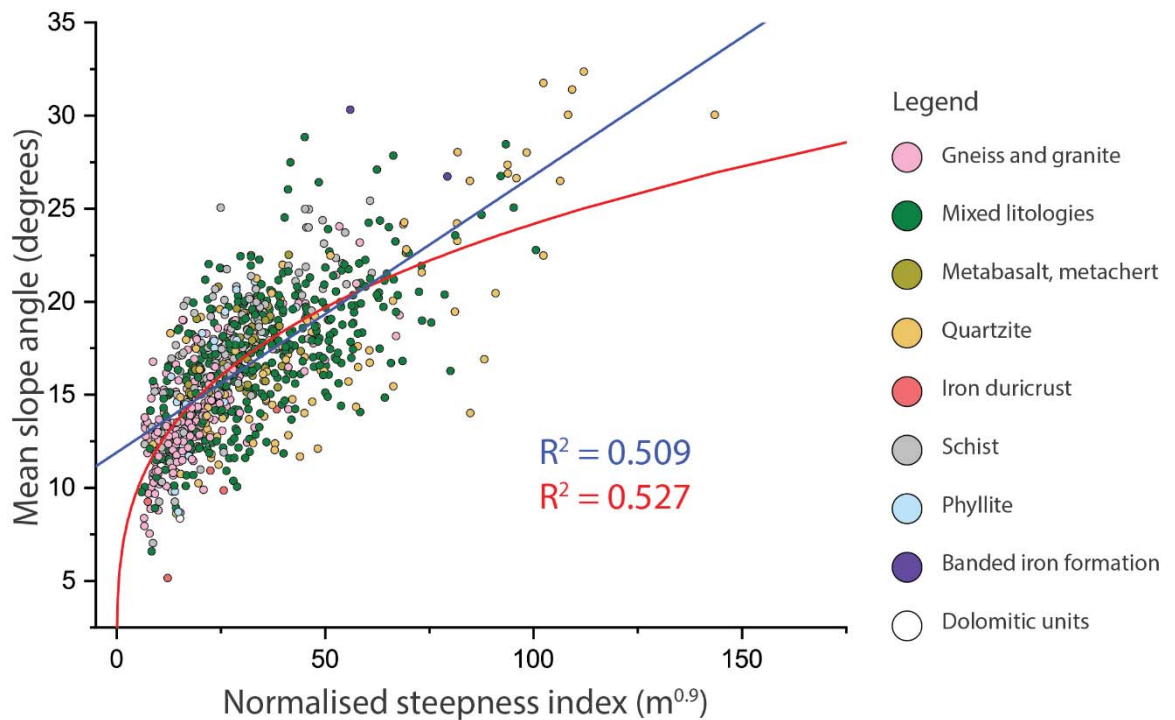
Tables 3 and 4 and the data in Appendix A indicate that the regression between basin area and any other parameter yields a relationship with a  $p$ -value  $> 0.05$  and associated minimal values of  $R^2$ . The parameter mean elevation shows a very low correlation with every other topographic metric, except maximum elevation ( $R^2 = 0.636$ ;  $p$ -value  $< 0.01$ ). The parameter mean slope angle is well correlated with  $k_{sn}$  ( $R^2 = 0.475$ ;  $p$ -value  $< 0.05$ ), local relief ( $R^2 = 0.727$ ;  $p$ -value  $< 0.01$ ), and basin relief ( $R^2 = 0.483$ ;  $p$ -value  $< 0.05$ ), and it displays low correlation values with the other metrics. By contrast, local relief is the second most powerful regressor among all the geomorphic parameters; it has a very strong relationship with catchment-averaged  $k_{sn}$  ( $R^2 = 0.895$ ;  $p$ -value  $< 0.01$ ), with basin relief ( $R^2 = 0.708$ ;  $p$ -value  $< 0.01$ ), and with maximum elevation ( $R^2 = 0.591$ ;  $p$ -value  $< 0.01$ ). The parameter  $k_{sn}$  is the topographic parameter displaying overall the highest correlation with all other topographic metrics, including mean slope ( $R^2 = 0.627$ ;  $p$ -value  $< 0.01$ ), local relief ( $R^2 = 0.895$ ;  $p$ -value  $< 0.01$ ), basin relief ( $R^2 = 0.717$ ;  $p$ -value  $< 0.01$ ) and knickpoint relief ( $R^2 = 0.716$ ;  $p$ -value  $< 0.01$ ). Basin relief is also well correlated with most of the parameters, except mean elevation and area. Knickpoint magnitude and relief are weakly correlated to all topographic metrics, except  $k_{sn}$  ( $R^2 \sim 0.6$ ) and local relief ( $R^2 \sim 0.5$ ). In summary, the parameters that are most strongly correlated with every other geomorphic metric are, in order,  $k_{sn}$ , local relief and basin relief.

**Table 3.** Mean  $R^2$  values between every pairwise combination of catchment-averaged parameters for the dataset comprising basins with area > 5 km<sup>2</sup>.

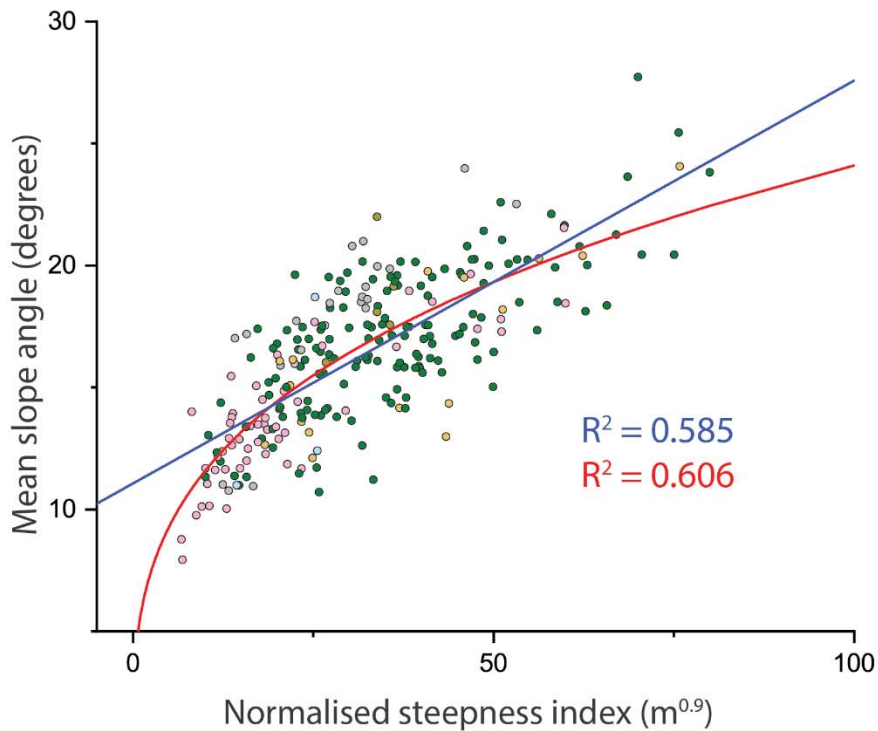
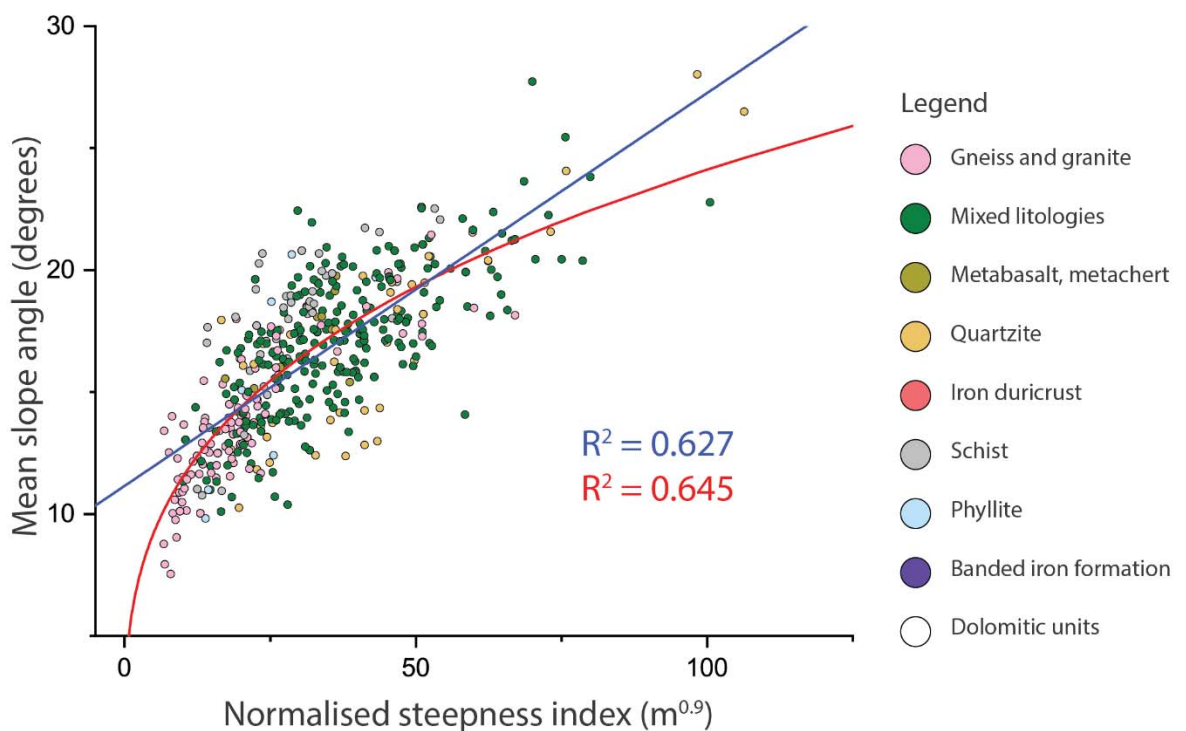
All basins with area > 5km <sup>2</sup> (n=492)									
Max. slope (°)	Mean slope (°)	Local relief (m)	Max. elevation (m)	Mean elevation (m)	Basin relief (m)	$k_{sn}$ (m <sup>0.9</sup> )	Knickpoint magnitude (m)	Knickpoint relief (m)	
0.169	0.002	0.000	0.104	0.003	0.183	0.006	0.001	0.001	Area (m <sup>2</sup> )
	0.213	0.322	0.385	0.117	0.475	0.296	0.219	0.263	Max. slope (°)
		0.727	0.315	0.109	0.483	0.627	0.225	0.361	Mean slope (°)
			0.591	0.263	0.708	0.895	0.46	0.663	Local relief (m)
				0.636	0.694	0.551	0.283	0.378	Max. elevation (m)
	$R^2 < 0.4$				0.16	0.257	0.115	0.122	Mean elevation (m)
	$0.4 < R^2 < 0.6$					0.717	0.373	0.528	Basin relief (m)
	$R^2 > 0.6$						0.543	0.716	$k_{sn}$ (m <sup>0.9</sup> )
								0.886	knickpoint magnitude (m)



Figures 30-31 show the effect of the nature and sample size of datasets on the bivariate regression of the parameters themselves. These plots represent bivariate regressions of catchment-averaged  $k_{sn}$  versus catchment mean slope angle for second-order (Figure 30A), third-order (Figure 30B), fourth-order basins (Figure 31A), and all basins with an area higher than 5 km<sup>2</sup> (Figure 31B). These figures show that the goodness-of-fit of the linear regression increases with basin order, from 0.423 (second-order basins dataset) to a maximum of 0.627 (basins with an area greater than 5 km<sup>2</sup>). This effect may be the result of decreasing the sample size, or may show that larger basins may effectively decrease the inherent topographic noise of the DEM that is possibly more pronounced in smaller catchments. Catchment-averaged mean slope angle increases with higher values of catchment-averaged  $k_{sn}$  (Figures 30-31). For lower order basins, the relationships between these variables are best explained by an allometric model ( $y=ax^b$ ; with  $b > 0$ ) rather than a linear model ( $y=ax+b$ ; with  $a < 0$ ), suggesting a sort of threshold value for  $k_{sn}$  (~50 m<sup>0.9</sup>) above which the mean slope angle is less sensitive to  $k_{sn}$  than for values lower than the threshold. There is a relationship also between the catchment-averaged topographic parameters and lithology, whereby basins underlain by gneiss and granite exhibit low  $k_{sn}$  and mean slope values (Figures 30-31). By contrast, the basins associated with high  $k_{sn}$  and mean slope angle values, in the right-top of the graphs, are mostly underlain by quartzite; the mixed lithology basins are spread around the middle portion of the graphs, with a wide scatter. The relationship between topographic parameters and lithology, however, is not simple and there are quartzite-dominated basins associated with lower  $k_{sn}$  and mean slope values.

**A. 2nd order basins (n=997)****B. 3rd order basins (n=865)**

**Figure 30.** Scatter plot of catchment-averaged mean slope angle and normalised steepness index for datasets consisting of: (A) second-order basins; (B) third-order basins. Blue  $R^2$  refers to the goodness-of-fit of the linear model, whereas the red  $R^2$  refers to a power model. Each symbol represents a basin. Lithologies are separated by colours, detailed in the bottom right of the figure.

**A. 4th order basins (n=865)****B. All basins with an area > than 5km<sup>2</sup> (n=492)**

**Figure 31.** Scatter plot of catchment-averaged mean slope angle and normalised steepness index for datasets consisting of: (top) fourth-order basins; (bottom) all basins with an area > than 5 km<sup>2</sup>. Blue  $R^2$  refers to the goodness-of-fit of the linear model, whereas the red  $R^2$  refers to a power model. Each symbol represents a basin. Lithologies are separated by colours, detailed in the bottom right of the figure.

#### 4.1.4 CLUSTER ANALYSIS

Cluster models, with the number of clusters ranging from 2 to 4 clusters, were determined using topographic and lithological criteria. The lithological and topographic cluster solutions are relatively similar for a lower number of clusters, and progressively more dissimilar as the number of cluster increases. For instance, 60% of the analysed basins have the same classification for the two-cluster topographic and lithological solutions. By contrast, for the four-cluster topographic and lithological solutions, only 43% of the basins have the same classification. Overall, the eastern part of the QF is associated with steep relief, yet the correlation relief-lithology is not perfect; particularly in the northeastern and northwestern corners of the QF, lithology is resistant but relief is gentle (Figure 32). The areas where lithology is weak but relief is steep are much more scarce and localised (Figure 32); in other words, steep terrain is restricted to areas underlain by strong rocks.

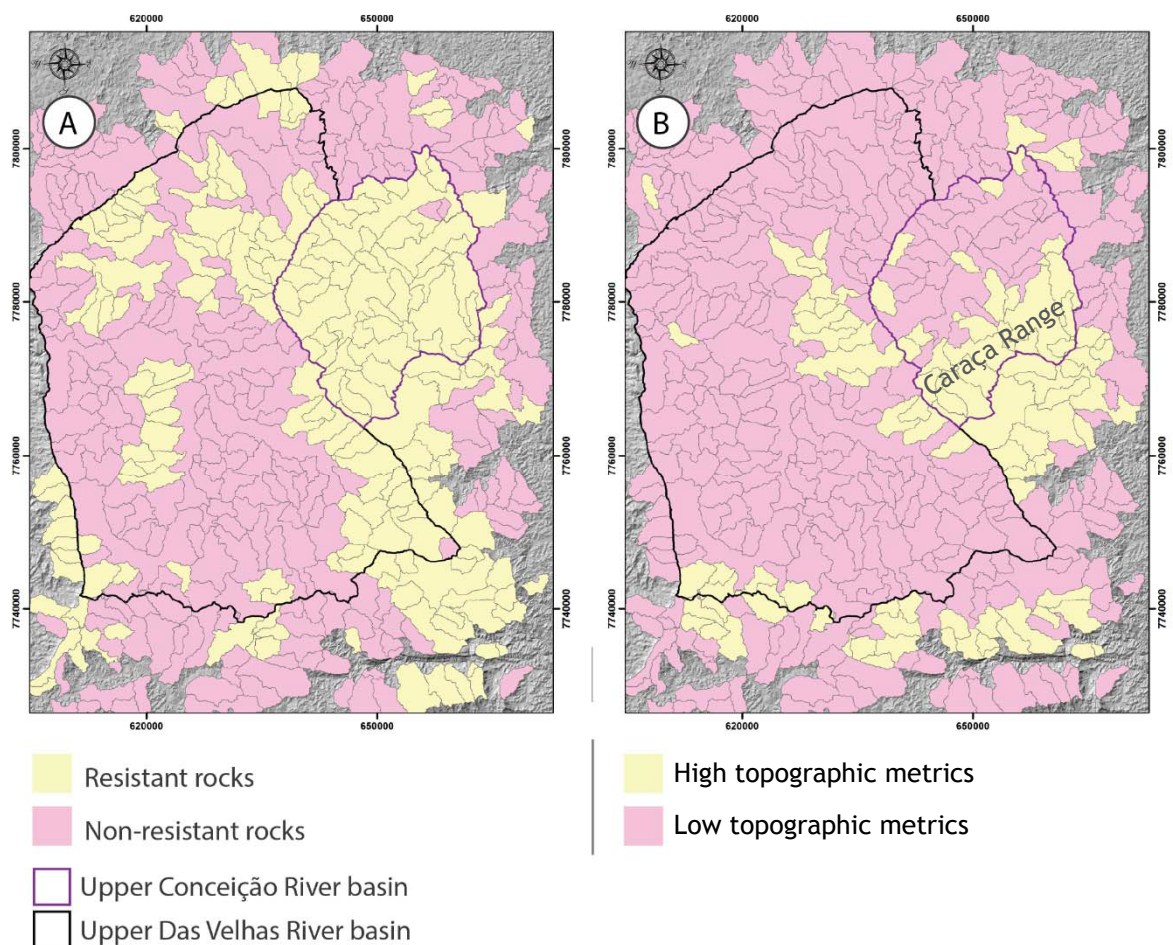


**Figure 32.** (A) Lithological and (B) topographic clusters for a two-cluster solution.

The three-cluster solution (Figure 33) displays marked differences between lithological and topographic clusters and the correlation between landforms and

rock resistance to erosion is not so clear. This lack of clarity is particularly evident in the the Caraça Range, which is classified as resistant lithology, whereas the topographic cluster model indicates that the western part of the Caraça Range has less pronounced relief than its easternmost part.

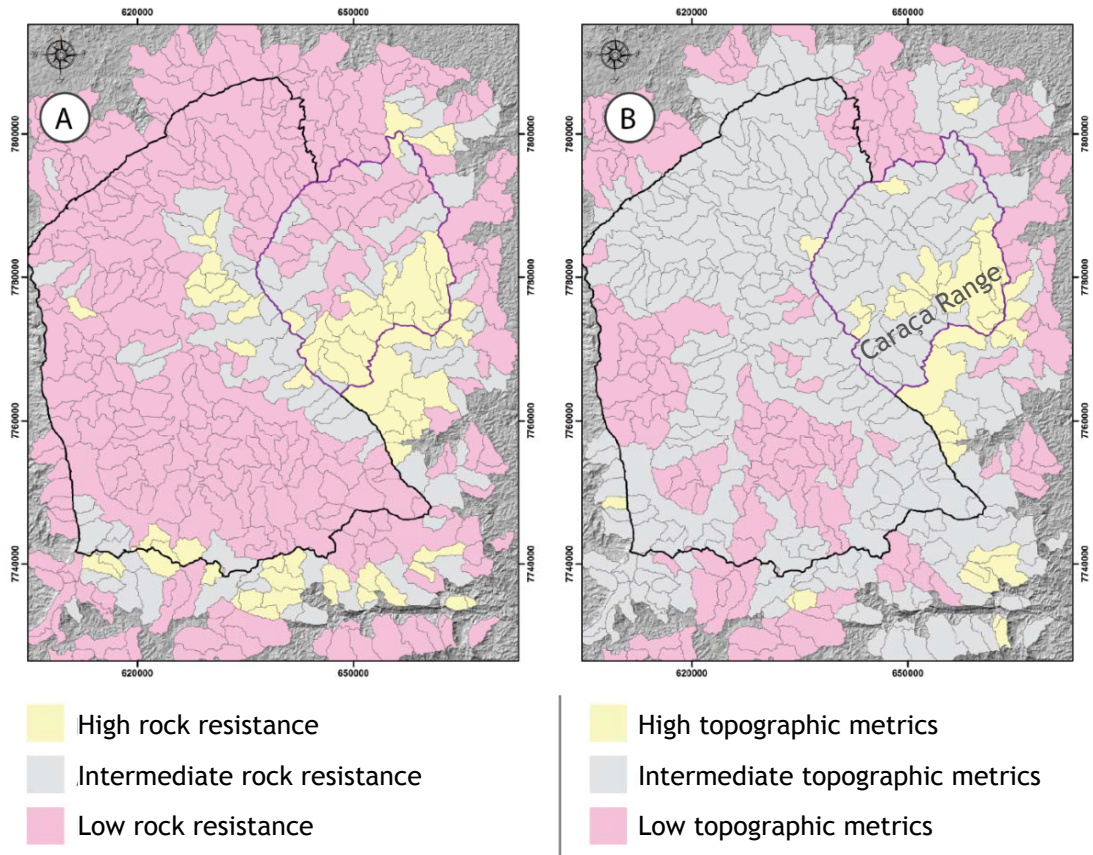


**Figure 33.** (A) Lithological and (B) topographic clusters for a three-cluster solution.

The mismatch between topographic and lithological cluster solutions becomes more pronounced with increasing the number of clusters to four (Figure 34). For example, the lithological cluster shows very few basins with an intermediate rock resistance, whereas the topographic cluster is dominated by basins with an intermediate relief; that is, not as steep as the eastern part of the Caraça Range and not as gentle as the southwestern part of the QF. The Caraça Range is a representative example of the differences between topographic and lithological models; whereas it is dominated by resistant rocks over its entire length, it is characterised by a marked spatial variability in catchment-averaged topography, whereby its eastern part is steeper and more rugged than its western part.

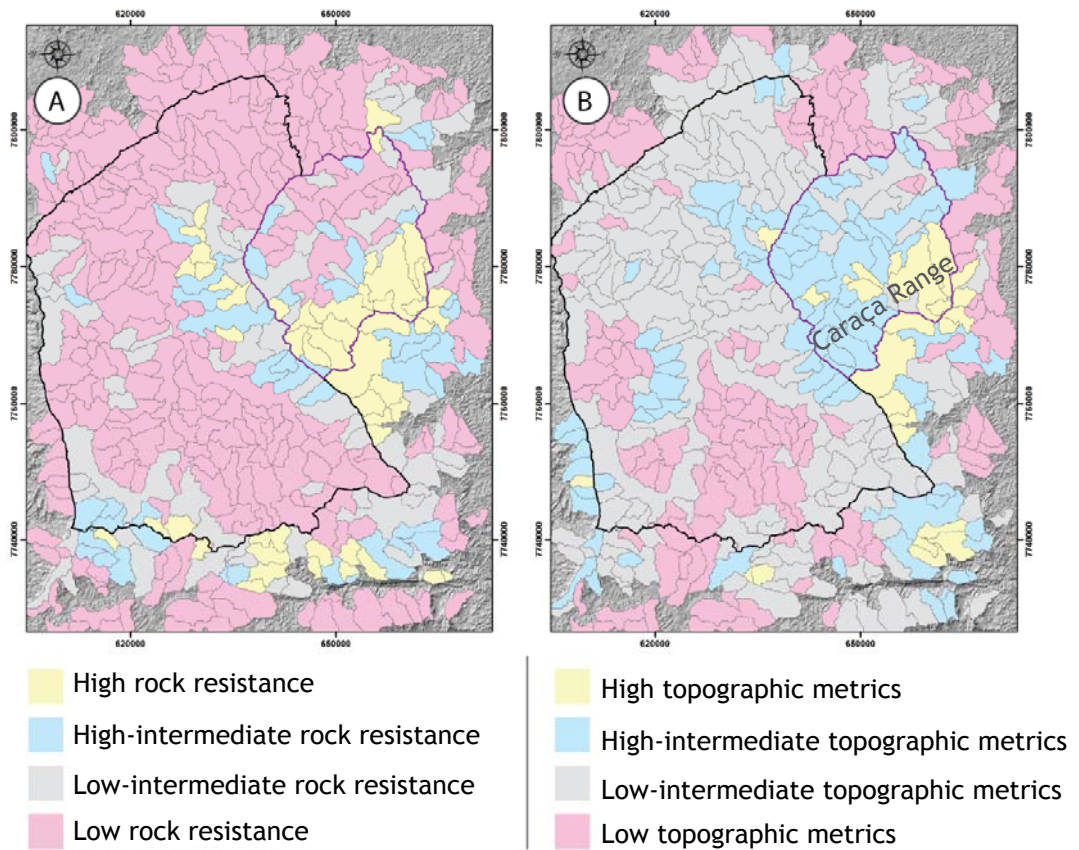


**Figure 34.** (A) Lithological and (B) topographic clusters for a four-cluster solution.

Clusters were analysed to determine if lithological clusters could explain the topographic variability of the QF. The lithological and topographic clusters were then statistically tested, for every geomorphic parameter quantified for the QF (including the parameters not used in the determination of topographic clusters), to determine if the differences in topography between groups (lithological and topographic) were real and not a result of chance or error. The null hypothesis was statistically tested using an alpha-level of 0.05. Excluding ‘basin area’, all other parameters yielded significant ANOVA results (i.e.,  $p$ -value < 0.05); a post-hoc test was used to examine the groups and parameters for which the null hypothesis is rejected (Table 5). Topographic clusters were overall statistically significant for every topographic parameter. The lithological clusters, however, were non-significant for the majority of topographic parameters for the three- or four-cluster solutions. In summary, lithological clusters were efficient in determining significant differences between the lowest and the highest topographic settings (and, in this case, the ANOVA test yielded significant results), but could not differentiate basins with intermediate topography from the steepest basins.

**Table 5.** Results of the post-hoc test for the lithological and topographic models for two, three, and four-cluster solutions.

Parameters	Is the null hypothesis rejected for every pairwise group combination?					
	Two-cluster solution		Three-cluster solution		Four-cluster solution	
	Lithological	Topographic	Lithological	Topographic	Lithological	Topographic
Area (m <sup>2</sup> )	No	No	No	No	No	No
Max. slope (°)	Yes	Yes	No	Yes	No	Yes
Mean slope (°)	No	Yes	No	Yes	No	Yes
Local relief (m)	Yes	Yes	Yes	Yes	No	Yes
Max. elevation (m)	Yes	Yes	No	Yes	No	Yes
Mean elevation (m)	No	Yes	No	Yes	No	No
Basin relief (m)	Yes	Yes	No	Yes	No	Yes
$k_{sn}$ (m <sup>0.9</sup> )	Yes	Yes	No	Yes	No	Yes
Knickpoint magnitude (m)	Yes	Yes	Yes	Yes	No	Yes
Knickpoint relief (m)	Yes	Yes	Yes	Yes	No	Yes
Mean annual precipitation	Yes	Yes	No	Yes	No	Yes

Yes, represented in red, designates a statistically significant result ( $p$ -value < 0.05), whereas no denotes  $p$ -values higher than 0.05.

#### 4.1.5 STREAM-PROFILE ANALYSIS

The QF is one of the highest elevation areas in southeastern Brazil; it is an important drainage divide, with two main tributaries of major drainage systems. The north-flowing Upper Das Velhas River is a tributary of the São Francisco River, the longest river flowing entirely in Brazilian territory, whereas the northeast-flowing Upper Conceição River is a tributary of the Doce River, flowing directly towards the Atlantic Ocean (Figure 1). The eastern limit of the Upper Das Velhas River is the main ‘barrier’ that roughly separates rivers flowing east/northeast (outside of the Upper Das Velhas River basin) from the rivers flowing west/northwest. The channel profiles within the QF display a wide variety of forms, featuring long low-gradient channel segments and steep reaches.

Rivers flowing away from the Caraça Range (Figure 35; represented in black) have their headwaters at high elevations (~2000 m), and they flow perpendicular to the strike of many old faults, crossing patches of high local relief. The longitudinal profiles of these rivers display many convexities, substantial elevation drops (up to 1.4 km over less than 5 km of downstream distance), and steep channel and hillslope gradients. Their slope-area plots show many knickpoints related to locally negative concavity ( $\theta$ ) values. These rivers flow, almost exclusively, over quartzite terrains. By contrast, rivers flowing over areas of low channel steepness index values (generally  $< 50 \text{ m}^{0.9}$ ; Figure 23), notably under granite and gneiss terrains in the southwestern and the northern part of the QF, exhibit characteristically concave-up longitudinal profiles, with small elevation drops (up to ~400 m over ~10-25 km of downstream distance). These rivers do not cross structural lineaments or patches of high local relief (Figure 35). However, some of these low steepness rivers still display ‘rare’ convexities in their profiles related with local rapids and small-relief ( $< 5 \text{ m}$  of elevation drop) waterfalls. In addition, rivers with many convexities in their long profiles but with a more limited elevation range than those flowing over the Caraca Range (~800 m of elevation drop over ~10 km of downstream distance), are ubiquitous in the QF, flowing away from patches of high local relief crossing perpendicularly old faults (Figure 35; represented in green, yellow and orange). These rivers cut across a variety of lithologies. A composite stream profile and associated slope-area data for rivers representing the groups described above are shown in Figure 36. Nonetheless, this summarisation of stream profiles is a simplification of the variety of channel forms in the QF.

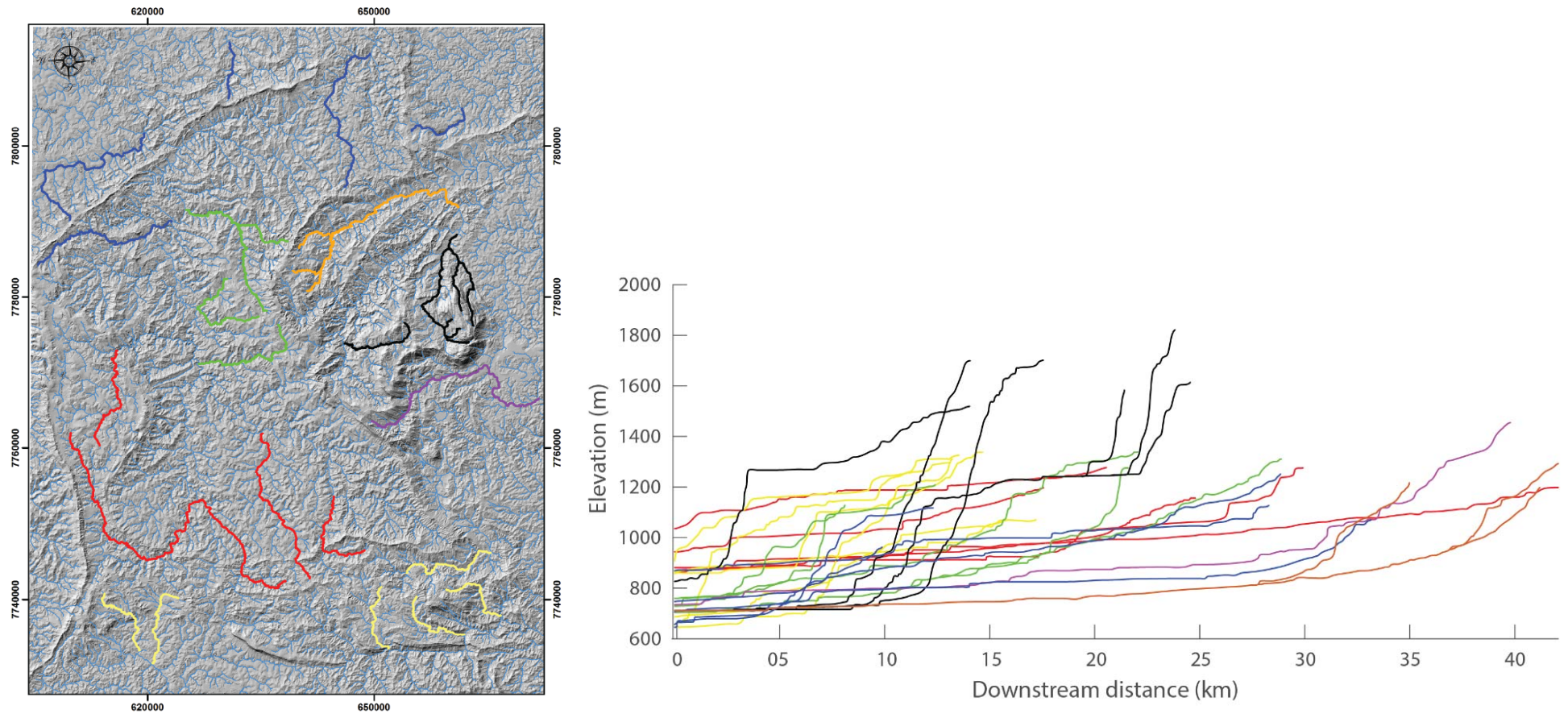


**Figure 35.** Longitudinal profiles of channels flowing in different geomorphic contexts in the QF. Colours were assigned to rivers displaying similar longitudinal profiles, flow direction, and geographical position. However, these are arbitrary to some extent. Overall, rivers flowing away from the Caraça Range are represented in black. Low-steepness rivers are represented in red and in blue. Intermediate-steepness rivers are represented in green, yellow and orange. Rivers flowing in the QF often display some convexity in their longitudinal profile. The downstream limit of each profile was the conjunction of the stream with a river with similar or larger basin area.

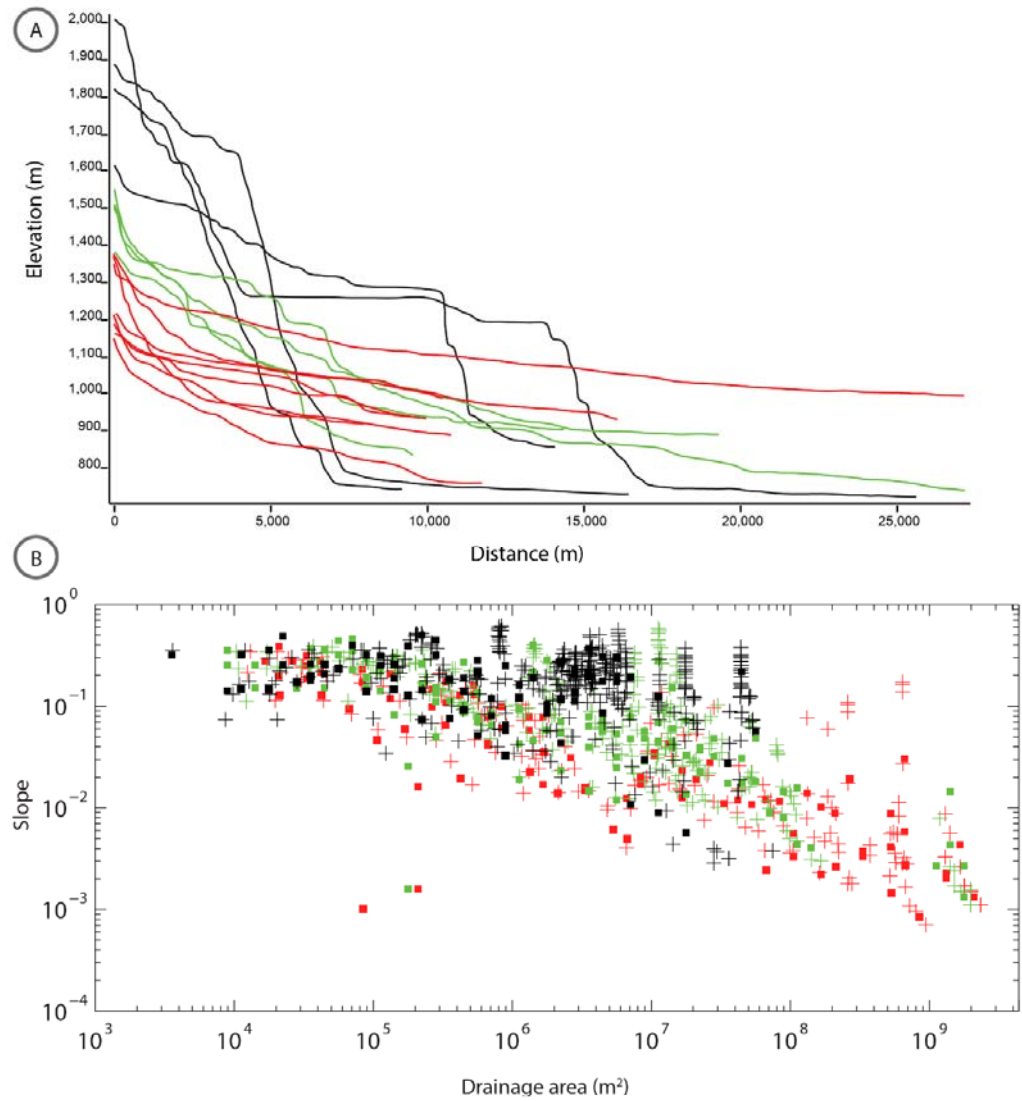


**Figure 36.** Composite stream-profiles and associated log slope versus log area plots for rivers flowing in different geomorphic contexts in the QF. Crosses represent raw data whereas squares represent area-binned data following Wobus et al. (2006). The colour scheme of this plot is the same as the colour scheme in Figure 39.

The unfiltered output of the automated knickpoint extraction algorithms (Neely et al., 2017) yielded a great number of knickpoints covering the entire QF, demonstrating that they are a common feature of this landscape (Figure 37). After filtering the knickpoints with a magnitude less than 50 m (for a detailed account of the filtering process, see session 3.3.6), 375 knickpoints were left (Figure 37). Knickpoints are concentrated in the eastern part of the QF, most notably in the easternmost limit of the Caraça Range. Knickpoints are also present in downstream sections from the main drainage divide between the Upper Conceição and the Upper Das Velhas Rivers, as well as in the northeast and southeast portion of the QF.

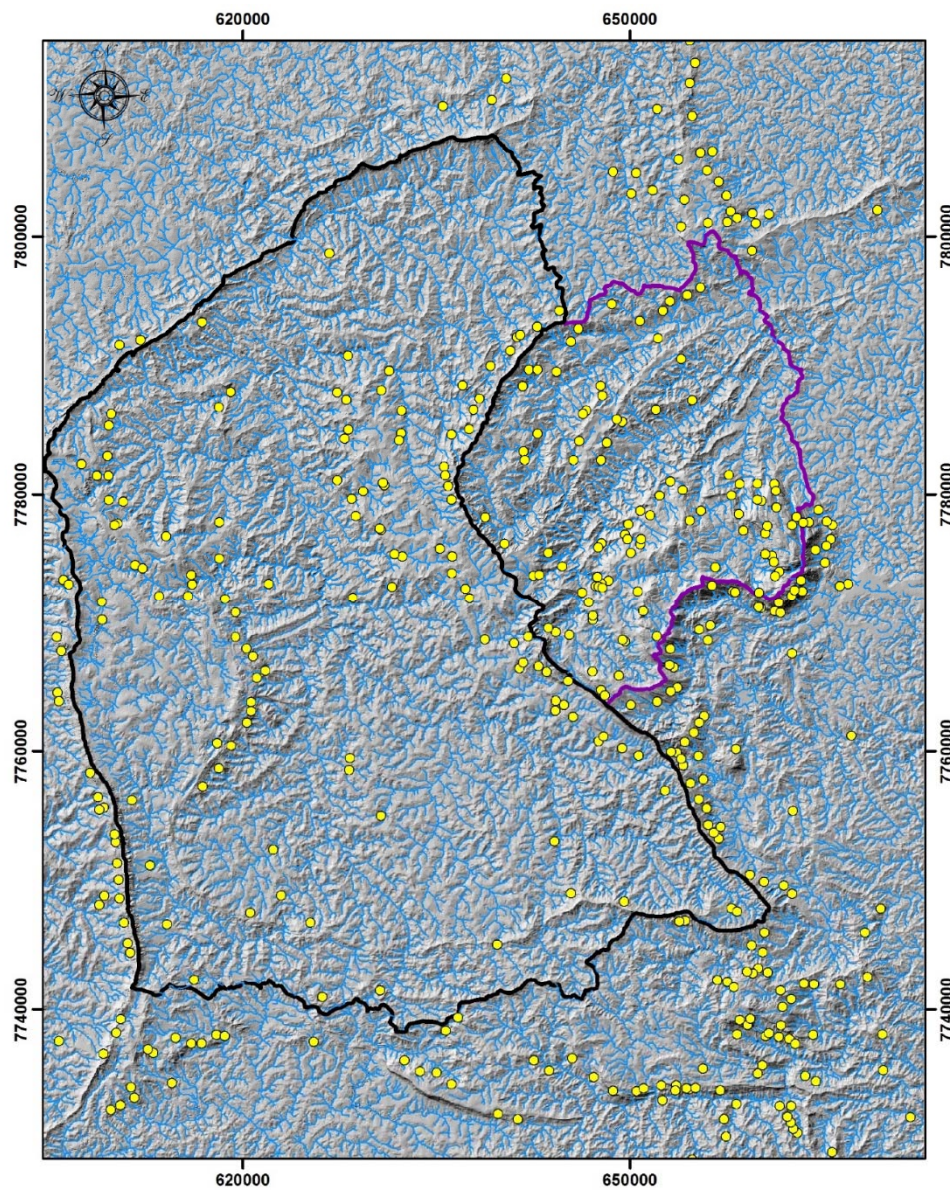


**Figure 37.** The spatial distribution of the filtered knickpoints with a magnitude > 50 m (yellow circles);  $n = 375$ .

Each knickpoint had its elevation determined. The distribution of knickpoints with elevation (Figures 38-39), indicates a main clustering of knickpoints within an elevation interval of 1000-1200 m. There is also a low frequency group of high elevation knickpoints (with an elevation between ~1500-1800 m) that is limited to the Caraça Range. Also, the QF displays lower elevation knickpoints (with elevation ~700-900 m) that are scattered primarily along the eastern QF, and within the lower elevation portions of the Upper Das Velhas River basin (Figures 38-39).

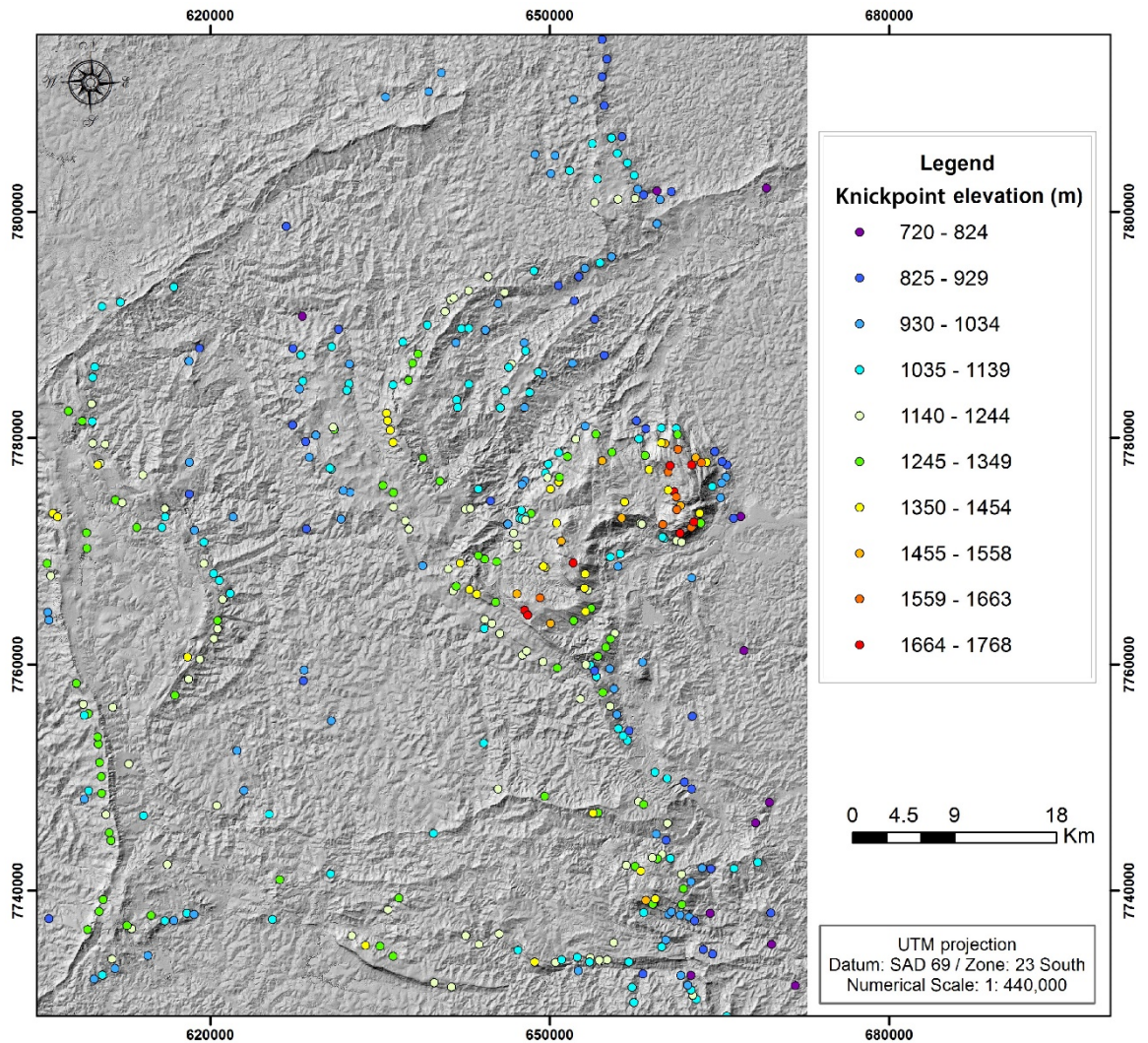


**Figure 38.** The distribution of the elevations of knickpoints (coloured circles) for the QF.

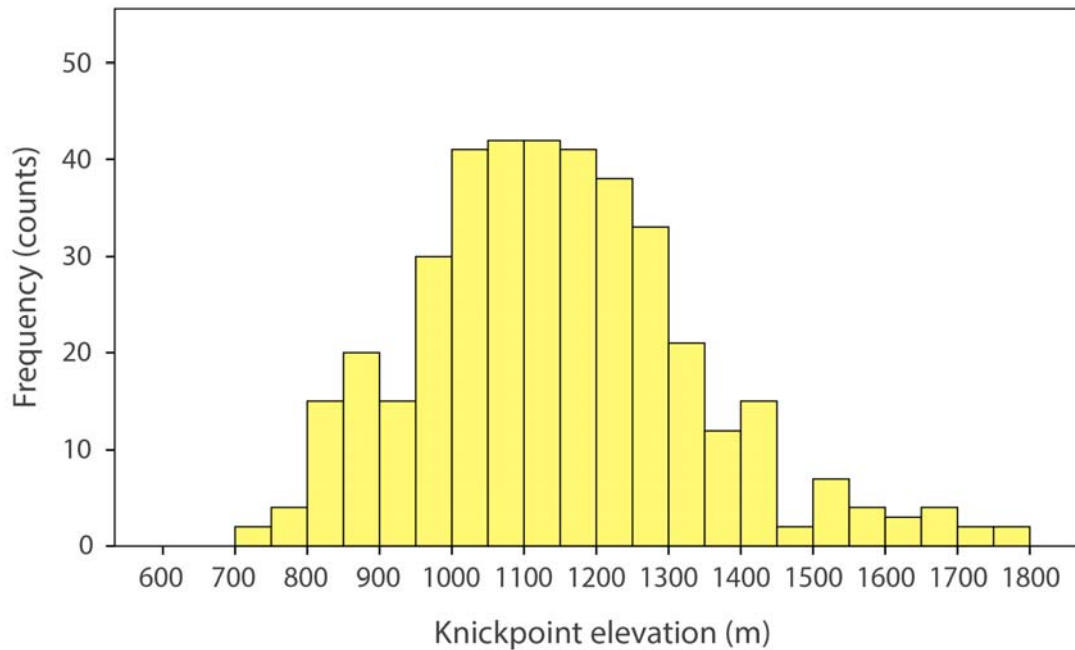
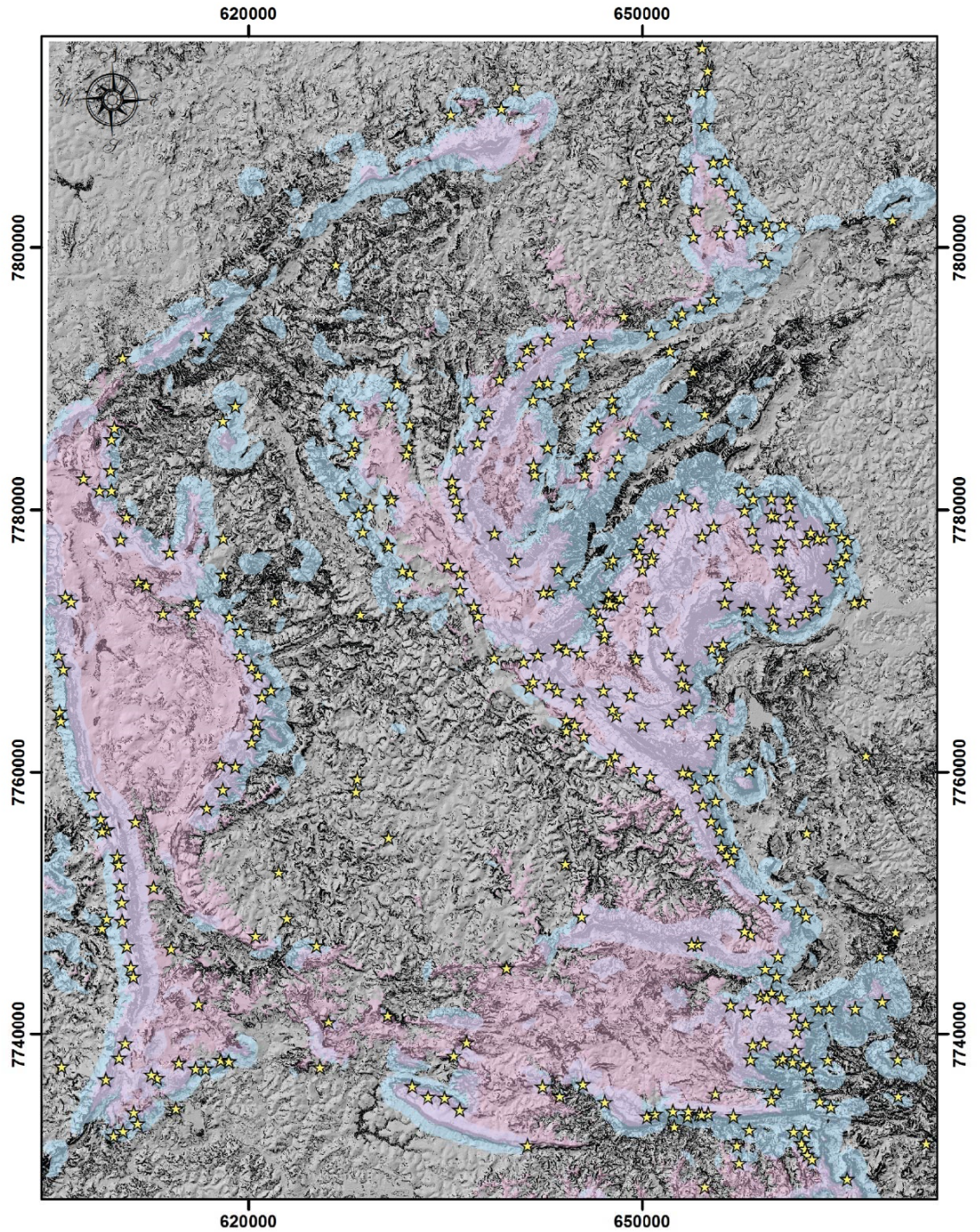


**Figure 39.** The distribution of knickpoints by elevation bins; with a width of 50 m.

The spatial distribution of knickpoints superimposed to the distribution of the highest quartile of local elevation, local relief, and local slope values (Figure 40) suggest that knickpoints lie primarily within the high local relief domain, approximately at the edges of high local elevations. Hence, high-elevation areas are surrounded by patches of high local relief that are spatially associated with the presence of many knickpoints. Within the eastern part of the QF and, in particular, in the Caraça Range, knickpoints are also found 'inside' the high-elevation domain where they are associated with steep upstream reaches (Figure 40; see for example the rivers represented in black in Figure 36).



Legend

-  Knickpoints
-  Elevation - 4<sup>th</sup> quartile
-  Local relief - 4<sup>th</sup> quartile
-  Slope - 4<sup>th</sup> quartile

**Figure 40.** The spatial distribution and superposition of the knickpoints of the QF, represented as yellow stars, and areas in the 4<sup>th</sup> quartile of the distribution: (A) elevation, represented in pink; (B) local relief, represented in blue; and (C) slope, represented in black. The intersection between (A) and (B) is represented in purple.

Knickpoints are primarily found within quartzites ( $n = 203$ ; Figure 41), yet there are knickpoints associated with other lithologies, such as schists ( $n = 43$ ; Figure 41); banded iron formations ( $n = 25$ ; Figure 41); and gneisses and granites ( $n = 35$ ; Figure 41). The superposition of the spatial distribution of the knickpoints and the lithologies of the QF (Figure 42) indicates that in many cases knickpoints coincide with a downstream transition from resistant (e.g., quartzite) to less resistant rock (e.g., schists), or are slightly upstream of this transition (the lithological boundary between a resistant to a less resistant rock is highlighted in blue in Figure 42). Knickpoints also lie close to pre-Paleozoic faults cutting across the QF, which are often also lithological boundaries (Lobato et al., 2005; see Figure 9). On the other hand, the eastern part of the Caraça Range displays knickpoints ‘inside’ the quartzite domain that may not be associated with lithological boundaries. The distributions of knickpoint magnitude, relief, and elevation, versus northing and easting coordinates are shown in Figures 43-44. These plots suggest that peak knickpoint parameters are associated with quartzites and that the most pronounced knickpoint magnitude, relief, and elevation are found around 7770000 northing and 660000 easting, corresponding to the Caraça Range in the eastern part of the QF.

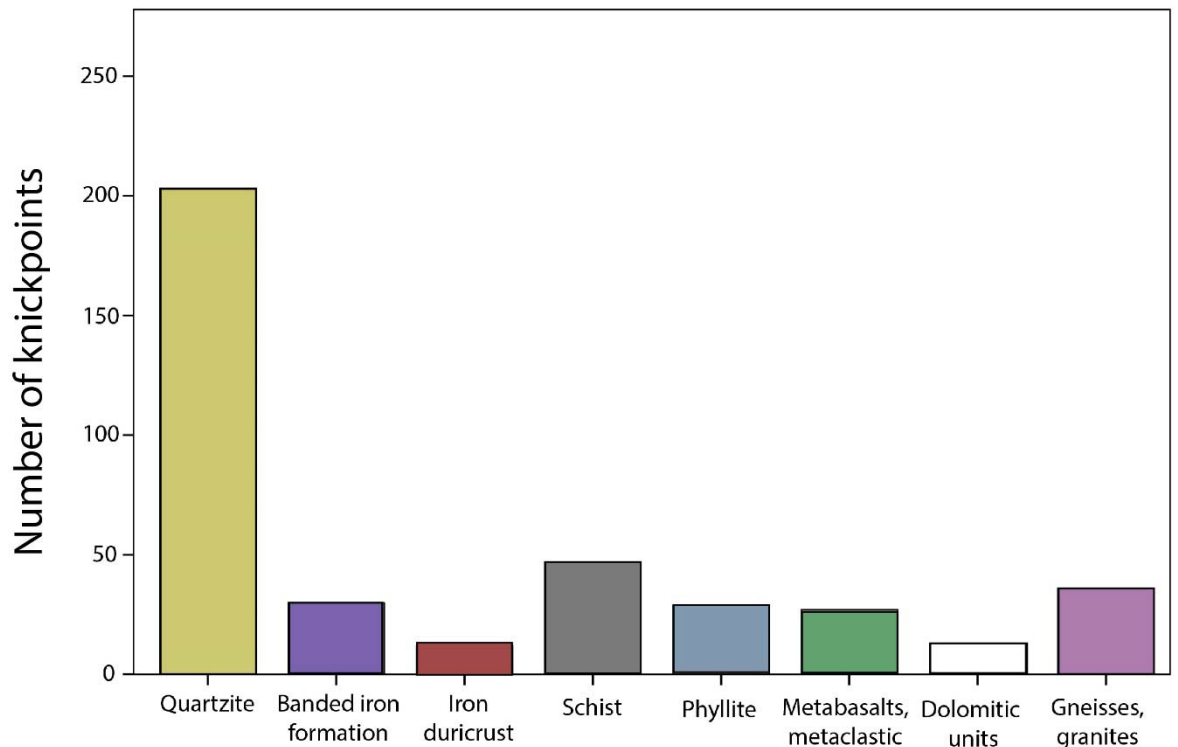


**Figure 41.** Frequency counts of knickpoints per lithological groups.

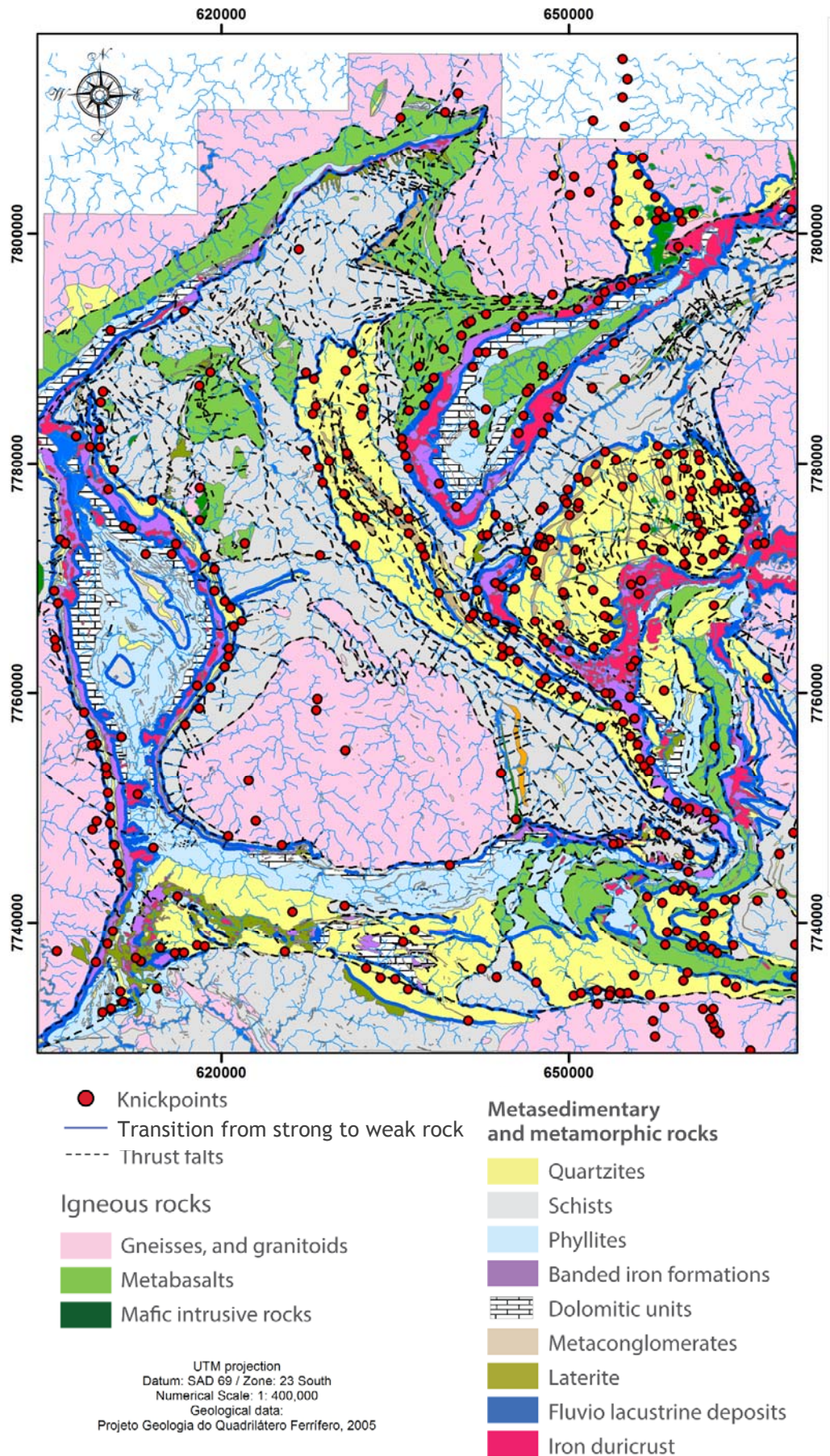
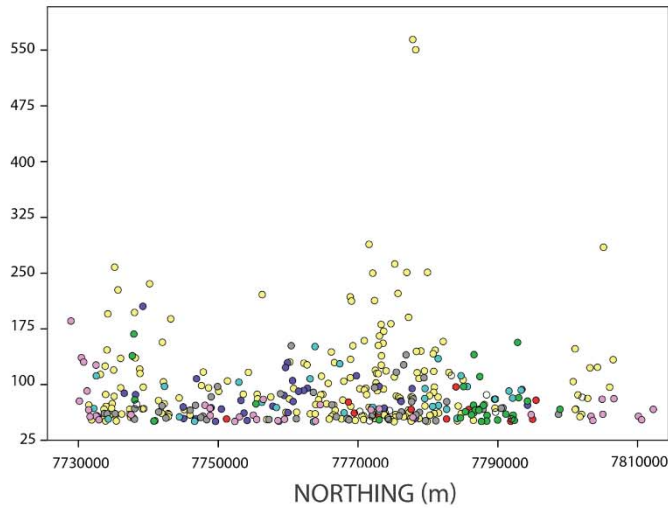
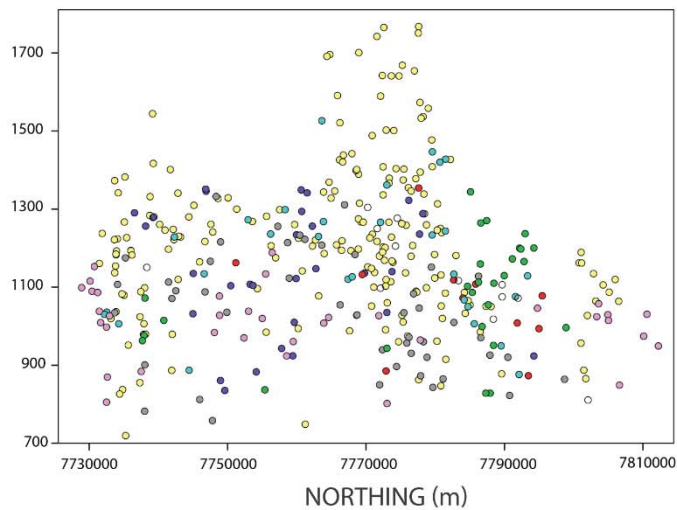


**Figure 42.** The superposition of knickpoints (red circles), the lithological boundaries from strong to weak rocks (thick blue lines), and the lithology map for the QF. Lithological boundaries were extracted from geological mapping at 1: 25,000.

A. Knickpoint magnitude (m)



B. Knickzone elevation (m)



C. Knickpoint relief (m)

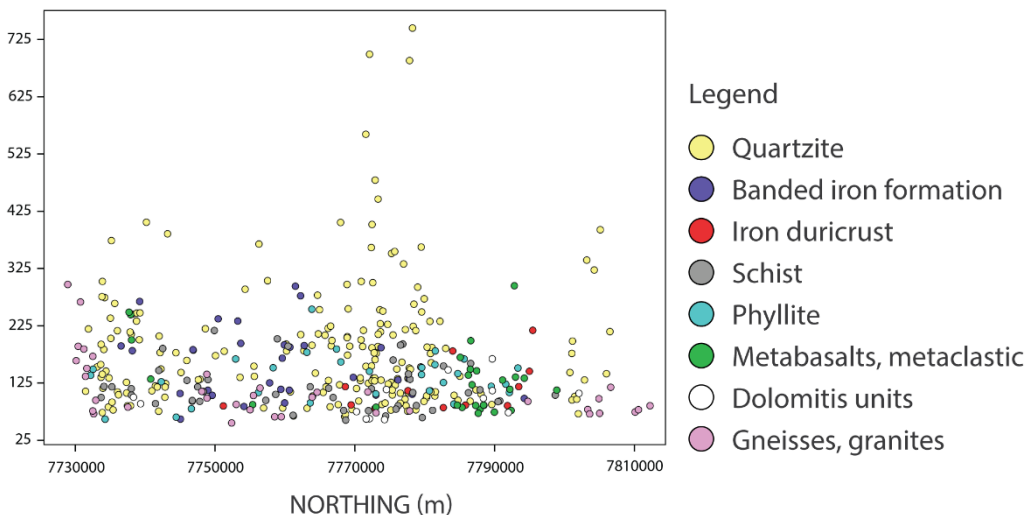
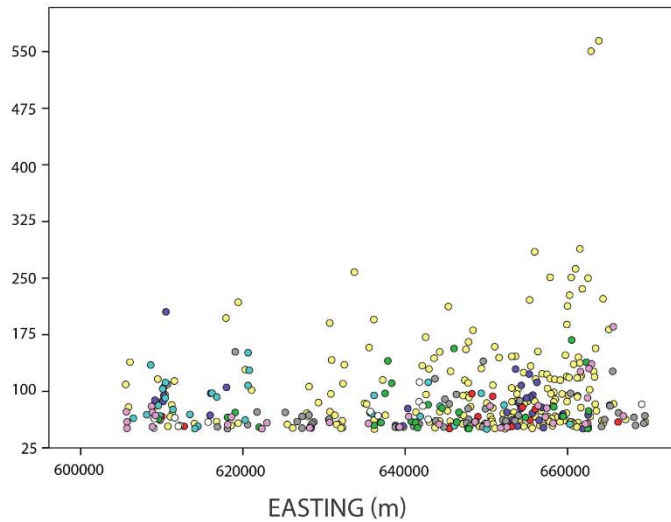
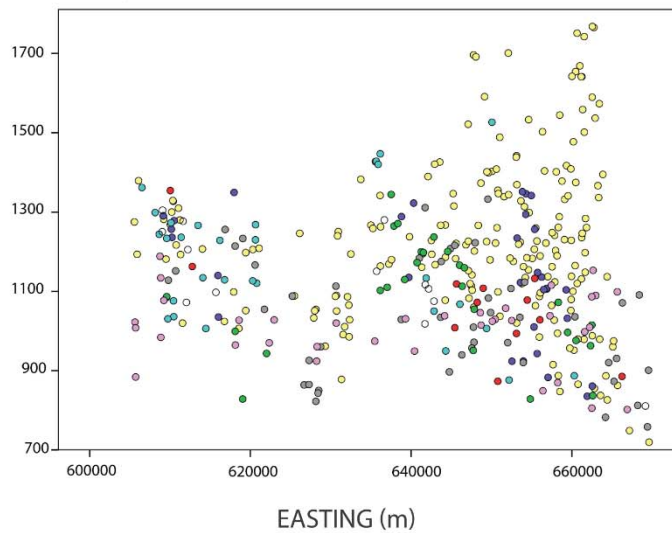


**Figure 43.** The distribution of knickpoint parameters versus northing coordinates. The knickpoint parameters are, from the top to the bottom of the figure: (A) magnitude; (B) elevation; (C) relief. Knickpoints are represented by circles and the colour scheme is detailed in the bottom right of the figure.

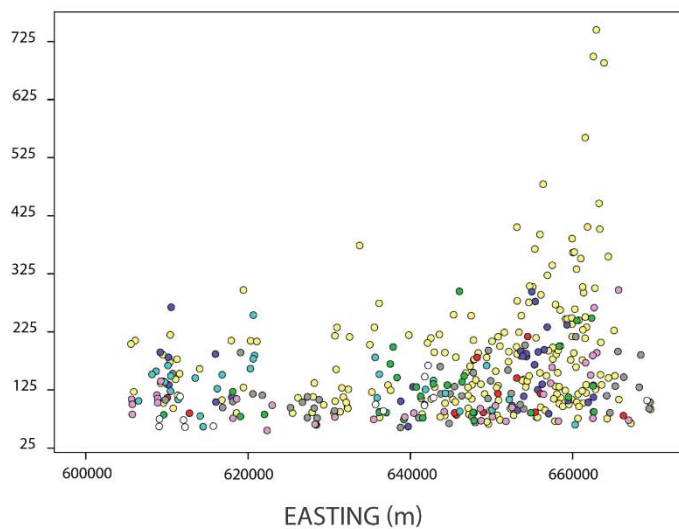
A. Knickpoint magnitude (m)



B. Knickpoint elevation (m)



C. Knickpoint relief (m)



Legend

- Quartzite
- Banded iron formation
- Iron duricrust
- Schist
- Phyllite
- Metabasalts, metaclastic
- Dolomitic units
- Gneisses, granites

**Figure 44.** The distribution of knickpoint parameters versus easting coordinates. The knickpoint parameters are, from the top to the bottom of the figure: (A) magnitude; (B) elevation; (c) relief. Knickpoints are represented by circles and the colour scheme is detailed in the bottom right of the figure.

#### 4.1.6 SUMMARY OF THE RESULTS

- The bulk of local topography of the QF is associated with low values of geomorphic parameters. However, extremely high but infrequent values are typical features for all topographic parameters;
- Local geomorphic parameters are positively related to the exposed lithology resistance, whereby areas under quartzites and banded iron formations have higher local geomorphic parameters than other lithologies. However, there are areas under quartzites with intermediate relief, notably in the western part of the Caraça Range;
- Catchment-averaged topographic parameters are positively related to each other. The parameters  $k_{sn}$ , local relief, and basin relief are associated with the highest correlation values with every other topographic parameter;
- Knickpoints are common features in the drainage network of the QF;
- Rivers flowing away from the Caraça Range are associated with very high elevation drops (~1.2 km) and successive knickpoints in their longitudinal profiles. Rivers flowing over less resistant lithologies, internally within the Upper Das Velhas River basin, are associated with concave-up channel profiles, featuring only minor local convexities;
- Knickpoints are primarily associated with quartzites and also lie close to old faults. Peak knickpoint magnitude, relief, and elevation, are concentrated in the eastern QF, notably at the Caraça Range. The highest values of knickpoint parameters are associated with quartzite knickpoints;
- Lithological clusters were efficient in determining significant differences between the lowest and the highest values of topographic parameters, yet lithological clusters could not differentiate basins with intermediate topographic values from basins with the highest values.

## 4.2 DISCUSSION

The main research question of this chapter is whether the current morphology of the Quadrilátero Ferrífero is that of a typical post-orogenic setting characterized by an abundance of concave-up channels, no knickpoints and a clear, positive relationship between steepness and relief and the bedrock resistance (Baldwin et al., 2003; Lague, 2014; Bursztyn et al., 2015), or if it is similar to the topography of transient landscapes, with knickpoints, convex stream profiles and a less well defined relationship between the morphology of the landscape and the bedrock lithology (Kirby and Whipple, 2012; Lague, 2014).

The empirical dataset presented here demonstrates that the post-orogenic relief of the QF is inherently complex, with a large variability in topographic features. There are stream profiles that are concave-up, as well as channels that are convex-up in form. For example, in the eastern part of the QF, and in particular on the eastern side of the Caraça Range, extremely steep channel and hillslope gradients are present, contrasting with the southwestern part of the QF that is associated with gently-sloping valleys and subdued relief. Knickpoints are common features in the drainage network, and the histograms of the distribution of every local topographic metrics of the QF show rare, but extremely high values. The variability in steepness and relief is not randomly distributed, but is rather controlled by the bedrock strength. That is, generally speaking, steep terrains are associated with resistant rocks (quartzites, banded iron formations and iron duricrust), contrasting with low-steepness terrain under low-resistance rocks, such as gneiss and granitic rocks which tend to be relatively weak in a tropical climate. Also, whereas local steepness and relief may be extremely high in some cases, these are rare and very localised, and thus the ‘average’ topography of the QF is associated with subdued steepness and relief. These results indicate that a post-orogenic landscape may be associated with a wide range of topographic characteristics that may, if taken individually, lead to contradictory geomorphic interpretations. For instance, whereas the widespread presence of high-relief knickpoints and high local values of steepness and relief could be argued as indications of a transient landscape still responding to a perturbation, the adjustment of steepness and relief to bedrock strength, as well as the presence of concave-up profiles and an overall subdued relief could be taken as indications of a steady-state landscape. I argue that these topographic characteristics are not

necessarily contradictory, and I provide important information to constrain and understand the evolution of post-orogenic landscapes. The transient state of the landscape can be tested by measuring denudation rates in areas with pronounced and gentle relief as well as strong and weak rocks of the QF, for resurgence implies high denudation rates over the transient areas, whereas the ‘preserved’, high relief areas, should be associated with lower denudation rates. Hence, quantifying the topography of the QF is a necessary step to identify areas where denudation rates should be different and to test models of long-term landscape evolution.

#### **4.2.1 TOPOGRAPHY OF THE QF AS A CLASSIC POST-OROGENIC SETTING**

The positive association between steepness and relief with bedrock strength indicated by the empirical dataset supports the old geomorphic wisdom that terrains underlain by strong rocks display higher topographic relief and steeper channel gradients when compared to areas underlain by weak rocks (e.g., Playfair, 1802; Gilbert, 1877; Hack, 1960; Leopold and Bull, 1979; Miller, 1990; Stock and Montgomery, 1999). The correlation between rock type and topographic form and relief has been so often reported that it is taken for granted as a fundamental control on how landscapes evolve (Bishop, 2007). The most common reasoning for the role of lithology on landscape evolution refers back to Hack (1960; 1975); he proposed that in the areas where resistant rocks are exposed, relief needs to be steeper than in gentle-relief areas under low-resistant rocks for denudation rates to be spatially invariant (in equilibrium). In other words, in a Hack-type landscape, geomorphological features and the processes sculpting them are part of an open system in which all topographic elements are adjusted to each other, downwasting at the same rate (Hack, 1960, 1975). This hypothesis is empirically testable as it implies spatially invariant denudation rates, and Chapter 5 presents data that will test Hack’s model of landscape evolution for the QF. Another way of explaining the relationship between topographic forms and rock type is to consider the indirect role of lithology in controlling the grain size and amount of sediment load delivered to channels by hillslopes (Whipple and Tucker, 2002; Sklar and Dietrich, 2001; Sklar and Dietrich, 2006; Pelletier, 2008). Resistant lithologies will generate coarser sediment at low supply rates, that will act as tools for fluvial incision and ultimately may result in steeper channel and hillslope gradients than areas under low-resistance lithologies that generate fine and abundant sediment that, in turn

will cover the channel bed, inhibiting erosion (Sklar and Dietrich, 2001; Sklar and Dietrich, 2006; Pelletier, 2008). In addition, resistant lithologies may also slow the transmission of upstream-migrating knickpoints due to their low erodibility (cf. Bishop and Goldrick, 2010).

Whereas the above described hypotheses may be consistent with the observed association of topographic form and rock type in the QF, there is a marked variability in topographic characteristics within areas underlain the same resistant rock type that is not addressed by these hypotheses. For instance, the Caraça Range is underlain by quartzites over its entire length, yet its western part is associated with much lower relief than its eastern part, which is characterised by extremely rugged and steep topography. The variability in steepness and relief in resistant rocks is the main reason why lithological clusters performed worse than topographic clusters in the post-hoc tests (see section 4.1.4). Similar findings were reported by Hack (1982) for the Appalachians Mountains, where “although the conspicuously high areas do contain what appear to be resistant units, all these resistant units also occur in low relief areas... This relation between topographic forms and rock types suggests that both tectonic forces and rock control have operated to produce the present forms, tectonic processes playing a major role” (Hack, 1982, p. 25). For Hack (1982), spatial differences in Appalachian topography can be explained in many cases by differences in rock strength, whereas some variations in steepness and relief can only be explained by differential rates or histories of active uplift. The occurrence of differential uplift has been used to explain geomorphic features that are apparently not justified by rock resistance in other contexts (e.g., the Colorado Plateau; Crow et al., 2014). For the case of the QF, the hypothesis that the steep and high relief areas of the eastern part of the Caraça are the result of localised ongoing tectonic activity have been invoked by geomorphic work describing evidence of local Cenozoic deformation in small graben-like basins concentrated in this area (e.g., Saadi, 1991; Saadi et al. 1992; Sant’anna et al., 1997; Cabral and Koglin, 2014). The hypothesis that the eastern side of the Caraca Range is more recently tectonically active is tested in Chapter 5; as shown in other ‘passive settings’ (e.g., Quigley et al., 2007), ongoing tectonic activity would imply higher denudation rates (as well as steeper relief) than in the non-active, gently-sloping areas.

The histograms of every topographic parameter for the QF are dominated by low values, which is consistent with the conceptual framework where post-orogenic landscapes are slowly decreasing in relief and elevation over the long-term (Bishop, 2007). There are, however, steep channel and hillslope gradients; despite being local rare features, they are comparable with other mountainous post-orogenic terrains (e.g., Cape Mountains, Africa; e.g., Scharf et al., 2013), as well as to tectonically active settings. For instance, the QF exhibits river channels with local ' $K_{sn}$ ' values (with ' $\theta$ ' = 0.45) as high as  $1220 \text{ m}^{0.9}$ , which would be considered high end-member values in the Cape Mountains in Africa (e.g., Scharf et al., 2013, p. 332, Figure 1), the southern Appalachians (Gallen et al., 2013, p. 6, Figure 1), East Tibet (e.g., Kirby et al., 2003, p. 15, Figure 8), Calabria in Italy (e.g., Roda-Boluda and Whittaker, 2017, p. 711, Figure 6), central Nepal (e.g., Kirby and Whipple, 2012, p.14, Figure 9), southern California (DiBiase et al., 2010, p. 138, Figure 2), south-central Crete (Gallen and Wegmann, 2017, p.169, Figure 4), or the Garhwal Himalaya (Scherler et al., 2014, p. 95, Figure 6).

The observation of these low-frequency, extremely steep topographic features implies that the topography of the QF is at odds with conceptual, analytical and numerical models of relief reduction through time, because the topography of the QF is not featureless. Analytical and numerical solutions are either based on the detachment-limited stream power model (e.g., Pelletier, 2008; Baldwin et al., 2013); a transition to transport-limited conditions during the topographic decay (e.g., Baldwin et al., 2013); the added effects of isostatic rebound (Pelletier, 2008; Baldwin et al., 2013), a critical shear stress for erosion and flood discharges stochasticity (e.g., Baldwin et al., 2013); or the abrasion-saltation sediment flux-driven erosion (e.g., Pelletier, 2008; Egholm et al., 2013). These solutions indicate that the 'residual' topography of post-orogenic terrain is likely to resemble a planation state (in a Davisian sense; Davis, 1869) or transport-limit system, with little to no relief, and with "main valleys that become permanently alluviated when the available stream power decreases below the threshold required for sediment transport" (Egholm et al., 2013, p. 477). Steep landforms in post-orogenic settings are not exclusive to the QF, having been reported in other settings (e.g., von Blanckenburg, 2004; Quigley et al., 2007; Bishop and Goldrick, 2010; Cogné et al., 2012; Gallen et al., 2013; Scharf et al., 2013), and future

numerical modeling studies must consider the presence of steep features in post-orogenic landscapes to constrain their evolution.

#### 4.2.2 RIVER CHANNELS IN THE QF

The traditional framework for the typical characteristics of post-orogenic channels is that “where not disturbed by contrasts in lithology... [post-orogenic] channel profiles show semi-logarithmic forms (smooth, concave-up profiles) that are very similar to “steady state” forms expected and observed in actively uplifted ranges” (Baldwin et al., 2003, p. 2). Whereas many rivers in the QF have profiles that are consistent with the above description, notably in the southwestern corner of the QF, knickpoints are common features in the drainage network of the entire area. Likewise, channel profiles in other post-orogenic terrains that were traditionally associated with concave-up and smooth profiles has also been described as featuring pronounced knickpoints that may define a ‘relict’ gentle upstream reach and an ‘adjusted’ downstream segment (e.g., Bishop and Goldrick, 2010; Gallen et al., 2013; Prince and Spotilla, 2013). Conceptually, knickpoints represent adjustments in channel form as the result of changes in base level that are, in turn, the consequence of spatial and temporal changes in boundary conditions, such as tectonic changes in rock uplift rate (e.g., Pazzaglia and Brandon, 1996; Gallen et al., 2013), denudational isostatic rebound (e.g., Bishop and Goldrick, 2010), or mantle dynamics (e.g., Pazzaglia and Gardner, 1994; Moucha et al., 2008). Once formed, knickpoints migrate upstream at ‘predictable’ rates, depending on the bedrock erodibility ( $K$ ) and drainage area (for  $n = 1$  and detachment-limited channels; cf. Bishop et al., 2005; Crosby and Whipple, 2006; Bishop and Goldrick, 2010). For a steady-state landscape with constant bedrock erodibility (where  $dK/dx = 0$ ), knickpoints may migrate upstream at a quasi-constant vertical rate (e.g., Niemann et al., 2001; cf. Kirby and Whipple, 2012), producing, in map-view, a systematic radial ‘contour-like’ pattern of knickpoints, with an overall altitudinal consistency (Figure 45; e.g., Crosby and Whipple, 2006; cf. Kirby and Whipple, 2012). If bedrock erodibility changes, however, knickpoint retreat rate also changes (cf. Bishop and Goldrick, 2010). In this case, knickpoints would be expected to concentrate in resistant rocks, because strong lithologies act to slow their propagation and knickpoints become practically ‘stalled’ on strong rocks (cf. Bishop and Goldrick, 2010). The QF displays a very complex combination of strong and weak lithologies (cf. Dorr, 1969); in these situations,

where rivers cross-cut many rock boundaries,  $K$  is expected to vary along practically every channel, and a contour-like pattern of knickpoints is unlikely. Knickpoints in the QF do, however, show some altitudinal consistency as they cluster within an elevation interval of 1000-1200 m, and are concentrated in areas of high local relief at or just downstream of the boundary with the high, low-relief areas (Figure 40,42). In these terms, the knickpoints in the QF represent topographic breaks that are effectively separating an upstream lower relief area from a downstream area associated with high relief. There are different possible explanations for the many knickpoints found in the QF. For instance, these knickpoints may have been originated by a denudational isostatic compensation event (or events) that rejuvenated the post-orogenic topography 'bottom-up' (from the local base level of rivers draining east/northeast and west/northwest, up into the mountains), as described by Bishop and Goldrick (2010) in the case of southeastern Australia. Given that the knickpoints also lie close to pre-Paleozoic faults, a differential, active tectonic uplift may be a possible explanation for their origin. In addition, there is a group of knickpoints found inside the high-elevation domain in the eastern part of the Caraça Range; these are associated with higher elevations (1500-1800 m) than the other knickpoints, but, as many of the others, are underlain by quartzites and are close to old faults (Figures 40,42). An alternative explanation is that the presence of large convexities in stream profiles in post-orogenic settings are not 'abnormal' or the result of an external perturbation but rather a typical channel form in these settings, possibly related to the spatial distribution of rocks with different resistance to denudation.

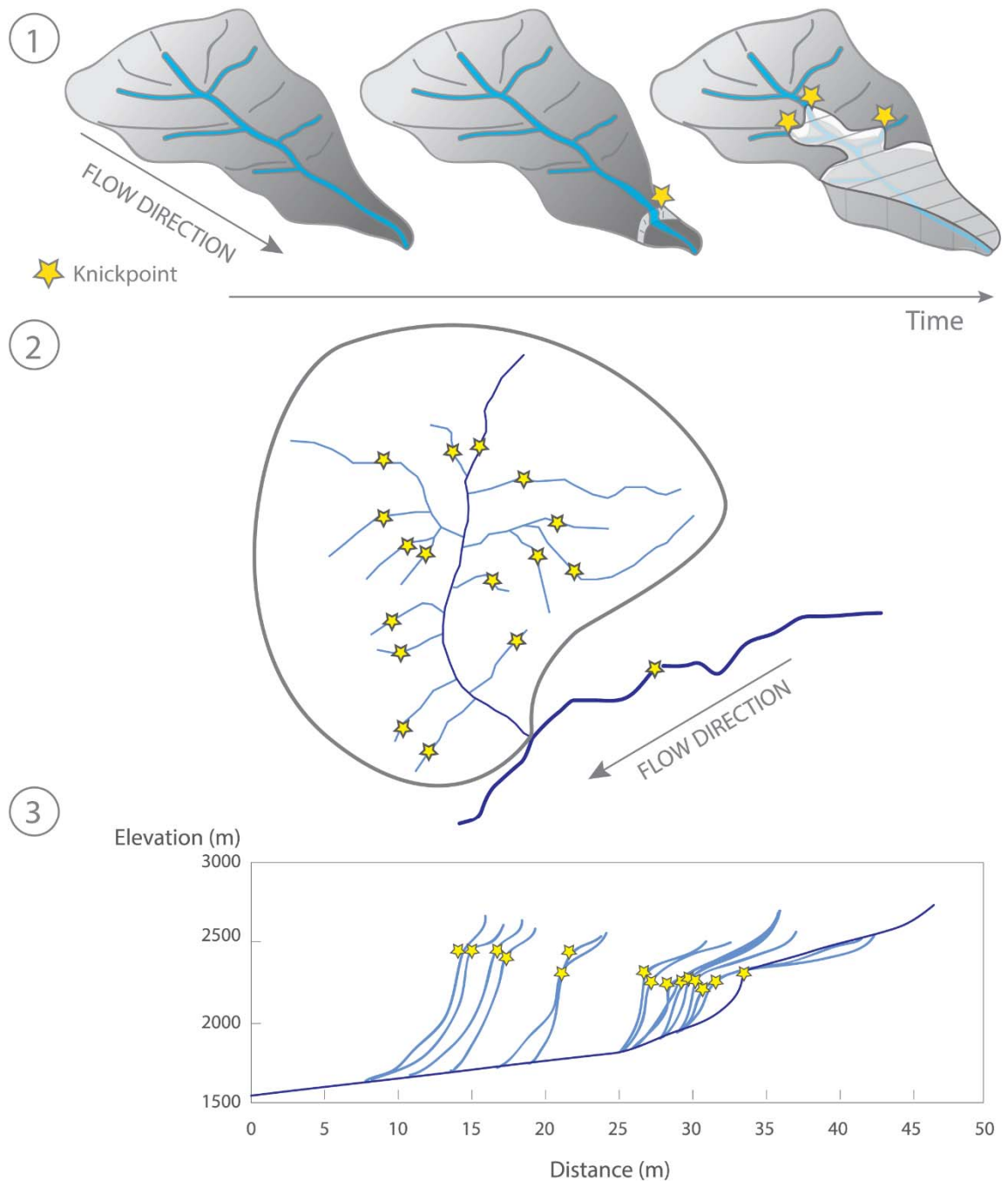


**Figure 45.** (1) A representative sketch of the temporal evolution of a relative base level fall event within a particular basin. A perturbation (e.g., denudational isostatic rebound) triggers a transient channel response of incision and the formation of an upstream-migrating vertical slope-break knickpoint in the trunk stream. The migrating trunk stream knickpoint lowers the base level of its tributaries resulting in the formation of upstream-migrating knickpoints in these. Modified from Gallen et al. (2013). (2) Map-view of the typical spatial distribution of knickpoints within a basin that experienced a base-level fall event that overprints its topography. This catchment is formed in a single lithology. Knickpoints display a contour-like pattern, with consistency in the number of knickpoints per tributary. Modified from Whipple et al. (2013). (3) Composite longitudinal profile of all rivers within the catchment exhibit in panel 2.

### 4.2.3 CATCHMENT-AVERAGED TOPOGRAPHY

The fact that catchment-averaged topography is independent of stream order implies that basin area, at least for the range considered in this study (i.e., second- to seventh-order basins), is not a critical parameter. This interpretation is supported by the weak statistical correlation between basin area and any other metric, for every catchment. The parameter mean elevation is also poorly correlated with every topographic parameter, except maximum elevation. These findings contrast with several studies (e.g., Milliman and Syvitski, 1992) and have important implications for the evolution of post-orogenic relief, as topographic decay is often quantified using mean elevation as the main parameter that determines denudation rates (e.g., Pinet and Souriau, 1988; cf. Pelletier, 2008).

For lower order basins, the relationship between catchment-averaged  $k_{sn}$  and mean slope angle is best explained by an allometric model rather than a linear model. This finding is apparently odd because a non-linear positive relationship between these variables is often reported for tectonically active settings, but not for passive settings (e.g., Ouimet et al., 2009; DiBiase et al., 2010). In active landscapes, the non-linear relationship is conceptually explained by the connection between channel steepness and tectonic uplift (the higher the tectonic uplift, the steeper the channels will be); by contrast, in these settings, slope angle and uplift are instead ‘decoupled’, because the slope angle is limited by lithology and responds to incision by increasing landslide frequency rather than steepening (Larsen and Montgomery, 2012). The empirical dataset of this contribution was not designed for investigating the coupling of hillslope and fluvial processes. However, I speculate that the non-linear coupling between these variables for the QF may be the result of a lag time in the hillslope response to a bottom-up rejuvenation event that is steepening the channels and migrating upstream slowly, due to the resistance of the bedrock.

### 4.2.4 TOPOGRAPHY AND LANDSCAPE EVOLUTION IN THE QF

Research in landscape evolution of ancient high-relief settings has focused on two-end members either post-orogenic relief is (i) a long-lasting remnant of an ancient topography that persists precisely because of the tectonic stability and the

presence of strong rocks (e.g., Twidale, 1999; Twidale, 2016); or the post-orogenic relief is (ii) a product of a recent (i.e., post-orogenic) rejuvenation (e.g., Gallen et al., 2013). An additional alternative is that post-orogenic settings (iii) are in a dynamic equilibrium whereby topography is set primarily by the spatial distribution of rocks with different resistance, and denudation rates are spatially invariant (Hack, 1960; Matmon et al., 2003a). In summary, the quantitative analysis of the topography of the QF has shown an array of topographic elements that could possibly be interpreted as evidence of either (i), (ii), or (iii). For instance, the positive relationship between steepness and relief to bedrock strength could easily be interpreted in terms of (i) or (iii). At the same time, these two hypotheses imply a different pattern of denudation, whereby in (i) strong rocks form uplands, because they are associated with low denudation rates that are lower than the denudation rates of downstream areas under less resistant rocks. In contrast, the hypothesis (iii) implies that denudation rates are everywhere the same, despite differences in rock type. On the other hand, the topographic and lithological data from the QF and the cluster analyses indicate that much, but crucially not all, of the topography can be explained as an effect of rock resistance to denudation and weathering. In other words, the variability in steepness and relief between areas under the same resistant rock type, such as in the western and eastern parts of the Caraça Range, indicates that either the understanding of how lithology controls the development of relief is somewhat incomplete, or that some other geologic processes, such as rejuvenation assumed in hypothesis (ii) must be accounted for. Hence, the rates at which the eastern part of the Caraça Range is denuding are fundamental for constraining and understanding the landscape evolution of the QF. In short, if differential uplift is the main control in the pattern of denudation, the steep channel and hillslope gradients of the eastern part of the Caraça Range will be associated with higher denudation rates than the rest of the QF. If the high relief is, instead, surviving on account of being underlain by resistant quartzites, denudation rates will be extremely low, irrespective of the steep topography. Finally, the presence of knickpoints may also be explained without invoking any active tectonic phase. Denudational isostatic compensation, which acts to ‘prolong’ the timespan of ancient mountain belts, may, at the same time, be responsible for a ‘passive’ (non-tectonic) base level fall that would trigger drainage net rejuvenation, and that could possibly explain the pattern and distribution of knickpoints in the QF.

Thus, the analysis of the pattern of denudation of the QF is fundamental for understanding its post-orogenic geomorphic history.

### 4.3 CONCLUSION

The QF has been taken as an exemplary case of a post-orogenic landscape. The quantitative analyses of its topography reveal that post-orogenic relief is complex, with topographic characteristics that vary spatially. Whereas the post-orogenic relief of the QF is for the most part subdued, similarly to what is defined as a 'classic' post-orogenic landscape (cf. Baldwin et al., 2003; Bishop, 2007), it is still marked by extremely steep channel and hillslope gradients that are comparable to those found in tectonically active settings (as well as other post-orogenic landscapes). Hence, the current morphology of the QF is at odds with the conceptual representation of post-orogenic topography as approaching the planation state (cf. Kooi and Beaumont, 1996) or with a transport-limited condition where stream power is overall lower than the threshold for the transport of sediments (e.g., Egholm, 2013). To sum it up, the post-orogenic topography of the QF is not featureless.

The variability in steepness and relief in the QF is primarily controlled by bedrock resistance. The adjustment of topographic forms to rock type has been identified in many other post-orogenic settings, and was often interpreted as an indication that strong rocks had sustained post-orogenic relief by being 'out of reach' of denudation, as well as an indication of a long-term equilibrium condition due to tectonic stability.

High relief knickpoints are common features in the channel network of the QF, primarily associated with the presence of strong lithologies, but also located close to pre-Paleozoic faults. In addition, the cluster analysis demonstrated that lithological clusters solutions are rough but imperfect approximations of the topography; that is, the topography under resistant rocks is not steep in the same way everywhere. The steepest and more rugged areas of the QF are located in the eastern part of the Caraça Range and are underlain by quartzites. The analysis of the spatial variation in denudation rates of the QF, presented in Chapter 5, is fundamental for testing contrasting hypotheses for the landscape evolution of the QF and, more generally, of post-orogenic landscapes.

**CHAPTER 5:**  
**QUANTIFYING DENUDATION RATES IN THE QF**



# CHAPTER 5: QUANTIFYING DENUDATION RATES IN THE QF

## 5.1 INTRODUCTION

The fundamental question that underpins geomorphology is how landscapes and landforms evolve to be as they are empirically observed (Summerfield, 1991). The empirical dataset presented in Chapter 4 indicates that the post-orogenic relief of the QF is complex, with large spatial variability in topographic characteristics. Generally speaking, areas under quartzites have high slopes, steep channels, and high relief. By contrast, areas under gneisses and granites have low-steepness slopes and channels, as well as low relief. Also, there are areas in the QF of intermediate steepness, associated primarily with schists and mixed lithology basins. The channel profiles of the QF are also associated with spatial variability in form and characteristics, ranging from low relief concave-upwards channels to high relief convex-up channels, the latter being particularly common in the eastern part of the QF. In summary, the dataset presented in Chapter 4 shows that the post-orogenic relief of the QF is positively related to rock resistance.

In this chapter, I present cosmogenic  $^{10}\text{Be}$ -derived data measured in fluvial sediments that quantify denudation rates in 25 catchments in the QF; these basins were strategically selected on the base of the lithology (or lithologies) present and their topographical characteristics, aiming to capture basins that are representative of the spatially variable geomorphic contexts of the QF. The  $^{10}\text{Be}$ -derived denudation rates were used to quantify the relationships between denudation, topography, and the exposed lithology in the QF.

In section 5.2, I discuss how average rates of surface lowering can be estimated and the principles of cosmogenic isotope analysis. In section 5.3, I describe the strategy behind sample collection; finally, the cosmogenic derived results are presented and compared to potential controls in section 5.4, and discussed in section 5.5.

## 5.2 THEORETICAL BACKGROUND

### 5.2.1 ESTIMATING DENUDATION RATES

Landscapes evolve through time by the net effect of various geomorphic processes that weather and move materials downslope, in the direction of the base level, and their balance with tectonic drivers and feedback mechanisms (Willet and Brandon, 2002). The rate at which different surface processes operate is thus a central piece of information for understanding how the landscape evolves (Bishop, 2007). Estimating rates of net surface change is a complex task, given that the landscapes and landforms that existed before the change are not there anymore; yet it is an exercise necessary for tackling most questions of geomorphology, either for explaining the landforms that may be observed empirically, to conjecture about past geomorphic history, and also to predict future changes (Granger and Schaller, 2014).

There are various methods for quantifying average rates of landscape change. The first and perhaps most common method for estimating denudation rates (at least until the blossom of newer techniques) is the measurement of solid and dissolved sediment load from modern rivers. Its rationale is that all the sediment that passes through a cross-section of a modern river had its origin in an upstream reach of its drainage basin, and every material that is carried out of the drainage basin must pass through this specific cross-section (Ahnert, 1970). Hence, the measurement of stream loads generates a value of the total mass of exported material per unit of time. This quantity can, in turn, be divided by the density of bedrock to yield a volumetric equivalent that is further converted to an average value of surface lowering for the entire drainage basin, assuming non-significant sediment storage and uniform contribution from all parts of the basin (Ahnert, 1970; Summerfield, 1991).

This approach led to the understanding of the quantitative link between topography and denudation rates (e.g., Schumm, 1956, 1963; Ruxton and McDougall, 1967; Ahnert, 1970; Pinet and Souriau, 1988; Summerfield and Hulton, 1994) that still underpins the background knowledge of landscape evolution in erosive landscapes (cf. Wobus et al., 2006; Kirby and Whipple, 2012). However, there are many caveats to this approach (e.g., Summerfield, 1991; Granger and

Schaeller, 2014). For instance, stream-load data is likely to miss rare flood events that may be meaningful to the erosional history of the analysed basin (Kirchner et al., 2001); sediment load data may not be representative of the 'typical' geomorphic behavior of the analysed basin (e.g., due to seasonal or longer-term variations in sediment yields); and anthropogenic impacts on modern stream-data might complicate its interpretation as 'natural' rates of basin-wide surface lowering (e.g., Summerfield, 1991).

Alternative approaches for estimating denudation rates include (i) the quantification of a volume of datable sediment deposited in a lake or reservoir (e.g., Foster et al., 1985), or other datable deposits (e.g., alluvial fans); (ii) the use of geomorphic features that mark a former river bed or landform (e.g., a fluvial terrace) of a known age, and its current topographic position (e.g., Ruxton and McDougall, 1967; Bishop et al., 1985); and (iii) inferring the long-term cooling path of a rock through the crust as a result of denudation, by means of thermochronology (Gallagher et al., 1998; Reiners and Shuster, 2009). Each of these methods provides estimates of denudation rates over different timescales. For example, stream load data yield estimates of denudation rates over short timescales ( $\sim 10^1$  years), contrasting with the very long timescales of thermochronology ( $\sim 10^5$ - $10^8$  years). These approaches are clearly used to answer different geomorphic questions.

In the last 25 years or so, the application of cosmogenic nuclides (Dunai, 2010; Dunai and Lifton, 2014) has revolutionised the study of long-term landscape evolution (Dunai, 2010; Bishop, 2007). The analysis of cosmogenic isotopes relies on the quantification of the concentration of cosmogenic nuclides in surface materials to derive estimates of denudation rates over millennial timescales ( $\sim 10^3$ - $10^5$  yr). The rationale of the technique is that cosmogenic nuclides are only produced in surface materials (and atmospheric gases) when they are exposed to cosmogenic radiation (Dunai, 2010; von Blackenburg and Willenbring, 2014). Hence, as the production rate of cosmogenic nuclides in target minerals can be empirically estimated (e.g., Nishiizumi et al., 1989; Lal, 1991; Balco et al., 2008; Dunai and Lifton, 2014), the concentration of nuclides in surface materials may be used to provide rates of denudation, or, in specific conditions, surface exposure ages. This contribution applied the analysis of cosmogenic nuclides to estimate

denudation rates for the QF. This method was chosen because (i) this technique is currently “the ‘gold standard’ for determining erosion rates of rocks and watersheds” (Granger and Schaller, 2014, p. 373), having been applied worldwide in thousands of basins with different tectonic and climatic environments (e.g., Portenga and Bierman, 2011; Harel et al., 2016); (ii) the QF has a wide distribution of quartz-rich lithologies (the target mineral of the cosmogenic nuclide used in this contribution,  $^{10}\text{Be}$ ); and (iii) a substantial body of empirical geomorphic work has reported a non-linear positive relationship between channel steepness and  $^{10}\text{Be}$ -derived catchment-averaged denudation rates (cf. Wobus, 2006; Kirby and Whipple, 2012), suggesting that channel steepness may be a good approximation of catchment-averaged rates of denudation.

### **5.2.2 PRINCIPLES OF THE ANALYSIS OF COSMOGENIC ISOTOPES**

Cosmogenic nuclides are a by-product of the interaction of high-energy charged particles, termed cosmic rays, with target atomic nuclei (protons and neutrons) of various atoms in the Earth’s atmosphere and surface (Dunai, 2010; Dunai and Lifton, 2014). These high-energy cosmic rays interact with atmospheric gases and surface materials, producing nuclides that are either stable (e.g.,  $^3\text{He}$  and  $^{21}\text{Ne}$ ) or radioactive (e.g.,  $^{10}\text{Be}$ ,  $^{14}\text{C}$ ,  $^{26}\text{Al}$  and  $^{36}\text{Cl}$ ). Cosmogenic nuclides produced in surface materials are termed in situ or terrestrial nuclides, as opposed to ‘meteoric’ nuclides, which are produced in the Earth’s atmosphere. Atmospheric cosmogenic nuclides are produced in larger quantities compared to those produced at the Earth’s surface. For instance, the meteoric flux of  $^{10}\text{Be}$  is ~1 million atoms per  $\text{cm}^2/\text{yr}$ , contrasting with its in situ production of ~4-5 atoms per gram of mineral per year (von Blanckenburg and Willenbring, 2014).

The production of cosmogenic nuclides is controlled by the isotropic flux of cosmic rays derived primarily from supernova explosions from outside our solar system (Diehl et al., 2006) and with a minor contribution from dynamic events on the Sun (Masarik and Reedy, 1995). This cosmic ray flux has been striking Earth from every angle at a nearly constant rate, at least over the last 10 Myr (Eidelman et al., 2004; Diehl et al., 2006; Dunai, 2010). As cosmic rays are high-energy charged particles, they are affected by the magnetic field of Earth that deflects the rays, and decreases their velocity, in effect, shielding the Earth that otherwise would

not be habitable (Dunai, 2010). For instance, at a given location on Earth, cosmic ray particles with kinetic energy below a certain threshold cannot breach the geomagnetic field, and this threshold is termed the cutoff rigidity  $R_c$ . Around the Earth's magnetic poles,  $R_c$  values are  $\sim 0$  and thus nearly all cosmic rays can penetrate the geomagnetic field (Dunai and Lifton, 2014). By contrast,  $R_c$  values are at their maximum near the Equator, which implies that, at low latitudes, a significant portion of the flux of cosmic rays is blocked by the geomagnetic field (Dunai and Lifton, 2014).

The cosmic rays collide with target atoms in the atmosphere, stripping them of protons and neutrons; the results of these interactions are atoms with a lower mass number than they had before the collision (Dunai and Lifton, 2014). This process is referred to as 'spallation'; the atomic particles 'ejected' by each spallation event can, in turn, induce spallation in other atoms, creating a cascade reaction (Dunai, 2010). Spallation can also occur at the Earth's surface, up to a few meters below, depending on the density of the material that the particles need to pass through (Dunai and Lifton, 2014). Spallation reactions are the most frequent nuclear reactions contributing to cosmogenic nuclides production; yet there are other nuclear reactions that may produce cosmogenic nuclides, such as neutron capture and muon reactions (Dunai and Lifton, 2014).

Every interaction between cosmic rays and target nuclei needs energy, and thus the cosmic flux decreases as it penetrates the atmosphere, losing its ability to produce cosmogenic-induced nuclides (Dunai, 2010). Hence, there is a maximum amount ( $N_0$ ) of cosmic ray-induced nuclides at the top of the atmosphere, and its quantity decreases exponentially toward the Earth's surface, with increasing atmospheric depth (Equation 18; Dunai, 2010):

$$N(d) = N_0(atm)e^{-d/\Lambda} \quad (18)$$

with 'd' as the atmospheric depth ( $\text{g}/\text{cm}^2$ ),  $N_0(atm)$  is the maximum number of nucleons at the top of the atmosphere, and  $\Lambda$  is the attenuation length ( $\text{g}/\text{cm}^2$ ). The attenuation length is not constant, varying as a function of the deflection of the geomagnetic field and the altitude (Lal 1991; Desilets and Zreda, 2003; Dunai

and Lifton, 2014); maximum production is therefore near the poles at the highest elevation. In addition, the collision of primary cosmic ray flux with targets in the atmosphere, besides resulting in ‘meteoric’ nuclides and secondary particles dominated by neutrons, also produces elemental particles (pions) that decay very fast into charged (positively or negatively) muons (Dunai and Lifton, 2014). Muons interact only weakly with matter and they have higher penetration depth than the neutrons and protons produced during spallation (Dunai, 2010). Because of their high penetration depth, muons are important contributors to the subsurface production of in situ cosmogenic nuclides (Dunai, 2010; Dunai and Lifton, 2014).

At the surface, the decline in cosmic ray secondary flux (as a result of its interactions with surface materials) is similar to the attenuation described for the atmosphere, but given that the surface materials (water or rocks) have a much higher density than air, the attenuation length is much shorter. The variation of nucleon flux at or below the surface of the Earth is described by Equation 19 (Dunne et al. 1999; Dunai, 2010):

$$N(z) = N_0 e^{-z_d \rho / \Lambda_s} \quad (19)$$

where  $z_d$  is depth below the surface,  $N_0$  is the flux at the surface,  $\rho$  is the density of rock, and  $\Lambda_s$  is the attenuation length for Earth surface materials. The attenuation length  $\Lambda_s$  can be conceptualized as the distance below the surface over which the cosmic-ray flux decreases by a factor of  $1/e$  (or ~63%), and it is specific to the density of material ( $\rho$ ) and the energy of the cosmic ray flux considered (Gosse and Phillips, 2001; Dunai, 2010). The value of  $\Lambda_s$  for high-energy neutrons at the surface of Earth typically ranges between 150-190 g/cm<sup>2</sup> (e.g., Gosse and Phillips 2001; Dunai, 2010). By contrast, the typical value of  $\Lambda_s$  for negative muons ranges between 800-1500 g/cm<sup>2</sup> (Gosse and Phillips, 2001; Dunai, 2010), and  $\Lambda_s$  for fast muons reaches a value of ~5300 g/cm<sup>2</sup> (Braucher, 2003). For a rock with density of 2.65 g/cm<sup>3</sup>, the attenuation path length for the high-energy neutron flux is ~57-68 cm; the denser the rock, the shorter the penetration depth. Below the depth of about five attenuation path lengths (~2.5-3 m for most rocks), less than one percent of the initial high-energy neutron flux that hit the surface

remains, and thus the production of in situ cosmogenic nuclides is nearly negligible below this point and is dominated by muon reactions (Dunai, 2010).

In summary, the production of cosmogenic nuclides is a function of the energy spectrum of cosmic ray particles striking the Earth and the probability of these highly energetic particles to collide with a target in the atmosphere and at the Earth's surface (Reedy, 2013; Dunai and Lifton, 2014). The energy spectrum is a function of (i) the geomagnetic field, whereby the energy is highest at the poles and lowest at the equator; and (ii) altitude, with the highest energy at the top of the atmosphere, and decreasing toward the surface of the Earth (Dunai, 2010). Also, any solid mass that blocks or attenuates the cosmic ray flux ('shielding effect') will affect the production of cosmogenic nuclides (Dunai, 2010). This shielding effect has to be accounted for when collecting the samples and all the topographic elements that may have obstructed the cosmic rays need to be considered (Balco et al., 2008). The standard procedure to account for shielding is the calculation of a single 'shielding factor' that corrects all topographic effects in the production of cosmogenic nuclides (Balco et al., 2008). This 'shielding factor' is based on the difference between the cosmic ray flux of a standardised horizontal surface (without obstructions) and the cosmic ray flux of the surface considered that has topographic obstructions (Codilean, 2006; Balco et al., 2008). Older methods for accounting for topographic shielding relied on the compartmentation of the horizon measured from the sampling site into arc segments, for which the average 'height of obstruction' was measured as zenith angles (Codilean, 2006). By contrast, recent techniques use DEMs for quantifying pixel-by-pixel 'topographic obstruction' by means of hillshade modelling (e.g., Codilean, 2006; Mudd et al., 2016), thus enabling the assessment of more precise topographic shielding. Hence, production rates of in situ cosmogenic nuclides vary spatially as a function of elevation, latitude, and shielding, and these variations must be accounted when deriving exposure ages or erosion rates (e.g., Lal, 1991; Stone, 2000; Desilets and Zreda, 2003; Balco et al., 2008; Dunai, 2010; Dunai and Lifton, 2014). The geomagnetic field also varies over time, and several scaling schemes account for time-dependent changes in the production of cosmogenic nuclides (e.g., Dunai, 2001; Desilets and Zreda, 2003; Lifton et al., 2014).

This contribution has derived catchment-averaged denudation rates from measurements of the concentration of in situ  $^{10}\text{Be}$  in alluvial sediment. The  $^{10}\text{Be}$  is the in situ cosmogenic nuclide most often used in geomorphic research (Granger et al., 2013), due to different reasons, including the abundance of its target mineral (quartz); the well-constrained production rate of  $^{10}\text{Be}$  when compared to other cosmogenic nuclides (Granger et al., 2013); the existence of a standardized procedure for sample preparation (Kohl and Nishiizumi, 1992; Granger et al., 2013); and the good precision in  $^{10}\text{Be}$  AMS (Accelerator Mass Spectrometry) analysis (Granger et al., 2013; von Blanckenburg, 2005). In the following section, the rationale for how to obtain denudation rates from measurements of in situ cosmogenic nuclide inventories is outlined.

### 5.2.3 DENUDATION RATES FROM IN SITU COSMOGENIC ISOTOPES

A geomorphic surface exposed continuously to cosmic rays will accumulate cosmogenic nuclides; their concentration in the rock, combined with the production rate, will provide the exposure time  $t$ , i.e., for how long the rock has been exposed at the surface of the Earth. When erosion is zero, the total cosmogenic nuclide concentration ( $C_{total}$ ) at any depth below the surface ( $z_d$ ) and for any time  $t$  can be described by Equation 20 (Lal, 1991; Dunai, 2010):

$$C_{total}(t, z_d) = C_{inh}(z_d)e^{-t\lambda} + \sum_i \frac{P_i(z_d)}{\lambda}(1 - e^{-t\lambda}) \quad (20)$$

where  $C_{inh}$  represent all inherited cosmogenic nuclides from previous exposures or non-cosmogenic production,  $\lambda$  denotes the decay constant for radioactive nuclides,  $P$  is the production rate, and  $i$  designates the various types of nuclear reactions that may produce cosmogenic nuclides (e.g., spallation, neutron capture, muon reactions; Dunai, 2010). The decay constant is the probability that a nucleus will decay in one second, and thus each radioactive cosmogenic nuclide is associated with a unique  $\lambda$  that can be related to the radionuclide half-life ( $T_{1/2}$ ; Table 6) by Equation 21:

$$T_{1/2} = \frac{\ln 2}{\lambda} \quad (21)$$

**Table 6.** Information on commonly used cosmogenic nuclides at sea level and high latitude.  $^{10}\text{Be}$  is highlighted in blue.

Nuclide	Half-life ( $T_{1/2}$ )	Target mineral used	Production rate
$^3\text{He}$	stable	Olivine, pyroxene	75-120 atoms $\text{g}^{-1}\text{y}^{-1}$
$^{21}\text{Ne}$	stable	Quartz, olivine, pyroxene	18-21 atoms $\text{g}^{-1}\text{y}^{-1}$
$^{10}\text{Be}$	1.4 Myr	Quartz	4-5 atoms $\text{g}^{-1}\text{y}^{-1}$
$^{14}\text{C}$	5720 yr	Quartz	18-20 atoms $\text{g}^{-1}\text{y}^{-1}$
$^{26}\text{Al}$	0.7 Myr	Quartz	35 atoms $\text{g}^{-1}\text{y}^{-1}$
$^{36}\text{Cl}$	0.3 Myr	K-feldspar, calcite	70 atoms $\text{g}^{-1}\text{y}^{-1}$ (Ca) 200 atoms $\text{g}^{-1}\text{y}^{-1}$ (K)

Data source: von Blanckenburg and Willenbring, 2014.

The production rate ( $P$ ) decays exponentially with depth below the surface following Equation 22:

$$P_i(z) = P_{i_0} e^{-z\rho/\Lambda_s} \quad (22)$$

Considering a short exposure history, where the exposure time  $t$  is considerably shorter than the half-life of the radioactive cosmogenic nuclide used (or in the case of stable nuclides), the Equation 20 can be reduced to the Equation 23 (Dunai, 2010):

$$C_{total}(t, z_d) = C_{inh}(z_d) + \sum_i P_i(z_d)t \quad (23)$$

Hence, if the presence of cosmogenic nuclides from previous exposure or non-cosmogenic production is excluded ( $C_{inh} = 0$ ), then the cosmogenic nuclide concentration ( $C_{cos}$ ) can be used to quantify an exposure age  $T_{exp}$  for the surface material analysed (Equation 24; Lal, 1991; Dunai, 2010):

$$T_{exp} = -\frac{1}{\lambda} \ln \left( 1 - \frac{C_{total}(z_d, T_{exp})\lambda}{\sum_i P_i(z_d)e^{-z_d\rho/\Lambda_s}} \right) \quad (24)$$

For a surface sample (i.e., where  $z_d = 0$ ), Equation 24 can be further simplified into Equation 25:

$$T_{exp} = \frac{C_{cos}(0, T_{exp})}{\sum_i P_i(0)} \quad (25)$$

Equations (20,22-25) neglect the possible effects of erosion on the concentration of the cosmogenic nuclide inventories (Dunai, 2010). Concentrations of cosmogenic nuclides in an eroding surface reflect the amount of time the sample has spent being brought toward the surface through the nuclide production zone. Equation (25) assumes the sample has been at the surface the entire time, which implies that  $T_{exp}$  quantified for an eroding surface will result in the minimum time the sample has spent in the production zone, rather than an ‘age’ (Dunai, 2010).

The accumulation of cosmogenic nuclides for surfaces that are eroding through time may be described by Equation 26 (Lal, 1991; Niedermann, 2002; Dunai, 2010), assuming a constant erosion rate ( $\varepsilon$ ) and a surface depth ( $z_0$ ) from which cosmic rays start to produce cosmogenic nuclides:

$$C_{total}(t, z_d) = C_{inh}(z_d)e^{-t\lambda} + \sum_i \frac{P_i(z_d)}{\lambda + \rho\varepsilon/\Lambda_{s,i}} e^{-\rho(z_0 - \varepsilon t)} (1 - e^{-(\lambda + \frac{\rho\varepsilon}{\Lambda_{s,i}})t}) \quad (26)$$

For the case of a constant erosion rate ‘ $\varepsilon$ ’ through a period of time that is much larger than  $T_{exp}$  (i.e.,  $T_{exp} \gg 1/(\lambda + \rho\varepsilon/\Lambda_{s,i})$ ), the concentration of cosmogenic

nuclides is not dependent on time, but is instead a function of the erosion rate (Lal, 1991; Dunai, 2010). This implies that, assuming a steady-state condition (Lal, 1991), surface materials in transit from a position  $z_0$  to the surface ( $z_d = 0$ ) will contain a concentration of cosmogenic nuclides directly proportional to the time needed for the rock to transit from  $z_0$  to  $z_d$ , which is a function of  $\varepsilon$  (Dunai, 2010). Assuming a negligible inheritance of cosmogenic nuclides from previous exposure or non-cosmogenic production (i.e.,  $C_{inh} = 0$ ), the concentration of cosmogenic nuclides for surface samples subjected to a constant erosion rate  $\varepsilon$  is given by Equations 27 and 28 for radioactive and stable nuclides, respectively (Dunai, 2010):

$$C(z_d) = \sum_i \frac{P_i(z_d)}{\lambda + \rho\varepsilon/\Lambda_{s,i}} \quad (27)$$

$$C(z_d) = \sum_i \frac{P_i(z_d)}{\rho\varepsilon/\Lambda_{s,i}} \quad (28)$$

Considering cases where the constant erosion rate  $\varepsilon$  is so slow that muon-produced cosmogenic nuclides decay before reaching the surface, Equation 27 can be further simplified into Equation 29, representing the spallogenic-produced cosmogenic nuclide concentration (Dunai, 2010):

$$C(0) = \frac{P(0)}{\lambda + \rho\varepsilon/\Lambda_{s,i}} \quad (29)$$

Equation 29 can be rearranged to solve for  $\varepsilon$  (Equation 30):

$$\varepsilon = \left( \frac{P(0)}{C(0)} - \lambda \right) \frac{\Lambda_{s,i}}{\rho} \quad (30)$$

Equation (30) shows that it is possible to quantify the steady-state erosion rate  $\varepsilon$  by measuring the concentration of a cosmogenic nuclide in a surface sample, if  $P$ ,  $\rho$  and  $\Lambda_{s,i}$  are known (Dunai, 2010). The material that used to cover the present surface may have been removed via erosion or dissolution; for this reason, cosmogenic isotope inventories provides denudation and not erosion (*sensu strictu*) rates (von Blackenburg, 2005; Dunai, 2010; Granger and Schaller, 2014).

Since the mid-1990s there has been an attempt to upscale this method to the drainage basin (cf. Bierman and Nichols, 2004; Granger et al., 1996; Granger and Riebe, 2013; Granger and Schaller, 2014). This new approach means that, as long as the assumptions listed in Table 7 are fulfilled, the concentration of a cosmogenic isotope in alluvial sediment collected in an active channel may be used to quantify catchment-averaged erosion rates (von Blanckenburg, 2005; Granger and Schaller, 2014). This approach basically assumes that Equation (30) can be applied to a catchment as a whole and that the resulting concentrations are integrated down the fluvial network (von Blanckenburg, 2005; Granger and Schaller, 2014).

When using the catchment-averaged approach, the analysed alluvial sediment is assumed to be an assemblage of grains that were sourced from all areas upstream of the sample location. Hence, intra-basin differences in denudation rates are effectively averaged within the cosmogenic nuclide concentration of the sediment sample (von Blanckenburg, 2005; Granger and Schaller, 2014; von Blanckenburg and Willenbring, 2014). For example, if two areas of the upstream catchment are associated with different denudation rates, the concentration of nuclides in the alluvial sediment downstream of these areas will reflect the spatially-averaged denudation rate of the two areas (von Blanckenburg, 2005; Granger and Schaller, 2014; von Blanckenburg and Willenbring, 2014); the area with faster denudation rates will provide a larger amount of sediment with low concentrations of cosmogenic nuclides, whereas the areas with slower denudation rates will provide a lesser quantity of sediment with higher concentrations. The timescale of denudation recorded by this approach is similar to that described for the steady-state erosion in Equation 27, whereby the production rates are integrated over the time required for a surface material to transit from  $z_0$  to the surface  $z_d$ . This results in a long-term average denudation rate capable of integrating large and infrequent erosional events (Kirchner et al., 2001) that is, at the same time, relatively insensitive to 'recent' changes (e.g., due to anthropogenic activities; von Blanckenburg, 2005; Granger and Schaller, 2014).

**Table 7.** Assumptions for the use of in situ cosmogenic nuclides for catchments.

<b>Assumptions</b>	
1	Denudation is constant over transit time from $z_0$ to the surface
2	All lithologies contribute to the target sediment load consistently to their denudation rates
3	Target mineral have the same grain size for all lithologies
4	The denudational timescale is smaller than the nuclide half-life ( $T_{1/2}$ )
5	Sediment storage is minimal compared to the denudation timescale

Data source: Dunai, 2010.

The assumptions listed in Table 7 imply that some basins would not be suited for this analysis, for they may violate some of these assumptions (Dunai, 2010). For instance, assumption (1) may be difficult to meet for tectonically active settings, whereby landslides are frequent and important to the denudational dynamics of many basins (Niemi et al. 2005, Puchol et al., 2014). However, the sampling strategy may account for these possible violations, and thus, it is possible to sample larger catchments for attenuating landslide bias in cosmogenic inventories (e.g., Niemi et al. 2005, von Blanckenburg, 2005; Puchol et al., 2014). For the case where sediment storage is not minimal, and where the denudation rate is so low that it is comparable to the cosmogenic isotope half-life ( $T_{1/2}$ ), radioactive decay may be meaningful during the denudation timescale (transit time from ‘ $z_0$ ’ to the surface ‘ $z_d$ ’) and sediment samples may not reflect the ‘current’ denudational regime as the averaging timescale becomes very long (Dunai, 2010; von Blanckenburg, 2005). For instance, the cosmogenic nuclide  $^{10}\text{Be}$  should be compatible with the basin-wide approach for basins associated with denudation rates faster than 0.3 m/Myr (von Blanckenburg, 2005; Dunai, 2010). Assumption (2) can be easily fulfilled by sampling sub-catchments with the same lithology. However, such sampling may not be possible for complex geological settings, and it may not address the geomorphic questions essential for such a complex configuration (e.g., Bierman et al., 2005). Also, if the target mineral sampled does not have the same grain size the results may be biased (Brown et al. 1995, von Blanckenburg 2005; Dunai, 2010), so the standard approach is to sample the same grain size unless other questions regarding different grain size inventories are being asked. In summary, some violation of certain assumptions is often inevitable (von Blanckenburg, 2005). However, “the accuracy of the method is usually

sufficient for many of the potential applications and would anyway yield a more robust estimate than many other estimates of denudation” (von Blanckenburg, 2005, p. 229).

## **5.3 METHODS AND DATA**

### **5.3.1 OVERVIEW**

The research design is detailed in Figure 46. The sampling strategy was based on the results of the quantitative topographic analysis detailed in Chapter 4. The sampling strategy is described in detailed in section 5.3.2. Samples collected from active channel beds were then prepared and  $^{10}\text{Be}$  extracted following procedures detailed in section 5.3.5.  $^{10}\text{Be}$  concentrations were determined using the accelerator mass spectrometer (AMS) at the Scottish Universities Environmental Research Centre (SUERC) facility in Glasgow, UK. The ‘raw’ AMS results were further reduced (Balco et al., 2008) and used to calculate millennial-scale catchment-averaged denudation rates for the QF. For every basin sampled for detrital  $^{10}\text{Be}$  analysis, catchment-averaged parameters were quantified from a TanDEM-X 12 m resolution DEM. The resulting  $^{10}\text{Be}$ -derived catchment-averaged denudation rates were then utilised to decipher the long-term evolution of the landscape and the factor(s) that control it.

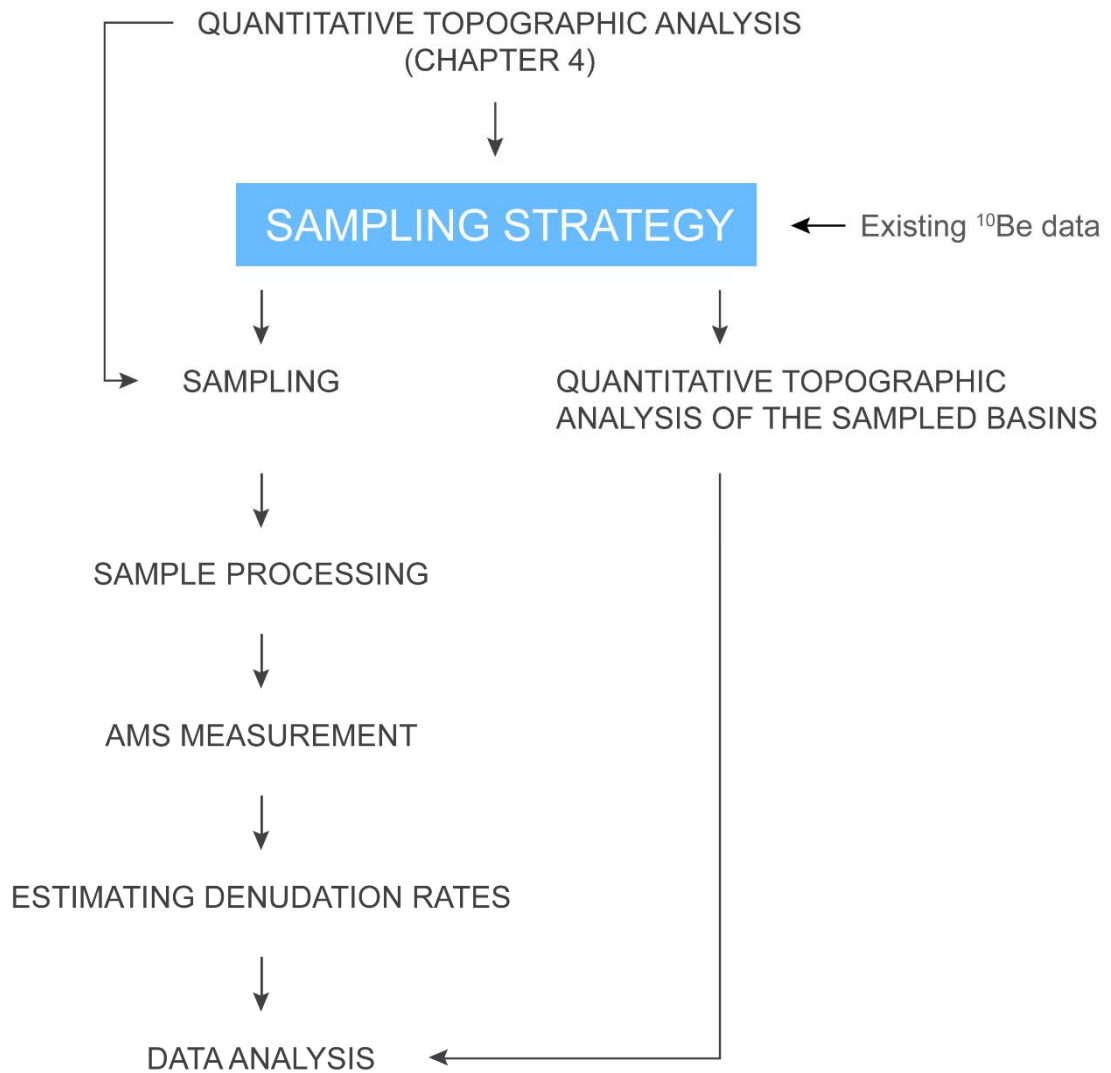


**Figure 46.** The workflow of the methodological steps of the research.

### 5.3.2 SAMPLING STRATEGY

The decision of which basins to sample was guided by the analysis of the topography of the QF, presented in Chapters 3 and 4. The sampling design includes drainage basins displaying different topographic characteristics, ranging from subdued to pronounced topography, and different exposed bedrock resistance, from the resistant quartzites to the weak, gneisses and granitic rocks.

The sampled basins are divided into three groups: (i) low-steepness basins under low-resistance lithologies; (ii) high-steepness basins under resistant lithologies; (iii) intermediate-steepness basins under schists, mixed lithologies, and resistant lithologies. Basins associated with group (iii) display a larger variability in topographic characteristics than groups (i) and (ii). These groups can be identified

in the scatter plot shown in Figure 47. Whereas the choice of boundaries between the groups represented in Figure 47 may be arbitrary to some extent, the extreme range of values in topographic parameters, as well as the variability in basin lithology, indicate that the sampling design included basins with varying geomorphic characteristics, which is fundamental to quantify the pattern of denudation in the QF.

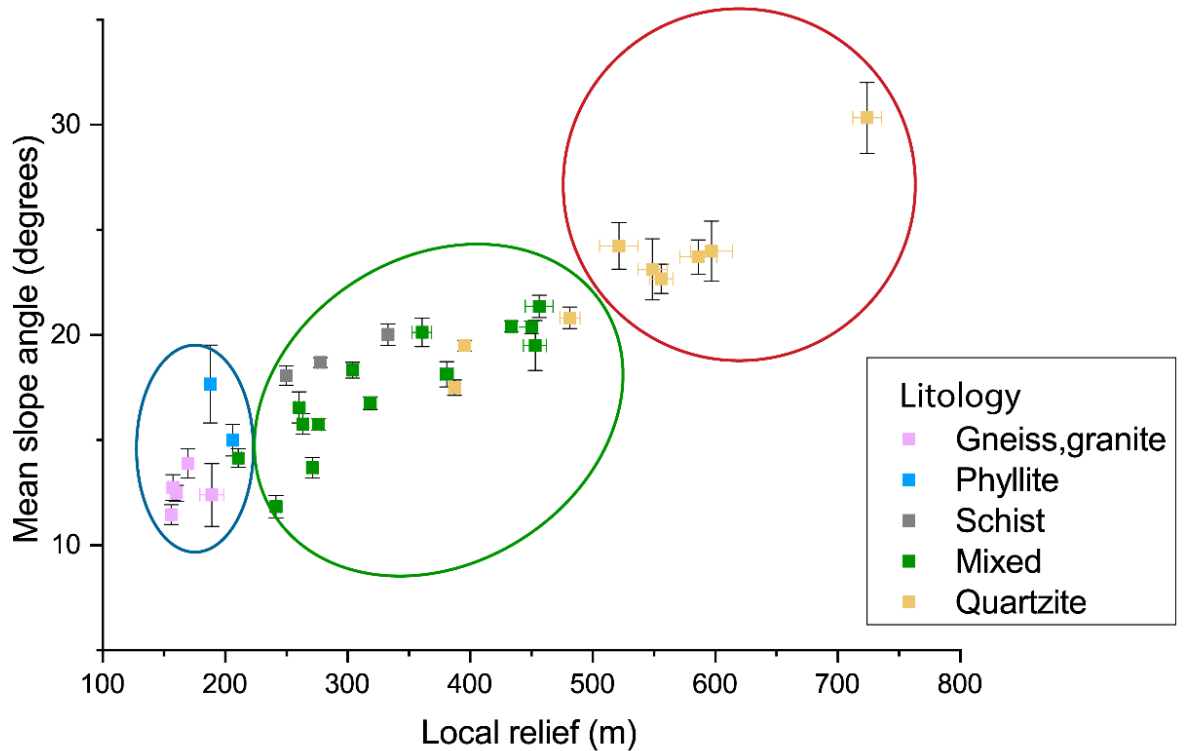


**Figure 47.** Scatter plot of catchment-averaged local relief and mean slope angle for the analysed basins. (i) 'Low-steepness' basins are highlighted by the blue circle; (ii) 'high-steepness' basins are highlighted in red; (iii) 'intermediate-steepness' basins are highlighted in green. Error bars represent the standard deviation of the mean of each parameter.

The published detrital  $^{10}\text{Be}$  data for the QF have been interpreted as indicating that denudation is primarily controlled by the different strength of the exposed lithologies (Salgado et al., 2007a, 2007b, 2008). Basins underlain by resistant rocks display low denudation rates ( $\sim 0.3$  to  $2$  m/Myr); basins underlain by the intermediate-resistance schists and phyllites are associated with intermediate denudation rates ( $\sim 8$  to  $12$  m/Myr); and the basins underlain by the low-resistance the 'granite-gneisses are associated with higher denudation rates ( $\sim 13$  m/Myr). The location of the basins sampled by Salgado and colleagues (Salgado et al., 2007a, 2007b, 2008) is shown in Figure 48. These data suggest a correlation between denudation rates and rock type (Salgado et al., 2007a, 2007b, 2008), but their spatial location and paucity do not permit to quantitatively define and assess

how denudation rates, geomorphic parameters, and lithological resistance are related. Nonetheless,

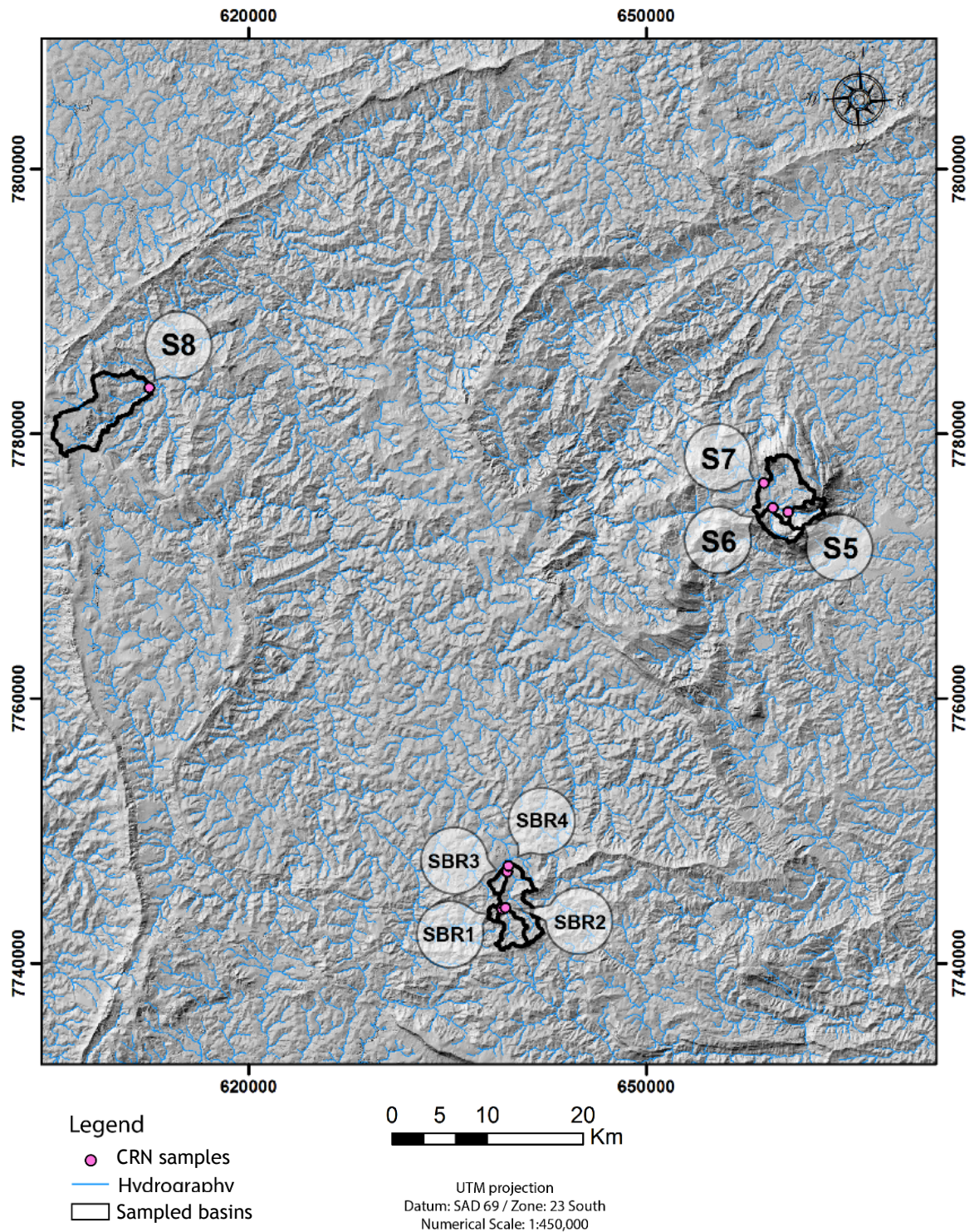


**Figure 48.** The spatial distribution of the basins sampled by Salgado and colleagues (Salgado et al., 2007a, 2007b, 2008).

The basins sampled for this study are shown in Figures 49-50. The denudation rates for the basins analysed by Salgado et al. (2007a, 2007b, 2008) have been incorporated in this project, but their denudation rates were recalculated using

the same method as for the basins sampled in this contribution, that is, using a pixel-by-pixel production rate and shielding factors obtained by the application of the CAIRN method (Mudd et al., 2016). The manner in which this study estimated denudation rates from detrital  $^{10}\text{Be}$  concentrations is discussed in section 5.3.6.

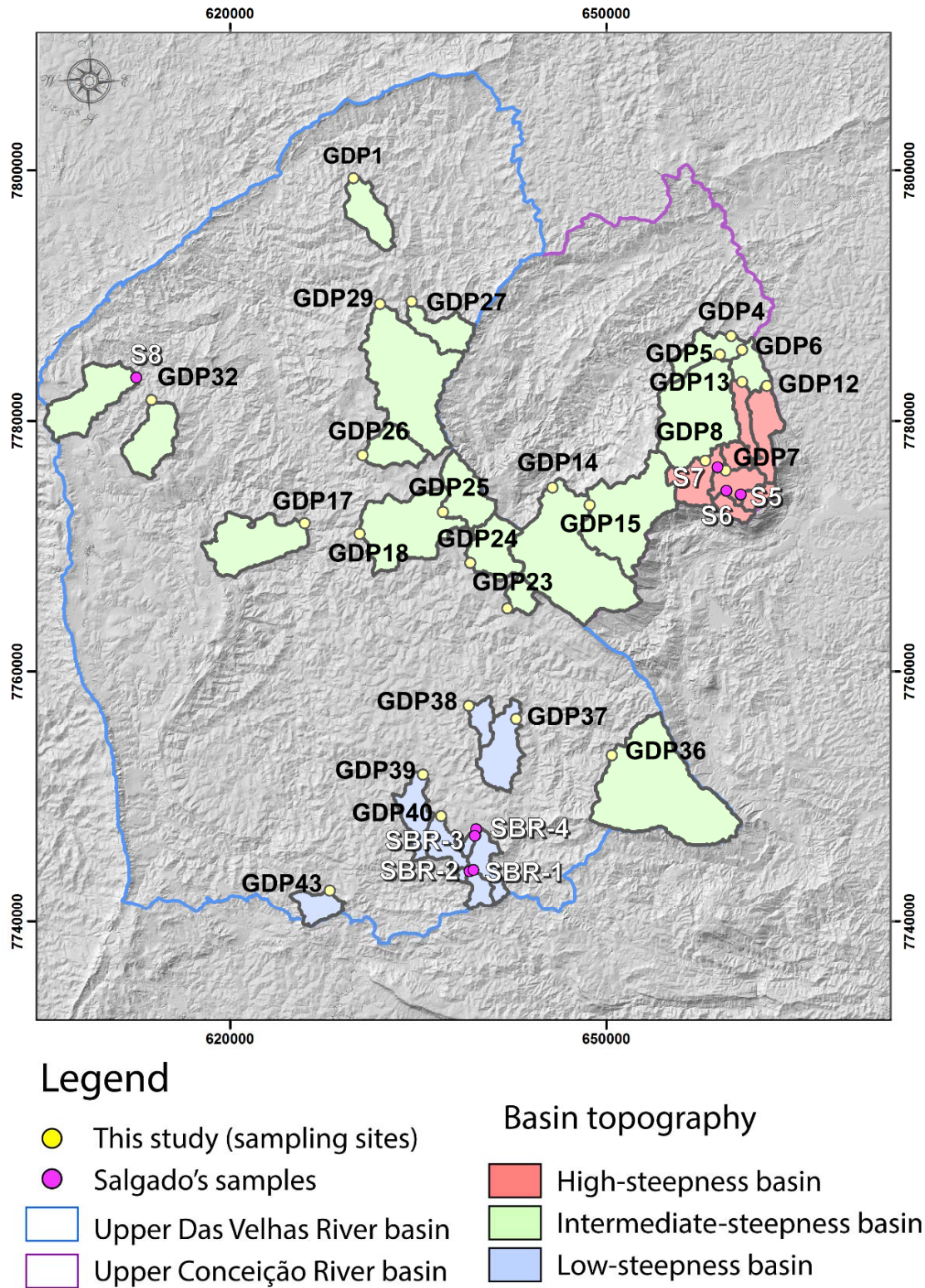
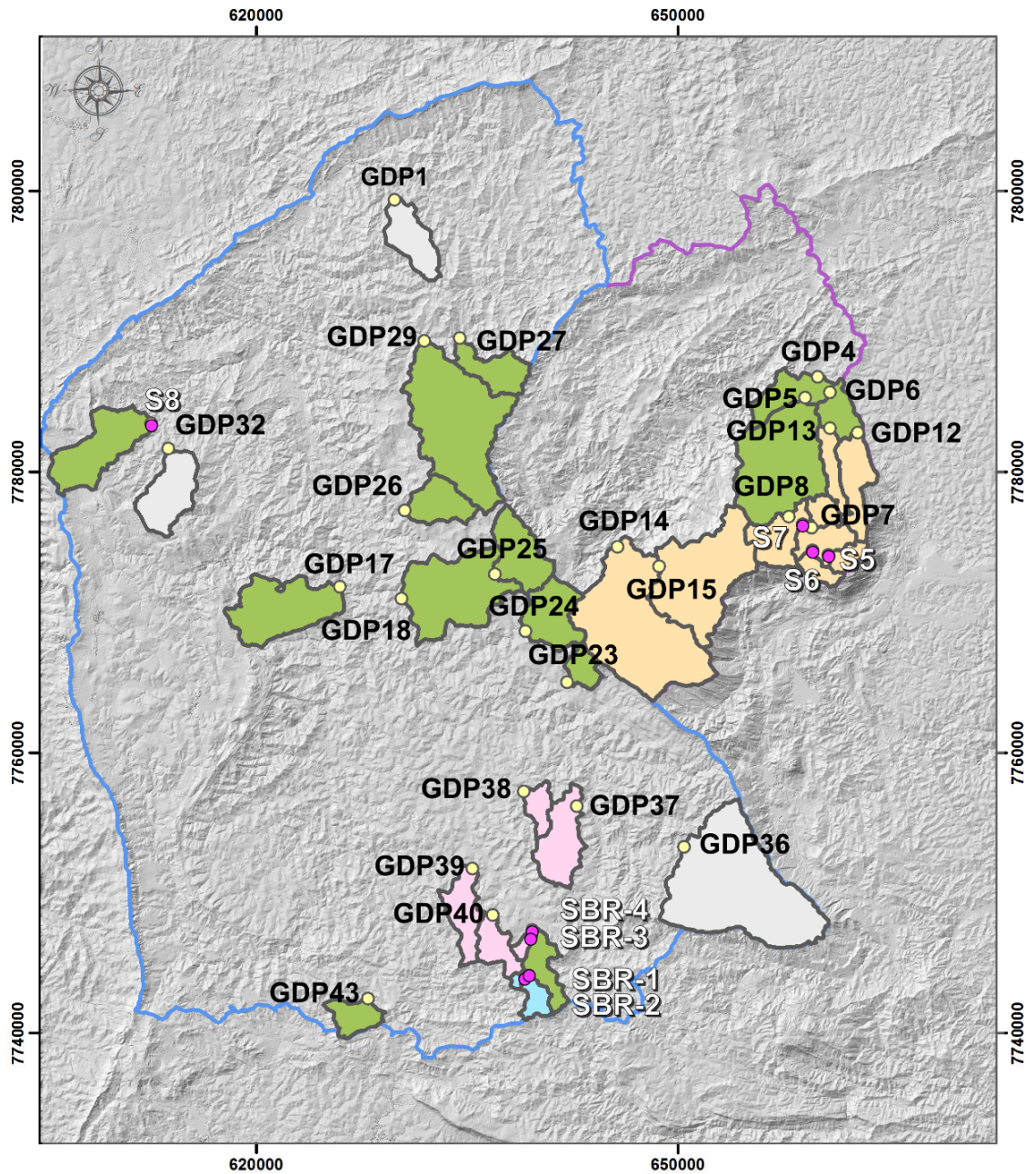


**Figure 49.** The topographic characteristics of the 25 basins analysed in this study (GDP\_') and the eight sampled by Salgado et al. ('S'; Salgado et al., 2007a, 2007b, 2008). Basins were classified according to the topographic cluster classification of Chapter 4.



**Legend**

- This study (sampling sites)
- Salgado's samples
- Upper Das Velhas River basin
- Upper Conceição River basin

Numerical scale: 1:400,000

**Basin lithology**

- Gneisses, granites
- Phyllites
- Schists
- Mixed lithology
- Quartzites

**Figure 50.** The main lithology of the 25 basins analysed in this study (GDP\_') and the eight sampled by Salgado et al. ('S'; Salgado et al., 2007a, 2007b, 2008).

The eastern part of the Caraça Range (including basins GDP4, GDP5, GDP6, GDP7, GDP8, GDP12, GDP13; S5, S6, S7) has the most pronounced relief of the QF. Rivers flowing away this portion of the Caraça Range have their upstream sections on quartzites, transitioning downstream to schists. These rivers typically display extremely high elevation drops (~1.2 km), many convexities in their longitudinal profiles (Figure 51) associated with locally negative  $\theta$  values. Also, this is the area in the QF where knickpoints are most numerous and most extreme, showing the highest values of magnitude, relief, and elevation. The eastern part of the Caraça Range is also the region considered as the most affected by Cenozoic deformation in the QF (e.g., Saadi, 1991; Maizatto and Castro, 1993; Maizatto, 1997; Sant'anna et al., 1997), and it has recently experienced low magnitude earthquakes (Figure 8). The research has been designed to concentrate samples in this area to constrain (i) the denudational rates of quartzite basins nested upstream into the mountains, characterised by different channel and hillslope steepness (e.g., basins GDP12, GDP13, GDP7, S5 are extremely steep, whereas basins GDP8 and S7 are less steep); (ii) the effect of the additional areal contribution of schists on the denudation rates of the mixed lithology basins (Figures 52-53); and (iii) the effect of the low magnitude earthquakes reported for this region (Figure 8) on denudation rates. Basin GDP8 is the same as S7 of Salgado et al. (2008): its denudation rate tests the consistency between this study and the previous estimates (Salgado et al., 2007a, 2007b, 2008). Basins GDP5 and GDP4 are analysed to investigate the effect of mixing of sediments on the determination of catchment-averaged denudation rate.

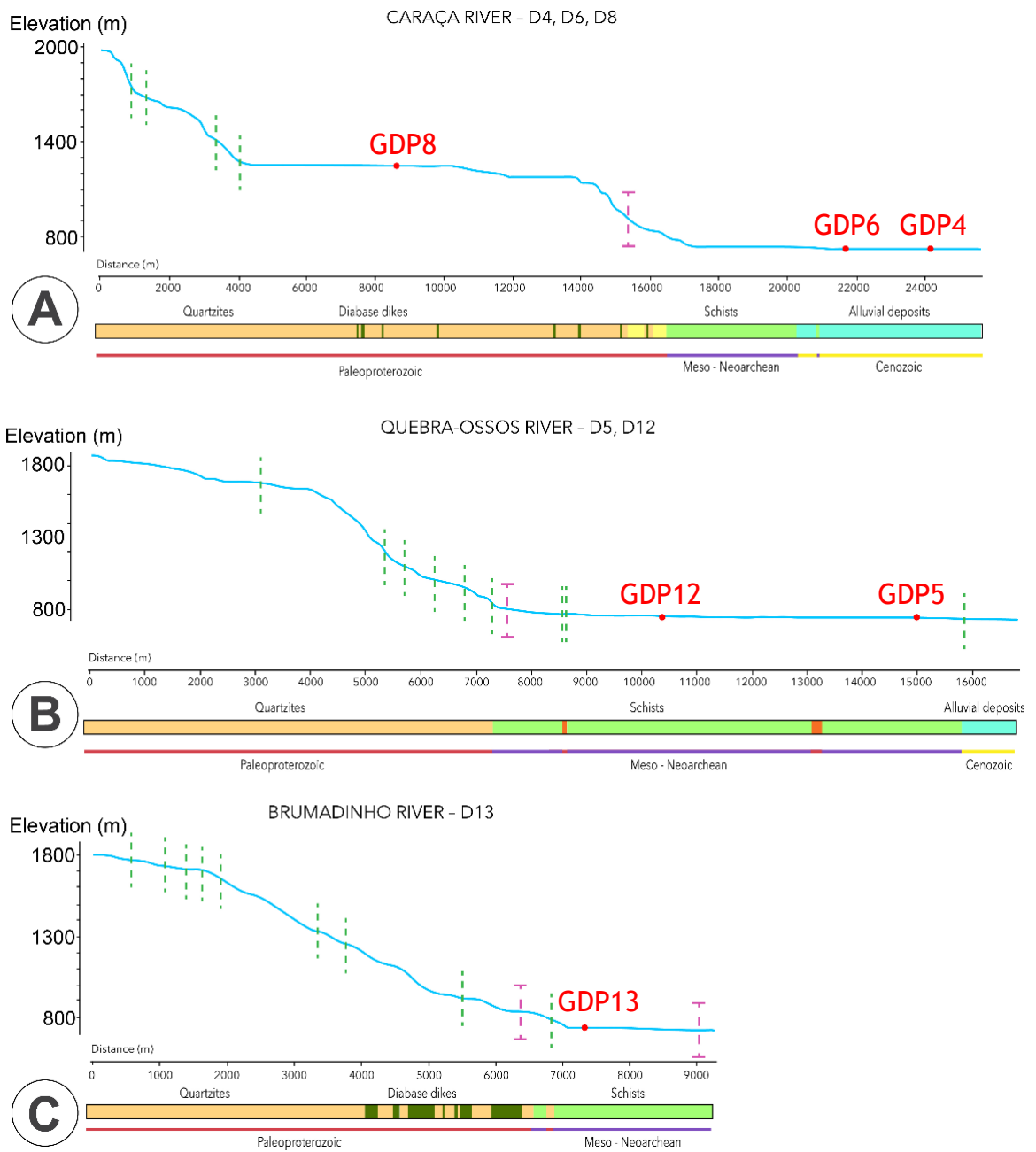


**Figure 51.** Examples of longitudinal profiles of rivers flowing away from the eastern part of the Caraça Range. Red points represent sampling sites. Dashed lines represent ancient faults crossing the rivers; pink dashed lines denote well-studied faults (i.e., faults with names). Every river flowing away from the eastern part of the Caraça Range is associated with high elevation drops (> 1 km) and convex-up channel forms.

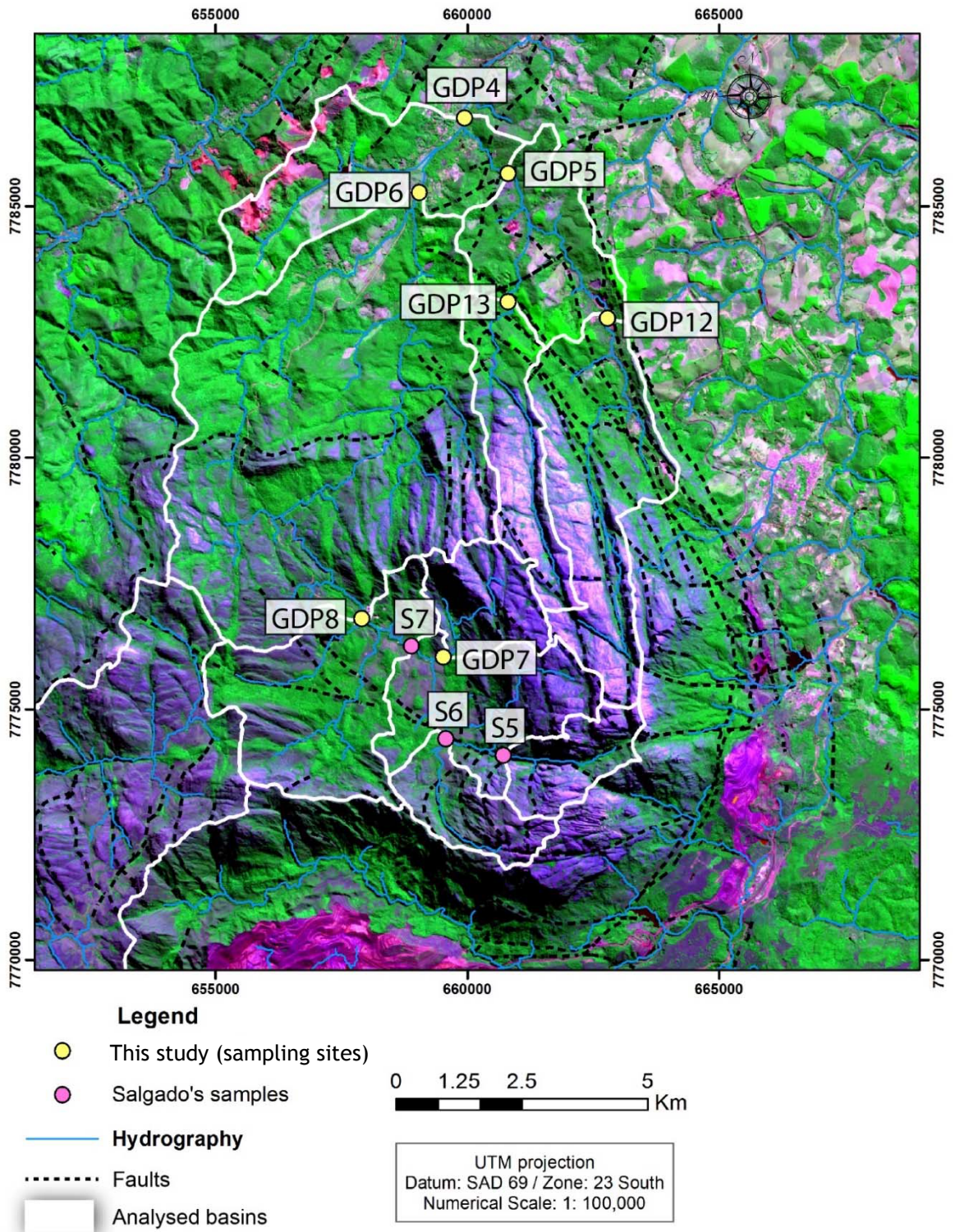


**Figure 52.** The spatial distribution of the nested basins in the eastern part of the Caraça Range. Faults are shown as dashed black lines. Background is a false color mosaic using a Sentinel-2 satellite image, thus in this context green areas represent vegetation; purple areas represent rock outcrops, and pink areas are related to human occupation.



**Figure 53.** The spatial distribution of lithology in the nested basins in the eastern part of the Caraça Range. Local normalised steepness index is represented by coloured lines. Faults are shown as dashed black lines. Geological data: Lobato et al., 2005.

### 5.3.3 CATCHMENT-AVERAGED GEOMORPHIC PARAMETERS

The basins analysed in Chapter 4 are different from the sampled basins for the analysis of detrital  $^{10}\text{Be}$  concentrations. Hence, a new quantitative analysis of the topography of the sampled basins was performed. For that, catchment-averaged geomorphic parameters were extracted from the 12 m TanDEM-X DEM. The selection of the quantified geomorphic parameters includes the factors that are usually considered as essential for constraining landscape evolution, and for which available data have an adequate resolution. In addition to the parameters quantified in Chapter 4, the present-day density of vegetation was also calculated because vegetation is often considered a potential controlling factor on denudation (e.g., Portenga and Bierman, 2011; Harel et al., 2016).

All parameters except for the density of vegetation were quantified following the same procedures described in Chapter 3. The density of vegetation was calculated using the Enhanced Vegetation Index (EVI; e.g., Miura et al., 2001; Huete et al., 2002). The EVI is quantified using Equation 31:

$$EVI = 2.5 * \frac{(NIR - RED)}{(NIR + C_1) * (RED - C_2) * (BLUE + L_v)} \quad (31)$$

with  $C_1$ ,  $C_2$ , and  $L_v$  as coefficients for the atmospheric condition; whereas these coefficients were developed for the Moderate Resolution Imaging Spectroradiometer (MODIS) sensor, the same coefficients are used for quantifying EVI for different sensors (e.g., Huete et al., 2002; Frampton et al., 2013). The ‘NIR’ (near-infrared band), ‘RED’ (visible band), and ‘BLUE’ (blue band), are atmospherically-corrected surface reflectance values derived from these specific bands of the electromagnetic spectrum. A Sentinel-2 satellite image, with 0% cloud coverage and 10 m resolution, was used to quantify EVI for the QF (Copernicus, Sentinel data, taken on 07/13/2016; downloaded from <https://scihub.copernicus.eu/>, accessed January 2018) by applying routines of the Semi-Automatic Classification Plugin (Congedo, 2016) available for the software QGIS v. 2.18.16.

### 5.3.4 SAMPLING

Sampling was carried out in January 2016. Alluvial sediments were collected from the bed of 25 active channels, during base flow conditions. Care was taken to sample sand-sized material only. Areas associated with obstacles to the normal flow of the river, such as vegetation and large boulders, were avoided in the sampling. None of the sampled basins has shown evidence of deep mass movements in the field (i.e., there was no clear signs of landslide activity, such as landslide scars). These procedures represent an effort to minimise possible effects of different bias in cosmogenic inventories, such as varying sediment grain size or significant sediment storage. Figure 54 displays a mosaic consisting of field photos of several sampling locations.

### 5.3.5 SAMPLE PROCESSING

Each sample was processed to obtain ultrapure quartz separates, and subsequently the  $^{10}\text{Be}$  was isolated following standard procedures (cf. Kohl and Nishiizumi, 1992; e.g., Bierman and Caffee, 2002), at the SUERC Cosmogenic Nuclide Laboratory in Glasgow, UK. The AMS measurements for quantifying  $^{10}\text{Be}/^9\text{Be}$  ratios were carried out at the SUERC AMS laboratory (Xu et al., 2015). The resulting  $^{10}\text{Be}$  concentrations were based on the  $2.79 \times 10^{-11}$   $^{10}\text{Be}/^9\text{Be}$  ratio for the standard NIST SRM4325, and using a  $^{10}\text{Be}$  half-life of  $1.36 \times 10^6$  year (Chmeleff et al., 2010; Korschinek et al., 2010). The resulting  $^{10}\text{Be}/^9\text{Be}$  ratios for each sample were corrected for the processed blank ratios ( $n = 2$ ), ranging between 0.2 and 3.2 % of the sample  $^{10}\text{Be}/^9\text{Be}$  ratios.

The sample processing from the first step up to the preparation of AMS targets (cf. Kohl and Nishiizumi, 1992; e.g., Bierman and Caffee, 2002) may be summarised as follows:

**Part A:** Quartz separation and pre-treatment

- A.1 sieving;
- A.2 washing;
- A.3 magnetic separation;
- A.4 heavy liquid separation.

**Part B:** Ultrasonic quartz cleaning and leeching

B.1 Aqua Regia bath;

B.2 leaching sample in 1% HF + 1% HNO<sub>3</sub> acid mixture in the ultrasonic tank (3 times);

**Part C:** Quartz dissolution and ion-exchange column separation chemistry

C.1 measuring Al in the part sample aliquot (PSA) on the ICP-OES;

C.2 quartz dissolution and addition of Be carrier;

C.4 Fe column;

C.5 Be column;

C.6 purifying Be fraction.

**Part D:** Preparing samples for AMS targets and AMS target loading

D.1 drying Al+Be samples in a dry bath;

D.2 burning samples in tube furnace;

D.3 loading samples into AMS targets.



Figure 54. Sampling sites in the QF. The sample ID is shown in the top left of each picture.

### 5.3.6 ESTIMATING DENUDATION RATES FROM $^{10}\text{Be}$ CONCENTRATIONS

The  $^{10}\text{Be}/^9\text{Be}$  ratios obtained from the AMS were blank-corrected and reduced to  $^{10}\text{Be}$  concentration in quartz using the scheme described by Balco (2008). Catchment-averaged denudation rates were derived from  $^{10}\text{Be}$  concentrations using the CRONUS-Earth online calculator version 2.3 (<http://hess.ess.washington.edu/>, accessed January 2018; Balco et al., 2008). Production rates vary spatially as an effect of elevation, latitude, shielding and sample density, and  $^{10}\text{Be}$ -derived denudation rates need to be corrected for these factors (e.g., Lal, 1991; Stone, 2000; Desilets and Zreda, 2003; Balco et al., 2008; Dunai, 2010; Dunai and Lifton, 2014; see section 5.2.2). The CRONUS-Earth online calculator requires the value of these factors as inputs, including a catchment-averaged atmospheric pressure (or alternatively, elevation), an average shielding factor, and the sample density. I used the CAIRN method (Mudd et al., 2016) to quantify an effective catchment-averaged pressure and a mean catchment-averaged topographic shielding for every basin, using a pixel-by-pixel approach (Mudd et al., 2016). The quantification of topographic shielding relied on modeling hillshade from all points in the sky, in which azimuth values vary from  $0\text{-}360^\circ$ , and zenith values vary from  $0\text{-}90^\circ$  (Codilean, 2006; Mudd et al., 2016). The input parameters azimuth ( $\Delta\varphi$ ) and zenith ( $\Delta\theta$ ) define the angular increments in the calculation of topographic shielding, and thus smaller values in both parameters determine higher accuracy in the shielding results. I have used the values  $\Delta\theta = 5$  and  $\Delta\varphi = 8$  as suggested by Mudd et al. (2016).

Different scaling schemes have been proposed to account for the effects of elevation and the geomagnetic field in production rates of cosmogenic nuclides. The most often used scaling scheme is the model reported by Lal (1991) and later modified by Stone (2000), referred as the Lal/Stone scaling scheme (Dunai, 2010; Dunai and Lifton, 2014). This scheme is time-independent as it does not account for time-dependent variations, such as changes in the geomagnetic field (Dunai, 2010). Other models were proposed to account for time-dependent changes in the production of cosmogenic nuclides (e.g., Dunai, 2001; Desilets and Zreda, 2003; Lifton et al., 2014). Recent work has shown that the classic Lal/Stone scheme performs similarly to other time-dependent scaling schemes (e.g., Borchers et al., 2016; Phillips et al., 2016). The calculated denudation rates for the analysed

basins in this contribution are very similar using either the time-independent or the time-dependent Lal/Stone scheme. I follow the procedure described by Mudd et al. (2016) and I report the denudation rates for the QF using the time-independent Lal/Stone scaling scheme. However, denudation rates estimated using time-dependent scaling factors are reported in Appendix B.

The sample density used for the calculation of denudation rates from  $^{10}\text{Be}$  concentrations is often reported as a standard value, generally ranging from 2.6 to 2.7 g/cm<sup>3</sup>, irrespective to the lithology of the basin (e.g., Scherler et al., 2014; Mudd et al., 2016; Lupker et al., 2017). I quantified catchment-averaged sample densities (Tables 8 and 9), considering the areal contribution of each lithology per basin and the reported average density values per lithology from geology textbooks (Table 8; Telford et al., 1990; Schön, 2015). Figure 55 shows that the calculated denudation rates do not change appreciably if these average density values or a standard sample density of 2.6 g/cm<sup>3</sup> is used. I decided to report denudation rates from the standard sample density method, because the average density per lithology described by the textbooks may not be correct for the lithologies of the QF.

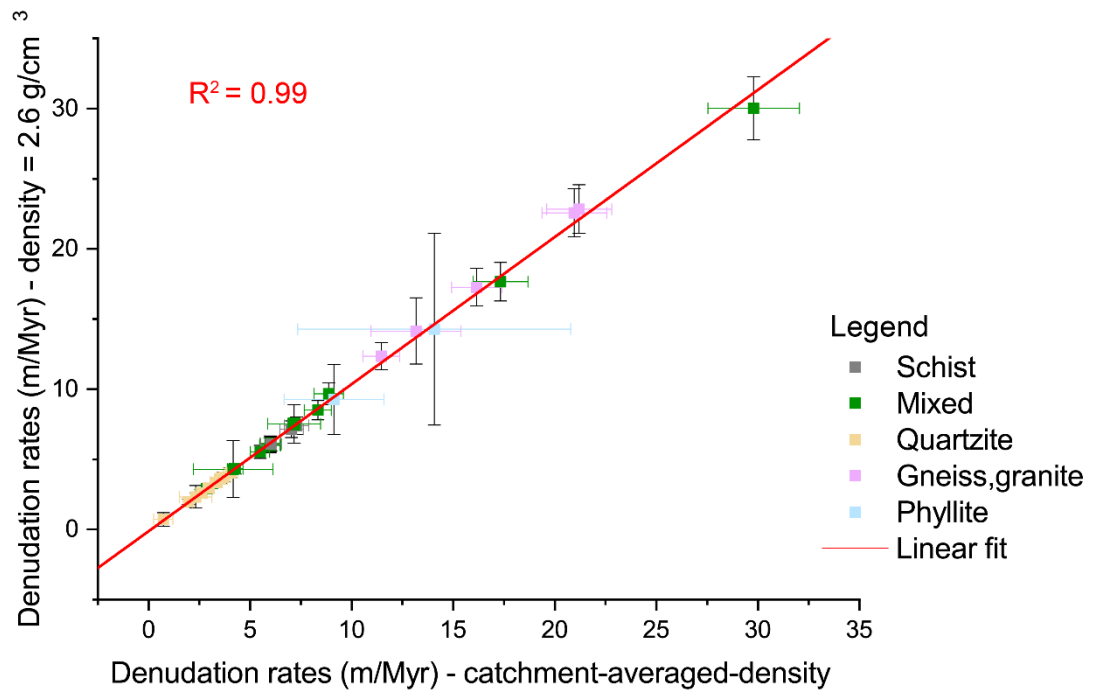


**Figure 55.** Scatter plot of basin denudation quantified using either a standard density for each sample of 2.6 g/cm<sup>3</sup> or a catchment-averaged density. See Table 8 for catchment-averaged density values.

**Table 8.** Average density values per lithology.

Lithology	Average density (g/cm <sup>3</sup> )
Quartzite	2.6
Schist	2.64
Gneiss	2.8
Basalt	2.99
Phyllite	2.62
Banded iron formation	3.1

Data source: Telford et al., (1990); Schön (2015).

**Table 9.** Catchment-averaged density values for the analysed basins using the values on Table 8 as input.

Sample #	Main lithology	Catchment-averaged density (g/cm <sup>3</sup> )
GDP1	Schist	2.64
GDP4	Mixed	2.63
GDP5	Mixed	2.62
GDP6	Mixed	2.63
GDP7	Quartzite	2.60
GDP8	Quartzite	2.62
GDP12A	Quartzite	2.61
GDP13F	Quartzite	2.63
GDP14	Quartzite	2.63
GDP15	Quartzite	2.61
GDP17	Mixed	2.65
GDP18	Mixed	2.62
GDP23	Mixed	2.66
GDP24	Mixed	2.62
GDP25F	Mixed	2.65
GDP26	Mixed	2.60
GDP27	Mixed	2.83
GDP29	Mixed	2.65
GDP32	Schist	2.63
GDP36	Schist	2.64
GDP37	Gneiss,granite	2.80
GDP38	Gneiss,granite	2.80
GDP39	Gneiss,granite	2.80
GDP40	Gneiss,granite	2.78
GDP43	Mixed	2.62
SBR01	Phyllite	2.64
SBR02	Phyllite	2.64
SBR03	Gneiss,granite	2.79
SBR04	Mixed	2.69
S05	Quartzite	2.60
S06	Quartzite	2.60
S07	Quartzite	2.60
S08	Mixed	2.73

### 5.3.7 BIVARIATE REGRESSIONS BETWEEN DENUDATION RATES AND GEOMORPHIC PARAMETERS

<sup>10</sup>Be-derived denudation rates were analysed in terms of their possible relationship with the topography and/or the lithology(ies) of the basins they pertain to. I performed bivariate regression analyses to quantitatively estimate the relationships between catchment-averaged denudation rates and every catchment-averaged geomorphic parameter, using the software OriginPro v.2018. The central tendency, dispersion and the shape of the distributions of denudation rates per lithology were also calculated using the software OriginPro v.2018.

### 5.3.8 PRELIMINARY ESTIMATION OF BEDROCK ERODIBILITY FACTOR FOR THE QF

The denudation rates for each basin have also been used to estimate the bedrock erodibility factor  $K$ , which is considered “the most difficult stream power law parameter to estimate” (Harel et al. 2016, p. 193). There is a limited body of work that attempts to constrain  $K$  (e.g., Stock and Montgomery, 1999; Sklar and Dietrich, 2001; Bursztyn et al., 2015; Harel et al., 2016) and, in this contribution, I follow the approach reported by Pelletier (2010) who provides a first approximation for  $K$  using Equation 32 (a rearrangement of the stream-power law for  $K$ ):

$$K = \frac{\varepsilon}{S^m A^n} \quad (32)$$

The area exponent  $m$  is set to 0.4 as a mean to derive estimates of  $K$  in a comparable scale to the values reported by Stock and Montgomery (1999). The slope exponent  $n$  is made to vary from 2/3 to 2, to test how different  $n$  values affect the estimated  $K$  values for the analysed basins. This approach yields a preliminary estimate of the relative values of  $K$ , which (should) correspond to distinct erodibility zones (Pelletier, 2010). In order to estimate bedrock erodibility values for the QF, I quantified the local channel slope ( $S$  in Equation 32) for every channel reach with more than 120 m of extension (i.e., ten times the resolution

of DEM). Catchment-averaged local channel slope was derived as the average of every local channel slope for each basin. The results of this contribution are described in the following section.

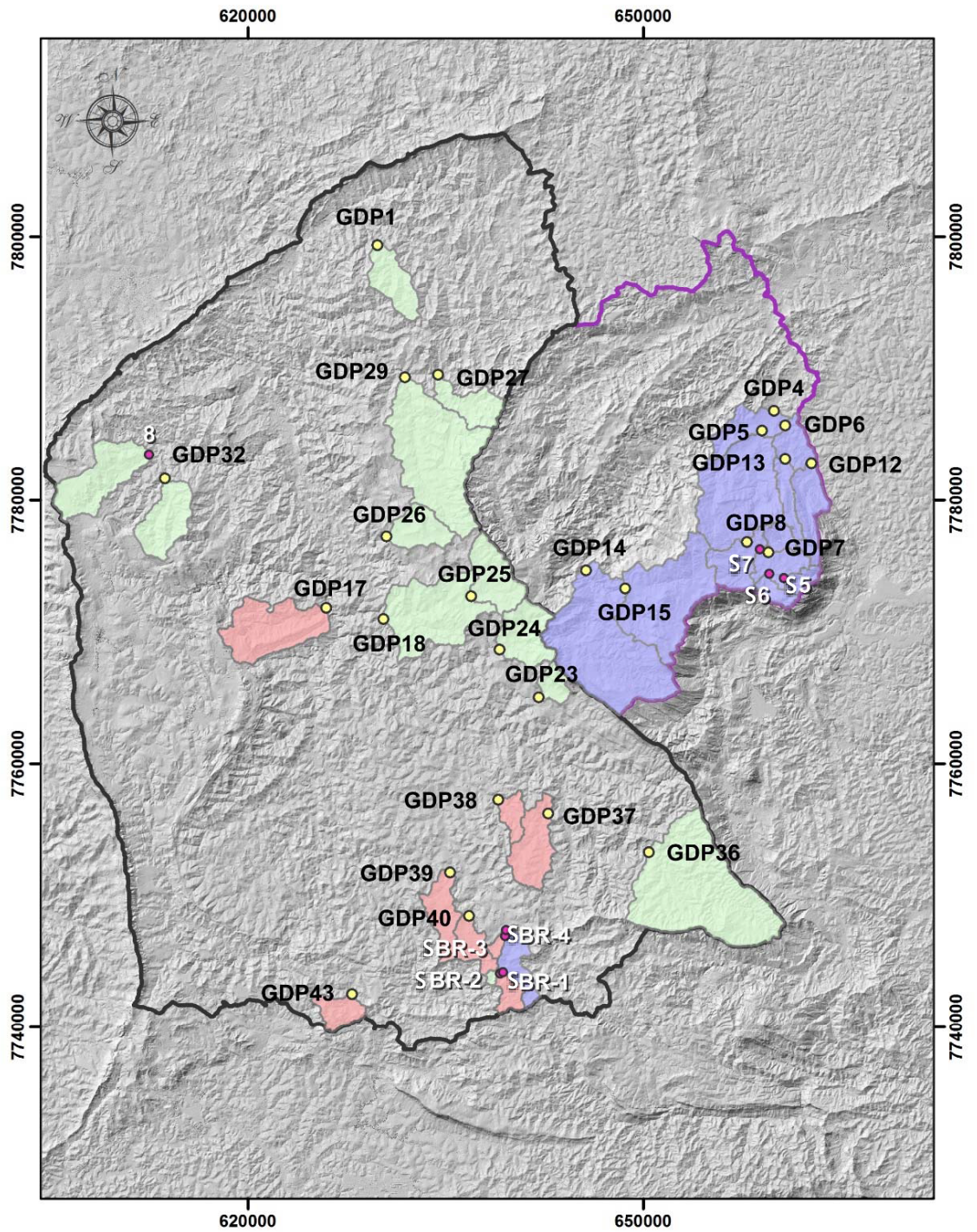
## 5.4 RESULTS

### 5.4.1 PATTERN OF DENUDATION OF THE QF

The QF  $^{10}\text{Be}$ -derived catchment-averaged denudation rates are overall low ( $\leq 30$  m/Myr), yet there is a marked spatial variation: the basins over the Caraça Range are associated with slow denudation rates, contrasting with the higher values of basins located in the central and southern part of the QF (Figure 56, Table 10). The overall mean denudation rate of the QF is 9.6 m/Myr, whereas the median is 7.3 m/Myr. The dataset is marked by a high standard deviation of 7.6 m/Myr, a value that is higher than the overall median of the dataset. This trend reflects the high spatial variability of the data; GDP43, the basin associated with the maximum denudation rate of the entire dataset ( $30 \pm 2.2$  m/Myr), is denuding  $\sim 42$  times faster than basin S5, where denudation rates are only  $0.7 \pm 0.4$  m/Myr.

In the eastern QF, the sub-basins of the Upper Conceição River, flowing away from the Caraça Range in a roughly northeast direction, yield the lowest denudation rates of the QF, with a median of 3.5 m/Myr and a standard deviation of 1.1 m/Myr. The minimum and maximum denudation rates are  $0.7 \pm 0.4$  m/Myr and  $4.3 \pm 0.3$  m/Myr, for the S5 and GDP5 basins, respectively (Figure 56; Table 10). The sub-basins of the Upper Das Velhas River, in central- to western QF, denude faster, displaying a median denudation rate of 13.1 m/Myr and a standard deviation of 7.5 m/Myr, indicating a pronounced variability in denudation rates within these sub-basins. Basins clustered over the eastern and northern parts of the Upper Das Velhas River basin are associated with denudation rates that are lower than 10 m/Myr, displaying a median denudation rate of 7.9 m/Myr and a standard deviation of 3.6 m/Myr. Basins located in the central and southern portion of the Upper Das Velhas River are associated with faster denudation rates that are consistently higher than 10 m/Myr, up to  $30 \pm 2.2$  m/Myr (Figure 56; Table 10). These basins are associated with a median denudation rate of 16.3 m/Myr and a high standard deviation of 8.3 m/Myr. There are two outliers. Basin SBR4 is associated with a low denudation rate of  $4.3 \pm 2.0$  m/Myr, despite its location

downstream of basins that are denuding faster (up to  $14.2 \pm 6.8$  m/Myr). Basin GDP17 has a mean denudation rate of  $17.6 \pm 1.3$  m/Myr despite being located close to basins with denudation rates lower than 10 m/Myr. If the mean denudation rate of the eastern QF basins (3.5 m/Myr) is set as a reference value, then the Upper Das Velhas River sub-basins, denuding at rates lower than 10 m/Myr, display an average denudational pace that is ~2 times faster than the reference, whereas the Upper Das Velhas River sub-basins that are denuding at rates higher than 10 m/Myr, show an average denudational pace that is ~5 times faster (Figure 56; Table 10).



**Legend**

- |                                |                          |
|--------------------------------|--------------------------|
| ● This study (sampling sites)  | Denudation rates (m/Myr) |
| ● Salgado's samples            | ■ 0.7 - 4.9              |
| □ Upper Das Velhas River basin | ■ 5.0 - 10.0             |
| □ Upper Conceição River basin  | ■ 10.1 - 30.0            |

Numerical scale: 1:400,000

**Figure 56.** The spatial distribution of <sup>10</sup>Be-derived catchment-averaged denudation rates (m/Myr) for the QF. See text for explanation.

Table 10.  $^{10}\text{Be}$  analytical results and derived denudation rate data

Sample # <sup>a</sup>	Latitude (°N)	Longitude (°E)	$^{10}\text{Be}$ concentration (atoms/g quartz)	Shielding factor <sup>b</sup>	Effective pressure (hPa)	Surface production rate (atoms/g/y)		Denudation rate (m/Myr) <sup>d</sup>	External uncertainty (m/Myr) <sup>e</sup>	Main lithology <sup>f</sup>
						Spallogenic <sup>c</sup>	Muogenic			
GDP1	-19.897642	-43.759600	$6.37823 \times 10^5$	0.988	903.7	6.16	0.251	7.4	0.6	Schist
GDP4	-20.009216	-43.471022	$1.249429 \times 10^6$	0.989	925.9	5.3	0.234	2.9	0.2	Mixed
GDP5	-20.019157	-43.462649	$1.755194 \times 10^6$	0.967	882.1	7.01	0.268	2.5	0.2	Mixed
GDP6	-20.022748	-43.479488	$1.239967 \times 10^6$	0.971	869.0	7.71	0.279	4.3	0.3	Mixed
GDP7	-20.106104	-43.474100	$2.104119 \times 10^6$	0.957	834.3	9.68	0.31	2.9	0.2	Quartzite
GDP8	-20.099350	-43.489663	$1.485511 \times 10^6$	0.987	862.2	8.23	0.285	3.7	0.3	Quartzite
GDP12	-20.044950	-43.443529	$2.359658 \times 10^6$	0.957	869.0	7.6	0.279	1.9	0.2	Quartzite
GDP13	-20.042191	-43.462444	$1.558672 \times 10^6$	0.957	864.9	7.82	0.282	3.3	0.3	Quartzite
GDP14	-20.119664	-43.606195	$1.068534 \times 10^6$	0.998	923.7	5.45	0.236	3.6	0.3	Quartzite
GDP15	-20.131882	-43.577703	$1.483740 \times 10^6$	0.981	850.1	8.89	0.296	4.0	0.3	Quartzite
GDP17	-20.146675	-43.794839	$2.97856 \times 10^5$	0.986	900.4	6.32	0.253	17.6	1.3	Mixed
GDP18	-20.154037	-43.753081	$7.47911 \times 10^5$	0.989	921.5	5.49	0.237	5.5	0.4	Mixed
GDP23	-20.206811	-43.639792	$8.09690 \times 10^5$	0.999	893.1	6.74	0.259	6.1	0.5	Mixed
GDP24	-20.174492	-43.668537	$9.18009 \times 10^5$	0.980	872.1	7.64	0.276	6.0	0.5	Mixed
GDP25	-20.137979	-43.689560	$9.54005 \times 10^5$	0.990	864.8	8.12	0.282	6.1	0.5	Mixed
GDP26	-20.097445	-43.751247	$8.29933 \times 10^5$	0.999	892.4	6.76	0.259	5.9	0.5	Mixed
GDP27	-19.986362	-43.714708	$5.14668 \times 10^5$	0.980	898.7	6.33	0.254	9.6	0.7	Mixed
GDP29	-19.988267	-43.738913	$6.33226 \times 10^5$	0.984	883.0	7.09	0.267	8.5	0.6	Mixed
GDP32	-20.058638	-43.912363	$7.25806 \times 10^5$	0.997	912.6	5.86	0.244	6.0	0.5	Schist
GDP36	-20.312311	-43.559025	$6.65683 \times 10^5$	0.978	901.5	6.24	0.252	7.1	0.5	Schist
GDP37	-20.286504	-43.632389	$2.48558 \times 10^5$	0.995	893.7	6.7	0.258	22.5	1.7	Gneiss,granite
GDP38	-20.277352	-43.668669	$4.17539 \times 10^5$	0.993	899.7	6.42	0.254	12.3	0.9	Gneiss,granite
GDP39	-20.327337	-43.703368	$2.34501 \times 10^5$	0.998	903.2	6.3	0.251	22.8	1.7	Gneiss,granite
GDP40	-20.356956	-43.689118	$3.25619 \times 10^5$	0.993	889.4	6.9	0.262	17.2	1.3	Gneiss,granite
GDP43	-20.411434	-43.773774	$1.89214 \times 10^5$	0.993	895.4	6.63	0.257	30.0	2.2	Mixed

Sample #	Latitude (°N)	Longitude (°E)	<sup>10</sup> Be concentration (atoms/g quartz)	Shielding factor <sup>b</sup>	Effective pressure (hPa)	Surface production rate (atoms/g/y)		Denudation rates (m/Myr) <sup>d</sup>	External uncertainty (m/Myr) <sup>e</sup>	Main lithology
						Spallogenic <sup>c</sup>	Muogenic			
SBR1	-20.396356	-43.666478	6.6 × 10 <sup>5</sup>	0.987	879.9	7.34	0.27	9.2	2.4	Phyllite
SBR2	-20.395488	-43.664197	4.6 × 10 <sup>5</sup>	0.991	875.0	7.62	0.274	14.2	6.8	Phyllite
SBR3	-20.370767	-43.662926	4.24 × 10 <sup>5</sup>	0.993	891.2	6.82	0.26	14.1	2.3	Gneiss, granite
SBR4	-20.366611	-43.662154	1.301 × 10 <sup>6</sup>	0.992	880.3	7.34	0.269	4.3	2.0	Mixed
S5	-20.042534	-43.924107	5.186 × 10 <sup>6</sup>	0.986	881.2	7.2	0.268	0.7	0.4	Quartzite
S6	-20.123673	-43.462556	2.922 × 10 <sup>6</sup>	0.924	823.4	10.07	0.321	2.3	0.8	Quartzite
S7	-20.104213	-43.480221	2.07 × 10 <sup>6</sup>	0.997	873.8	7.67	0.275	2.6	0.3	Quartzite
S8	-20.120788	-43.473437	8.15 × 10 <sup>5</sup>	0.995	876.1	7.54	0.273	7.5	1.3	Mixed

(a) Basin IDs. GDP\_ (Glasgow Daniel Peifer) refers to the samples analysed in this contribution. S\_ (Salgado) refers to basins analysed by Salgado and colleagues (Salgado et al., 2007a, 2007b, 2008);

(b) Mean catchment-averaged topographic shielding quantified using  $\Delta\phi = 8$ ,  $\Delta\theta = 5$ ;

(c) Production rate according to time-dependent Lal (1991) /Stone (2001) scaling; see text for details;

(d) Denudation rates assuming bedrock density of 2.6 g/cm<sup>3</sup>; see text for details.

(e) External uncertainty refers to both measurement error in the nuclide concentration as well as errors related to the scaling scheme (Balco et al., 2008)

The nested basins within the eastern-most portion of the QF, over the Caraça Range (Figures 57-58), display low denudation rates, despite inter-basin differences in geomorphic metrics. Their median denudation rates are 3.3 m/Myr, with a small standard deviation of 1.1 m/Myr. Upstream samples (i.e., S5, S6, GDP7, GDP12, GDP13) are associated with the slowest denudation rates, contrasting with the slightly higher values for downstream samples, with a maximum of  $4.3 \pm 0.3$  m/Myr for basin GDP6. Upstream basins are typically associated with exposure of quartzite bedrock, whereas downstream areas are more densely vegetated (Figure 58). Overall in the eastern Caraça Range, denudation rates slightly increase downstream (Figure 57-58). The estimated denudation rate for the basin GDP5 ( $2.5 \pm 0.2$  m/Myr) is roughly the average between the denudation rates of basins GDP12 ( $1.9 \pm 0.2$  m/Myr) and GDP13 ( $3.3 \pm 0.3$  m/Myr), suggesting an efficient mixing of the sediment.

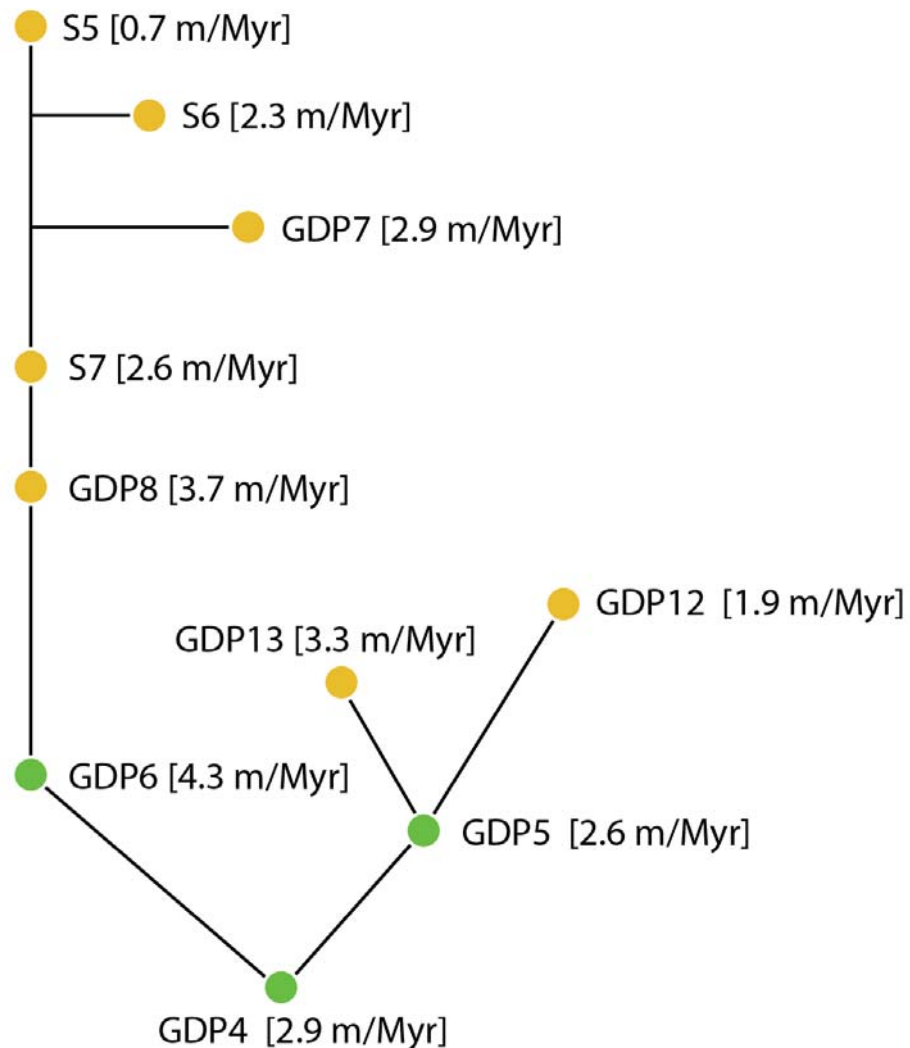


**Figure 57.** Scheme representing the denudation rates for the nested basins in the eastern part of the Caraça Range. The colours represent the main lithology of the basin; yellow for quartzites, and green for mixed lithologies.

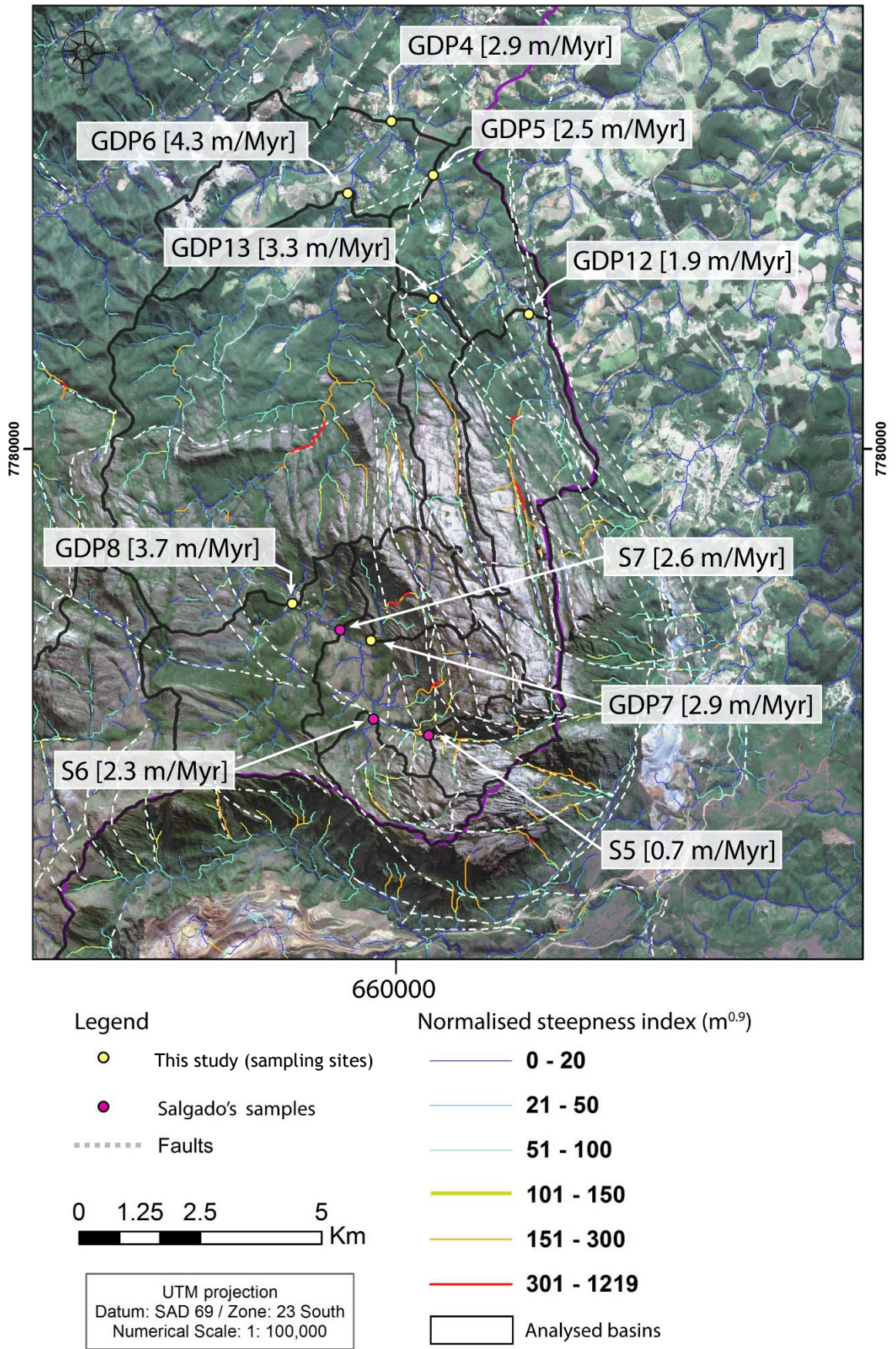
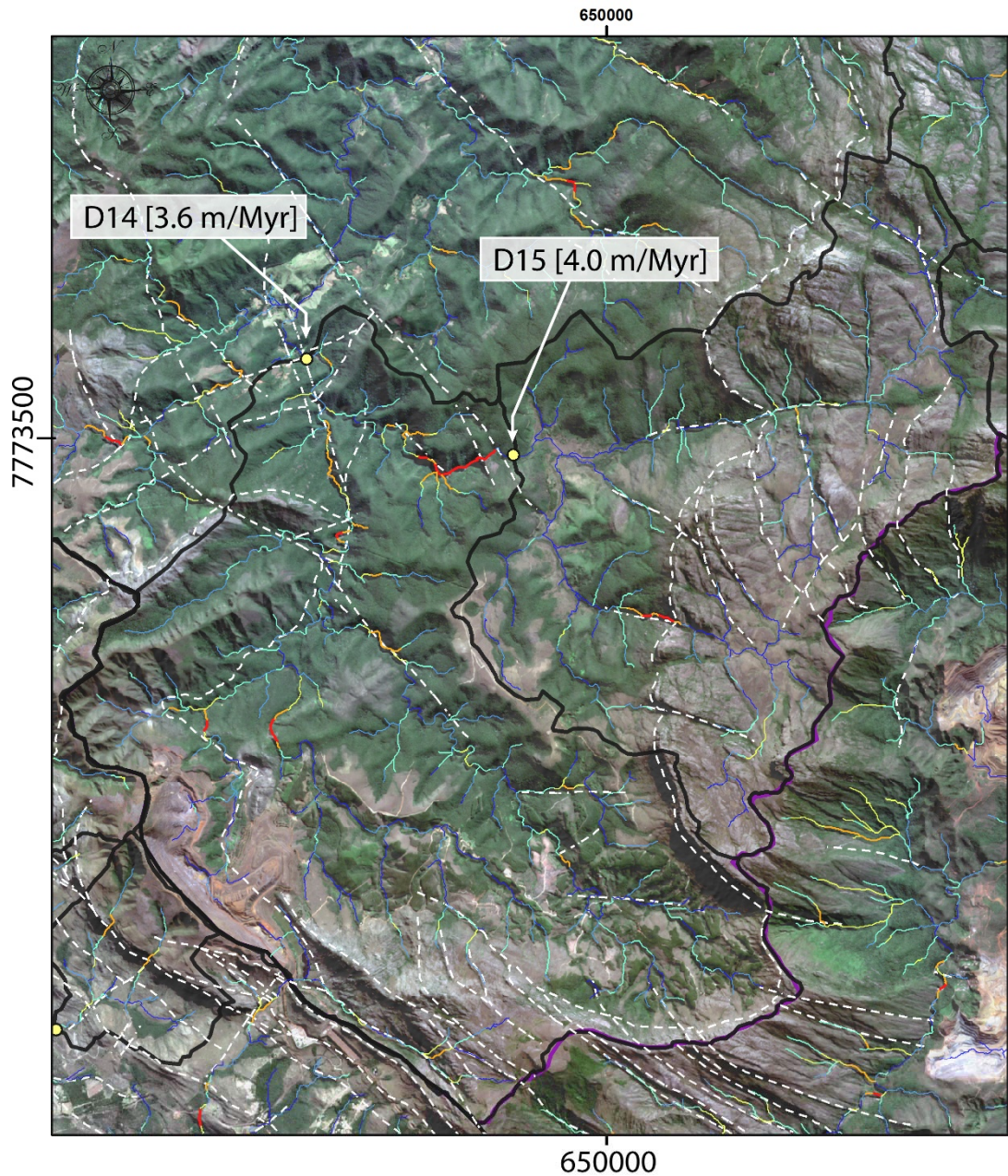


**Figure 58.** Denudation rates for the nested basins in the eastern part of the Caraça Range. Local normalised steepness index is represented by coloured lines. Faults are shown as dashed white lines. Background is a true color mosaic using Sentinel-2 satellite imagery.

Basins GDP14 and GDP15 are associated with the western section of the Caraça Range (Figure 59), which is topographically subdued in comparison with the eastern part. Basin GDP15 displays, among all quartzite basins, the lowest relief and the gentler channel gradients. However, in the western section of the Caraça Range channels can locally be very steep, in particular where they cross perpendicularly, pre-Paleozoic faults. Basin GDP14 is associated with channel and hillslope gradients that are steeper than basin GDP15; nonetheless, the relief of basin GDP15 is subdued if compared to the relief in the eastern part of the Caraça Range. Despite differences in relief between basins GDP14 and GDP15, their average denudation rates are similar, within the external uncertainty; respectively,  $3.6. \pm 0.3$  m/Myr and  $4.0 \pm 0.3$  m/Myr. Both basins yield denudation rates that are consistent with the other quartzite basins located in the eastern part of the Caraça Range, suggesting that the same lithology is associated with similar rates irrespective to differences in basin relief.



Legend

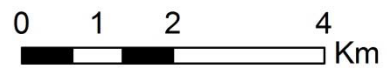
Normalised steepness index ( $m^{0.9}$ )

- 0 - 20
- 21 - 50
- 51 - 100
- 101 - 150
- 151 - 300
- 301 - 1219

○ This study (sampling sites)

----- Faults

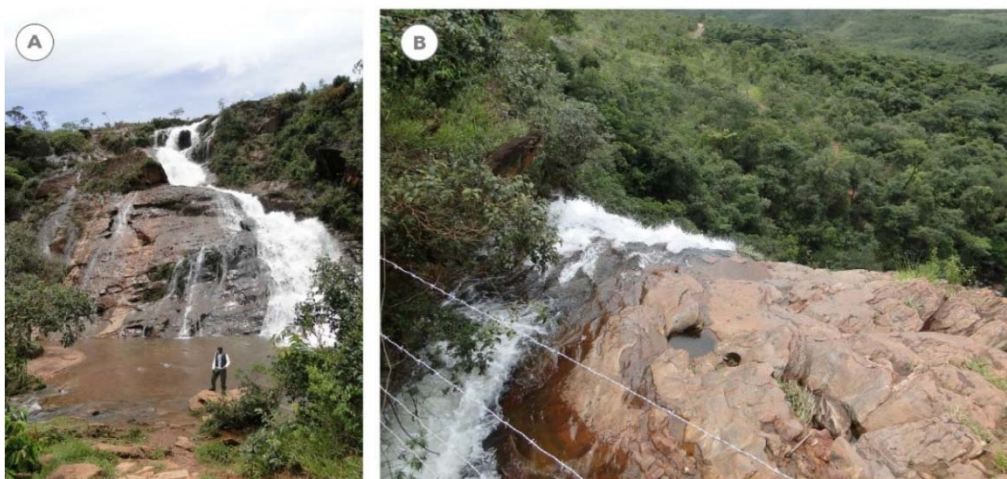
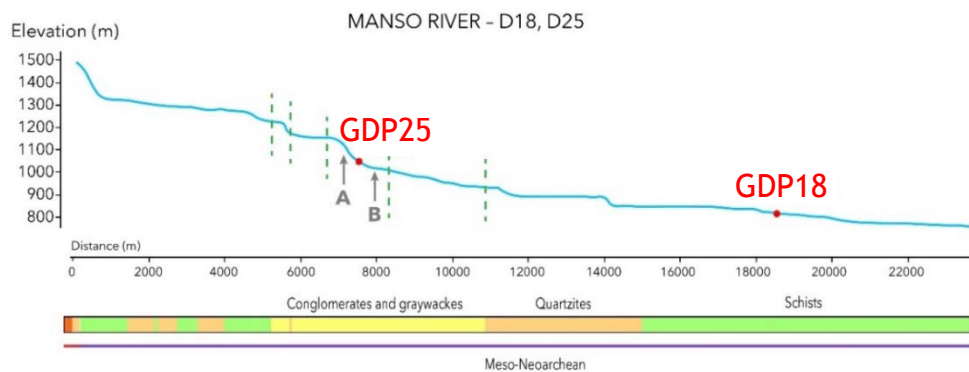
▭ Analysed basins



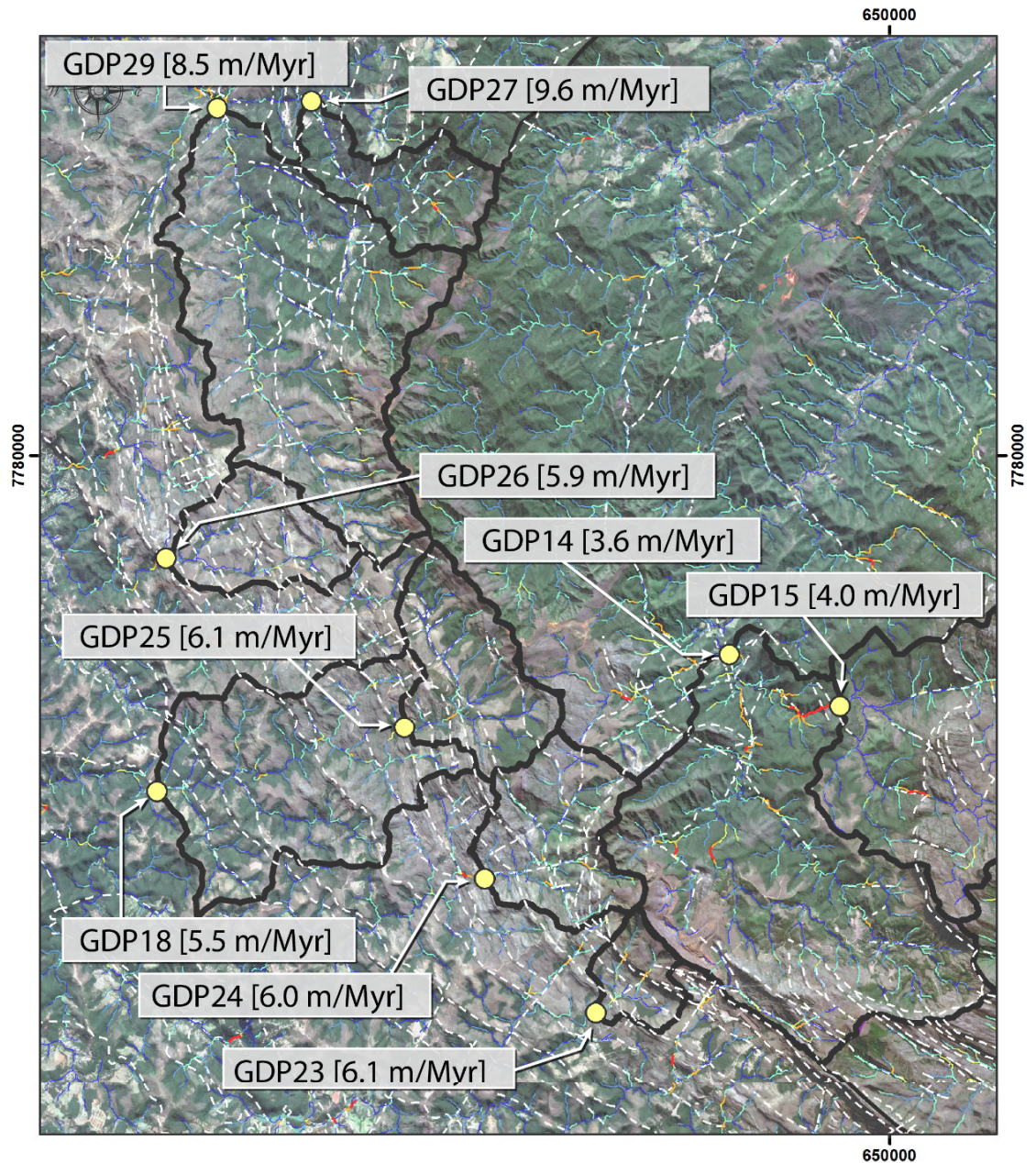
UTM projection  
Datum: SAD 69 / Zone: 23 South  
Numerical Scale: 1: 80,000

Figure 59. Denudation rates for the basins in the western part of the Caraça Range. Local normalised steepness index is represented by coloured lines. Faults are shown as dashed white lines. Background is a true color mosaic using Sentinel-2 satellite imagery.

The Upper Das Velhas River sub-basins denuding at rates lower than 10 m/Myr are typically developed on mixed lithology, consisting primarily of different proportions of schists and quartzites, or are schist-only basins. Schist basins, defined as having >80% of the area underlain by schists, yield median denudation rates of 8.4 m/Myr, whereas mixed lithology basins are associated with median denudation rates of 7.3 m/Myr (Figures 60-61). However, the standard deviation of mixed lithology basins is 8.0 m/Myr, reflecting a considerable variability in denudation rates in these basins. The basins under schists, instead, display a low standard deviation of 0.8 m/Myr. As a group, these sub-basins of the Upper Das Velhas River are associated with a relief that is subdued compared to the Caraça Range, but that is rugged in comparison with areas under gneisses and granites. The bulk of the topographic metrics of these basins have low values, yet they are marked by high local steepness that may be linked to the presence of faults (Figure 60A-B). Stream profiles are similar in form to the Caraça rivers, with many convexities, yet with less elevation drop.



**Figure 60.** Typical longitudinal profile of the trunk river of a mixed lithology basin, marked by subsequent waterfalls. (A) Waterfall upstream of the sampling site GDP25; (B) waterfall downstream of the sampling site GDP25. Quartzite bedrock is exposed in both A and B.



Legend

- This study (sampling sites)
- Salgado's samples
- ..... Faults



UTM projection  
Datum: SAD 69 / Zone: 23 South  
Numerical Scale: 1: 80,000

Normalised steepness index ( $m^{0.9}$ )

- 0 - 20
- 21 - 50
- 51 - 100
- 101 - 150
- 151 - 300
- 301 - 1219

Analysed basins

**Figure 61.** Denudation rates for the basins in the eastern part of the Upper Das Velhas River basin. Local normalised steepness index is represented by coloured lines. Faults are shown as dashed white lines. Background is a true color mosaic using a Sentinel-2 satellite imagery.

The Upper Das Velhas River sub-basins under gneisses and granites show the fastest denudation of the QF, with average denudation rates always higher than 10 m/Myr and corresponding median of 16.3 m/Myr. These basins are correlated with an overall distribution of low channel steepness. Their longitudinal channel profiles are typically concave-up, featuring small elevation drops (Figure 62). There are two outliers in the area: basin SBR4 with an average denudation rate of  $4.3 \pm 2.0$  m/Myr, despite having upstream reaches that show higher denudation rates (which, SBR1,  $9.2 \pm 2.4$  m/Myr; SBR2,  $14.2 \pm 6.8$  m/Myr; and SBR3,  $14.1 \pm 2.3$  m/Myr) and basin GDP43 which exhibits the fastest denudation rate of the QF of  $30.0 \pm 2.2$  m/Myr (Figure 63).

In summary, denudation rates in the QF are overall slow ( $\leq 30$  m/Myr), but spatially variable. Eastern QF basins underlain by quartzites are associated with the lowest denudation rates, contrasting with basins in the southwestern part of the QF, notably those underlain by low-resistance gneiss and granitic rocks, that are associated with faster denudation rates.

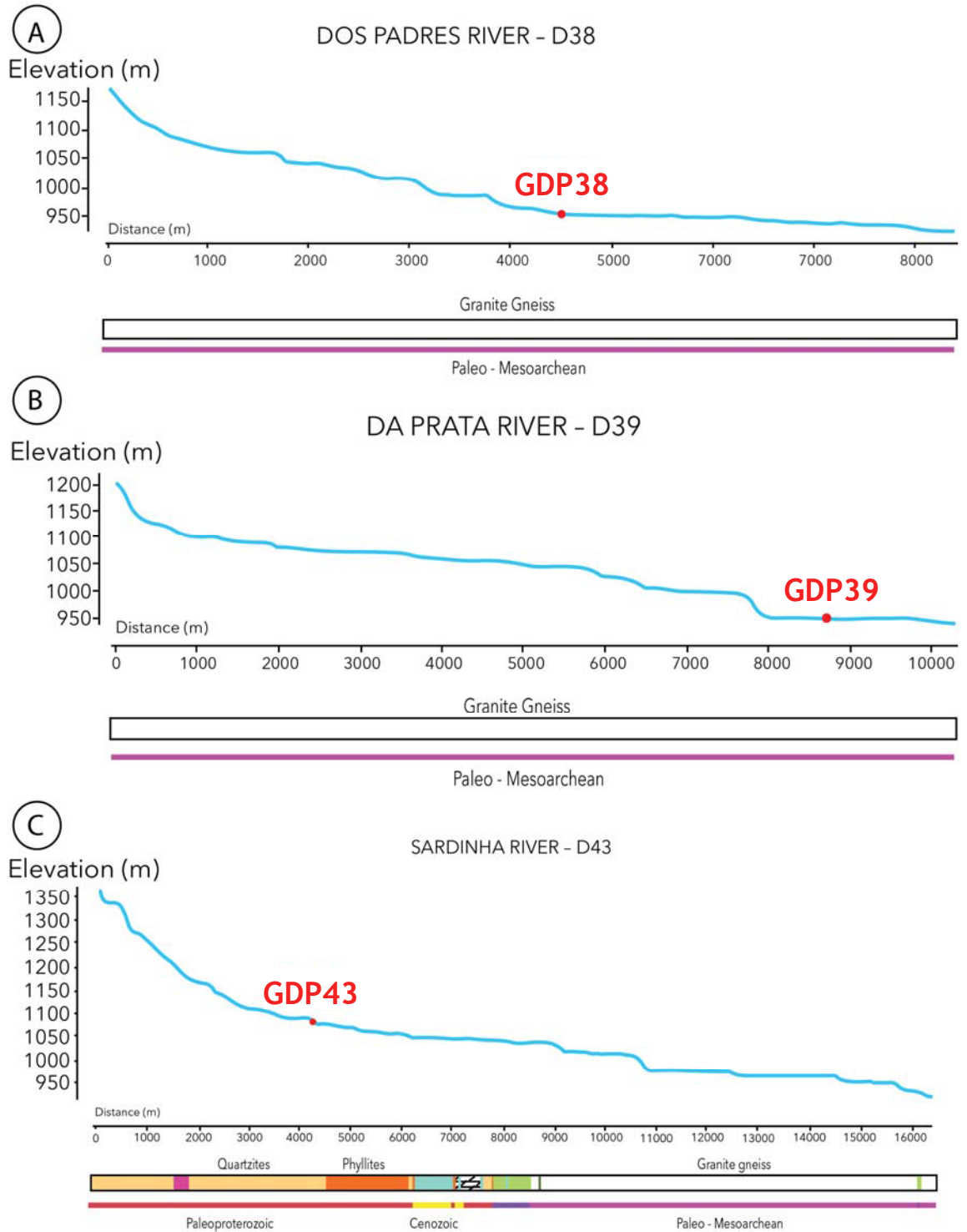


**Figure 62.** Examples of concave-up profiles of rivers associated with the central-south portion of the QF, associated primarily with gneisses and granitic rocks.

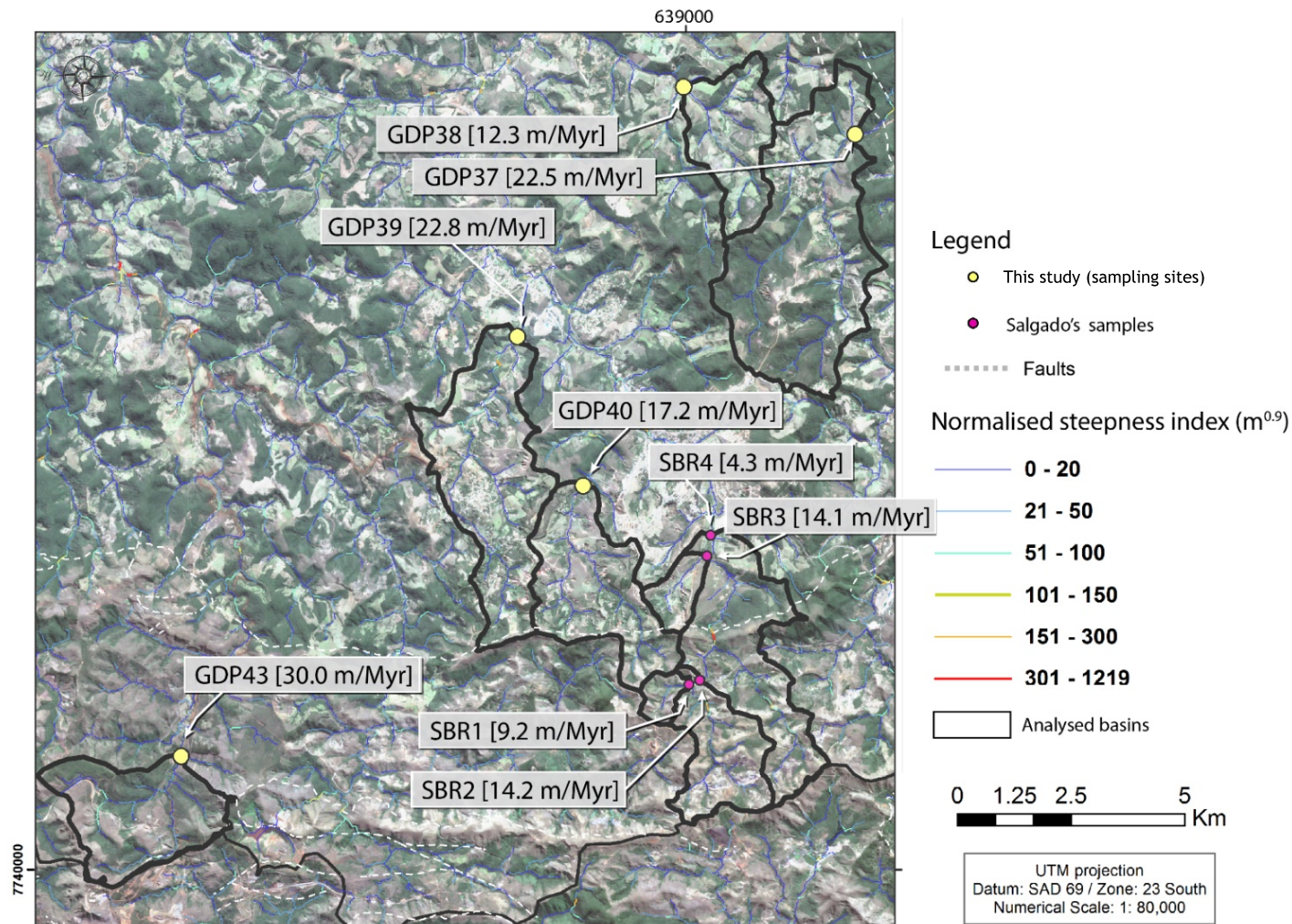


**Figure 63.** Denudation rates for the basins in the central and south parts of the Upper Das Velhas River basin. Local normalised steepness index is represented by coloured lines. Background is a true color mosaic using a Sentinel-2 satellite imagery; see section 4.3.3 for information.

### 5.4.2 BIVARIATE REGRESSIONS BETWEEN CATCHMENT-AVERAGED PARAMETERS

The bivariate regressions between catchment-averaged geomorphic parameters for the basins analysed for detrital  $^{10}\text{Be}$  concentrations yielded a similar pattern to those presented in Chapter 4; yet, with overall higher goodness-of-fit ( $R^2$  values). Normalised steepness index and local relief are the best regressors between the geomorphic parameters, showing an  $R^2$  value of 0.926 ( $p$ -value  $< 0.01$ ; Figure 64), and high  $R^2$  with the other metrics. All of the other parameters, except basin area and mean EVI, have a  $R^2$  often  $> 0.6$  and always  $> 0.4$  (and  $p$ -values  $< 0.01$ ). Even the parameter mean elevation that has shown low values of correlation to every topographic parameter in Chapter 4. By contrast, drainage area and mean EVI are poorly correlated with every other topographic parameter, showing  $p$ -values higher than 0.05 for every regression.

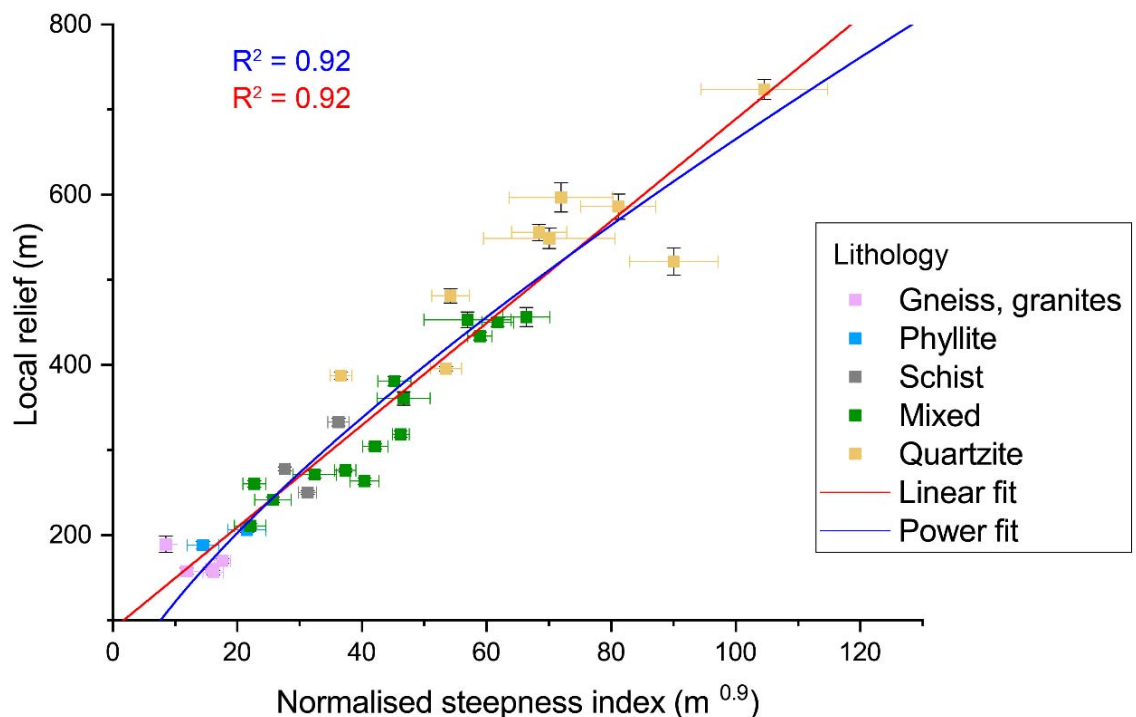
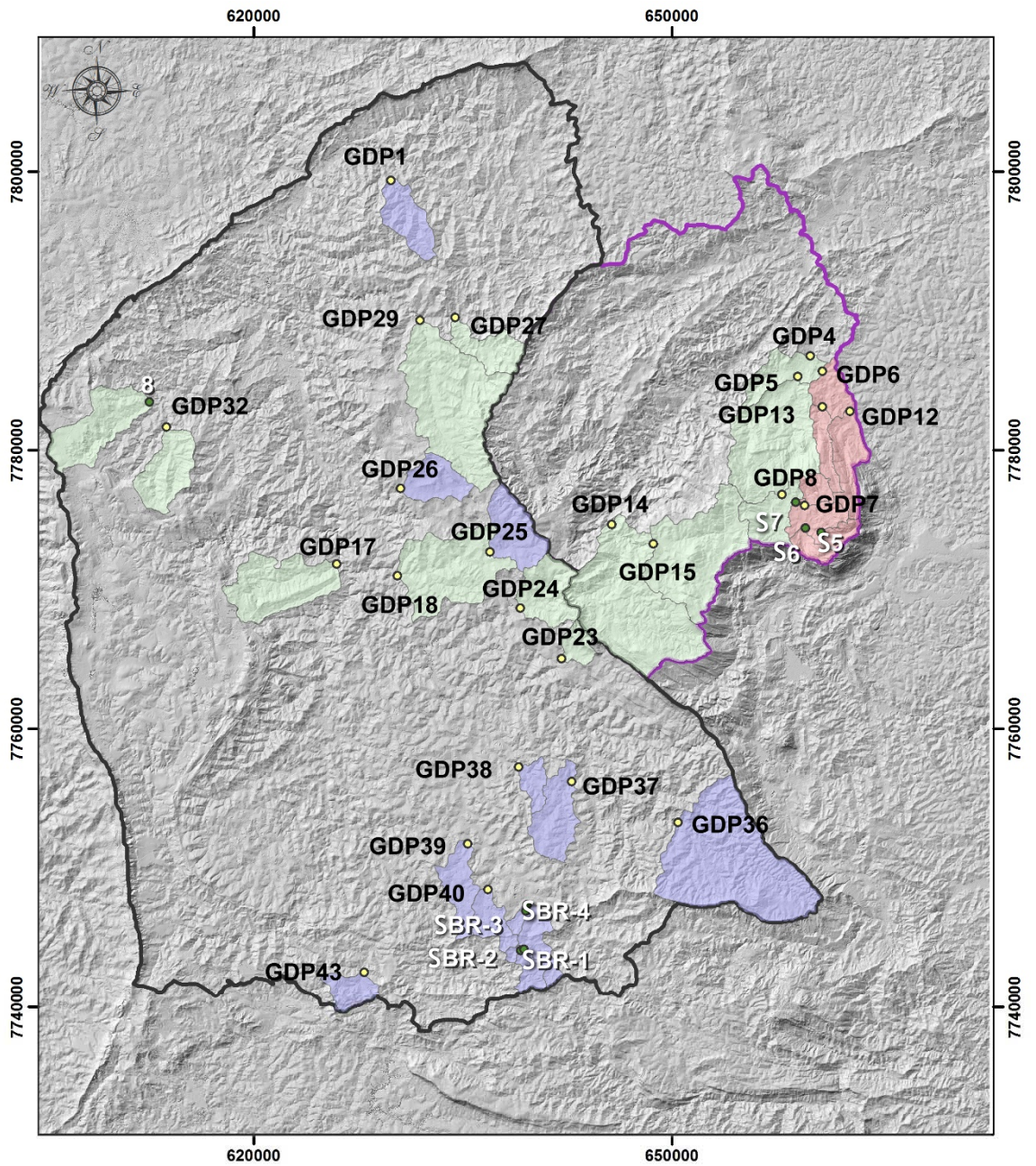


**Figure 64.** Scatter plot of catchment-averaged local relief and normalised steepness index for the analysed basins. Error bars represent the standard deviation of the mean of both parameters.

Catchment-averaged topographic parameters display an extensive range of values. For instance, the parameter normalised steepness index varies from  $\sim 5 \text{ m}^{0.9}$  for basins under gneiss and granitic rocks (e.g., basins GDP37 and GDP38), to  $\sim 100 \text{ m}^{0.9}$  for quartzite basins in the Caraça Range (e.g., basins S5 and GDP12). The Figure 65 shows that basins corresponding to low catchment-averaged normalised steepness index values are associated with low values of local relief. Also, whereas gneisses and granite basins are clustered within the bottom left of the plot, quartzite basins are primarily distributed in the top-right. However, there are several quartzite basins displaying relatively low local relief and normalised steepness index values (Figure 65). The spatial distribution of catchment-averaged normalised steepness index is highly variable; basins located in the eastern part of the Caraça Range are associated with high values of normalised steepness index (up to  $105 \text{ m}^{0.9}$ ), contrasting with the low values of this parameter (up to  $32 \text{ m}^{0.9}$ ) over the southwestern part of the QF (Figure 65).

Similar trends are found for the distribution of the other topographic parameters, which display an overall increase in values from southwest to northeast, with peak values associated with the eastern part of the Caraça Range. For instance, a minimum mean slope angle of  $11.4^\circ$  is associated with basin GDP39, contrasting with a maximum mean slope angle of  $30.3^\circ$  in basin S5 located in an upstream area of the Caraça Range (Figure 66). This pattern underpins the large dispersion in the distribution of every parameter.

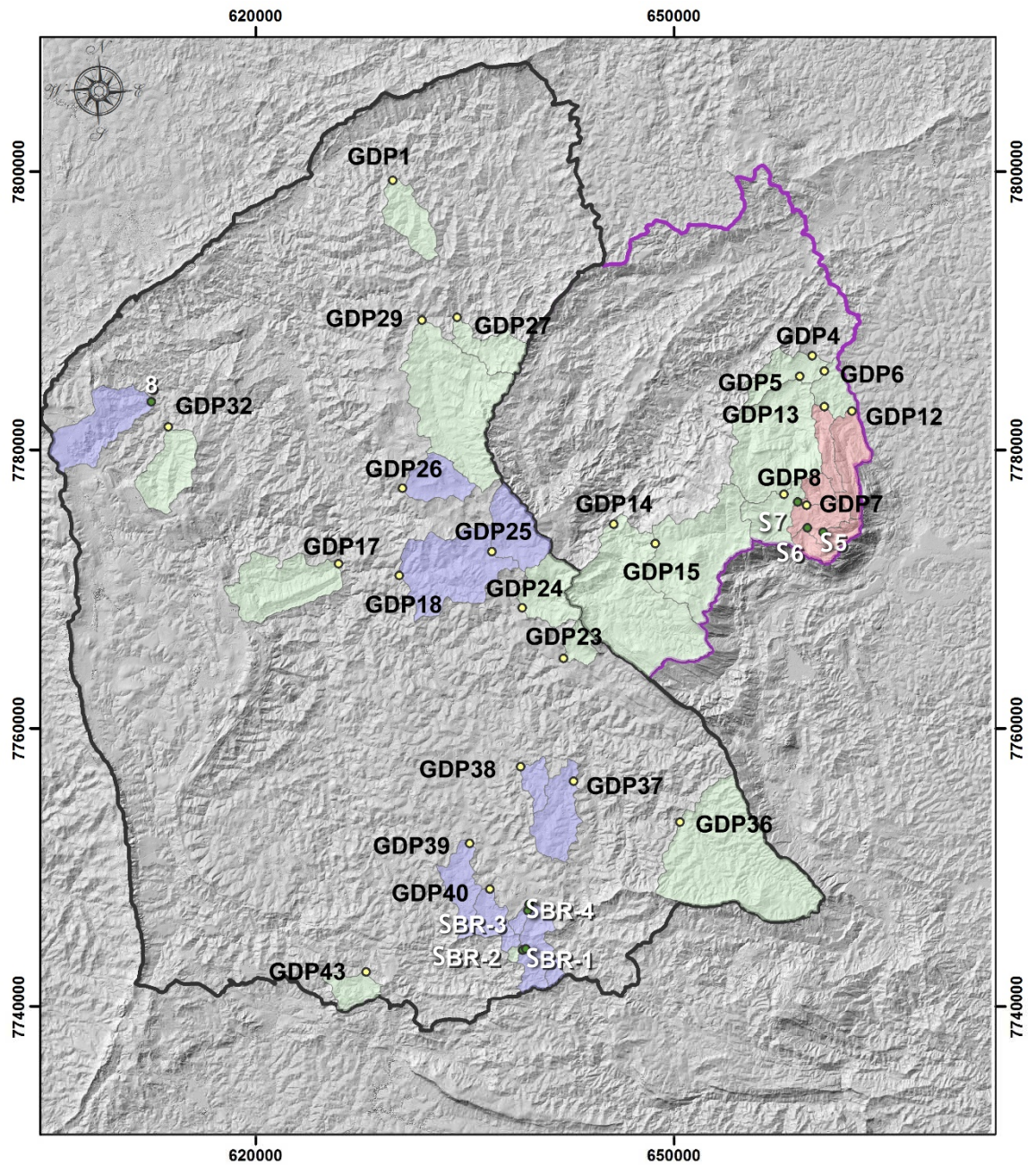


**Legend**

- |   |  |
|---|--|
| <span style="color: yellow;">●</span> This study (sampling sites)   | <span style="background-color: #b0c4de; border: 1px solid black; display: inline-block; width: 20px; height: 10px;"></span> 8 - 32   |
| <span style="color: green;">●</span> Salgado's samples  | <span style="background-color: #c8e6c9; border: 1px solid black; display: inline-block; width: 20px; height: 10px;"></span> 33 - 62  |
| <span style="border: 1px solid black; display: inline-block; width: 20px; height: 10px;"></span> Upper Das Velhas River basin | <span style="background-color: #f8bbd0; border: 1px solid black; display: inline-block; width: 20px; height: 10px;"></span> 63 - 105 |
| <span style="border: 1px solid purple; display: inline-block; width: 20px; height: 10px;"></span> Upper Conceição River basin |  |

Numerical scale: 1:400,000

**Figure 65.** The spatial distribution of catchment-averaged normalised steepness index for the analysed basins.



Legend

- |                                |                            |
|--------------------------------|----------------------------|
| ● This study (sampling sites)  | Mean slope angle (degrees) |
| ● Salgado's samples            | 11.4 - 15.8                |
| □ Upper Das Velhas River basin | 15.9 - 21.4                |
| □ Upper Conceição River basin  | 21.5- 30.3                 |

Numerical scale: 1:400,000

Figure 66. The spatial distribution of catchment-averaged mean slope angle for the analysed basins.

The parameter mean annual precipitation is strongly correlated to all parameters (except basin area and mean EVI), yet it is best correlated with the parameter mean elevation, showing an  $R^2$  value of 0.73 ( $p$ -value < 0.01; Figure 67). Low values of annual precipitation of ~1475 mm/yr are associated with low elevation basins underlain by gneiss and granites. By contrast, the highest mean annual precipitation value, up to 1694 mm/yr, is found for basin S5 in the eastern QF.

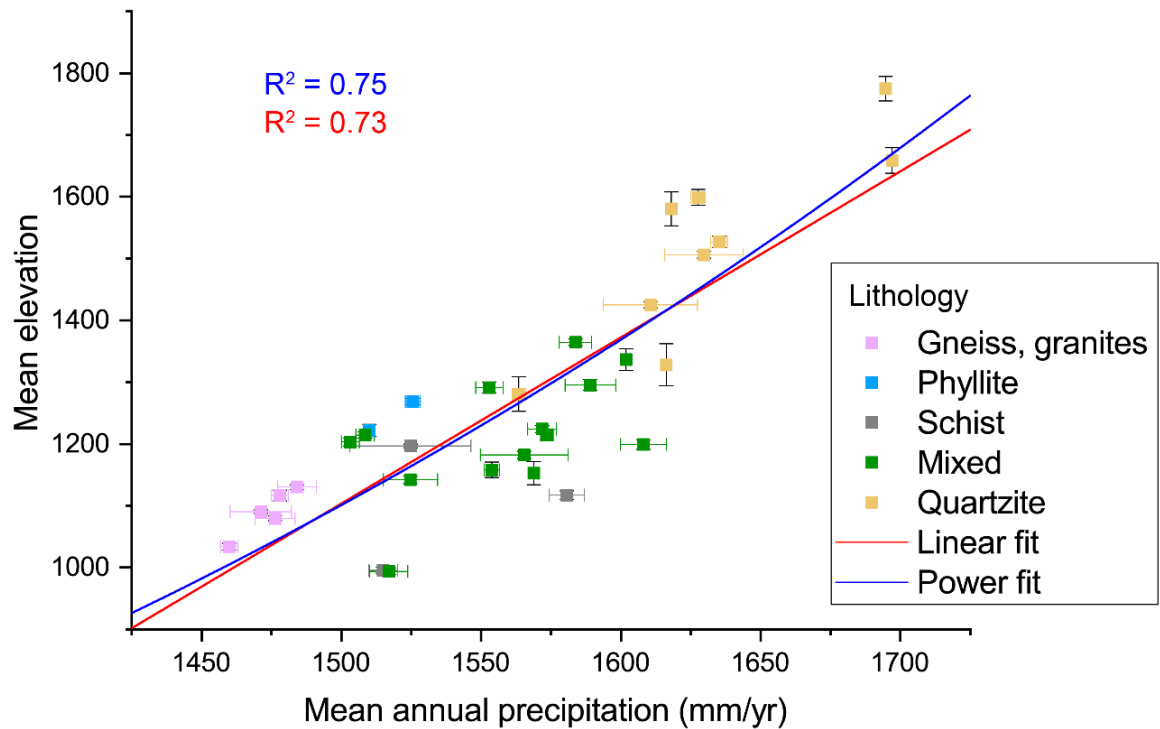


**Figure 67.** Scatter plot of catchment-averaged mean elevation and mean annual precipitation for the analysed basins. Error bars represent the standard deviation of the mean.

The areal distribution of strong rocks (lumped together as explained in section 3.3.5; strong rocks denote quartzites, banded iron formations, and iron duricrusts) is positively related to every catchment-averaged topographic parameter. For example, basins with 0% areal contribution of strong rocks correspond to low local relief values of ~200 m, contrasting with quartzite basins displaying high local relief (Figure 68). Mixed lithology basins show an increase in relief and channel steepness with an increase in the areal contribution of strong rocks, although this relationship is not as clear as in the case of the end-member lithological groups.

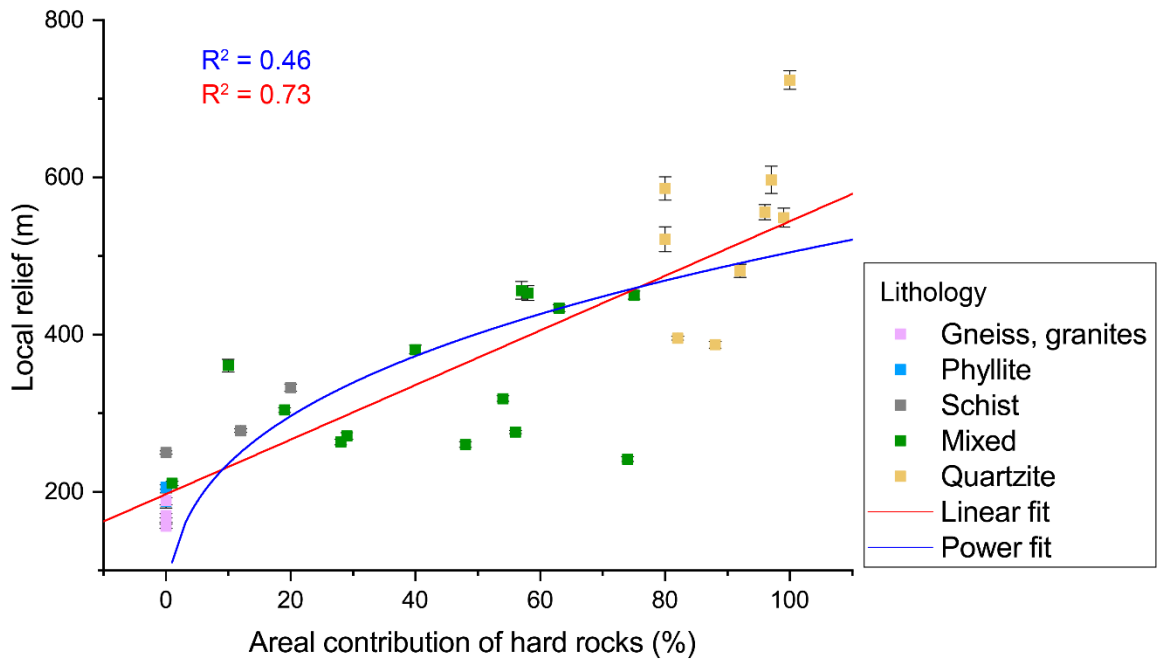


**Figure 68.** Scatter plot of catchment-averaged local relief and the areal contribution of hard rocks for the analysed basins. Error bars represent the standard deviation of the mean.

The relationship of catchment-averaged normalised steepness index and mean slope angle (Figure 69) yields the same pattern described for the other topographic parameters, with a positive relationship between these variables, and an overall association of low normalised steepness index and mean slope angle values with gneiss and granite basins, and the opposite for quartzite basins.

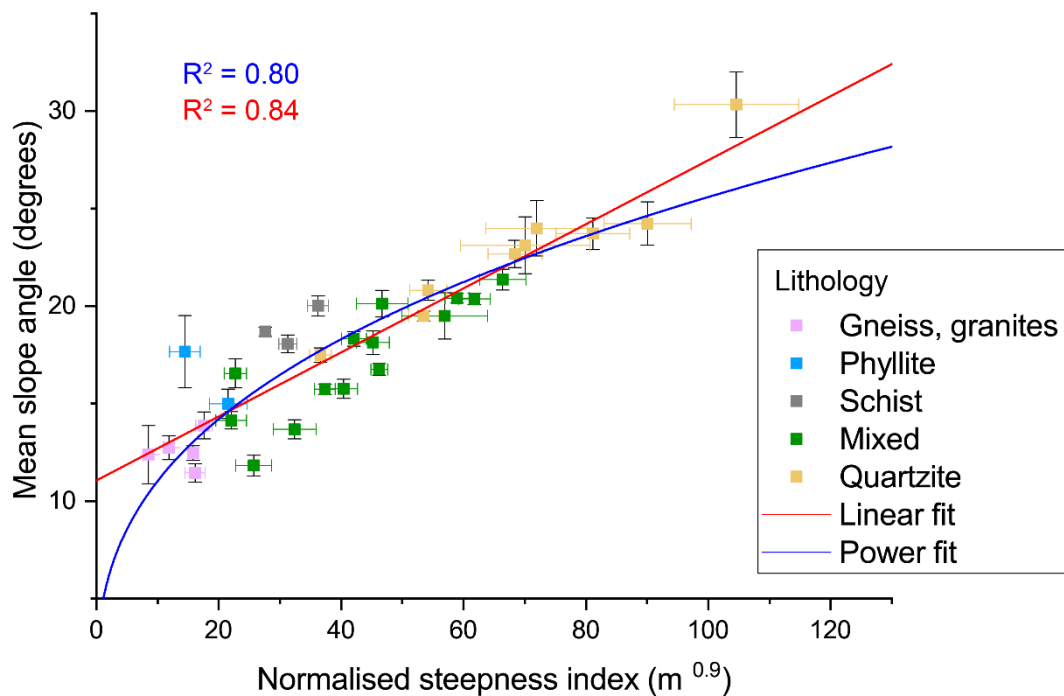


**Figure 69.** Scatter plot of catchment-averaged mean slope angle and the normalised steepness index. Error bars represent the standard deviation of the mean.

In summary, catchment-averaged topographic parameters are positively associated and covary for the analysed basins. In other words, a basin characterised by high normalised steepness index is also associated with high local relief, high mean slope angle, high mean annual precipitation, and so on. The correlation values for every pairwise combination of topographic parameters are shown in Table 11.

**Table 11.** Correlation matrix between the catchment-averaged parameters. R<sup>2</sup> values denote the goodness-of-fit of linear regressions.

<u>R<sup>2</sup> - Linear models</u>													
Max. Slope (°)	Mean Slope (°)	Local relief (m)	Max. Elevation (m)	Mean Elevation (m)	Basin relief (m)	K <sub>sn</sub> (m <sup>0.9</sup> )	Knickpoint magnitude (m)	Knickpoint relief (m)	Mean annual precipitation (mm/yr)	% of strong rocks	EVI	Kernel density of faults	
0.195	0.007	0.010	0.141	0.000	0.323	0.017	0.003	0.000	0.017	0.060	0.135	0.005	Area (m <sup>2</sup> )
	0.557	0.677	0.774	0.277	0.763	0.707	0.439	0.533	0.549	0.654	0	0.581	Max. slope (°)
		0.869	0.603	0.426	0.418	0.843	0.63	0.772	0.556	0.477	0.042	0.469	Mean slope (°)
			0.811	0.594	0.515	0.926	0.789	0.912	0.707	0.736	0.101	0.636	Local relief (m)
				0.545	0.726	0.745	0.629	0.715	0.635	0.774	0.038	0.538	Max. elevation (m)
					0.096	0.435	0.616	0.622	0.732	0.631	0.34	0.29	Mean elevation (m)
						0.614	0.301	0.383	0.287	0.451	0.022	0.41	Basin relief (m)
							0.705	0.833	0.643	0.647	0.056	0.631	K <sub>sn</sub> (m <sup>0.9</sup> )
								0.947	0.637	0.659	0.244	0.495	Knickpoint magnitude (m)
									0.665	0.72	0.194	0.544	Knickpoint relief (m)
										0.716	0.249	0.519	Mean annual precipitation (mm/yr)
											0.176	0.522	% strong rocks
												0.045	EVI

R<sup>2</sup> < 0.4  
R<sup>2</sup> = 0.4 - 0.6  
R<sup>2</sup> > 0.6

### 5.4.3 DENUDATION RATES VERSUS GEOMORPHIC METRICS

When  $^{10}\text{Be}$ -derived denudation rates are plotted against the catchment-averaged topographical parameters, a counter-intuitive, negative, statistically significant ( $p$ -values  $< 0.01$ ) allometric correlation ( $y = ax^b$ ; with a negative  $b$ ) is obtained (Figures 70-75). The relationships between denudation rates and topographic parameters indicate that denudation rates decrease non-linearly but monotonically with increasing catchment-averaged topographic metrics. Hence, basins associated with low normalised steepness index, or low catchment-averaged basin relief, or any other parameter, have higher average denudation rates than basins displaying lower catchment-averaged topographic metrics (Figures 70-72).

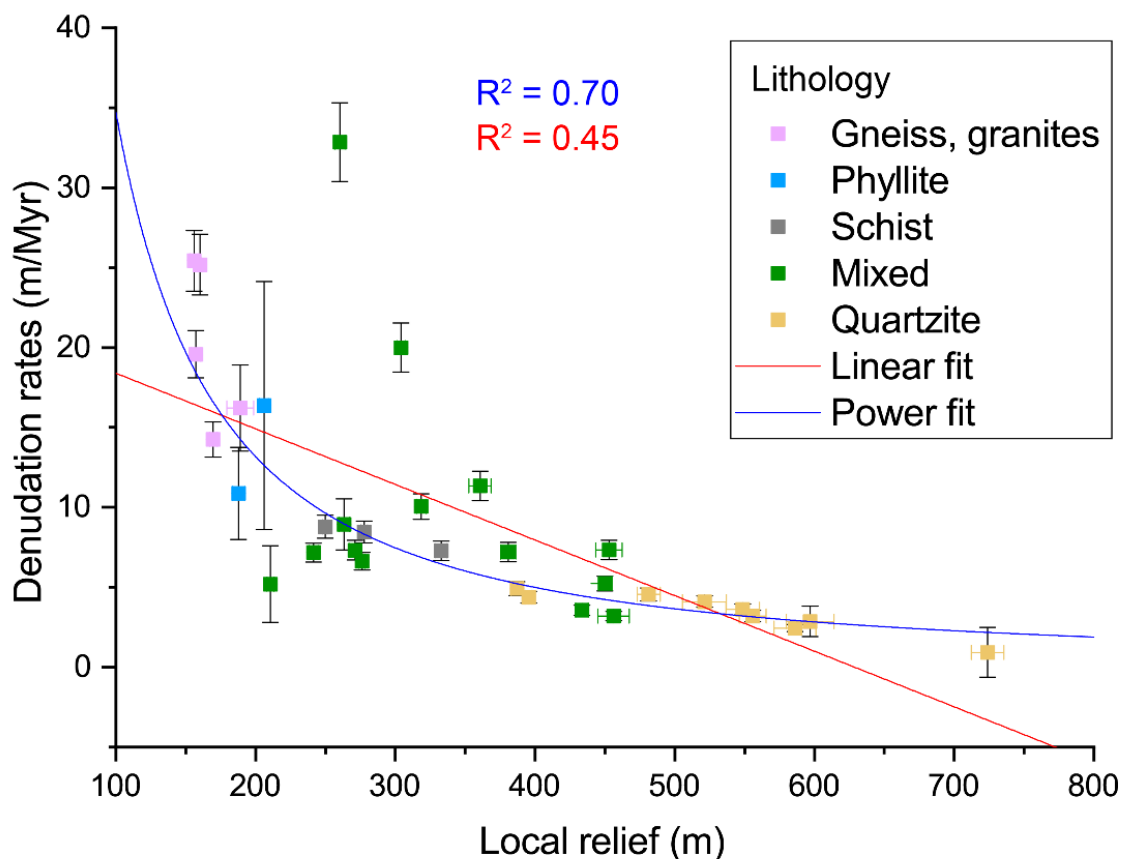


**Figure 70.** Scatter plot of catchment-averaged denudation rates and the local relief for the analysed basins. Y-error bars represent external uncertainty in denudation rates; X-error bars denote the standard deviation of the mean.

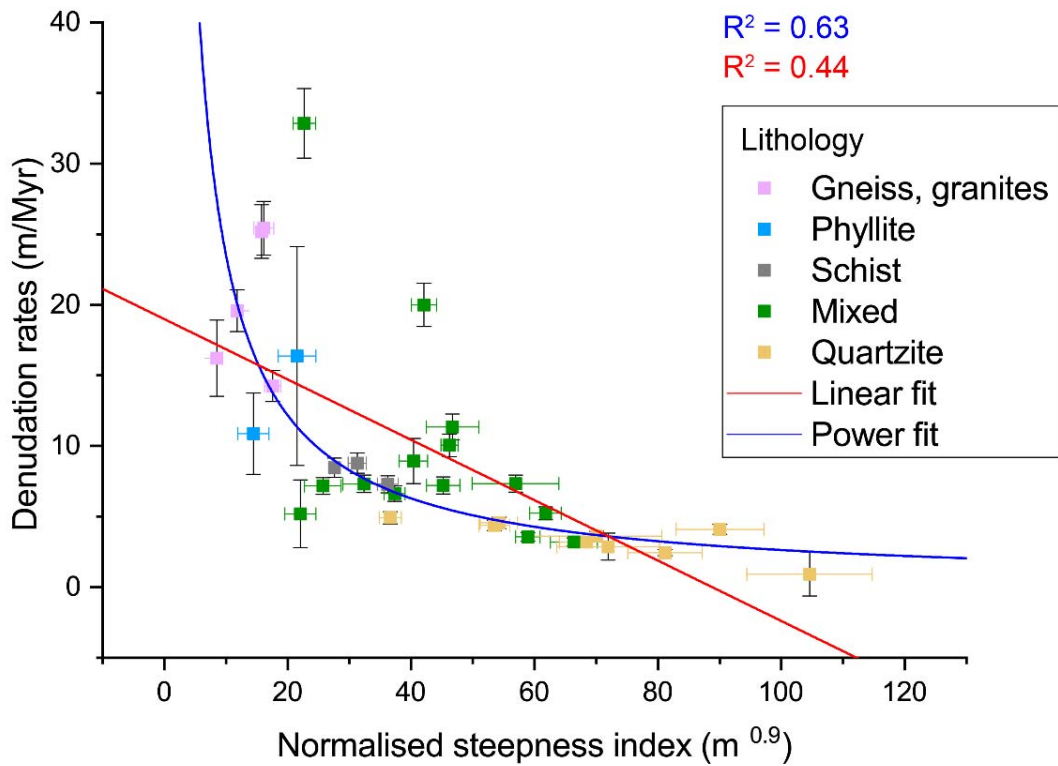


**Figure 71.** Scatter plot of catchment-averaged denudation rates and normalised steepness index for the analysed basins. Y-error bars represent external uncertainty in denudation rates; X-error bars denote the standard deviation of the mean.

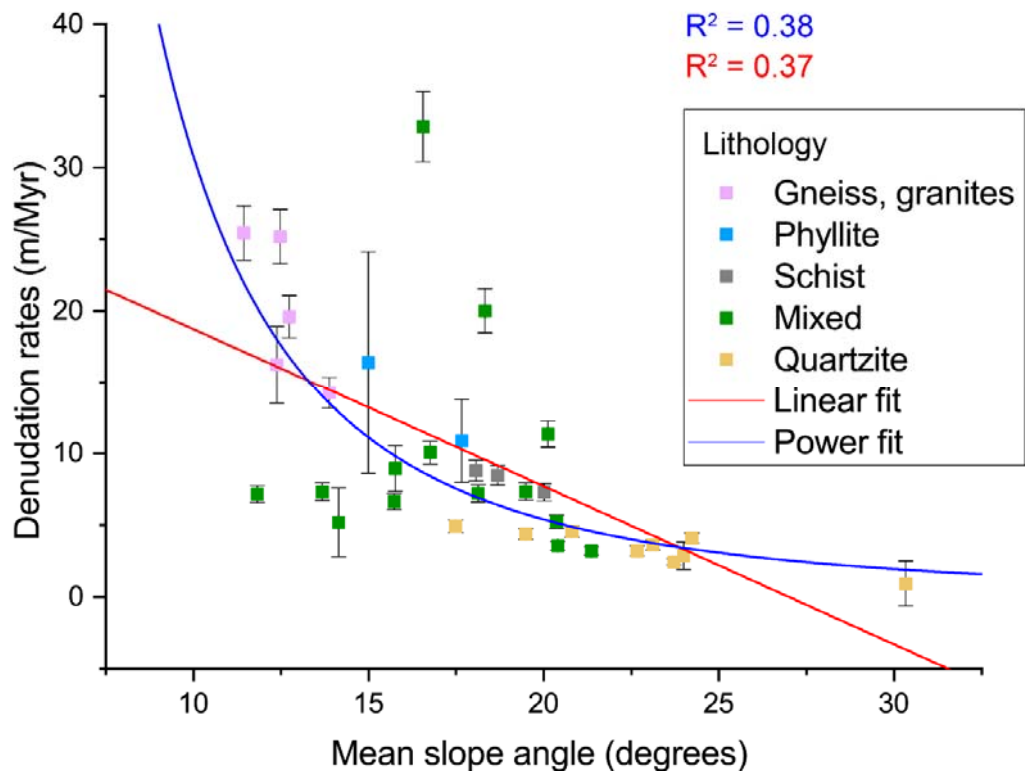


**Figure 72.** Scatter plot of catchment-averaged denudation rates and mean slope angle for the analysed basins. Y-error bars represent external uncertainty in denudation rates; X-error bars denote the standard deviation of the mean.

Power and linear models describe overall the relationship between denudation rates and catchment-averaged topographic metrics with similar goodness-of-fit (Table 12). The parameters local relief and normalised steepness index are the best regressors for denudation rates, with  $R^2$  values of 0.701 and 0.632, respectively, whereas mean elevation and basin relief yield the lowest correlation values of 0.324 and 0.344, respectively. Basin area is not correlated with denudation rates within an alpha-level of 0.05 (Figure 73). However, for a dataset consisting of only quartzite basins, basin area is weakly positively related with denudation rates ( $R^2 = 0.29$ ), meaning that quartzite basins with higher drainage areas are associated with higher denudation rates. The only parameter to yield a weak but positive relationship with denudation rates is the mean EVI (Figure 74). The goodness-of-fit of bivariate plots between denudation rates and every geomorphic parameter is shown in Table 12. A mosaic exhibiting the relationship between the other topographic parameters and denudation rates is presented in Figure 75.

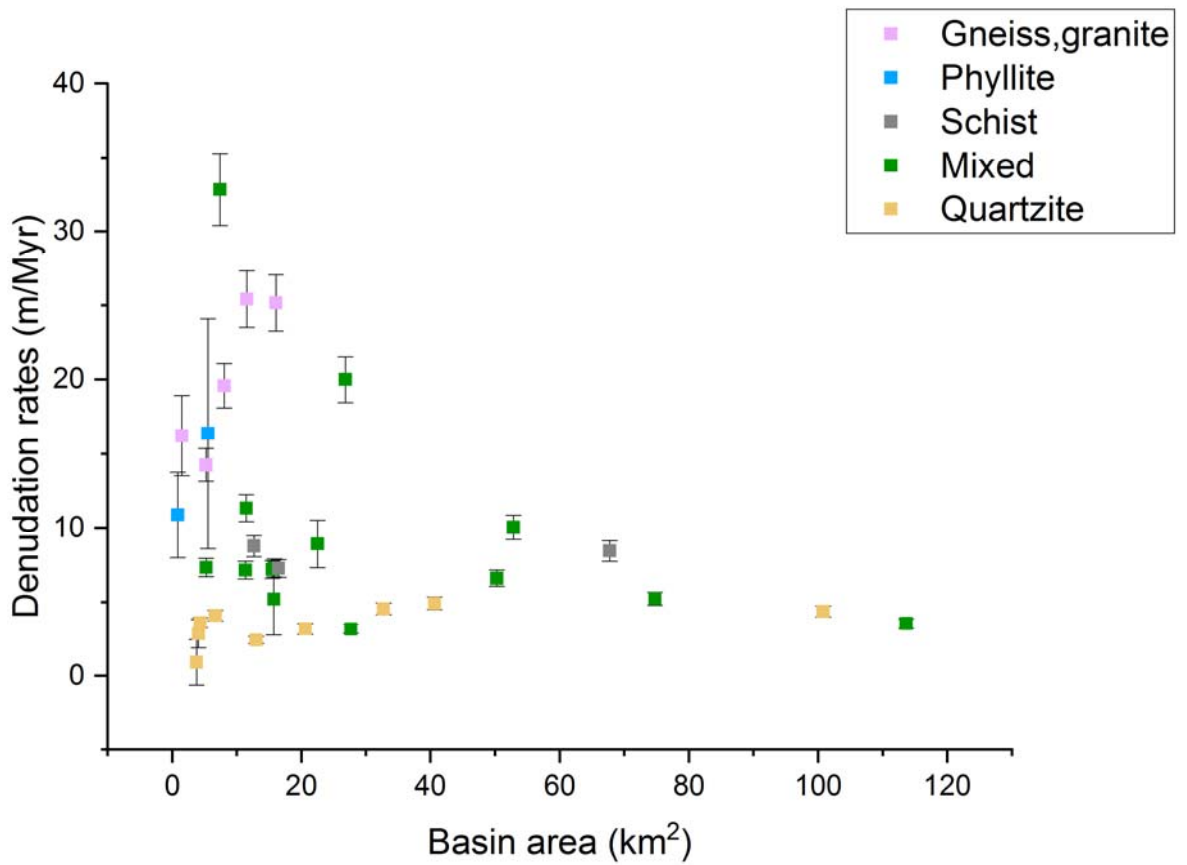


**Figure 73.** Scatter plot of catchment-averaged denudation rates and basin area for the analysed basins. Y-error bars represent external uncertainty in denudation rates.

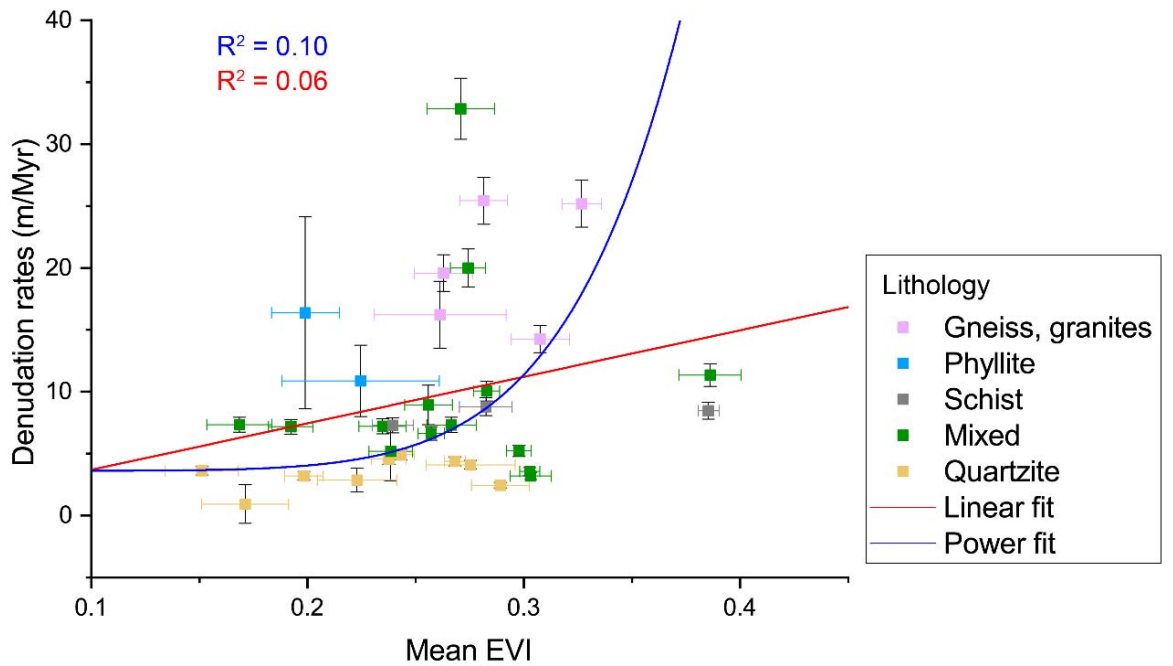


**Figure 74.** Scatter plot of catchment-averaged denudation rates and the mean EVI for the analysed basins. Y-error bars represent external uncertainty in denudation rates; X-error bars denote the standard deviation of the mean.

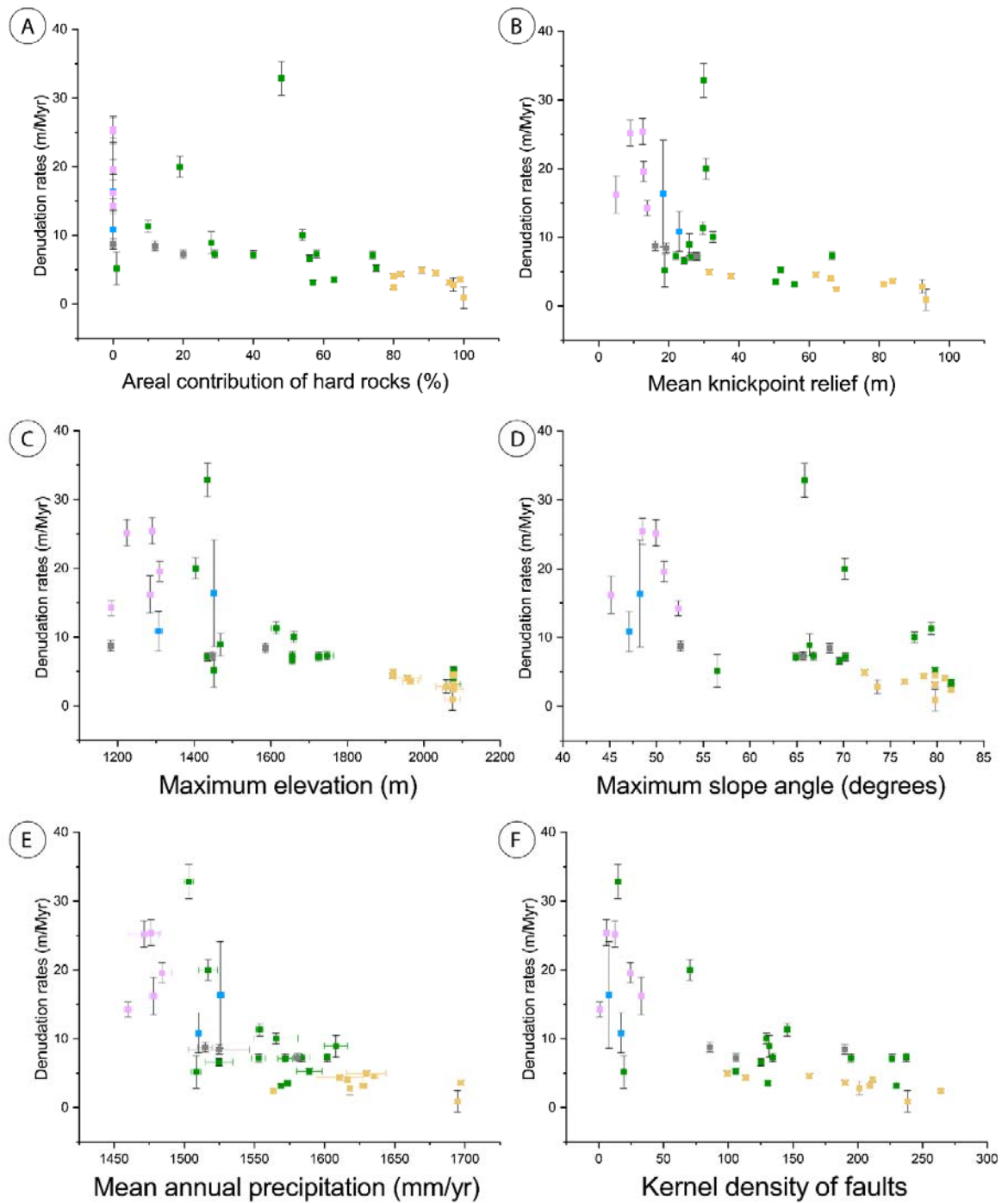


**Figure 75.** Mosaic of scatter plots between catchment-averaged denudation rates and the geomorphic parameters: (A) areal contribution of strong rocks; (B) mean knickpoint relief; (C) maximum elevation; (D) maximum slope angle; (E) mean annual precipitation; and (F) kernel density of faults. Y-error bars represent external uncertainty in denudation rates; X-error bars denote the standard deviation of the mean.

**Table 12.** Goodness-of-fit of linear and power models for bivariate plots between denudation rates and catchment-averaged parameters.

Geomorphic parameters	R <sup>2</sup> of bivariate regression with denudation rates	
	R <sup>2</sup> - Linear model	R <sup>2</sup> - Power model
Area (m <sup>2</sup> )	0.074	0.023
Max. slope (°)	0.381	0.532
Mean slope (°)	0.373	0.38
Local relief (m)	0.45	0.701
Max. elevation (m)	0.497	0.44
Mean elevation (m)	0.304	0.324
Basin relief (m)	0.368	0.344
$k_{sn}$ (m <sup>0.9</sup> )	0.44	0.632
Knickpoint magnitude (m)	0.314	0.401
Knickpoint relief (m)	0.352	0.52
Precipitation (mm/yr)	0.503	0.58
% of strong rocks	0.345	0.27
Mean EVI	0.067	0.101
kernel density of faults (km/km <sup>2</sup> )	0.517	0.45

Red - not significant at alpha-level of 0.05

Green - significant at alpha-level of 0.05, but not at 0.01

Blue - significant at alpha-level of 0.01

#### 5.4.4 LITHOLOGY AND ITS INFLUENCE ON TOPOGRAPHY AND DENUDATION RATES

The distribution of catchment-averaged topography per lithology indicates a positive relationship between topography and rock resistance, whereby in general the more resistant the exposed rock is to denudation, the steeper and more rugged is the topography of the catchment. Basins underlain by quartzites are associated with high catchment-averaged topography, contrasting primarily with gneisses, granites, and phyllite basins. For example, the median normalised steepness index for basins under quartzites (70 m<sup>0.9</sup>) is ~4.5 times higher than the median normalised steepness index for gneisses and granite basins (17 m<sup>0.9</sup>; Figure 76). The dispersion of values and the large standard deviation of the median for each parameter is visually clear in box plots, where the boxes are of different size depending on the lithological group considered. For instance, the distribution of maximum slope by lithological groups indicates that some mixed lithology basins are associated with a maximum slope angle that is as high as the highest slope angles for quartzite basins (Figure 77). However, the bulk of mixed lithology basins exhibit a maximum slope angle that is lower than the maximum slope angle for

quartzite basins. Also, basins under gneiss, granites, and phyllites are consistently associated with subdued catchment-averaged topographic parameters, and a lower variance, if compared to basins under quartzites or mixed lithologies. However, whereas the difference between end-member groups is pronounced, differences between the average-topography groups (i.e., basins under schists and mixed lithologies) and the end-member groups are less evident. For several geomorphic parameters, there is a marked overlapping between the higher-end of the distribution of mixed lithologies and quartzites basins, between the lower-end of the distribution of phyllites and gneiss and granite basins, and between the schist and mixed lithology basins. Also, there is a degree of overlap between the box plots for basins under schists and mixed lithologies, and basins under quartzites (Figure 77).

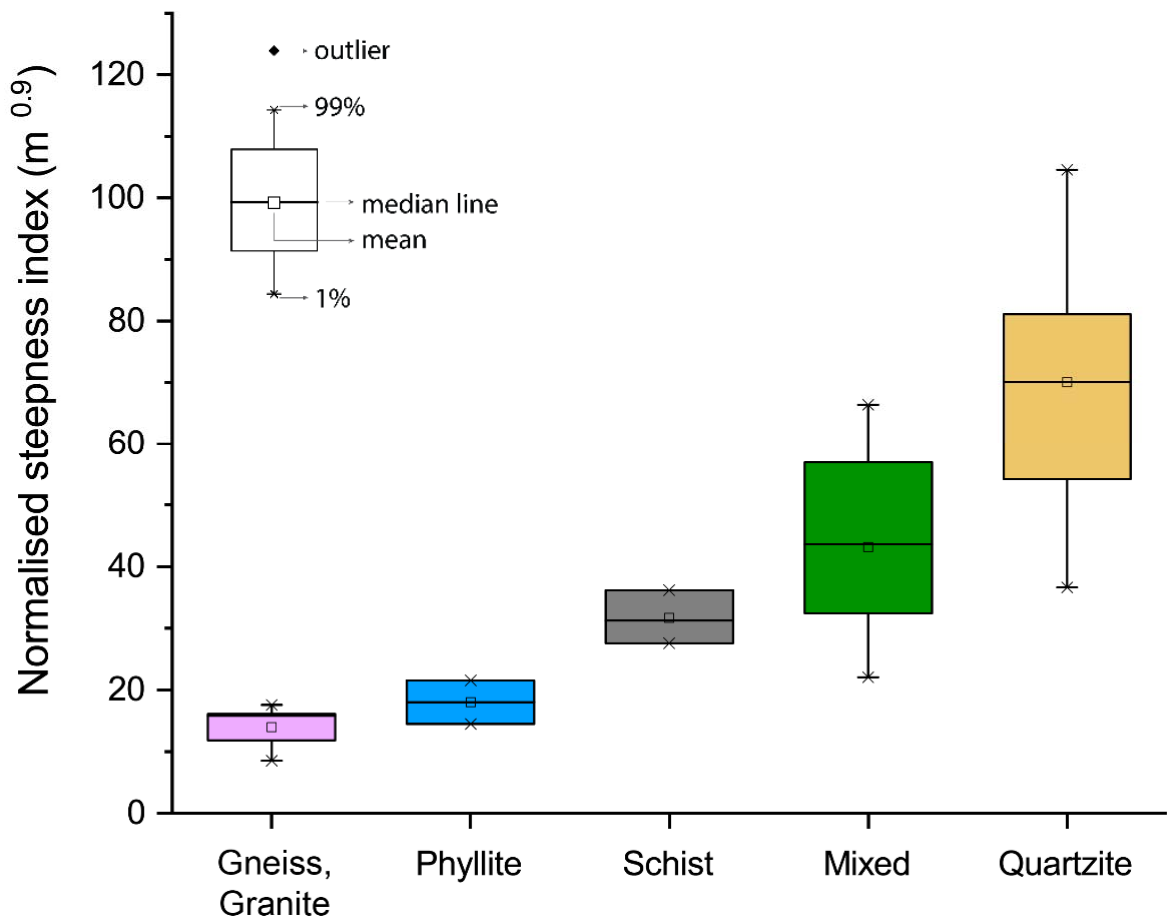
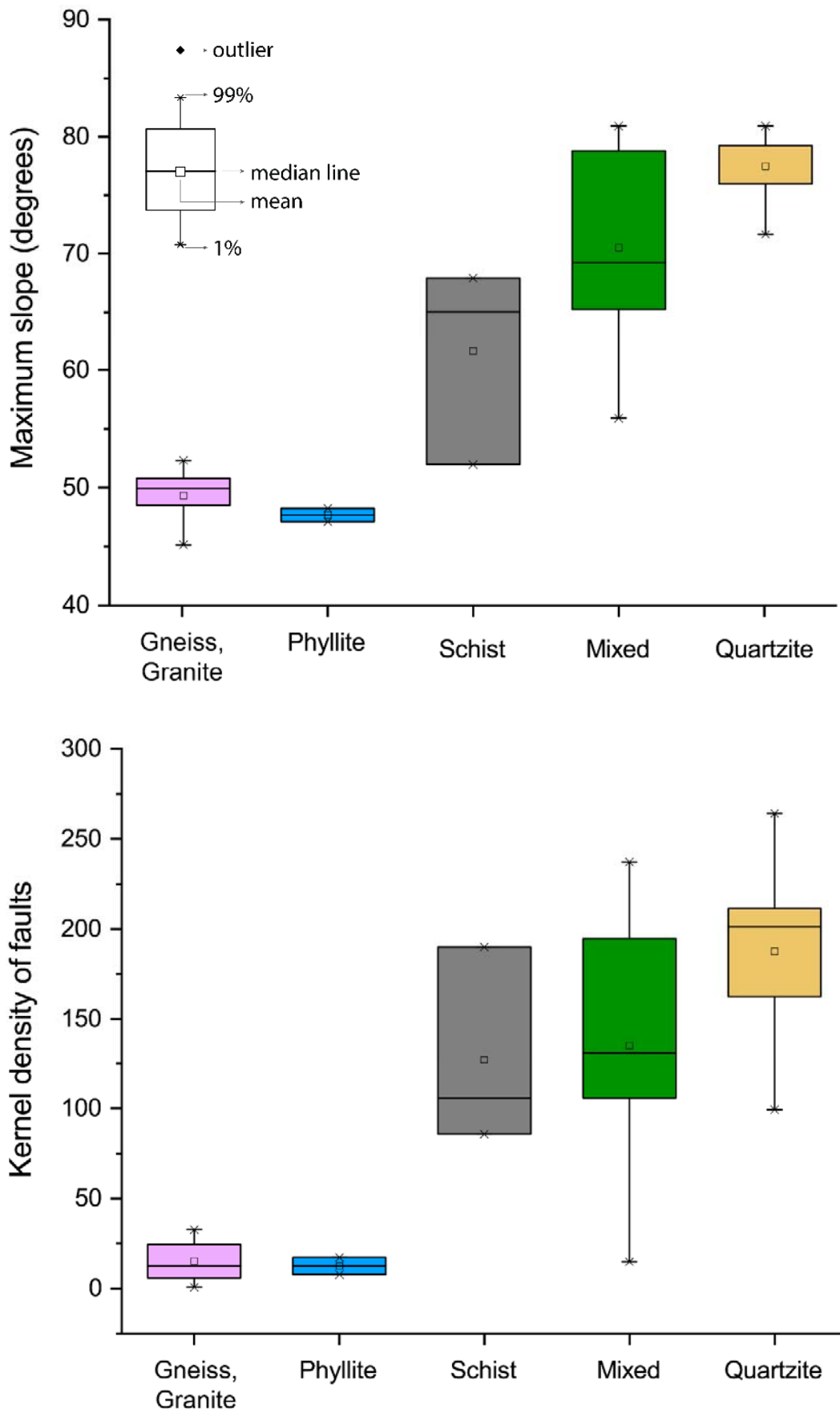


Figure 76. The distribution of catchment-averaged normalised steepness index per lithological group.



**Figure 77.** The distribution of catchment-averaged maximum slope angle (plot on the top of the figure) and kernel density of faults (plot on the bottom of the figure) per lithological group.

On the other hand, there is a positive relationship between rock resistance and denudation rates: the basins underlain by quartzites are associated with the slowest denudation rates ( $\sim 0.7\text{-}4\text{ m/Myr}$ ), the basins under non-resistant schists or mixed lithologies denude a little faster ( $\sim 4\text{-}10\text{ m/Myr}$ ), and the basins under the least-resistant gneisses and granitic rocks, as well as basins under phyllites, denude at faster rates of up to  $25\text{ m/Myr}$  (Figure 78).

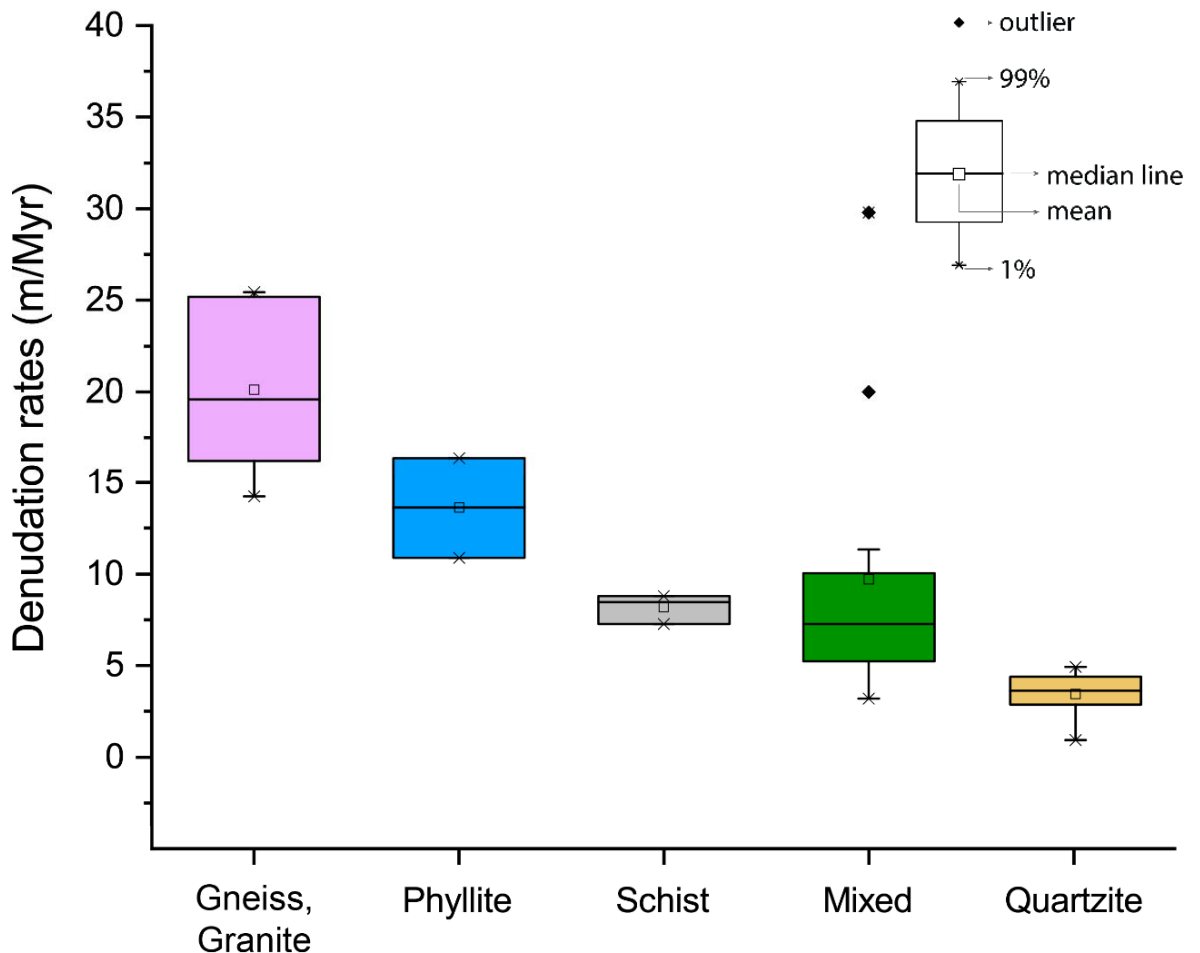


Figure 78. The distribution of catchment-averaged denudation rates per lithological group.

#### 5.4.5 PRELIMINARY ESTIMATES OF THE RELATIVE VALUES OF $K$ IN THE QF

The  $^{10}\text{Be}$ -derived denudation rates allow for the value of  $K$  to be estimated using Equation (32). If the drainage area exponent  $m$  is set to 0.4 (following Stock and Montgomery, 1999), and the slope exponent  $n$  is varied from  $2/3$  (Figure 79) to 1 (Figure 80) and then 2 (Figure 81), a series of values of  $K$  for the QF can be obtained. Irrespective of the values of  $n$ , the pattern of distribution of  $K$  values are the same. Basins underlain by quartzites, denuding slowly, display overall low  $K$  values. Basins underlain by schists and mixed lithologies are associated with

higher  $K$  values, whereas basins underlain by gneisses and granites, as well as phyllite basins, show  $K$  values that are two to three orders of magnitude higher than the  $K$  values for quartzite basins. Assuming  $m = 0.4$  and  $n = 1.0$ , the median  $K$  values for the quartzite basins are  $3.2 \times 10^{-8}$  ( $\text{m}^{0.2}/\text{yr}$ ), the basins underlain by schist and mixed lithologies display a median  $K$  of  $1.8 \times 10^{-7}$  ( $\text{m}^{0.2}/\text{yr}$ ), whereas the basins underlain by gneiss and granitic rocks, as well as phyllites, exhibit a median  $K$  of  $1.4 \times 10^{-6}$  ( $\text{m}^{0.2}/\text{yr}$ ). These values are on the low end, but comparable with the reported  $K$  values by Stock and Montgomery (1999; Table 13). Mixed lithology basins have variable preliminary  $K$  values, about an order of magnitude lower in those catchments where upstream quartzite is present.

**Table 13.** Bedrock erodibility factor ( $K$ ) values reported in this contribution and by Stock and Montgomery (1999).

Quadrilátero Ferrífero		
River	Lithology	Mean 'K'
Caraça	quartzites	$3.2 \times 10^{-8}$
Das Velhas	schists and mixed lithologies	$1.8 \times 10^{-7}$
Das Velhas	gneiss and granitic	$1.4 \times 10^{-6}$
Australia		
River	Lithology	Mean 'K'
Tumambarumba	granitoids	$1.1 \times 10^{-6}$
Tumut	metasediments	$2.3 \times 10^{-6}$
Wheeo	granitoids	$4.4 \times 10^{-7}$
Lachlan	metasediments	$4.3 \times 10^{-6}$
California		
River	Lithology	Mean 'K'
Cowlet	volcaniclastics	$8.2 \times 10^{-5}$
French	volcaniclastics	$4.8 \times 10^{-5}$
Swede	volcaniclastics	$3.0 \times 10^{-4}$
Japan		
River	Lithology	Mean 'K'
Iwaki	mudstones	$7.0 \times 10^{-3}$
Sakuzawa	volcaniclastics	$4.7 \times 10^{-4}$

Assuming  $m = 0.4$  and  $n = 1.0$ . Data source: Stock and Montgomery, 1999.

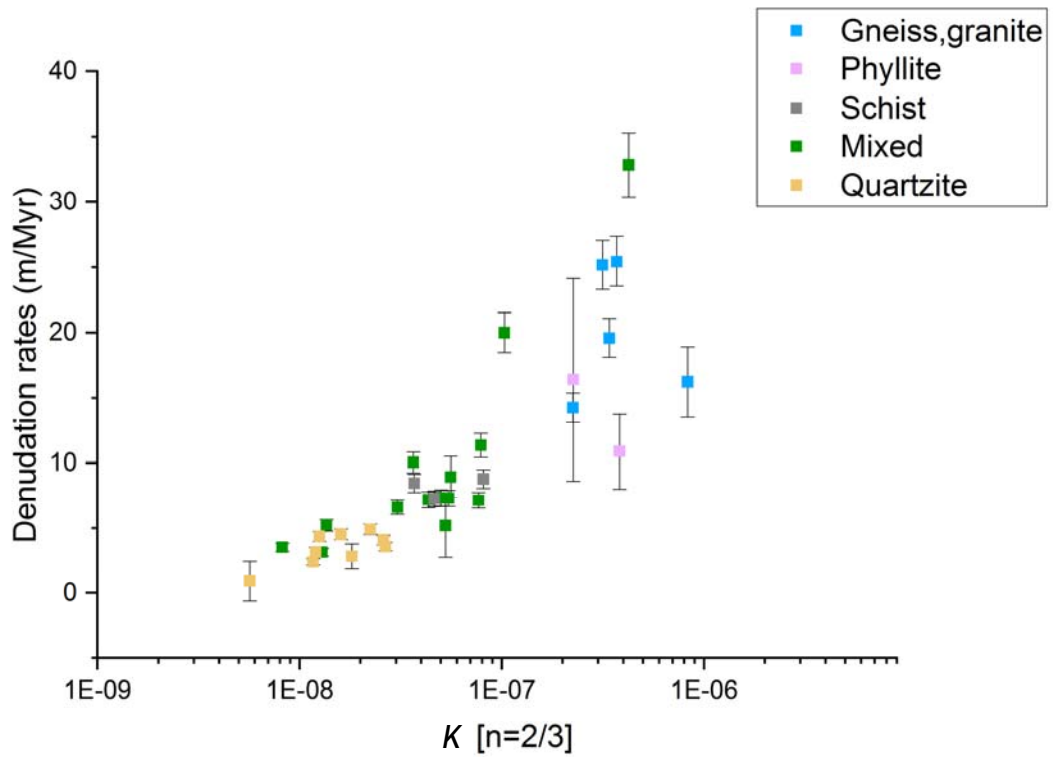


**Figure 79.** Scatter plot of the preliminary estimates of K per basin, and its associated denudation rates. Assuming  $m = 0.4$ , and  $n = 2/3$ . Y-error bars represent external uncertainty in denudation rates.

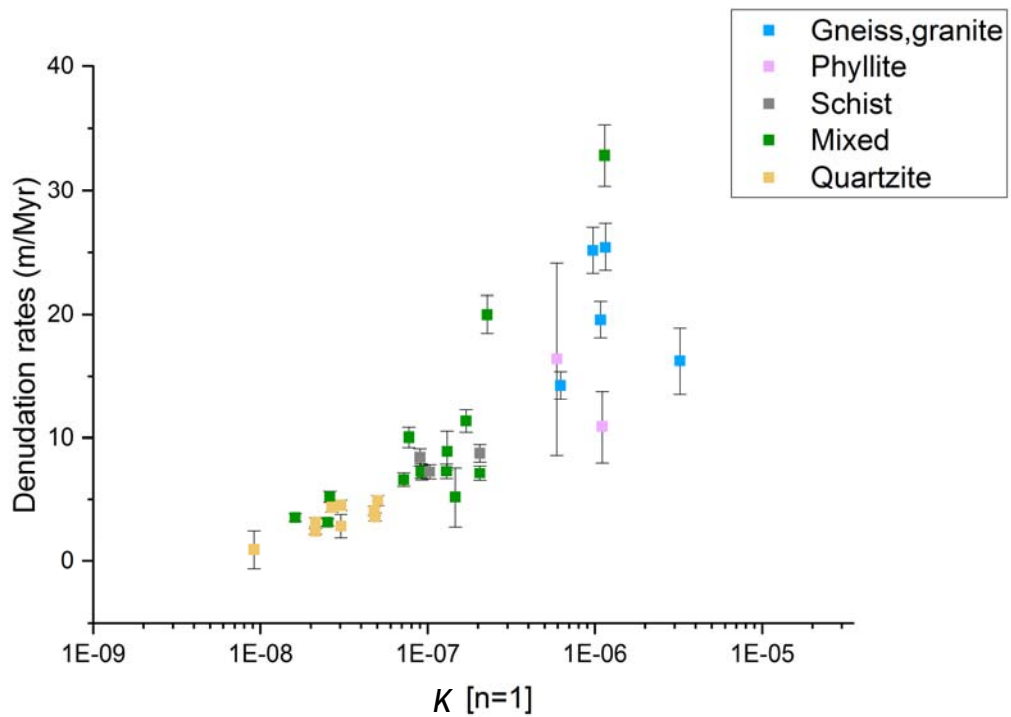


**Figure 80.** Scatter plot of the preliminary estimates of K per basin, and its associated denudation rates. Assuming  $m = 0.4$ , and  $n = 1$ . Y-error bars represent external uncertainty in denudation rates.

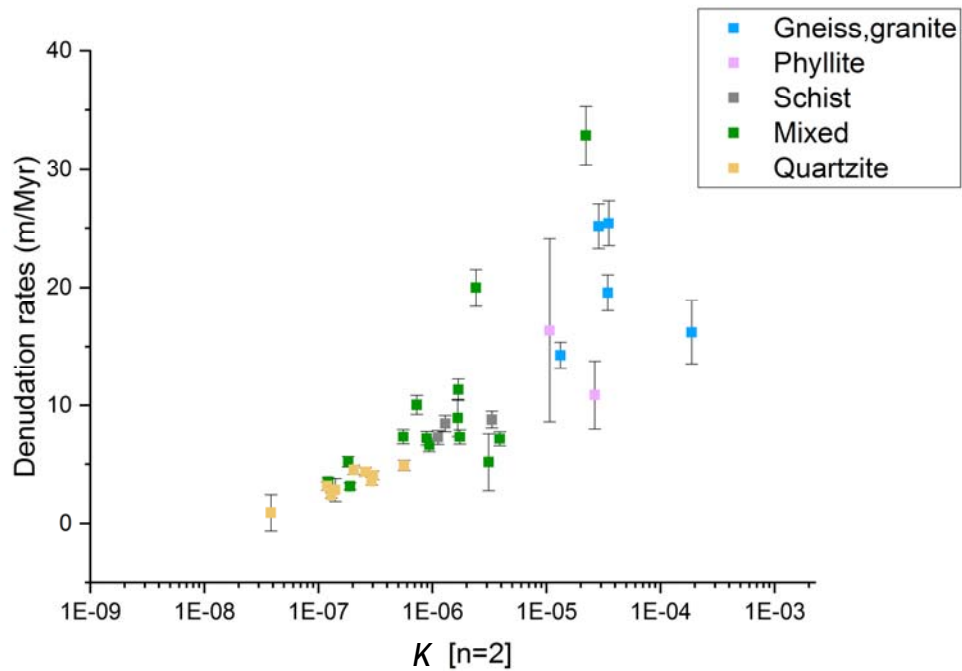


**Figure 81.** Scatter plot of the preliminary estimates of  $K$  per basin, and its associated denudation rates. Assuming  $m = 0.4$ , and  $n = 2$ . Y-error bars represent external uncertainty in denudation rates.

#### 5.4.6 SUMMARY OF THE RESULTS

- The  $^{10}\text{Be}$ -derived catchment-averaged denudation rates for the QF are overall low ( $\leq 30$  m/Myr);
- Denudation rates are spatially variable in the QF. Basins located in the eastern part of the QF, over the Caraça Range, are associated with low denudation rates, contrasting with the faster denudation rates of basins located in the southwestern part of the QF;
- Catchment-averaged denudation rates display a negative correlation with every catchment-averaged topographic parameter, including the normalised steepness index, local relief, and mean slope angle;
- Rock resistance and topography are positively related in the QF; the more resistant the exposed rock is to denudation, the higher and more rugged is the basin relief;
- Rock resistance and denudation rates are positively related: basins underlain by quartzite denude slowly ( $0.7 \pm 0.4 - 4.0 \pm 0.3$  m/Myr), the catchments underlain by less resistant schists or mixed lithologies denude a little faster ( $\sim 4-10$  m/Myr), and the basins

underlain by the least-resistant gneisses and granitic rocks, as well as phyllites, denude the fastest at rates of up to 25 m/Myr;

- Preliminary estimates suggest a two- to three orders of magnitude gradient in  $K$  values in the QF, with basins under quartzites associated with low  $K$  values ( $3.2 \times 10^{-8} \text{ m}^{0.2}/\text{yr}$ ), contrasting with higher  $K$  ( $1.4 \times 10^{-6} \text{ m}^{0.2}/\text{yr}$ ) values related to basins under gneisses and granites, and phyllites.

## 5.5 DISCUSSION

The analysis presented in Chapter 4 has shown that the post-orogenic landscape of the QF has a wide range of topographic forms, with a generally subdued steepness and relief but marked by rare, extremely steep channel and hillslope gradients. Steepness and relief appear to be adjusted to bedrock strength, consistent with the old geomorphic maxim that steep terrains are related to strong rocks and vice-versa (e.g., Playfair, 1802; Gilbert, 1877). This apparent adjustment of topography to rock resistance prompts the question if this is a result of an equilibrium adjustment as hypothesized by Hack (1975), implying that denudation rates would be spatially uniform, or if relief is set by the differential resistance of different rocks that are denuding at varying rates. In addition, the landscape presents different forms under rocks of the same resistance; in particular the eastern part of the Caraça Range is extremely steep, associated with small magnitude earthquakes (Figure 8) and with Cenozoic deformations (e.g., Saadi et al. 1992; Sant'anna et al., 1997; Santos et al., 2004; Cabral and Koglin, 2014), contrasting with the lower relief and the less rugged topography of the western part of the Caraça Range. The variability in forms within the same rock type has been hypothesized, in general, as the result of differential rock uplift; in this case the areas affected by the higher rock uplift should yield higher denudation rates than the more stable areas (cf. Quigley et al., 2007). Quantification of denudation rates in catchments with different lithologies and topography is therefore the key to test these various hypotheses of landscape evolution in post-orogenic settings.

The denudation rates presented in this chapter suggest that the spatial distribution of rocks with different resistance is the first-order control on the

pattern of denudation in the QF. The extremely low denudation rates of the quartzite basins, irrespective of their topography, and the higher denudation rates of basins under less resistant rocks (and less rugged topography), demonstrate that exposed bedrock resistance is effectively overriding steepness (channel and hillslope) in determining denudation rates. The negative, statistically significant landscape-scale relationships between denudation rates and basin topography for the QF are counter-intuitive results, because the notion that denudation rates vary primarily as a function of the steepness and relief of landscapes is deeply rooted in geomorphology (cf. Wobus et al., 2006; Kirby and Whipple, 2012). The issue may be here that rates of denudation derived from the steep tectonically active terrains (e.g., Wobus et al., 2006; Kirby and Whipple, 2012) are usually orders of magnitude faster than those typical of low relief, post-orogenic landscapes (e.g., Bishop et al., 1985; Bishop and Goldrick, 2000; Bierman and Caffee, 2001, 2002; von Blanckenburg, 2004, 2005; Scharf et al., 2013); if these two types of landscapes are compared, then the positive relationship between steepness and denudation rates holds (e.g., Portenga and Bierman, 2011). The QF is not an exception to this empirical 'rule', exhibiting consistently low denudation rates of no more than 30 m/Myr. However, denudation rates are not uniformly slow, but vary by a factor of ~5 from east (< 4 m/Myr) to southwest (up to 30 m/Myr) in the QF. The empirical dataset presented in this chapter demonstrates that basins characterised by extremely steep terrain may be associated with lower denudation rates than lower steepness basins, if the lithology of the steep basins is more resistant than the lithology of the lesser steep basins. Other contributions have posited that lithology may override steepness and relief in the determination of denudation rates (Cyr et al., 2014), still the denudation pattern of the QF is the first empirical dataset to demonstrate how bedrock resistance can be the primary control on denudation, even inverting the normal, positive relationship between denudation and relief.

Estimates of denudation rates on post-orogenic settings are consistently low (Bishop et al., 1985; Bishop and Goldrick, 2000; Bierman and Caffee, 2001, 2002; von Blanckenburg, 2004, 2005; Scharf et al., 2013). This empirical observation, added to the consensual understanding that denudation rates vary as a function of steepness and relief, have led to an (almost implicit) interpretation that the low denudation rates of post-orogenic landscapes are a result of their subdued

topography (and related absence of ongoing tectonic activity). Hence, the association of low denudation rates and extremely steep channel and hillslope gradients found in other post-orogenic settings (e.g., von Blanckenburg, 2004; Scharf et al., 2013), has been difficult to explain, although the negative correlation between steepness and denudation rates has never been observed and measured before; there were a few examples of catchment-averaged denudation rates decoupled from basin topography, in which relief is controlled by bedrock erodibility (e.g. Riebe, et al., 2000; Cyr et al., 2014). One reason why the QF is the first area where denudation rates are found to be negatively correlated to relief may be a factor of the sampling strategy. Previous studies concentrated on high relief areas under resistant rocks, whereas low-steepness basins under low-resistance rocks were not sampled (e.g., von Blanckenburg, 2004; Scharf et al., 2013).

In previous studies, low denudation rates measured in high relief, post-orogenic areas have been taken to indicate that there is no active tectonics and that these landscapes are relicts that persist due to the high resistance of the bedrock lithology (e.g., von Blanckenburg, 2004; Scharf et al., 2013). In accordance, the antiquity of landscapes is a highly debated issue in geomorphology and, for many years, their existence and importance were championed by ‘dissonant voices’ (e.g., Twidale, 1976; Young, 1983; Twidale, 1999). Reasons given for their survival included long-term tectonic stability, the presence of rocks resistant to weathering and erosion, denudational isostatic compensation, and ‘unequal activity’ whereby the erosional power of the rivers is restricted to the channels and immediately adjacent areas, contrasting with the less erosive hillslopes (Twidale 1976, 1991, 1994, 1999). The spatial distribution of lithologies with different strength and the unequal characteristics of the erosional activity led to a geomorphic differentiation in the Twidale-type landscape and an increase of relief through time, with denudation concentrated in channels flowing through low-resistance rocks and the preservation of uplands under the resistant rocks (Twidale, 1976, 1991, 1994, 1999; Figure 82). This conceptual model lacked empirical data on rates of surface processes. On the contrary, available estimates of denudation rates from ‘ancient landscapes’ were interpreted as evidence against this conceptual model. By contrast, this contribution yields denudation rates that are consistent with this scheme, showing a landscape-scale record of

upstream basins under resistant lithologies and with steep basin topography associated with slow denudation, contrasting with basins under non-resistant lithologies that are denuding at a faster rate. One of the most significant implications of the spatial variability in denudation rates of the QF is that as the uplands, under resistant rocks, are denuding slower than downstream areas under lower resistance rocks, the uplands are not only being preserved, but relief is effectively increasing through time instead of decreasing. This finding is very reminiscent of Crickmay's (1975) unequal activity model, whereby the net activity of surfaces process is concentrated in river valleys, leaving uplands "dead quiet" (Crickmay, 1975, p. 105). In addition, the spatial variability of denudation rates also implicates that the hypothesis that the QF is in an equilibrium state, downwasting everywhere at the same rate, is not consistent with this empirical dataset.

Early estimations of the timescale of relief reduction on post-orogenic landscapes yielded decay timescales of ~10-25 Myr by using the straight-forward approach of dividing mean elevation by denudation rates (e.g., Gilluly, 1955; Schumm, 1963; Judson and Ritter, 1964; Thornbury, 1969). However, Young (1983) pointed out that the erosion rates used as input in these estimates may have been faster than the representative erosion rates of post-orogenic settings (Bishop, 2007). Using this rationale for the QF, the division of the mean elevation of quartzite basins (1520 m) by the median denudation rate (3.6 m/Myr) yields preliminary decay timescales of ~400 Myr; for mixed lithology basins decay timescales are ~160 Myr; gneiss and granite basins yield decay timescale of ~50 Myr. These rough estimates indicate much longer timescales of post-orogenic relief reduction than the estimates discussed in section 3.2.2. They thus suggest that the conceptual rationale of a post-orogenic landscape that may be able to maintain its relief over a very long time because of its extremely slow denudational pace can be reasonable, and, in the case of the QF, is consistent with the geological history. The antiquity of the QF landscape is also consistent with geochronological  $^{40}\text{Ar}/^{39}\text{Ar}$  ages from weathering profiles located in the Moeda plateau in the western part of the QF (e.g., Carmo and Vasconcelos, 2004; Spier et al., 2006) and goethite (U-Th)/He geochronology (Monteiro et al., 2014; Monteiro et al., 2018) on banded iron formations and iron duricrusts in the Moeda plateaux and the Gandarela Range that suggest that the QF has been sub-aerial for at least ~70

Myr. Also, the distribution of these thermochronometric ages with elevation indicates that surfaces at higher elevations are older than those lower down (Monteiro et al., 2014; Monteiro et al., 2018).

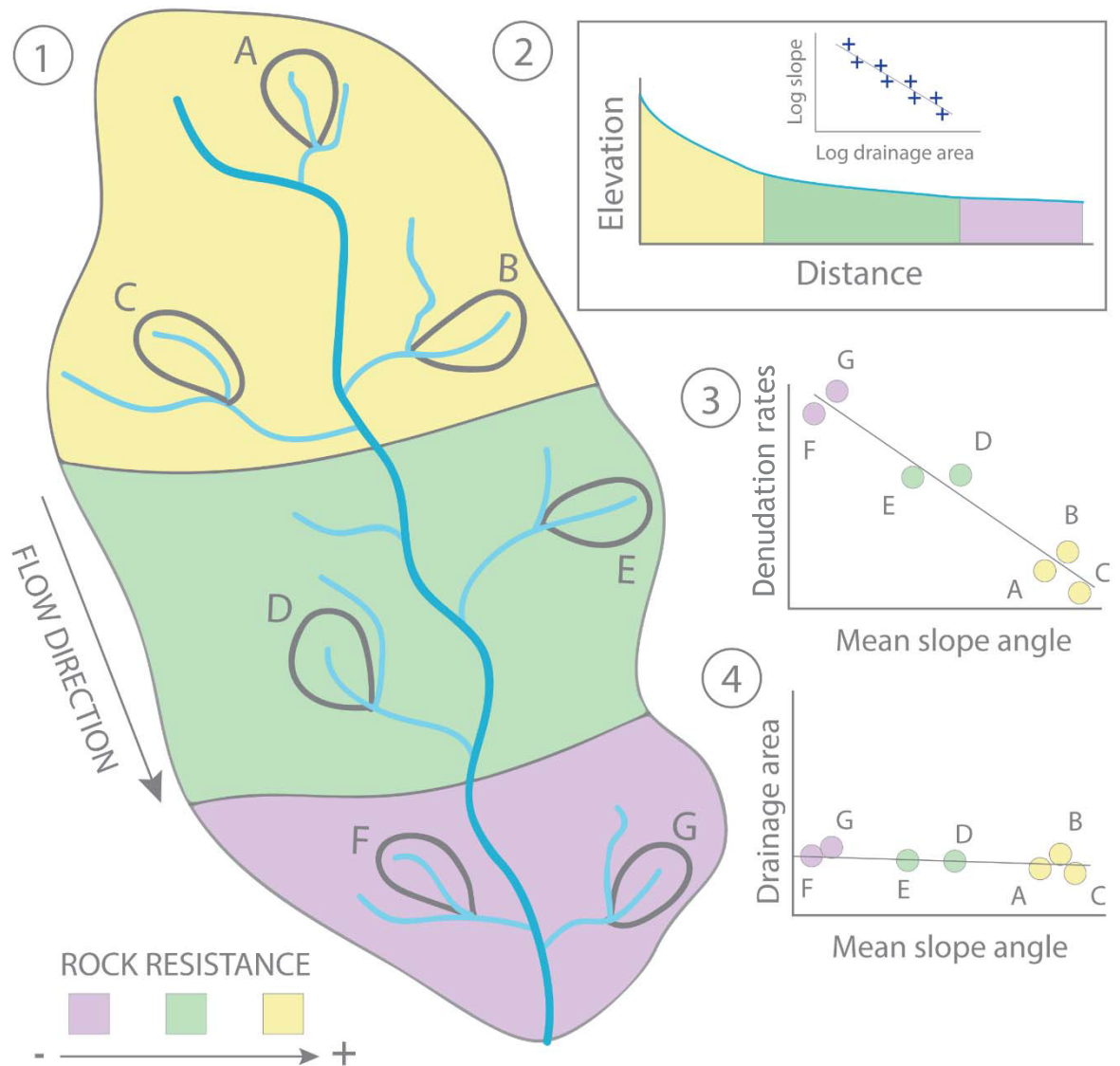


**Figure 82.** Schematic representation of the Twidale-type landscape. (1) Map-view of a representative Twidale-type drainage basin. (2) The main river displays a concave upward longitudinal profile with channel slope positively related to bedrock strength, and a regular scaling between slope and area in its slope-area plot. (3) Catchment-averaged erosion rates are inversely related to rock resistance and basin-wide geomorphic metrics. Catchment-averaged topography is positively correlated with rock resistance. (4) The sub-catchments A, B, C, D, E, F, G have similar areas. Uplands under resistant rocks are high because they denuded less and more slowly than their surroundings.

The addition of the effect of isostatic rebound to the simple calculations presented before increases the persistence of the landscape by a factor of 5-6 and thus, decay timescales would be ~2500 Myr for quartzite basins; ~1000 Myr for

mixed lithology basins, and ~300 Myr for basins underlain by gneisses and granitic rocks. In fact, “if we accept the fundamental reality of the principle of isostasy (Lachenbruch and Morgan, 1990), denudational rebound must follow as a matter of course, except in situations where such rebound is prevented by countervailing tendencies such as extreme crustal rigidity and/or active tectonic subsidence” (Bishop and Brown, 1992, p. 754). The interpretation that denudational isostatic compensation has played a role in the post-orogenic history of the QF reinforces the hypothesis that this landscape may be able to maintain its relief over hundreds of Myr even without ongoing tectonic activity (the estimated decay is much longer than the timespan since its last tectonic activity 500 Ma). The distribution of knickpoints presented in Chapter 4 and, in particular, with the fact that many of them lie at very similar elevation underlain by quartzites, separating a high relief downstream sector from a high elevation, low relief upstream areas, may be regarded as similar to the predicted for a landscape that is responding to a ‘bottom-up’ perturbation in which isostatic compensation could be the cause (cf. Bishop and Goldrick, 2010). On the other hand, the argument that knickpoints are related to the denudation-driven rebound is not conclusive. Some of the knickpoints are found at even higher elevations within the quartzite-dominated uplands, creating a localised high-relief landscape, and some lie close to pre-Paleozoic faults. If active tectonic activity can be recorded by an increase in denudation rates, as often hypothesised (e.g., Quigley et al., 2007), the cosmogenic data do not show any change in denudation rates near the faults, but more work is required to fully establish the role of these faults on the evolution of the present landscape.

The preliminary estimate of  $K$  values for the QF suggests that basins underlain by quartzites are associated with low median  $K$  values ( $3.2 \times 10^{-8} \text{ m}^{0.2}/\text{yr}$ ), contrasting with values that are two to three orders of magnitude higher for basins underlain by gneisses and granites. While these values may be only a first approximation, they are consistent with the reported  $K$  values by Stock and Montgomery (1999). These results may indicate that the bedrock resistance, and its associated  $K$  values, modulates the way the topography is linked to denudation rates. The ‘modulation’ occurs because the very low values found for the strong rocks swamp changes in the other parameters ( $A$  and  $S$ ) and dominate Equation (1), always reducing denudation rates to very low values; when  $K$  is higher, denudation rates

can also be higher. In the case of the QF, upstream areas underlain by quartzites (with very low  $K$ ) might be associated with steep and rugged relief and still exhibit a low denudation rates. By contrast, downstream areas, on rocks with higher  $K$ , are associated with a faster denudational pace, despite their gentle relief.

This way of interpreting  $K$  as a main factor in determining denudation rates prompts questions about the main-stream view of interpreting denudation as primarily controlled by the topographic parameters. For instance, Pinet and Souriau (1988) have shown that tectonically active and post-orogenic landscapes are characterised by contrasting relationships between basin topography and denudation, whereby in the former an increase in mean elevation is associated with a much higher increase in denudation rates than for the latter (Figure 83). Hence, the dataset in this contribution prompts the question of to what extent the differences in topographic and denudational behavior between active and inactive settings is a function of differences in bedrock erodibility  $K$  (Berner and Berner, 1987; Raymo and Ruddiman, 1992; Summerfield and Hulton, 1994). The positive relationship between mean EVI and the denudation rates of the QF (although with an extremely low correlation value), possibly indicates that weathering is critical, as the chemically inert quartzite must weather very slowly compared to the less resistant units in the QF (e.g., Dixon et al., 2009). Measuring how weathering rates vary as a function of lithology (as well as  $K$ ) for post-orogenic landscapes would be an important direction for future work.

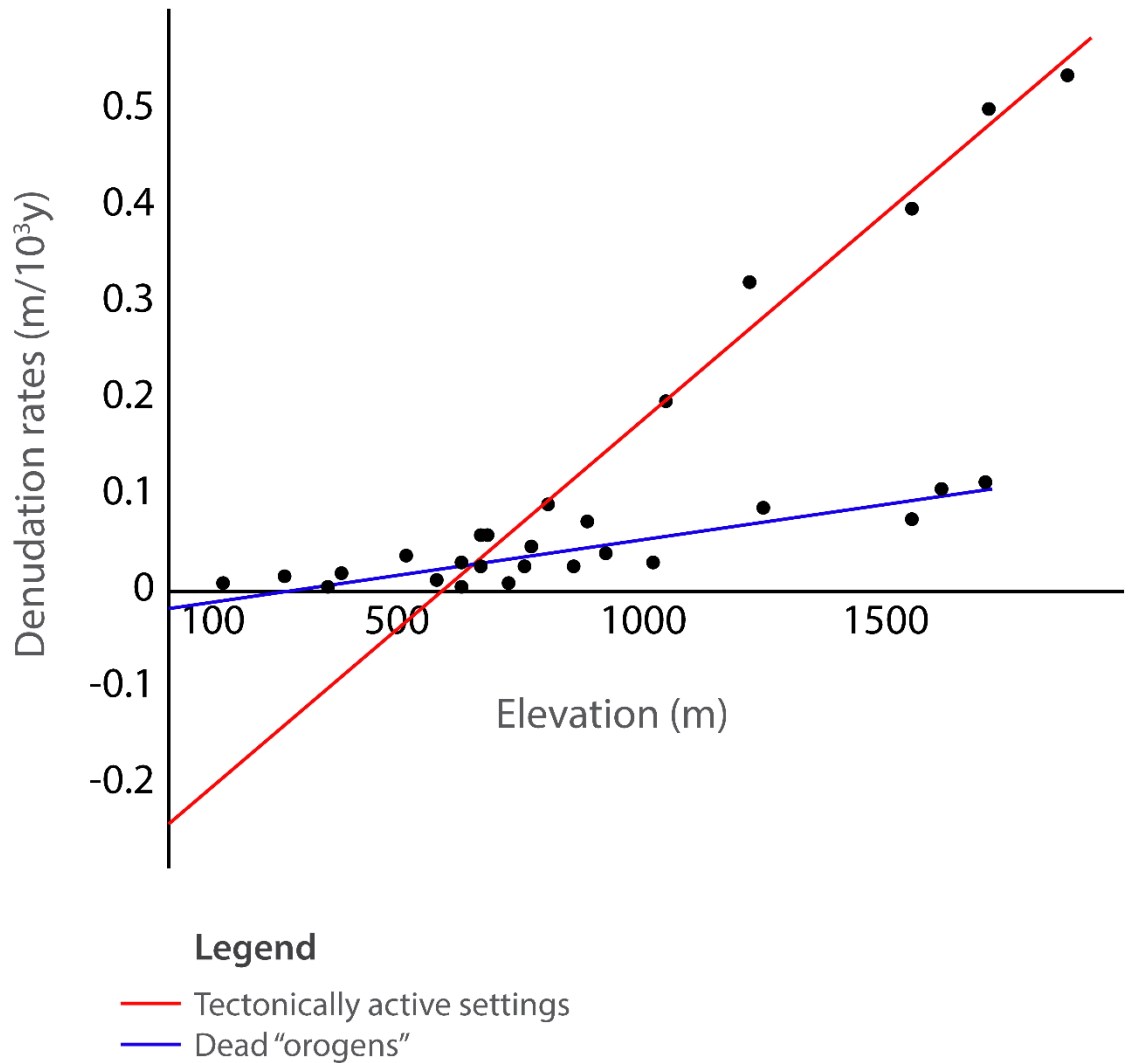


**Figure 83.** Schematic representation of how denudation rates and mean elevation are related in tectonically active settings (in red), and in 'dead' orogens (in blue). Modified from Pinet and Souriau (1988).

Other contributions indicating an association of low denudation rates and high basin relief in post-orogenic settings have ruled out the possibility of ongoing tectonic activity, principally because the denudation rates were very low (e.g., von Blanckenburg, 2004; Scharf et al., 2013). If the resistance of bedrock modulates the way that topography is linked to denudation rates, then basins under areas of very low  $K$  values may be associated with low denudation rates despite tectonic activity. Hence, if the ongoing tectonic activity was affecting a landscape by primarily making basins steeper, and these steep bits of the landscape were associated with rocks with very low  $K$  values, denudation rates would be low irrespective to the steep relief of these areas. The sampling strategy of this contribution included a large number of basins in the eastern part of the Caraça Range, the region often considered as the most affected by Cenozoic

deformation in the QF (e.g., Saadi, 1991; Maizatto and Castro, 1993; Maizatto, 1997; Sant'anna et al., 1997). However, these eastern Caraça Range basins are, irrespective of their steep relief, consistently associated with low denudation rates that decrease in the upstream direction, with a minimum denudation rate of  $0.7 \pm 0.4$  m/Myr for basin S5. Whereas there is no evidence of the influence of tectonic activity on the denudation rates of the QF, it is also not possible to rule it out.

In summary, the dataset presented in this chapter suggests that the exposed bedrock resistance is a first-order control on the pattern of denudation of the QF. The extremely low denudation rates of the quartzite basins, irrespective of their steep topography, and the contrasting denudation rates of basins under less resistant rocks associated with less rugged topography, support the hypothesis that the topography of the QF has an ancient origin and is able to survive for many millions of years, possibly even increasing the original relief, as the conceptual models of Twidale (1976, 1998) and Crickmay (1975) first suggested.

## 5.6 CONCLUSION

The spatial distribution of rocks with different resistance to weathering and denudation sets the denudational pattern of the Quadrilátero Ferrífero. Basins underlain by strong rocks are associated with low denudation rates, despite being characterised by steep channels and hillslopes. By contrast, low-steepness basins under low-resistance rocks are associated with faster denudation rates, irrespective of their low-steepness. This dataset indicates that lithology overrides channel and hillslope steepness in determining denudation rates in the QF. Basins underlain by strong rocks are associated with low values of the parameter  $K$  (bedrock erodibility factor), contrasting with basins under low-resistance rocks that are associated with  $K$  values that are two to three orders of magnitude higher. The extremely low  $K$  values of basins underlain by strong rocks determine their low denudation, irrespective of their steep relief. Also, the parameter  $K$  modulates the quantitative link between denudation rates and relief, and its spatial variability determines the landscape-scale negative relationships between denudation and relief for the QF. Denudation rates in the QF are overall low ( $< 30$  m/Myr) in agreement with the denudation rates measured in other post-orogenic

settings. However, there is a marked spatial variability in denudation rates in the QF, whereby basins in the eastern part of the QF are associated with low denudation rates ( $< 5$  m/Myr), contrasting with basins in the southwestern part of the QF, which are associated with higher denudation rates (up to 30 m/Myr). The variability in denudation rates implies that relief in the QF is growing as time goes by, instead of decaying.

**CHAPTER 6:**  
**KEY CONTRIBUTIONS, INTERPRETATION, AND FUTURE**  
**RESEARCH**



# CHAPTER 6: KEY CONTRIBUTIONS, INTERPRETATION, AND FUTURE RESEARCH

## 6.1 KEY CONTRIBUTIONS

The primary objective of this project was to assess how topography, denudation rates, and the spatial distribution of rocks with different resistance to weathering and denudation are related in post-orogenic landscapes. For that, I have (i) performed a quantitative analysis of channel and hillslope morphology, and (ii) measured how denudation rates vary in space for the Quadrilátero Ferrífero in the southwestern Brazil. The fundamental contributions of this thesis are a combination of empirical observations of landscape form and processes, millennial-scale denudation rates and their potential controlling variables. This sizeable empirical dataset is relevant in several meaningful ways, as explained below:

- 1) It reveals that lithology is the most important control factor on the pattern of denudation in the QF. In fact, most modern research has largely overlooked the potential role of lithology in controlling denudation, especially the possibility that the spatial variability of rock resistance to denudation may overrides topographic relief in controlling the rate of denudation, even inverting the normal, positive relationship between denudation and relief. For instance, none of the estimates of relief reduction through time, discussed in length in section 3.2.2, have accounted for spatial variabilities in rock strength;
- 2) It demonstrates that post-orogenic relief is not featureless as most (if not all) models of post-orogenic landscape evolution would imply for a landscape evolving for hundreds of Myr (see section 3.2.2). This observation prompts two discussions, first if the QF is indeed a post-orogenic landscape, and second, what post-orogenic landscapes really are. I discuss these two issues in section 6.2.2;
- 3) It predicts that post-orogenic settings are associated with significant (i.e., orders of magnitude) variability in the bedrock erodibility factor  $K$ , and that this variability in  $K$  likely modulates how denudation rates and channel and hillslope steepness are linked for every landscape patch associated with a

specific  $K$ . Ultimately, the variability in  $K$  will lead to a lithology-controlled differentiation in denudation rates, implying that relief will increase through time instead of decrease;

- 4) It indicates that knickpoints are standard features in a post-orogenic setting (cf. Bishop and Goldrick, 2010) and that these are concentrated mostly on strong rocks, or on the downstream transition from strong to weak rocks. If these strong rocks are also associated with extremely low  $K$  values, then denudation rates measured downstream and upstream of knickpoints 'stalled' on strong rocks would be very similar. This prediction is testable and might be explored in future work;
- 5) It suggests that the way through which rock type controls topography is different from the dynamic equilibrium hypothesis of Hack (1960, 1975) because denudation rates are clearly different for different rocks. First, the explanation for a profound Hack-type adjustment between topographic forms and rock type is (nearly) teleological, with the 'system trying to achieve equilibrium'. Different rocks are associated with different  $K$  values which, in turn, leads to geomorphic differentiation in denudation rates and on how denudation rates and relief are linked. There is no logical reason to expect denudation rates on different rocks (and different relief) to be everywhere the same. In addition, the dynamic equilibrium hypothesis ultimately requires ongoing tectonic uplift to be considered a possible explanation for how post-orogenic landscapes evolve through time, which is problematic for essentially stable post-orogenic settings (Kooi and Beaumont, 1996);
- 6) Terrain underlain by rocks with very low  $K$  values are likely associated with low denudation rates even if they are extremely steep because rocks with very low  $K$  values swamp changes in the topographic parameters traditionally treated as the primary controls in denudation ( $S$  and  $A$ ). Hence, denudation rates not necessarily differentiate areas undergoing topographic rejuvenation from areas that did not experience it, if these areas are associated with very low  $K$  values.

In summary, this thesis met its overall objective and quantitatively determined how lithology, denudation rates, and topography are related for the QF. In addition, the sizeable empirical dataset may be relevant for parameterising

numerical models of landscape evolution in post-orogenic settings (e.g., the  $K$  values per lithology estimated in this contribution). Also, the sampling strategy for the quantification of denudation rates in this contribution, based on the quantitative analysis of the topography of the entire landscape, should become a protocol for future studies that use detrital  $^{10}\text{Be}$  concentrations to constrain denudation in post-orogenic landscapes. In the following sections, I outline the theoretical context as well as my hypothesis of how post-orogenic landscapes evolve through time, based on the empirical findings of this thesis.

## 6.2 INTERPRETATION

### 6.2.1 THEORETICAL CONTEXT

Post-orogenic landscapes traditionally designate terrains that last experienced tectonic activity hundreds of Myr ago and still exhibit relief, despite having been exposed to the net activity of surface processes over an extended period of time (cf. Baldwin et al., 2003; Bishop, 2007). The key conundrum in the landscape evolution of post-orogenic settings is how the long persistence of relief may be coupled to the idea that this landscape has been denuding for hundreds of Myr. This context was framed as a paradox (cf. Pelletier, 2008), and paradoxes are known to be unsolvable. Nonetheless, the geomorphic research on post-orogenic landscapes may be divided between (i) works highlighting empirical evidence of passive geologic control on the landscape development, describing thus the profound adjustment between strong rocks and steep topography, as well as low denudation rates, that are more the result of a long-term history of passive geologic controls, including isostatic rebound, than the processes happening now (e.g., King, 1942, 1962; Twidale, 1976; Young, 1983); and (ii) works featuring evidence that the ‘long history’ of erosion hypothesised by the first group is unlikely to have happened (e.g., Hack, 1982; Pazzaglia and Gardner, 1994; Belton et al., 2004).

The 1960s transition towards process-form geomorphology, boosted by the accumulation of quantitative estimates of rates of denudational processes, led to the ‘abandonment’ of the first approach in research on post-orogenic landscape evolution (Bishop, 2007). Dividing the mean elevation of the allegedly ‘ancient’ surfaces by the empirical rates of denudation, showed that landscapes could not

be as old as previously argued (Baldwin et al., 2003; Bishop, 2007). At the same time, the geomorphic characteristics of the ‘ancient’ settings were at odds with their supposed ‘recency’ (e.g., Twidale, 1976; Young, 1983; Twidale, 1999). This contradiction established the paradox of post-orogenic relief, discussed in section 3.2.2, which has been largely neglected basically since it was defined as a paradox (cf. Baldwin et al., 2003; Bishop, 2007; Egholm et al., 2013). In fact, the conceptual representation of how post-orogenic landscapes look and develop through time does not differ much between the early geomorphic schemes, including the cyclic approaches created before the present-day framework of global plate tectonics (e.g., Davis, 1899; Penck, 1924; King, 1953), and its ‘modern’ representation (Bishop, 2007). Early geomorphic schemes envisaged that relief wanes through time in the absence of the “forces of deformation and uplift” (Davis, 1899, p.483), and although the sequence of forms that landscapes acquire during their development slightly changes from one model to the other, the direction and final stage of this evolution is the same for every model: a featureless lowland where surface processes are acting very slowly (Hack, 1975). Similarly, the modern framework whereby relief reduction is modelled using the stream-power model (Baldwin et al., 2003) or the sediment-flux-driven model (Pelletier, 2008; Egholm et al., 2013) represents post-orogenic settings as landscapes related to a slow denudational pace and subdued topography, in the rear end of the response curve, evolving very slowly (Kooi and Beaumont, 1996).

This intuitive scenario that sees the morphology of the ‘residual’ topography of post-orogenic settings as intrinsically linked with an absence of relief and very slow rates of geomorphic change is pervasive in geomorphology (Bishop, 2007). Geomorphologists acknowledged early the influence of topography on erosion rates (e.g., Powell, 1876; Gilbert, 1877; Davis, 1899), a notion that was confirmed and theoretically refined by a large body of empirical and numerical work (e.g., Ruxton and McDougall, 1967; Ahnert, 1970; Beaumont et al., 1992; Koons, 1989, 1990; Willett, 1999; Lavé and Avouac, 2001; Whipple, 2009; DiBiase and Whipple, 2011), and that this emerged into a framework of a robust, quantitatively determined link between topography and denudation rates (cf. Wobus et al., 2006; Kirby and Whipple, 2012; Portenga et al., 2011; Harel et al., 2016). At a global scale, this link is clear, as the steepest terrains are related to tectonically active settings (Wobus et al., 2006), which evolve at much faster denudational

pace than slowly eroding post-orogenic landscapes (e.g., Bishop et al., 1985; Bishop and Goldrick, 2000; Bierman and Caffee, 2001, 2002; von Blanckenburg, 2004, 2005; Scharf et al., 2013). Hence, to a large extent, the low denudation rates of post-orogenic landscapes are interpreted as a result of their subdued topography (and related absence of ongoing tectonic activity).

Many post-orogenic landscapes are associated with localised steep channel and hillslope gradients, such as the the Cape Mountains in Africa (e.g., Scharf et al., 2013); the Appalachian Mountains in the USA (e.g., Gallen et al., 2013); southeastern Australia (e.g., Quigley et al., 2007; Bishop and Goldrick, 2010); Sri Lanka (e.g., von Blanckenburg, 2004); and southeastern Brazil (e.g., Cogné et al., 2012). The pronounced topographic attributes of many post-orogenic settings, as well as their spatial pattern (e.g., how knickpoints are distributed on the drainage network) and with other empirical evidence, have led to the interpretation that the post-orogenic relief in these settings is the result of a recent topographic rejuvenation episode or episodes (e.g., Gallen et al., 2013; Prince and Spotila, 2013). On the other hand, despite the pronounced topographic relief of many post-orogenic landscapes, estimates of denudation rates on these settings yield consistently lower denudation rates than tectonically active settings (e.g., Portenga and Bierman, 2011; Harel et al., 2016). In a way, the availability of new data on erosion rates has deepened the conundrum, as they have demonstrated that many of these high relief post-orogenic areas are characterised by low denudation rates. The idea that these landscapes could indeed be very old has, in isolated cases, come back (von Blanckenburg, 2004; Scharf et al., 2013). The isolated champions of the hypothesis that landscapes might have been much older than previously thought (e.g., Twidale, 1976; Young, 1983; Twidale, 1999), have argued that some uplands under strong rocks are virtually ‘out of reach’ of denudation. However, this theoretical framework lacked empirical data, and where data on denudation rates were available, it was considered a counter-argument to the model because denudation, although at low rates, was actively happening (e.g., Quigley et al., 2007).

The empirical dataset presented in this thesis may bridge the gap between these different models of post-orogenic landscape evolution. I outline a conjecture on how post-orogenic landscape evolve in the next section.

## 6.2.2 FINAL REMARKS: TOWARDS A NEW HYPOTHESIS ON HOW POST-OROGENIC LANDSCAPES EVOLVE

The topography of post-orogenic landscapes has an ancient origin and has survived for many millions of years controlled primarily by the resistance of the underlying bedrock, whereby denudation rates under areas of strong rocks are low. The persistence of post-orogenic relief is a function of a long history of slow denudation rates, plus the effect of denudational isostatic rebound, a fundamental mechanism that acts to prolong the 'life' of post-orogenic settings. The long-term persistence of post-orogenic relief does not imply that the post-orogenic topography remains unaltered through time, but instead that the geomorphic changes are very slow, as a result of the high resistance of rocks underlying upstream areas, and denudational isostatic rebound. The landscape-scale spatial heterogeneity in  $K$  values (i.e., bedrock erodibility) means that different areas of the landscape will be associated with different denudation rates. The spatial variability in denudation rates, in turn, implies that post-orogenic relief may grow rather than decay, as usually assumed.

The association of steep channel and hillslope gradients and slow denudation rates is a function of the low  $K$  values related to the distribution of resistant rocks. Extremely low values of  $K$  effectively override channel and hillslope steepness in determining denudation rates. At the same time,  $K$  modulates the quantitative link between topography and denudation rates, whereby for areas associated with low  $K$  values, changes in channel and hillslope steepness represent a lesser variation in denudation than for areas associated with high  $K$  values, and thus denudation rates are overall low for steep relief under strong rocks. By contrast, areas underlain by the low-resistance rocks with higher  $K$  values have lower steepness and are associated with faster denudation rates. As  $K$  values increase, small variations in basin steepness will be associated with higher variations in denudation rates, and thus a basin characterised by low-steepness channels and hillslope gradients may display higher denudation rates, if compared to steep basins under strong rocks (and lower  $K$  values).

The low denudation rates over long timescales associated with post-orogenic landscapes often lead to an expectation that post-orogenic relief has topographic

characteristics similar to the geomorphic signature of steady-state landscapes such as concave-up channel longitudinal profiles and an overall absence of knickpoints. By contrast, locally extremely steep channel and hillslope gradients, comparable to steep topography in active settings, are clearly present in post-orogenic settings. The main difference between these settings is that extremely steep channel and hillslope gradients are less common in post-orogenic settings. Whereas it sounds like an obvious empirical observation, this means that post-orogenic relief is essentially not featureless, and this is important as it contradicts nearly all conceptual, numerical and analytical models for the relief of a post-orogenic landscape evolving for hundreds of Myr. The main driver for the topographic characteristics similar to transient landscapes (e.g., convex-up channel profiles, the widespread presence of knickpoints; spatial variability in channel and hillslope steepness for the same rock type) in post-orogenic landscapes is likely to be controlled by the denudational isostatic compensation. Denudational isostatic compensation may drive drainage net rejuvenation which leads, in turn, to the formation and upstream migration of knickpoints. Resistant lithologies (i.e., low ' $K$ ' values) act to slow the the retreat of knickpoints, which end up 'captured' by resistant lithologies, preserving the upstream areas from this topographic rejuvenation. Multiple knickpoints driven by denudational isostatic compensation and 'stalled' in resistant rocks, even coalescing into one large knickpoints, are to be expected (cf. Bishop and Goldrick, 2010). The relationship between catchment-averaged  $K_{sn}$  and mean slope angle may exhibit a non-linear scaling in post-orogenic settings, notably for lower-order streams, because the hillslope response to the bottom-up rejuvenation event (or events) will be extremely slow on resistant rocks and associated low  $K$  values, lagging behind the (already slow) channel response time.

The positive association of topographic forms and rock type is an empirical fact in post-orogenic landscapes. Still, it is possible that this relationship is not the result of an equilibrium adjustment as hypothesised by Hack (1960, 1975), because different rocks are associated with different denudation rates in the QF (and potentially in other post-orogenic settings). The positive association between steepness, relief and bedrock strength is likely a combination of (i) the indirect effect of lithology in controlling the size and amount of sediment load delivered to streams; and (ii) its resistance to weathering (e.g., quartzites are chemically

inert and most likely weather at slow rates) and physical erosion. Also, the association of steep channel and hillslope gradients and the presence of resistant lithologies may reflect, at least partly, the 'always adjusting' topographic characteristic of areas under resistant lithologies, whereby steep knickpoints are 'always' there because they retreat very slowly (or are stalled) under resistant rocks. This effect is reinforced if the landscape has been affected by a series of rejuvenation events or if knickpoints are stalled in lithological boundaries. The differences in topographic forms that are not explained by changes in lithology have been often taken as evidence of differential (active) uplift. Despite the fact that this explanation may be possible, active tectonism is not necessary to explain the topography. The steepness of relief for a given rock type only needs to be 'homogeneous' if an equilibrium adjustment such as hypothesised by Hack (1960, 1975) is assumed. Hence, it is possible for some areas to be less steep than others, even if both have the same lithology, as long as peak values of channel and hillslope steepness are correlated with resistant rocks. The issue of why topography may be very different under the same lithology is poorly understood, but this contribution is a first step in that direction. Further research should concentrate on the presence of these 'stalled' knickpoints in strong lithologies, as they may hold the key to understand the association of peak values of relief and steepness with exposed bedrock resistance.

In summary, post-orogenic landscapes are ancient in origin, having survived as significant erosive landscapes for hundreds of millions of years. However, surface processes are still on-going, and the surface materials that are on the surface now are not the same as those million years ago, even though the overall geomorphological configuration remains. Therefore, post-orogenic settings prompt the theoretical question of what are in fact landscapes and landforms, as the 'age' of the geomorphological configuration and the 'age' of the materials currently on the surface are different. The QF has many geomorphic characteristics shared with other post-orogenic settings, such as high relief, an alleged long-term tectonic stability, the combination of strong and weak lithologies, concave-upward as well as convex channel profiles, widespread knickpoints, a profound adjustment between topographic form and rock type, and a controversial landscape evolution. I expect my empirical observations for the QF to be, to a large extent, consistent with other post-orogenic settings.

## 6.3 FUTURE RESEARCH OPPORTUNITIES

The empirical contributions and the interpretation of how post-orogenic landscapes develop through time presented in this thesis are based on the analysis of a specific post-orogenic setting, the Quadrilátero Ferrífero (Brazil). The first-order question to be asked is to what extent do the empirical observations presented in this project hold for other high-relief post-orogenic settings. Whereas there are indications that similar patterns as those described by the empirical data of this project are associated with different post-orogenic settings (that is, low denudation rates in terrains underlain by strong rocks irrespective to their steep topography; e.g., the Cape Mountains, Scharf et al., 2013), estimates of denudation rates in those landscapes did not yield a landscape-scale non-linear negative correlation between denudation rates and every catchment-averaged topographic parameter. Numerical modelling of landscape evolution may be an essential alternative approach for moving forward in the direction of investigating landscape evolution in different post-orogenic landscapes, probably testing the results reported in this thesis (and in particular the reported values of  $K$  for different lithologies). Associated with this first-order question are other intriguing questions prompted by the results of this thesis, such as:

- Are there examples of terrains with low  $K$  values, such as the uplands in the QF, associated with higher denudation rates?
- In the case of knickpoints stalled in resistant lithologies (cf. Bishop and Goldrick, 2010), with associated low  $K$  values, do denudation rates upstream of the knickpoints differ from the denudation rates downstream of the knickpoints?
- Do other post-orogenic settings display the same non-linear relationship (notably in lower-order streams) between catchment-averaged mean slope angle and normalised steepness index? What is the explanation for this relationship?
- How do weathering rates vary as a function of lithology (as well as  $K$ ) for post-orogenic landscapes?



## References

- Abatzoglou, J.T., Dobrowski, S.Z., Parks, S.A. and Hegewisch, K.C., 2018. TerraClimate, a high-resolution global dataset of monthly climate and climatic water balance from 1958-2015. *Scientific data*, 5(170191), pp.1-12.
- Aguilar, C., Farina, F. and Lana, C., 2015. Constraining the timing of the Transamazonian metamorphic event in the Southern São Francisco Craton (Brazil): revealed by monazite and titanite dating. In: *8th Hutton Symposium on Granites and Related Rocks*. Florianópolis: Sociedade Brasileira de Geologia, pp.PT-127.
- Aguilar, C., Alkmim, F.F., Lana, C. and Farina, F., 2017. Palaeoproterozoic assembly of the São Francisco craton, SE Brazil: New insights from U-Pb titanite and monazite dating. *Precambrian Research*, 289, pp.95-115.
- Agurto-Detzel, H., Assumpção, M., Bianchi, M. and Pirchiner, M., 2015. Intraplate seismicity in mid-plate South America: correlations with geophysical lithospheric parameters. In: Landgraf, A., Kuebler, S., Hintersberger, E. and Stein, S. (Eds.), *Seismicity, Fault Rupture and Earthquake Hazards in Slowly Deforming Regions*. London: Geological Society Special Publications, pp.73-90.
- Ahnert, F., 1970. Functional relationships between denudation, relief, and uplift in large, mid-latitude drainage basins. *American Journal of Science*, 268(3), pp.243-263.
- Alkmim, F.F. and Marshak, S., 1998. Transamazonian orogeny in the Southern Sao Francisco craton region, Minas Gerais, Brazil: evidence for Paleoproterozoic collision and collapse in the Quadrilátero Ferrífero. *Precambrian Research*, 90(1-2), pp.29-58.
- Alkmim, F.F., 2004. O que faz de um cráton um cráton? O Cráton do São Francisco e as revelações Almeidianas ao delimitá-lo. In: Mantesso-Neto (Eds.), *Geologia do Continente Sul- Americano. Evolução da obra de Fernando Flávio Marques de Almeida*. São Paulo: Becca, pp. 17-35.

- Alkmim, F.F. and Martins-Neto, M.A., 2012. Proterozoic first-order sedimentary sequences of the São Francisco craton, eastern Brazil. *Marine and Petroleum Geology*, 33(1), pp.127-139.
- Alkmim, F.F. and Teixeira, W., 2017. The Paleoproterozoic Mineiro Belt and the Quadrilátero Ferrífero. In: Heilbron, M., Cordani, U. G., and Alkmim, F. F. (Eds.), *São Francisco Craton, Eastern Brazil*. Cham: Springer, pp.71-94.
- Almeida, F.F., Hasui, Y., de Brito Neves, B.B. and Fuck, R.A., 1981. Brazilian structural provinces: an introduction. *Earth-Science Reviews*, 17(1-2), pp.1-29.
- Annandale, G.W., 1995. Erodibility. *Journal of Hydraulic Research*, 33(4), pp.471-494.
- Assumpção, M., Ferreira, J., Barros, L., Bezerra, H., França, G.S., Barbosa, J.R., Menezes, E., Carlos Ribotta, L., Pirchiner, M., Nascimento, A.D. and Dourado, J.C., 2014. Intraplate seismicity in Brazil. In: Talwani, P. (Eds.), *Intraplate Earthquakes*. Cambridge: Cambridge University Press, pp. 50-71.
- Babinski, M., Chemale Jr, F. and Van Schmus, W.R., 1995. The PB/PB age of the minas supergroup carbonate rocks, Quadrilátero Ferrífero, Brazil. *Precambrian Research*, 72(3-4), pp.235-245.
- Bagnold, R.A., 1966. An approach to the sediment transport problem from general physics. *US Geological Survey Professional Paper*, 4221, pp.1-37.
- Balco, G., 2006. Converting Al and Be isotope ratio measurements to nuclide concentrations in quartz. *Documentation—Be-10/26-Al exposure age calculator*.
- Balco, G., Stone, J.O., Lifton, N.A. and Dunai, T.J., 2008. A complete and easily accessible means of calculating surface exposure ages or erosion rates from <sup>10</sup>Be and <sup>26</sup>Al measurements. *Quaternary Geochronology*, 3(3), pp.174-195.
- Baldwin, J.A., Whipple, K.X. and Tucker, G.E., 2003. Implications of the shear stress river incision model for the timescale of postorogenic decay of topography. *Journal of Geophysical Research: Solid Earth*, 108(B3), pp.7(1)-7(17).

- Baltazar, O.F. and Zucchetti, M., 2007. Lithofacies associations and structural evolution of the Archean Rio das Velhas greenstone belt, Quadrilátero Ferrífero, Brazil: A review of the setting of gold deposits. *Ore Geology Reviews*, 32(3-4), pp.471-499.
- Barbosa, G.V. and Rodrigues, D.M.S., 1965. O Quadrilátero Ferrífero e seus problemas geomorfológicos. *Boletim Mineiro de Geografia*, 10(11), pp.3-35.
- Barbosa, G.V., 1980. Superfícies de erosão no Quadrilátero Ferrífero, Minas Gerais. *Brazilian Journal of Geology*, 10(1), pp.89-101.
- Beaumont, C., Fullsack, P. and Hamilton, J., 1992. Erosional control of active compressional orogens. In: McClay, K.R. (Eds.), *Thrust Tectonics*. Dordrecht: Springer, pp.1-18.
- Behling, H., 1998. Late Quaternary vegetational and climatic changes in Brazil. *Review of Palaeobotany and Palynology*, 99(2), pp.143-156.
- Belton, D.X., Brown, R.W., Kohn, B.P., Fink, D. and Farley, K.A., 2004. Quantitative resolution of the debate over antiquity of the central Australian landscape: implications for the tectonic and geomorphic stability of cratonic interiors. *Earth and Planetary Science Letters*, 219(1-2), pp.21-34.
- Berner, E.K. and Berner, R.A., 1987. *Global Water Cycle: geochemistry and environment*. New Jersey: Prentice-Hall.
- Bierman, P. and Steig, E.J., 1996. Estimating rates of denudation using cosmogenic isotope abundances in sediment. *Earth Surface Processes and Landforms*, 21(2), pp.125-139.
- Bierman, P.R. and Caffee, M., 2001. Slow rates of rock surface erosion and sediment production across the Namib Desert and escarpment, southern Africa. *American Journal of Science*, 301(4-5), pp.326-358.

- Bierman, P.R. and Caffee, M., 2002. Cosmogenic exposure and erosion history of Australian bedrock landforms. *Geological Society of America Bulletin*, 114(7), pp.787-803.
- Bierman, P. and Nichols, K.K., 2004. Rock to sediment – slope to sea with  $^{10}\text{Be}$  – rates of landscape change. *Annual Review of Earth and Planetary Sciences*, 32, pp.215-255.
- Bierman, P.R., Reuter, J.M., Pavich, M., Gellis, A.C., Caffee, M.W. and Larsen, J., 2005. Using cosmogenic nuclides to contrast rates of erosion and sediment yield in a semi-arid, arroyo-dominated landscape, Rio Puerco Basin, New Mexico. *Earth Surface Processes and Landforms*, 30(8), pp.935-953.
- Binnie, S.A., Phillips, W.M., Summerfield, M.A. and Fifield, L.K., 2007. Tectonic uplift, threshold hillslopes, and denudation rates in a developing mountain range. *Geology*, 35(8), pp.743-746.
- Bishop, P., Young, R.W. and McDougall, I., 1985. Stream profile change and longterm landscape evolution: Early Miocene and modern rivers of the east Australian highland crest, central New South Wales, Australia. *The Journal of Geology*, 93(4), pp.455-474.
- Bishop, P. and Brown, R., 1992. Denudational isostatic rebound of intraplate highlands: the Lachlan River valley, Australia. *Earth Surface Processes and Landforms*, 17(4), pp.345-360.
- Bishop, P. and Goldrick, G., 2000. Geomorphological evolution of the East Australian continental margin. In: Summerfield, M.A. (Eds.), *Geomorphology and Global Tectonics*. Chichester: Wiley, pp.227-255.
- Bishop, P., Hoey, T.B., Jansen, J.D. and Artza, I.L., 2005. Knickpoint recession rate and catchment area: the case of uplifted rivers in Eastern Scotland. *Earth Surface Processes and Landforms*, 30(6), pp.767-778.
- Bishop, P., 2007. Long-term landscape evolution: linking tectonics and surface processes. *Earth Surface Processes and Landforms*, 32(3), pp.329-365.

Bishop, P. and Goldrick, G., 2010. Lithology and the evolution of bedrock rivers in post-orogenic settings: constraints from the high-elevation passive continental margin of SE Australia. *Geological Society, London, Special Publications*, 346(1), pp.267-287.

Bishop, P., 2011. Landscape Evolution and Tectonics. In: Gregory, K.J. and Goudie, A.S. (Eds.), *The SAGE Handbook of Geomorphology*. London: Sage Publications.

Borchers, B., Marrero, S., Balco, G., Caffee, M., Goehring, B., Lifton, N., Nishiizumi, K., Phillips, F., Schaefer, J. and Stone, J., 2016. Geological calibration of spallation production rates in the CRONUS-Earth project. *Quaternary Geochronology*, 31, pp.188-198.

Brajnikov, B., 1947. Essai sur la tectonique de la region a l'est de Belo Horizonte, Minas Gerais, Bresil. *Bulletin de la Société Géologique de France*, 5(4-6), pp.321-335.

Brown, E.T., Stallard, R.F., Larsen, M.C., Raisbeck, G.M. and Yiou, F., 1995. Denudation rates determined from the accumulation of in situ-produced  $^{10}\text{Be}$  in the Luquillo Experimental Forest, Puerto Rico. *Earth and Planetary Science Letters*, 129(1-4), pp.193-202.

Brueckner, H.K., Cunningham, D., Alkmin, F.F. and Marshak, S., 2000. Tectonic implications of Precambrian Sm-Nd dates from the southern Sao Francisco craton and adjacent Araçuaí and Ribeira belts, Brazil. *Precambrian Research*, 99(3-4), pp.255-269.

Burbank, D.W., 1992. Causes of recent Himalayan uplift deduced from deposited patterns in the Ganges basin. *Nature*, 357(6380), p.680-683.

Burbank, D.W., Leland, J., Fielding, E., Anderson, R.S., Brozovic, N., Reid, M.R. and Duncan, C., 1996. Bedrock incision, rock uplift and threshold hillslopes in the northwestern Himalayas. *Nature*, 379(6565), pp.505-510.

- Burrough, P.A. and McDonnell, R.A., 1998. *Principles of GIS*. London: Oxford University Press.
- Bursztyn, N., Pederson, J.L., Tressler, C., Mackley, R.D. and Mitchell, K.J., 2015. Rock strength along a fluvial transect of the Colorado Plateau-quantifying a fundamental control on geomorphology. *Earth and Planetary Science Letters*, 429, pp.90-100.
- Cabral, A.R., Zeh, A., Koglin, N., Gomes Jr, A.A.S., Viana, D.J. and Lehmann, B., 2012. Dating the Itabira iron formation, Quadrilátero Ferrífero of Minas Gerais, Brazil, at 2.65 Ga: depositional U-Pb age of zircon from a metavolcanic layer. *Precambrian Research*, 204, pp.40-45.
- Cabral, A.R. and Koglin, N., 2014. Hydrothermal overprint on Cenozoic sediments in the Quadrilátero Ferrífero of Minas Gerais: implications for precious metals in cratonic terrains. *Terra Nova*, 26(2), pp.111-119.
- Carmo, I.D.O. and Vasconcelos, P., 2004. Geochronological evidence for pervasive miocene weathering, Minas Gerais, Brazil. *Earth Surface Processes and Landforms*, 29(11), pp.1303-1320.
- Chemale Jr, F., Rosière, C.A. and Endo, I., 1994. The tectonic evolution of the Quadrilátero Ferrífero, Minas Gerais, Brazil. *Precambrian Research*, 65(1-4), pp.25-54.
- Chmeleff, J., von Blanckenburg, F., Kossert, K. and Jakob, D., 2010. Determination of the  $^{10}\text{Be}$  half-life by multicollector ICP-MS and liquid scintillation counting. *Nuclear Instruments and Methods in Physics Research Section B: Beam Interactions with Materials and Atoms*, 268(2), pp.192-199.
- Chorley, R.J., Dunn, A.J. and Beckinsale, R.P., 1964. *The History of the Study of Landforms: Geomorphology before Davis* (Vol. 1). London: Methuen.
- Clayton, K. and Shamon, N., 1999. A new approach to the relief of Great Britain: III. Derivation of the contribution of neotectonic movements and exceptional regional denudation to the present relief. *Geomorphology*, 27(3-4), pp.173-189.

- Codilean, A. T., 2006. Calculation of the cosmogenic nuclide production topographic shielding scaling factor for large areas using DEMs. *Earth Surface Processes and Landforms*, 31(6), pp.785-794.
- Cogné, N., Gallagher, K., Cobbold, P.R., Riccomini, C. and Gautheron, C., 2012. Post-breakup tectonics in southeast Brazil from thermochronological data and combined inverse-forward thermal history modeling. *Journal of Geophysical Research: Solid Earth*, 117(B11413), pp.1-16.
- Congedo, L., 2016. Semi-automatic classification plugin documentation. *Release*, 5.3.6.1.
- Copernicus, Sentinel data, 2016. Available at: <https://scihub.copernicus.eu/> [accessed January 2018].
- Crickmay, C. H. 1975. The hypothesis of unequal activity. *In: Melhorn, W.M. and Flemal, R. C. (Eds.), Theories of Landform Development*. London: George, Allen and Unwin, pp.103-109.
- Crosby, B.T. and Whipple, K.X., 2006. Knickpoint initiation and distribution within fluvial networks: 236 waterfalls in the Waipaoa River, North Island, New Zealand. *Geomorphology*, 82(1-2), pp.16-38.
- Cyr, A.J., Granger, D.E., Olivetti, V. and Molin, P., 2014. Distinguishing between tectonic and lithologic controls on bedrock channel longitudinal profiles using cosmogenic  $^{10}\text{Be}$  erosion rates and channel steepness index. *Geomorphology*, 209, pp.27-38.
- Davis, W.M., 1899. The geographical cycle. *The Geographical Journal*, 14(5), pp.481-504.
- Demoulin, A., Mather, A. and Whittaker, A., 2017. Fluvial archives, a valuable record of vertical crustal deformation. *Quaternary Science Reviews*, 166, pp.10-37.

- Derby, O.A., 1906. The Serra do Espinhaço, Brazil. *The Journal of Geology*, 14(5), pp.374-401.
- Derby, O.A., 1911. Mineralization of the gold-bearing lode of Passagem, Minas Geraes, Brazil. *American Journal of Science*, (189), pp.185-190.
- Desilets, D. and Zreda, M., 2003. Spatial and temporal distribution of secondary cosmic-ray nucleon intensities and applications to in situ cosmogenic dating. *Earth and Planetary Science Letters*, 206(1-2), pp.21-42.
- DiBiase, R.A. and Whipple, K.X., 2010. The influence of erosion thresholds and runoff variability on the relationships among topography, climate, and erosion rate. *Journal of Geophysical Research: Earth Surface*, 116(F4), pp.134-144.
- Diehl, R., Halloin, H., Kretschmer, K., Lichti, G.G., Schönfelder, V., Strong, A.W., Von Kienlin, A., Wang, W., Jean, P., Knödseder, J., Roques, J.P., Weidenspointner, G., Schanne, S., Hartmann, D.H., Winkler, C. and Wunderer, C., 2006. Radioactive <sup>26</sup>Al from massive stars in the Galaxy. *Nature*, 439(7072), p.45.
- Dixon, J.L., Heimsath, A.M. and Amundson, R., 2009. The critical role of climate and saprolite weathering in landscape evolution. *Earth Surface Processes and Landforms*, 34(11), pp.1507-1521.
- Dopico, C.I.M., Lana, C., Moreira, H.S., Cassino, L.F. and Alkmim, F.F., 2017. U-Pb ages and Hf-isotope data of detrital zircons from the late Neoproterozoic-Paleoproterozoic Minas Basin, SE Brazil. *Precambrian Research*, 291, pp.143-161.
- Dorr, J.V.N., 1964. Supergene iron ores of Minas Gerais, Brazil. *Economic Geology*, 59(7), pp.1203-1240.
- Dorr, J.V.N., 1969. Physiographic, stratigraphic, and structural development of the Quadrilátero Ferrífero, Minas Gerais, Brazil. *US Geological Survey Professional Paper*, 641-A, pp. A1-A110.

- Dunai, T.J., 2001. Influence of secular variation of the geomagnetic field on production rates of in situ produced cosmogenic nuclides. *Earth and Planetary Science Letters*, 193(1-2), pp.197-212.
- Dunai, T.J., 2010. *Cosmogenic Nuclides: Principles, Concepts and Applications in the Earth Surface Sciences*. Cambridge: Cambridge University Press.
- Dunai, T.J. and Lifton, N.A., 2014. The nuts and bolts of cosmogenic nuclide production. *Elements*, 10(5), pp.347-350.
- Dunne, J., Elmore, D. and Muzikar, P., 1999. Scaling factors for the rates of production of cosmogenic nuclides for geometric shielding and attenuation at depth on sloped surfaces. *Geomorphology*, 27(1-2), pp.3-11.
- Duvall, A., Kirby, E. and Burbank, D., 2004. Tectonic and lithologic controls on bedrock channel profiles and processes in coastal California. *Journal of Geophysical Research: Earth Surface*, 109(F03002), pp.1-18.
- Egholm, D.L., Knudsen, M.F. and Sandiford, M., 2013. Lifespan of mountain ranges scaled by feedbacks between landsliding and erosion by rivers. *Nature*, 498(7455), p.475-478.
- Eidelman, S., Hayes, K.G., Olive, K.E., Aguilar-Benitez, M., Amsler, C., Asner, D., Babu, K.S., Barnett, R.M., Beringer, J., Burchat, P.R., Carone, C.D., Caso, S., Conforto, G., Dahl, O., D'Ambrosio, G., Doser, M., Feng, J.L., ..., and Zhu, R.Y., 2004. Review of particle physics. *Physics Letters B*, 592(1-4), pp.1-5.
- Endo, I. and Fonseca, M.A., 1992. Sistema de cisalhamento Fundao-Cambotas no Quadrilátero Ferrífero, MG: geometria e cinemática. *Revista da Escola de Minas*, 45, pp.28-31.
- Farina, F., Albert, C. and Lana, C., 2015. The Neoproterozoic transition between medium- and high-K granitoids: Clues from the Southern São Francisco Craton (Brazil). *Precambrian Research*, 266, pp.375-394.

- Farina, F., Albert, C., Dopico, C.M., Gil, C.A., Moreira, H., Hippertt, J.P., Cutts, K., Alkmim, F.F. and Lana, C., 2016. The Archean-Paleoproterozoic evolution of the Quadrilátero Ferrífero (Brasil): Current models and open questions. *Journal of South American Earth Sciences*, 68, pp.4-21.
- Fick, S. E., Hijmans, R. J., 2017. WorldClim 2: new 1-km spatial resolution climate surfaces for global land areas. *International Journal of Climatology*, 37(12), pp. 4302-4315.
- Flint, J.J., 1974. Stream gradient as a function of order, magnitude, and discharge. *Water Resources Research*, 10(5), pp.969-973.
- Forte, A.M., Yanites, B.J. and Whipple, K.X., 2016. Complexities of landscape evolution during incision through layered stratigraphy with contrasts in rock strength. *Earth Surface Processes and Landforms*, 41(12), pp.1736-1757.
- Foster, I.D., Dearing, J.A., Simpson, A., Carter, A.D. and Appleby, P.G., 1985. Lake catchment based studies of erosion and denudation in the Merevale catchment, Warwickshire, UK. *Earth Surface Processes and Landforms*, 10(1), pp.45-68.
- Frampton, W. J., Dash, J., Watmough, G., and Milton, E. J., 2013. Evaluating the capabilities of Sentinel-2 for quantitative estimation of biophysical variables in vegetation. *ISPRS Journal of Photogrammetry and Remote Sensing*, 82, pp. 83-92.
- Gallagher, K., Brown, R. and Johnson, C., 1998. Fission track analysis and its applications to geological problems. *Annual Review of Earth and Planetary Sciences*, 26(1), pp.519-572.
- Gallen, S.F., Wegmann, K.W. and Bohnenstiehl, D.R., 2013. Miocene rejuvenation of topographic relief in the southern Appalachians. *Geological Society of America Today*, 23(2), pp.4-10.
- Gallen, S.F. and Wegmann, K.W., 2017. River profile response to normal fault growth and linkage: an example from the Hellenic forearc of south-central Crete, Greece. *Earth Surface Dynamics*, 5(1), p.161-186.

- Gorceix, H., 1884. Bacias terciárias d'agua doce nos arredores de Ouro Preto (Gandarela e Fonseca), Minas Gerais, Brasil. *Annaes da Escola de Minas*, 3, pp.95-114.
- Gilbert, G., 1877. *Report of the geology of the Henry Mountains*. Washington: Geographical and Geological Survey of the Rocky Mountains Region. U.S., Government Printing Office.
- Gilchrist, A.R., Summerfield, M.A. and Cockburn, H.A.P., 1994. Landscape dissection, isostatic uplift, and the morphologic development of orogens. *Geology*, 22(11), pp.963-966.
- Gilluly, J., 1955. Geologic contrasts between continents and ocean basins. *Geological Society of America Special Paper*, 62, pp.7-18.
- Gosse, J.C. and Phillips, F.M., 2001. Terrestrial in situ cosmogenic nuclides: theory and application. *Quaternary Science Reviews*, 20(14), pp.1475-1560.
- Granger, D.E., Kirchner, J.W. and Finkel, R., 1996. Spatially averaged long-term erosion rates measured from in situ-produced cosmogenic nuclides in alluvial sediment. *The Journal of Geology*, 104(3), pp.249-257.
- Granger, D.E., Lifton, N.A. and Willenbring, J.K., 2013. A cosmic trip: 25 years of cosmogenic nuclides in geology. *GSA Bulletin*, 125(9-10), pp.1379-1402.
- Granger, D.E., Riebe, C.S., 2013. Cosmogenic nuclides in weathering and erosion. In: Drever J.I. (Eds.), *Surface and Groundwater, Weathering and Soils. Treatise on Geochemistry*, 5. Oxford: Elsevier.
- Granger, D.E. and Schaller, M., 2014. Cosmogenic nuclides and erosion at the watershed scale. *Elements*, 10(5), pp.369-373.
- Green, S.B. and Salkind, N.J., 2016. *Using SPSS for Windows and Macintosh: Analyzing and Understanding Data*. 8th edition. New York: Pearson.
- Guimarães, D., 1931. Contribuição à geologia do estado de Minas Gerais, Brasil. *Boletim - Serviço Geológico e Mineralógico do Brasil*, 55, pp.1-36

- Hack, J.T., 1957. Studies of longitudinal stream profiles in Virginia Maryland. *US Geological Survey Professional Paper*, 294-B, pp.45-95.
- Hack, J.T., 1960. Interpretation of erosional topography in humid temperate regions. *American Journal of Science*, 258, pp.80-97.
- Hack, J.T., 1975. Dynamic equilibrium and landscape evolution. *Theories of landform development*, 1, pp.87-102.
- Hack, J.T., 1982. Physiographic divisions and differential uplift in the Piedmont and Blue Ridge. *US Geological Survey Professional Paper*, 1265, pp.1-49.
- Harder, E.C. and Chamberlin, R.T., 1915. The geology of central Minas Geraes, Brazil. *The Journal of Geology*, 23(5), pp.385-424.
- Harel, M.A., Mudd, S.M. and Attal, M., 2016. Global analysis of the stream power law parameters based on worldwide <sup>10</sup>Be denudation rates. *Geomorphology*, 268, pp.184-196.
- Hartmann, L.A., Endo, I., Suita, M.T.F., Santos, J.O.S., Frantz, J.C., Carneiro, M.A., McNaughton, N.J. and Barley, M.E., 2006. Provenance and age delimitation of Quadrilátero Ferrífero sandstones based on zircon U-Pb isotopes. *Journal of South American Earth Sciences*, 20(4), pp.273-285.
- Heilbron, M., Cordani, U.G. and Alkmim, F.F., 2017. *São Francisco Craton, Eastern Brazil: Tectonic Genealogy of a Miniature Continent*. Cham: Springer.
- Heimsath, A.M., Dietrich, W.E., Nishiizumi, K. and Finkel, R.C., 1997. The soil production function and landscape equilibrium. *Nature*, 388(6640), p.358-361.
- Hippertt, J.F., Borba, R.P. and Nalini Jr, H.A., 1992. O contato Formação Moeda-Complexo Bonfim: Uma zona de cisalhamento normal na borda oeste do Quadrilátero Ferrífero, MG. *Revista da Escola de Minas*, 45(1/2), pp.32-34.
- Howard, A.D. and Kerby, G., 1983. Channel changes in badlands. *Geological Society of America Bulletin*, 94(6), pp.739-752.

- Howard, A.D., 1994. A detachment-limited model of drainage basin evolution. *Water Resources Research*, 30(7), pp.2261-2285.
- Huete, A., Didan, K., Miura, T., Rodriguez, E.P., Gao, X. and Ferreira, L.G., 2002. Overview of the radiometric and biophysical performance of the MODIS vegetation indices. *Remote Sensing of Environment*, 83(1-2), pp.195-213.
- Hurst, M.D., Ellis, M.A., Royse, K.R., Lee, K.A. and Freeborough, K., 2013. Controls on the magnitude-frequency scaling of an inventory of secular landslides. *Earth Surface Dynamics*, 1(1), p.67.
- Jain, A.K., 2010. Data clustering: 50 years beyond K-means. *Pattern Recognition Letters*, 31(8), pp.651-666.
- Jansen, J.D., Codilean, A.T., Bishop, P. and Hoey, T.B., 2010. Scale dependence of lithological control on topography: Bedrock channel geometry and catchment morphometry in western Scotland. *The Journal of geology*, 118(3), pp.223-246.
- James, P.E., 1933. The surface configuration of southeastern Brazil. *Annals of the Association of American Geographers*, 23(3), pp.165-193.
- Japsen, P., Bonow, J.M., Green, P.F., Cobbold, P.R., Chiossi, D., Lilletveit, R., Magnavita, L.P. and Pedreira, A., 2012. Episodic burial and exhumation in NE Brazil after opening of the South Atlantic. *Bulletin*, 124(5-6), pp.800-816.
- Judson, S. and Ritter, D.F., 1964. Rates of regional denudation in the United States. *Journal of Geophysical Research*, 69(16), pp.3395-3401.
- Judson, S., 1975. Evolution of Appalachian topography. In: Melhorn, W.M. and Flemal, R. C. (Eds.), *Theories of Landform Development*. London: George, Allen and Unwin, pp.29-44.
- King, L.C., 1942. *South African scenery. A textbook of geomorphology*. London: Oliver and Boyd.

- King, L.C., 1953. Canons of landscape evolution. *Geological Society of America Bulletin*, 64(7), pp.721-752.
- King, L.C., 1956. A Geomorfologia do Brasil Oriental. *Revista Brasileira de Geociências*, 18, pp.147-265.
- King, L.C., 1962. *The morphology of the earth*. London: Oliver and Boyd.
- Kirby, E. and Whipple, K., 2001. Quantifying differential rock-uplift rates via stream profile analysis. *Geology*, 29(5), pp.415-418.
- Kirby, E., Whipple, K.X., Tang, W. and Chen, Z., 2003. Distribution of active rock uplift along the eastern margin of the Tibetan Plateau: Inferences from bedrock channel longitudinal profiles. *Journal of Geophysical Research: Solid Earth*, 108(B4), pp.16(1)-16(24).
- Kirby, E. and Whipple, K.X., 2012. Expression of active tectonics in erosional landscapes. *Journal of Structural Geology*, 44, pp.54-75.
- Kirchner, J.W., Finkel, R.C., Riebe, C.S., Granger, D.E., Clayton, J.L., King, J.G. and Megahan, W.F., 2001. Mountain erosion over 10 yr, 10 ky, and 10 my time scales. *Geology*, 29(7), pp.591-594.
- Koglin, N., Zeh, A., Cabral, A.R., Gomes Jr, A.A.S., Neto, A.V.C., Brunetto, W.J. and Galbiatti, H., 2014. Depositional age and sediment source of the auriferous Moeda Formation, Quadrilátero Ferrífero of Minas Gerais, Brazil: New constraints from U-Pb-Hf isotopes in zircon and xenotime. *Precambrian Research*, 255, pp.96-108.
- Kohl, C.P. and Nishiizumi, K., 1992. Chemical isolation of quartz for measurement of in-situ-produced cosmogenic nuclides. *Geochimica et Cosmochimica Acta*, 56(9), pp.3583-3587.
- Kooi, H. and Beaumont, C., 1996. Large-scale geomorphology: Classical concepts reconciled and integrated with contemporary ideas via a surface processes model. *Journal of Geophysical Research: Solid Earth*, 101(B2), pp.3361-3386.

- Koons, P.O., 1989. The topographic evolution of collisional mountain belts; a numerical look at the Southern Alps, New Zealand. *American journal of Science*, 289(9), pp.1041-1069.
- Koons, P.O., 1990. Two-sided orogen: Collision and erosion from the sandbox to the Southern Alps, New Zealand. *Geology*, 18(8), pp.679-682.
- Korschinek, G., Bergmaier, A., Faestermann, T., Gerstmann, U.C., Knie, K., Rugel, G., Wallner, A., Dillmann, I., Dollinger, G., Von Gostomski, C.L. and Kossert, K., 2010. A new value for the half-life of  $^{10}\text{Be}$  by heavy-ion elastic recoil detection and liquid scintillation counting. *Nuclear Instruments and Methods in Physics Research Section B: Beam Interactions with Materials and Atoms*, 268(2), pp.187-191.
- Korup, O., 2008. Rock type leaves topographic signature in landslide-dominated mountain ranges. *Geophysical Research Letters*, 35(11), pp.1-5.
- Kwang, J. S., and Parker, G., 2017. Landscape evolution models using the stream power incision model show unrealistic behavior when  $m/n$  equals 0.5. *Earth Surface Dynamics*, 5(4), pp. 807-820.
- Lachenbruch, A.H. and Morgan, P., 1990. Continental extension, magmatism and elevation; formal relations and rules of thumb. *Tectonophysics*, 174(1-2), pp.39-62.
- Lal, D., 1991. Cosmic ray labeling of erosion surfaces: in situ nuclide production rates and erosion models. *Earth and Planetary Science Letters*, 104(2-4), pp.424-439.
- Lana, C., Alkmim, F.F., Armstrong, R., Scholz, R., Romano, R. and Nalini Jr, H.A., 2013. The ancestry and magmatic evolution of Archaean TTG rocks of the Quadrilátero Ferrífero province, southeast Brazil. *Precambrian Research*, 231, pp.157-173.
- Lague, D., Davy, P. and Crave, A., 2000. Estimating uplift rate and erodibility from the area-slope relationship: Examples from Brittany (France) and numerical

modelling. *Physics and Chemistry of the Earth, Part A: Solid Earth and Geodesy*, 25(6-7), pp.543-548.

Lague, D., 2014. The stream power river incision model: evidence, theory and beyond. *Earth Surface Processes and Landforms*, 39(1), pp.38-61.

Larsen, I.J. and Montgomery, D.R., 2012. Landslide erosion coupled to tectonics and river incision. *Nature Geoscience*, 5(7), p.468-473.

Larsen, R.J. and Marx, M.L., 2017. *An Introduction to Mathematical Statistics and its Applications*. 5th edition. Boston: Pearson.

Lavé, J. and Avouac, J.P., 2001. Fluvial incision and tectonic uplift across the Himalayas of central Nepal. *Journal of Geophysical Research: Solid Earth*, 106(B11), pp.26561-26591.

Leopold, L.B., Wolman, M.G. and Miller, J.P., 1964. *Fluvial Processes in Geomorphology*. San Francisco: Freeman and Company.

Leopold, L.B. and Bull, W.B., 1979. Base level, aggradation, and grade. *Proceedings of the American Philosophical Society*, 123(3), pp.168-202.

Lifton, N., Sato, T. and Dunai, T.J., 2014. Scaling in situ cosmogenic nuclide production rates using analytical approximations to atmospheric cosmic-ray fluxes. *Earth and Planetary Science Letters*, 386, pp.149-160.

Lipski, M., 2002. *Tectonismo Cenozóico no Quadrilátero Ferrífero, Minas Gerais*. MD Thesis. Federal University of Ouro Preto.

Lobato, L., Ribeiro-Rodrigues, L., Zucchetti, M., Noce, C., Baltazar, O., Da Silva, L. and Pinto, C., 2001. Brazil's premier gold province. Part I: The tectonic, magmatic, and structural setting of the Archean Rio das Velhas greenstone belt, Quadrilátero Ferrífero. *Mineralium Deposita*, 36(3-4), pp.228-248.

Lobato, L.M., Baltazar, O.F., Reis, L.B., Achtschin, A.B., Baars, F.J., Timbó, M.A., Berni, G.V, Mendonça, B.R.V. and Ferreira, D.V., 2005. *Projeto Geologia do*

*Quadrilátero Ferrífero - Integração e Correção Cartográfica em SIG com Nota Explicativa*. [Geological database] Belo Horizonte: CODEMIG.

Lupker, M., Lavé, J., France-Lanord, C., Christl, M., Bourlès, D., Carcaillet, J., Maden, C., Wieler, R., Rahman, M., Bezbaruah, D. and Xiaohan, L., 2017. 10 Be systematics in the Tsangpo-Brahmaputra catchment: the cosmogenic nuclide legacy of the eastern Himalayan syntaxis. *Earth Surface Dynamics*, 5(3).

Machado, N., Noce, C.M., Ladeira, E.A. and De Oliveira, O.B., 1992. U-Pb geochronology of Archean magmatism and Proterozoic metamorphism in the Quadrilátero Ferrífero, southern São Francisco craton, Brazil. *Geological Society of America Bulletin*, 104(9), pp.1221-1227.

Machado, N., Schrank, A., Noce, C.M. and Gauthier, G., 1996. Ages of detrital zircon from Archean-Paleoproterozoic sequences: Implications for Greenstone Belt setting and evolution of a Transamazonian foreland basin in Quadrilátero Ferrífero, southeast Brazil. *Earth and Planetary Science Letters*, 141(1-4), pp.259-276.

Maizatto, J.R. and Castro, P.T.A., 1993. Origem e evolução da bacia do Gandarela-Quadrilátero Ferrífero, Minas Gerais. In: *Simpósio Nacional de Estudos Tectônicos*, 12. Belo Horizonte: Sociedade Brasileira de Geologia, pp.325-329.

Maizatto, J.R., 1997. *Análise paleoecológica e bioestratigráfica dos sedimentos cenozóicos da Bacia do Gandarela, Quadrilátero Ferrífero - Minas Gerais - com base nos aspectos palinológicos e sedimentares*. MSc Thesis. Federal University of Ouro Preto.

Marsal, D., 1979. *Statistics for geoscientists*. Stuttgart: Schweizerbart. (Translation by Merriam, D.F., 1987, Oxford: Pergamon Press).

Masarik, J. and Reedy, R.C., 1995. Terrestrial cosmogenic-nuclide production systematics calculated from numerical simulations. *Earth and Planetary Science Letters*, 136(3-4), pp.381-395.

Masarik, J. and Beer, J., 1999. Simulation of particle fluxes and cosmogenic nuclide production in the Earth's atmosphere. *Journal of Geophysical Research: Atmospheres*, 104(D10), pp.12099-12111.

Marshak, S. and Alkmim, F.F., 1989. Proterozoic extension/contraction tectonics of the São Francisco Craton and adjacent regions, Minas Gerais, Brazil: a kinematic model relating Quadrilátero Ferrífero, São Francisco Basin and Cordilheira do Espinhaço. *Tectonics*, 8(3), pp.555-571.

Marshak, S., Tinkham, D., Alkmim, F., Brueckner, H. and Bornhorst, T., 1997. Dome-and-keel provinces formed during Paleoproterozoic orogenic collapse-core complexes, diapirs, or neither?: Examples from the Quadrilátero Ferrífero and the Penokean orogen. *Geology*, 25(5), pp.415-418.

Matmon, A., Bierman, P.R., Larsen, J., Southworth, S., Pavich, M. and Caffee, M., 2003a. Temporally and spatially uniform rates of erosion in the southern Appalachian Great Smoky Mountains. *Geology*, 31(2), pp.155-158.

Matmon, A., Bierman, P.R., Larsen, J., Southworth, S., Pavich, M., Finkel, R. and Caffee, M., 2003b. Erosion of an ancient mountain range, the Great Smoky Mountains, North Carolina and Tennessee. *American Journal of Science*, 303(9), pp.817-855.

Matsushita, B., Yang, W., Chen, J., Onda, Y. and Qiu, G., 2007. Sensitivity of the enhanced vegetation index (EVI) and normalized difference vegetation index (NDVI) to topographic effects: a case study in high-density cypress forest. *Sensors*, 7(11), pp.2636-2651.

McKeon, R.E., Zeitler, P.K., Pazzaglia, F.J., Idleman, B.D. and Enkelmann, E., 2014. Decay of an old orogen: Inferences about Appalachian landscape evolution from low-temperature thermochronology. *Geological Society of America Bulletin*, 126(1-2), pp.31-46.

Mendes, M.D.C.O., Lobato, L.M., Suckau, V. and Lana, C., 2014. Datação U-Pb in situ por LA-ICPMS em zircões detríticos da Formação Cercadinho, Supergrupo Minas. *Geologia USP. Série Científica*, 14(1), pp.55-68.

- Miller, J.R., 1991. The influence of bedrock geology on knickpoint development and channel-bed degradation along downcutting streams in south-central Indiana. *The Journal of Geology*, 99(4), pp.591-605.
- Miller, S.R., Sak, P.B., Kirby, E. and Bierman, P.R., 2013. Neogene rejuvenation of central Appalachian topography: Evidence for differential rock uplift from stream profiles and erosion rates. *Earth and Planetary Science Letters*, 369, pp.1-12.
- Milliman, J.D. and Syvitski, J.P., 1992. Geomorphic/tectonic control of sediment discharge to the ocean: the importance of small mountainous rivers. *The Journal of Geology*, 100(5), pp.525-544.
- Miura, T., Huete, A.R., Yoshioka, H. and Holben, B.N., 2001. An error and sensitivity analysis of atmospheric resistant vegetation indices derived from dark target-based atmospheric correction. *Remote Sensing of Environment*, 78(3), pp.284-298.
- Molnar, P. and England, P., 1990. Late Cenozoic uplift of mountain ranges and global climate change: chicken or egg?. *Nature*, 346(6279), pp.29-34.
- Monteiro, H.S., Vasconcelos, P.M., Farley, K.A., Spier, C.A. and Mello, C.L., 2014. (U-Th)/He geochronology of goethite and the origin and evolution of cangas. *Geochimica et Cosmochimica Acta*, 131, pp.267-289.
- Monteiro, H.S., Vasconcelos, P.M.P. and Farley, K.A., 2018. A combined (U-Th)/He and Cosmogenic <sup>3</sup>He Record of Landscape Armoring by Biogeochemical Iron Cycling. *Journal of Geophysical Research: Earth Surface*, 123(2), 298-323.
- Montgomery, D.R. and Foufoula-Georgiou, E., 1993. Channel network source representation using digital elevation models. *Water Resources Research*, 29(12), pp.3925-3934.
- Montgomery, D.R. and Brandon, M.T., 2002. Topographic controls on erosion rates in tectonically active mountain ranges. *Earth and Planetary Science Letters*, 201(3-4), pp.481-489.

Mooney, W.D., Ritsema, J. and Hwang, Y.K., 2012. Crustal seismicity and the earthquake catalog maximum moment magnitude ( $M_{\text{cmax}}$ ) in stable continental regions (SCRs): Correlation with the seismic velocity of the lithosphere. *Earth and Planetary Science Letters*, 357, pp.78-83.

Moraes, L.D. and Guimarães, D., 1930. Geologia da região diamantífera do norte de Minas Gerais. *Anais da Academia Brasileira de Ciências*, 2(2), pp.153-186.

Moucha, R., Forte, A.M., Mitrovica, J.X., Rowley, D.B., Quéré, S., Simmons, N.A. and Grand, S.P., 2008. Dynamic topography and long-term sea-level variations: There is no such thing as a stable continental platform. *Earth and Planetary Science Letters*, 271(1-4), pp.101-108.

Mudd, S.M., Attal, M., Milodowski, D.T., Grieve, S.W. and Valters, D.A., 2014. A statistical framework to quantify spatial variation in channel gradients using the integral method of channel profile analysis. *Journal of Geophysical Research: Earth Surface*, 119(2), pp.138-152.

Mudd, S.M., Harel, M.A., Hurst, M.D., Grieve, S.W.D. and Marrero, S.M., 2016. The CAIRN method: automated, reproducible calculation of catchment-averaged denudation rates from cosmogenic nuclide concentrations. *Earth Surface Dynamics*, 4(3), pp.655-674.

Neely, A.B., Bookhagen, B. and Burbank, D.W., 2017. An automated knickzone selection algorithm (KZ-Picker) to analyze transient landscapes: Calibration and validation. *Journal of Geophysical Research: Earth Surface*, 122, pp.1236-1261.

Niedermann, S., 2002. Cosmic-ray-produced noble gases in terrestrial rocks: dating tools for surface processes. *Reviews in Mineralogy and Geochemistry*, 47(1), pp.731-784.

Niemann, J.D., Gasparini, N.M., Tucker, G.E. and Bras, R.L., 2001. A quantitative evaluation of Playfair's law and its use in testing long-term stream erosion models. *Earth Surface Processes and Landforms*, 26(12), pp.1317-1332.

- Niemi, N.A., Oskin, M., Burbank, D.W., Heimsath, A.M. and Gabet, E.J., 2005. Effects of bedrock landslides on cosmogenically determined erosion rates. *Earth and Planetary Science Letters*, 237(3-4), pp.480-498.
- Nishiizumi, K., Winterer, E.L., Kohl, C.P., Klein, J., Middleton, R., Lal, D. and Arnold, J.R., 1989. Cosmic ray production rates of  $^{10}\text{Be}$  and  $^{26}\text{Al}$  in quartz from glacially polished rocks. *Journal of Geophysical Research: Solid Earth*, 94(B12), pp.17907-17915.
- Noce, C.M., Machado, N. and Teixeira, W., 1998. U-Pb geochronology of gneisses and granitoids in the Quadrilátero Ferrífero (Southern Sao Francisco craton, Brazil): age constraints for Archean and paleoproterozoic magmatism and metamorphism. *Revista Brasileira de Geociências*, 28(1), pp.95-102.
- Noce, C.M., Zuccheti, M., Baltazar, O.F., Armstrong, R., Dantas, E., Renger, F.E. and Lobato, L.M., 2005. Age of felsic volcanism and the role of ancient continental crust in the evolution of the Neoproterozoic Rio das Velhas Greenstone belt (Quadrilátero Ferrífero, Brazil): U-Pb zircon dating of volcanoclastic graywackes. *Precambrian Research*, 141(1-2), pp.67-82.
- Ouimet, W.B., Whipple, K.X. and Granger, D.E., 2009. Beyond threshold hillslopes: Channel adjustment to base-level fall in tectonically active mountain ranges. *Geology*, 37(7), pp.579-582.
- Pazzaglia, F.J. and Gardner, T.W., 1994. Late Cenozoic flexural deformation of the middle US Atlantic passive margin. *Journal of Geophysical Research: Solid Earth*, 99(B6), pp.12143-12157.
- Pazzaglia, F.J. and Brandon, M.T., 1996. Macroeomorphic evolution of the post-Triassic Appalachian mountains determined by deconvolution of the offshore basin sedimentary record. *Basin Research*, 8(3), pp.255-278.
- Pelletier, J.D., 2008. *Quantitative modeling of earth surface processes*. Cambridge: Cambridge University Press.

- Pelletier, J.D., 2010. Numerical modeling of the late Cenozoic geomorphic evolution of Grand Canyon, Arizona. *Geological Society of America Bulletin*, 122(3-4), pp.595-608.
- Penck, W., 1924. *Die Morphologyische Analyse*. Stuttgart: J. Engelhorn's Nachfolger. (Translation by H. Czech and K.C. Boswell, 1953, New York: St. Martin's Press).
- Perron, J.T. and Royden, L., 2013. An integral approach to bedrock river profile analysis. *Earth Surface Processes and Landforms*, 38(6), pp.570-576.
- Phillips, F.M., Argento, D.C., Balco, G., Caffee, M.W., Clem, J., Dunai, T.J., Finkel, R., Goehring, B., Gosse, J.C., Hudson, A.M., Jull, A.T., Kelly, M.A., Kurz, M., Lal, D., Lifton, N., Marrero, S., Nishiizumi, K., Reedy, R.C., and Zreda, M.G., 2016. The CRONUS-Earth project: a synthesis. *Quaternary Geochronology*, 31, pp.119-154.
- Pinet, P. and Souriau, M., 1988. Continental erosion and large-scale relief. *Tectonics*, 7(3), pp.563-582.
- Pitman, W.C. and Golovchenko, X., 1991. The effect of sea level changes on the morphology of mountain belts. *Journal of Geophysical Research: Solid Earth*, 96(B4), pp.6879-6891.
- Playfair, J., 1802. *Illustrations of the Huttonian Theory of the Earth*. Edinburgh: Cadell and Davies.
- Portenga, E.W. and Bierman, P.R., 2011. Understanding Earth's eroding surface with  $^{10}\text{Be}$ . *Geological Society of America Today*, 21(8), pp.4-10.
- Portenga, E.W., Bierman, P.R., Rizzo, D.M. and Rood, D.H., 2013. Low rates of bedrock outcrop erosion in the central Appalachian Mountains inferred from in situ  $^{10}\text{Be}$ . *Geological Society of America Bulletin*, 125(1-2), pp.201-215.

Powell, J.W., 1876. *Report on the geology of the eastern portion of the Uinta Mountains and a region of country adjacent thereto*. Washington: US Geological and Geographical Survey of the Territories, Government Printing Office.

Prince, P.S., Spotila, J.A. and Henika, W.S., 2011. Stream capture as driver of transient landscape evolution in a tectonically quiescent setting. *Geology*, 39(9), pp.823-826.

Prince, P.S. and Spotila, J.A., 2013. Evidence of transient topographic disequilibrium in a landward passive margin river system: knickpoints and paleo-landscapes of the New River basin, southern Appalachians. *Earth Surface Processes and Landforms*, 38(14), pp.1685-1699.

Puchol, N., Lavé, J., Lupker, M., Blard, P.H., Gallo, F., France-Lanord, C. and ASTER Team, 2014. Grain-size dependent concentration of cosmogenic  $^{10}\text{Be}$  and erosion dynamics in a landslide-dominated Himalayan watershed. *Geomorphology*, 224, pp.55-68.

Quigley, M., Sandiford, M., Fifield, K. and Alimanovic, A., 2007. Bedrock erosion and relief production in the northern Flinders Ranges, Australia. *Earth Surface Processes and Landforms*, 32(6), pp.929-944.

Ramsey, L.A., Hovius, N., Lague, D. and Liu, C.S., 2006. Topographic characteristics of the submarine Taiwan orogen. *Journal of Geophysical Research: Earth Surface*, 111(F2), pp.1-21.

Raymo, M.E. and Ruddiman, W.F., 1992. Tectonic forcing of late Cenozoic climate. *Nature*, 359(6391), p.117-122.

Reedy, R.C., 2013. Cosmogenic-nuclide production rates: Reaction cross section update. *Nuclear Instruments and Methods in Physics Research Section B: Beam Interactions with Materials and Atoms*, 294, pp.470-474.

Reiners, P.W., Ehlers, T.A. and Zeitler, P.K., 2005. Past, present, and future of thermochronology. *Reviews in Mineralogy and Geochemistry*, 58(1), pp.1-18.

- Reiners, P.W. and Brandon, M.T., 2006. Using thermochronology to understand orogenic erosion. *Annual Review of Earth and Planetary Sciences*, 34, pp.419-466.
- Reiners, P.W. and Shuster, D.L., 2009. Thermochronology and landscape evolution. *Physics Today*, 62(9), p.31.
- Riebe, C.S., Kirchner, J.W., Granger, D.E. and Finkel, R.C., 2000. Erosional equilibrium and disequilibrium in the Sierra Nevada, inferred from cosmogenic  $^{26}\text{Al}$  and  $^{10}\text{Be}$  in alluvial sediment. *Geology*, 28(9), pp.803-806.
- Roda-Boluda, D.C. and Whittaker, A.C., 2017. Structural and geomorphological constraints on active normal faulting and landscape evolution in Calabria, Italy. *Journal of the Geological Society*, 174(4), pp.701-720.
- Rodríguez Tribaldos, V., White, N.J., Roberts, G.G. and Hoggard, M.J., 2017. Spatial and Temporal Uplift History of South America from Calibrated Drainage Analysis. *Geochemistry, Geophysics, Geosystems*, 18(6), pp.2321-2353.
- Romano, R., Lana, C., Alkmim, F.F., Stevens, G. and Armstrong, R., 2013. Stabilization of the southern portion of the São Francisco craton, SE Brazil, through a long-lived period of potassic magmatism. *Precambrian Research*, 224, pp.143-159.
- Rosière, C.A., Siemes, H., Quade, H., Brokmeier, H.G. and Jansen, E.M., 2001. Microstructures, textures and deformation mechanisms in hematite. *Journal of Structural Geology*, 23(9), pp.1429-1440.
- Rousseeuw, P.J., 1987. Silhouettes: a graphical aid to the interpretation and validation of cluster analysis. *Journal of Computational and Applied Mathematics*, 20, pp.53-65.
- Ruellan, F., 1950. Contribuição ao estudo da Serra do Caraça. *Anais Associados dos Geógrafos Brasileiros*, 4(2), pp.77-106.

Ruxton, B.P. and McDougall, I., 1967. Denudation rates in northeast Papua from potassium-argon dating of lavas. *American Journal of Science*, 265(7), pp.545-561.

Saadi, A., 1991. *Ensaio sobre a Morfotectônica de Minas Gerais: Tensões Intra-Placa, Descontinuidades Crustais e Morfogênese*. Habilitation thesis. Federal University of Minas Gerais.

Saadi, A., Sgarbi, G.N.C. and Rosière, C.A., 1992. A Bacia do Gongo Soco; nova bacia terciária no Quadrilátero Ferrífero: controle cárstico e/ou tectônico. In: *Congresso Brasileiro de Geologia*, 37. São Paulo: Sociedade Brasileira de Geologia, pp.600-601.

Safran, E.B., Bierman, P.R., Aalto, R., Dunne, T., Whipple, K.X. and Caffee, M., 2005. Erosion rates driven by channel network incision in the Bolivian Andes. *Earth Surface Processes and Landforms*, 30(8), pp.1007-1024.

Salgado, A.A.R., Varajão, C.A.C., Colin, F., Braucher, R., Varajão, A.F.D.C. and Nalini Jr, H.A., 2007a. Study of the erosion rates in the upper Maracujá Basin (Quadrilátero Ferrífero/MG, Brazil) by the in situ produced cosmogenic  $^{10}\text{Be}$  method. *Earth Surface Processes and Landforms*, 32(6), pp.905-911.

Salgado, A.A.R., Varajão, C.A.C., Colin, F., Braucher, R., Varajão, A.F.D.C., Júnior, H.A.N., Cherem, L.F.S., Marrent, B.R. and Brindusa, C.B., 2007b. Estimativa das Taxas de Erosão das Terras Altas da Alta Bacia do Rio Das Velhas no Quadrilátero Ferrífero: Implicações para A Evolução Do Relevo. *Revista Brasileira de Geomorfologia*, 8(2), pp.3-10.

Salgado, A.A.R., Braucher, R., Varajao, A.C., Colin, F., Varajão, A.F.D.C. and Nalini Jr, H.A., 2008. Relief evolution of the Quadrilátero Ferrífero (Minas Gerais, Brazil) by means of ( $^{10}\text{Be}$ ) cosmogenic nuclei. *Zeitschrift für Geomorphologie*, 52(3), pp.317-323.

Salgado, A.A.R. and Carmo, F.F., 2015. 'Quadrilátero Ferrífero': a beautiful and neglected landscape between the gold and iron ore reservoirs. In: Vieira B.,

- Salgado A., Santos L. (Eds.), *Landscapes and Landforms of Brazil*. Dordrecht: Springer, pp.319-330.
- Sant'Anna, L.G., Schorscher, H.D. and Riccomini, C., 1997. Cenozoic tectonics of the Fonseca basin region, eastern Quadrilátero Ferrífero, MG, Brazil. *Journal of South American Earth Sciences*, 10(3-4), pp.275-284.
- Santos, M.C., Varajão, A.F.D.C. and Yvon, J., 2004. Genesis of clayey bodies in Quadrilátero Ferrífero, Minas Gerais, Brazil. *Catena*, 55(3), pp.277-291.
- Scharf, T.E., Codilean, A.T., De Wit, M., Jansen, J.D. and Kubik, P.W., 2013. Strong rocks sustain ancient postorogenic topography in southern Africa. *Geology*, 41(3), pp.331-334.
- Scherler, D., Bookhagen, B. and Strecker, M.R., 2014. Tectonic control on <sup>10</sup>Be-derived erosion rates in the Garhwal Himalaya, India. *Journal of Geophysical Research: Earth Surface*, 119(2), pp.83-105.
- Schön, J.H., 2015. *Physical Properties of Rocks: Fundamentals and principles of petrophysics*, 65. 2nd edition. Oxford: Elsevier.
- Schumm, S.A., 1956. Evolution of drainage systems and slopes in badlands at Perth Amboy, New Jersey. *Geological Society of America Bulletin*, 67(5), pp.597-646.
- Schumm, S.A., 1963. The disparity between present rates of denudation and orogeny. *US Geological Survey Professional Paper*, 454-H, pp.H1-H13.
- Schumm, S.A. and Lichtig, R.W., 1965. Time, space, and causality in geomorphology. *American Journal of Science*, 263(2), pp.110-119.
- Schwanghart, W. and Scherler, D., 2014. TopoToolbox 2-MATLAB-based software for topographic analysis and modeling in Earth surface sciences. *Earth Surface Dynamics*, 2(1), p.1-7.

SEA (Secretaria de Estado de Agricultura), 1980. Atlas de zoneamento agroclimático do Estado de Minas Gerais. Available at: <http://www.ide.ufv.br/geominas/> [accessed January 2018].

Silverman, B.W., 1986. *Density Estimation for Statistics and Data Analysis*. London: Chapman and Hall.

Sklar, L.S. and Dietrich, W.E., 2001. Sediment and rock strength controls on river incision into bedrock. *Geology*, 29(12), pp.1087-1090.

Sklar, L.S. and Dietrich, W.E., 2004. A mechanistic model for river incision into bedrock by saltating bed load. *Water Resources Research*, 40(6), pp.1-21.

Spier, C.A., Vasconcelos, P.M. and Oliviera, S.M., 2006.  $^{40}\text{Ar}/^{39}\text{Ar}$  geochronological constraints on the evolution of lateritic iron deposits in the Quadrilátero Ferrífero, Minas Gerais, Brazil. *Chemical Geology*, 234(1-2), pp.79-104.

Starke, J., Ehlers, T.A. and Schaller, M., 2017. Tectonic and climatic controls on the spatial distribution of denudation rates in northern Chile ( $18^\circ\text{ S}$  to  $23^\circ\text{ S}$ ) determined from cosmogenic nuclides. *Journal of Geophysical Research: Earth Surface*, 122(10), pp.1949-1971.

Stock, J.D. and Montgomery, D.R., 1999. Geologic constraints on bedrock river incision using the stream power law. *Journal of Geophysical Research: Solid Earth*, 104(B3), pp.4983-4993.

Stock, G.M., Frankel, K.L., Ehlers, T.A., Schaller, M., Briggs, S.M. and Finkel, R.C., 2009. Spatial and temporal variations in denudation of the Wasatch Mountains, Utah, USA. *Lithosphere*, 1(1), pp.34-40.

Stone, J.O., 2000. Air pressure and cosmogenic isotope production. *Journal of Geophysical Research: Solid Earth*, 105(B10), pp.23753-23759.

Strahler, A.N., 1957. Quantitative analysis of watershed geomorphology. *Eos, Transactions American Geophysical Union*, 38(6), pp.913-920.

- Summerfield, M.A., 1991. *Global Geomorphology*. New York: Longman, London, and John Wiley.
- Summerfield, M.A. and Hulton, N.J., 1994. Natural controls of fluvial denudation rates in major world drainage basins. *Journal of Geophysical Research: Solid Earth*, 99(B7), pp.13871-13883.
- Teixeira, W., Oliveira, E.P. and Marques, L.S., 2017. Nature and evolution of the Archean crust of the São Francisco Craton. In: Heilbron, M., Cordani, U. G., and Alkmim, F. F. (Eds.), *São Francisco Craton, Eastern Brazil*. Cham: Springer, pp.29-56.
- Telford, W.M., Telford, W.M., Geldart, L.P. and Sheriff, R.E., 1990. *Applied geophysics*. Cambridge: Cambridge University Press.
- Thornbury, W.D., 1969. *Principles of geomorphology*. 2nd edition. New York: Wiley.
- Twidale, C.R., 1976. On the survival of palaeoforms. *American Journal of Science*, 276(1), pp.77-95.
- Twidale, C.R., 1991. A model of landscape evolution involving increased and increasing relief amplitude. *Zeitschrift fur Geomorphologie*, 35(1), pp.85-109.
- Twidale, C.R., 1994. Gondwanan (Late Jurassic and Cretaceous) palaeosurfaces of the Australian craton. *Palaeogeography, Palaeoclimatology, Palaeoecology*, 112(1-2), pp.157-186.
- Twidale, C.R., 1998. Antiquity of landforms: an 'extremely unlikely' concept vindicated. *Australian Journal of Earth Sciences*, 45(5), pp.657-668.
- Twidale, C.R., 1999. Landforms ancient and recent: the paradox. *Geografiska Annaler: Series A, Physical Geography*, 81(3), pp.431-441.
- Twidale, C.R., 2016. Enigmatic mesozoic paleoforms revisited: the Australian experience. *Earth-science reviews*, 155, pp.82-92.

- Varajão, C.A.C., 1991. A questão da correlação das superfícies de erosão do Quadrilátero Ferrífero, Minas Gerais. *Revista Brasileira de Geociências*, 21(2), pp.138-145.
- Vasconcelos, P. M., 1999.  $^{40}\text{Ar}/^{39}\text{Ar}$  geochronology of supergene processes in ore deposits. *Economic Geology*, 12, pp.73-113.
- Vial, D.S., Duarte, B.P., Fuzikawa, K. and Vieira, M.B.H., 2007. An epigenetic origin for the Passagem de Mariana gold deposit, Quadrilátero Ferrífero, Minas Gerais, Brazil. *Ore Geology Reviews*, 32(3-4), pp.596-613.
- von Blanckenburg, F., Hewawasam, T. and Kubik, P.W., 2004. Cosmogenic nuclide evidence for low weathering and denudation in the wet, tropical highlands of Sri Lanka. *Journal of Geophysical Research: Earth Surface*, 109(F03), pp.1-22.
- von Blanckenburg, F., 2005. The control mechanisms of erosion and weathering at basin scale from cosmogenic nuclides in river sediment. *Earth and Planetary Science Letters*, 242(3-4), pp.462-479.
- von Blanckenburg, F. and Willenbring, J.K., 2014. Cosmogenic nuclides: Dates and rates of Earth-surface change. *Elements*, 10(5), pp.341-346.
- von Eschwege, W. L., 1833. *Pluto Brasiliensis*. Berlin: G. Reimer.
- Xu, S., Freeman, S.P., Rood, D.H. and Shanks, R.P., 2015. Decadal  $^{10}\text{Be}$ ,  $^{26}\text{Al}$  and  $^{36}\text{Cl}$  QA measurements on the SUERC 5 MV accelerator mass spectrometer. *Nuclear Instruments and Methods in Physics Research Section B: Beam Interactions with Materials and Atoms*, 361, pp.39-42.
- Young, R.W., 1983. The tempo of geomorphological change: evidence from southeastern Australia. *The Journal of Geology*, 91(2), pp.221-230.
- Ward, D.J., Spotila, J.A., Hancock, G.S. and Galbraith, J.M., 2005. New constraints on the late Cenozoic incision history of the New River, Virginia. *Geomorphology*, 72(1-4), pp.54-72.

- Wessel, B., 2016. TanDEM-X Ground Segment-DEM Products Specification Document. *Public Document TD-GS-PS-0021*, 3.1. Oberpfaffenhofen: DLR, pp.1-46.
- Whipple, K.X. and Tucker, G.E., 1999. Dynamics of the stream-power river incision model: Implications for height limits of mountain ranges, landscape response timescales, and research needs. *Journal of Geophysical Research: Solid Earth*, 104(B8), pp.17661-17674.
- Whipple, K.X., 2001. Fluvial landscape response time: How plausible is steady-state denudation?. *American Journal of Science*, 301(4-5), pp.313-325.
- Whipple, K.X. and Tucker, G.E., 2002. Implications of sediment-flux-dependent river incision models for landscape evolution. *Journal of Geophysical Research: Solid Earth*, 107(B2).
- Whipple, K.X., 2004. Bedrock rivers and the geomorphology of active orogens. *Annual Review of Earth and Planetary Sciences*, 32, pp.151-185.
- Whipple, K.X., DiBiase, R.A. and Crosby, B.T., 2013. Bedrock rivers. *In: Schroder, J. and Wohl E. (Eds.), Treatise on Geomorphology*. San Diego: Academic Press, pp.550-573.
- Whittaker, A.C., Cowie, P.A., Attal, M., Tucker, G.E. and Roberts, G.P., 2007. Bedrock channel adjustment to tectonic forcing: Implications for predicting river incision rates. *Geology*, 35(2), pp.103-106.
- Willenbring, J.K. and von Blanckenburg, F., 2010. Meteoric cosmogenic Beryllium-10 adsorbed to river sediment and soil: Applications for Earth-surface dynamics. *Earth-Science Reviews*, 98(1-2), pp.105-122.
- Willetts, S.D., 1999. Orogeny and orography: The effects of erosion on the structure of mountain belts. *Journal of Geophysical Research: Solid Earth*, 104(B12), pp.28957-28981.

Willett, S.D. and Brandon, M.T., 2002. On steady states in mountain belts. *Geology*, 30(2), pp.175-178.

Willgoose, G., Bras, R.L. and Rodriguez-Iturbe, I., 1991. A coupled channel network growth and hillslope evolution model: 1. Theory. *Water Resources Research*, 27(7), pp.1671-1684.

Wobus, C., Whipple, K.X., Kirby, E., Snyder, N., Johnson, J., Spyropolou, K., Crosby, B., Sheehan, D., 2006a. Tectonics from topography: procedures, promise, and pitfalls. *In: Willett, S.D., Hovius, N., Brandon, M.T., Fisher, D.M. (Eds.), Tectonics, Climate, and Landscape Evolution*. Boulder: Geological Society of America Special Paper, 398, pp.55-74.



## Appendix A

The purpose of this appendix is to provide the full dataset of bivariate regression analyses between every pairwise combination of catchment-averaged topographic parameters for basins datasets including:

- A. 2nd order basins (n=997) - Table A1;
- B. 3rd order basins (n=865) - Table A2;
- C. 4th order basins (n=253) - Table A3;
- D. 5th order basins (n=79) - Table A4;
- E. All basins (n=2200) - Table A5;
- F. All basins except basin order 1 and basin order 2 (n=1203) - Table A6;
- G. All basins with an area greater than 5 km<sup>2</sup> (n=492) - Table A7.

The correlation matrix for each dataset is presented in the sequence.

**Table A1.** Correlation between every pairwise combination of catchment-averaged parameters for the dataset comprising second-order basins (n=997).

<b>2nd order basins (n=997)</b>									
Max. slope (°)	Mean slope (°)	Local relief (m)	Max. elevation (m)	Mean elevation (m)	Basin relief (m)	$k_{sn}$ (m <sup>0.9</sup> )	Knickpoint magnitude (m)	Knickpoint relief (m)	
0.019	0	0	0.016	0.002	0.048	0.004	0	0.001	Area (m <sup>2</sup> )
	0.397	0.436	0.295	0.131	0.414	0.285	0.105	0.135	Max. slope (°)
		0.595	0.2	0.058	0.481	0.423	0.069	0.145	Mean slope (°)
			0.514	0.229	0.826	0.745	0.247	0.386	Local relief (m)
				0.846	0.455	0.342	0.119	0.173	Max. elevation (m)
					0.132	0.162	0.079	0.095	Mean elevation (m)
	R2 < 0.4					0.713	0.236	0.355	Basin relief (m)
	0.4 < R2 < 0.6						0.382	0.542	$k_{sn}$ (m <sup>0.9</sup> )
	R2 > 0.6							0.838	Knickpoint magnitude (m)
									Knickpoint relief (m)

**Table A2.** Correlation between every pairwise combination of catchment-averaged parameters for the dataset comprising third-order basins (n=865).

3rd order basins (n=865)									
Max. slope (°)	Mean slope (°)	Local relief (m)	Max. elevation (m)	Mean elevation (m)	Basin relief (m)	$k_{sn}$ (m <sup>0.9</sup> )	Knickpoint magnitude (m)	Knickpoint relief (m)	
0.068	0.000	0.000	0.053	0.014	0.093	0.002	0.000	0.001	Area (m <sup>2</sup> )
	0.288	0.369	0.357	0.162	0.425	0.277	0.121	0.149	Max. slope (°)
		0.648	0.27	0.099	0.466	0.509	0.113	0.22	Mean slope (°)
			0.553	0.252	0.758	0.829	0.349	0.539	Local relief (m)
				0.794	0.581	0.458	0.188	0.257	Max. elevation (m)
					0.174	0.234	0.105	0.126	Mean elevation (m)
	R2 < 0.4					0.702	0.282	0.407	Basin relief (m)
	0.4 < R2 < 0.6						0.421	0.605	$k_{sn}$ (m <sup>0.9</sup> )
	R2 > 0.6							0.852	Knickpoint magnitude (m)
									Knickpoint relief (m)

**Table A3.** Correlation between every pairwise combination of catchment-averaged parameters for the dataset comprising fourth-order basins (n=253).

<b>4th order basins (n=253)</b>									
Max. slope (°)	Mean slope (°)	Local relief (m)	Max. elevation (m)	Mean elevation (m)	Basin relief (m)	$k_{sn}$ (m <sup>0.9</sup> )	Knickpoint magnitude (m)	Knickpoint relief (m)	
0.090	0.000	0.000	0.098	0.027	0.135	0.002	0.003	0.002	Area (m <sup>2</sup> )
	0.169	0.279	0.393	0.153	0.391	0.251	0.156	0.202	Max. slope (°)
		0.685	0.278	0.072	0.419	0.585	0.194	0.275	Mean slope (°)
			0.525	0.158	0.676	0.878	0.503	0.642	Local relief (m)
				0.617	0.708	0.508	0.224	0.273	Max. elevation (m)
					0.14	0.176	0.041	0.042	Mean elevation (m)
	R <sup>2</sup> < 0.4					0.7	0.352	0.428	Basin relief (m)
	0.4 < R <sup>2</sup> < 0.6						0.483	0.596	$k_{sn}$ (m <sup>0.9</sup> )
	R <sup>2</sup> > 0.6							0.877	Knickpoint magnitude (m)
									Knickpoint relief (m)

**Table A4.** Correlation between every pairwise combination of catchment-averaged parameters for the dataset comprising fifth-order basins (n=79).

5th order basins (n=79)									
Max. slope (°)	Mean slope (°)	Local relief (m)	Max. elevation (m)	Mean elevation (m)	Basin relief (m)	$k_{sn}$ (m <sup>0.9</sup> )	Knickpoint magnitude (m)	Knickpoint relief (m)	
0.130	0.001	0.001	0.121	0.028	0.121	0.000	0.002	0.001	Area (m <sup>2</sup> )
	0.088	0.187	0.333	0.103	0.335	0.158	0.166	0.161	Max. slope (°)
		0.796	0.382	0.166	0.426	0.703	0.234	0.332	Mean slope (°)
			0.55	0.223	0.609	0.904	0.474	0.535	Local relief (m)
				0.501	0.815	0.547	0.344	0.339	Max. elevation (m)
					0.16	0.266	0.065	0.041	Mean elevation (m)
	$R^2 < 0.4$					0.628	0.452	0.486	Basin relief (m)
	$0.4 < R^2 < 0.6$						0.536	0.616	$k_{sn}$ (m <sup>0.9</sup> )
	$R^2 > 0.6$							0.904	Knickpoint magnitude (m)
									Knickpoint relief (m)

**Table A5.** Correlation between every pairwise combination of catchment-averaged parameters for the dataset comprising all basins (n=2200).

<u>All basins (n=2200)</u>									
Max. slope (°)	Mean slope (°)	Local relief (m)	Max. elevation (m)	Mean elevation (m)	Basin relief (m)	$k_{sn}$ (m <sup>0.9</sup> )	Knickpoint magnitude (m)	Knickpoint relief (m)	
0.026	0.000	0.000	0.016	0.000	0.048	0.000	0.000	0.000	Area (m <sup>2</sup> )
	0.24	0.294	0.348	0.096	0.486	0.226	0.08	0.099	Max. slope (°)
		0.628	0.221	0.077	0.337	0.474	0.089	0.178	Mean slope (°)
			0.496	0.231	0.569	0.793	0.289	0.447	Local relief (m)
				0.725	0.549	0.391	0.133	0.187	Max. elevation (m)
					0.097	0.192	0.082	0.101	Mean elevation (m)
	R <sup>2</sup> < 0.4					0.545	0.174	0.254	Basin relief (m)
	0.4 < R <sup>2</sup> < 0.6						0.389	0.554	$k_{sn}$ (m <sup>0.9</sup> )
	R <sup>2</sup> > 0.6							0.845	Knickpoint magnitude (m)
									Knickpoint relief (m)

**Table A6.** Correlation between every pairwise combination of catchment-averaged parameters for the dataset comprising all basins, except basin order 1 and basin order 2 (n=1203).

<b>All basins but order 1 and 2 (n=1203)</b>									
Max. slope (°)	Mean slope (°)	Local relief (m)	Max. elevation (m)	Mean elevation (m)	Basin relief (m)	$k_{sn}$ (m <sup>0.9</sup> )	Knickpoint magnitude (m)	Knickpoint relief (m)	
0.031	0.000	0.000	0.024	0.000	0.055	0.000	0.000	0.000	Area (m <sup>2</sup> )
	0.198	0.269	0.394	0.127	0.477	0.226	0.103	0.121	Max. slope (°)
		0.66	0.251	0.097	0.344	0.526	0.123	0.228	Mean slope (°)
			0.496	0.233	0.553	0.837	0.367	0.551	Local relief (m)
				0.687	0.633	0.441	0.177	0.235	Max. elevation (m)
					0.127	0.225	0.092	0.107	Mean elevation (m)
						0.555	0.222	0.308	Basin relief (m)
	R <sup>2</sup> < 0.4						0.428	0.6	$k_{sn}$ (m <sup>0.9</sup> )
	0.4 < R <sup>2</sup> < 0.6							0.856	Knickpoint magnitude (m)
	R <sup>2</sup> > 0.6								Knickpoint relief (m)

**Table A7.** Correlation between every pairwise combination of catchment-averaged parameters for the dataset comprising all basins with an area greater than 5 km<sup>2</sup> (n=492).

All basins with an area > than 5km2 (n=492)									
Max. slope (°)	Mean slope (°)	Local relief (m)	Max. elevation (m)	Mean elevation (m)	Basin relief (m)	$k_{sn}$ (m <sup>0.9</sup> )	Knickpoint magnitude (m)	Knickpoint relief (m)	
0.169	0.002	0.000	0.104	0.003	0.183	0.006	0.001	0.001	Area (m <sup>2</sup> )
	0.213	0.322	0.385	0.117	0.475	0.296	0.219	0.263	Max. slope (°)
		0.727	0.315	0.109	0.483	0.627	0.225	0.361	Mean slope (°)
			0.591	0.263	0.708	0.895	0.46	0.663	Local relief (m)
				0.636	0.694	0.551	0.283	0.378	Max. elevation (m)
	R <sup>2</sup> < 0.4				0.16	0.257	0.115	0.122	Mean elevation (m)
	0.4 < R <sup>2</sup> < 0.6					0.717	0.373	0.528	Basin relief (m)
	R <sup>2</sup> > 0.6						0.543	0.716	$k_{sn}$ (m <sup>0.9</sup> )
								0.886	Knickpoint magnitude (m)
									Knickpoint relief (m)

## Appendix B

The purpose of this appendix is to provide a dataset of denudation rates for the analysed basins in the QF, using time-dependent scaling factors. The estimates of denudation rates reported in Appendix B were obtained using the CRONUS-Earth online calculator version 2.3 (<http://hess.ess.washington.edu/>, accessed January 2018; Balco et al., 2008). Table B1 exhibit denudation rates based on the time-dependent scaling scheme reported by Dunai (2001); (Lifton et al., 2005); and Lal/Stone reported by Balco et al. (2008). Table B1 also shows the denudation rates presented in the main body of this thesis.

Table B1. Denudation rates for the analysed basins in the QF using different scaling schemes.

SAMPLE ID	Time-independent		Time-dependent					
	Lal(1991) / Stone(2000)		Dunai, 2001		Lifton et al., 2005		Lal(1991) / Stone(2000)	
	Denudation rate (m/Myr)	External uncertainty (m/Myr)						
GDP1	7.4	0.6	8.4	3.9	8.4	0.8	8.8	0.7
GDP4	2.9	0.3	3.3	1.6	3.3	0.3	3.6	0.3
GDP5	2.6	0.3	3.0	1.5	3.1	0.3	3.2	0.3
GDP6	4.3	0.4	5.0	2.4	5.1	0.5	5.2	0.5
GDP7	3.0	0.3	3.5	1.7	3.6	0.4	3.6	0.3
GDP8	3.7	0.3	4.3	2.1	4.4	0.4	4.6	0.4
GDP12A	2.0	0.2	2.3	2.2	2.4	1.2	2.5	0.2
GDP13F	3.4	0.3	3.9	3.0	4.0	0.4	4.1	0.4
GDP14	3.6	0.3	4.1	2.0	4.1	0.4	4.4	0.4
GDP15	4.0	0.4	4.7	2.3	4.8	0.5	4.9	0.4
GDP17	17.7	1.4	19.3	1.9	19.3	1.7	20.0	1.5
GDP18	5.5	0.5	6.2	3.0	6.2	0.6	6.6	0.6
GDP23	6.1	0.5	7.0	3.3	7.0	0.7	7.3	0.6
GDP24	6.0	0.5	6.9	4.5	7.0	0.7	7.2	0.6
GDP25F	6.1	0.5	7.0	4.5	7.1	0.7	7.3	0.6
GDP26	6.0	0.5	6.8	3.2	6.9	0.7	7.2	0.6
GDP27	9.7	0.8	10.9	1.1	10.9	1.0	11.3	0.9
GDP29	8.5	0.7	9.6	4.5	9.7	0.9	10.1	0.8
GDP32	6.1	0.5	6.9	3.3	6.9	0.7	7.3	0.6
GDP36	7.1	0.6	8.1	3.8	8.1	0.8	8.5	0.7
GDP37	22.6	1.7	24.5	2.4	24.4	2.1	25.2	1.9
GDP38	12.3	1.0	13.7	1.4	13.7	1.2	14.3	1.1
GDP39	22.8	1.7	24.7	2.4	24.5	2.1	25.4	1.9
GDP40	17.3	1.3	19.0	1.9	18.9	1.6	19.6	1.5
GDP43	30.0	2.3	32.1	3.1	31.9	2.7	32.9	2.5
SBR1	9.3	2.5	10.5	5.5	10.5	2.8	10.9	2.9
SBR2	14.3	6.8	15.9	7.6	15.9	7.6	16.4	7.8
SBR3	14.2	2.4	15.6	2.8	15.7	2.7	16.2	2.7
SBR4	4.3	2.0	5.0	3.3	5.0	2.3	5.2	2.4
S5	0.7	0.5	0.9	0.5	0.9	0.6	0.9	1.6
S6	2.3	0.8	2.8	1.6	2.8	1.7	2.9	1.0
S7	2.6	0.3	3.0	1.5	3.1	0.4	3.2	0.4
S8	7.5	1.4	8.6	4.2	8.6	1.6	8.9	1.6

